PSFC/RR-09-15 **DOE/ET-54512-369**

Plasma Flows in the Alcator C-Mod Scrape-Off Layer

Smick, N.

December 2009

Plasma Science and Fusion Center
Massachusetts Institute of Technology
Cambridge MA 02139 USA

This work was supported by the U.S. Department of Energy, Grant No. DE-FC02-99ER54512-CMOD.

Plasma Flows in the Alcator C-Mod Scrape-Off Layer

by

Noah M. Smick

Submitted to the Department of Nuclear Science and Engineering
in partial fulfillment of the requirements for the degree of

Doctor of Philosophy, Applied Plasma Physics

at the

MASSACHUSETTS INSTITUTE OF TECHNOLOGY

December 2009

Author .....
Department of Nuclear Science and Engineering
December 4, 2009

Certified by .....
Brian LaBombard
Principal Research Scientist, Plasma Science and Fusion Center
Thesis Supervisor

Certified by .....
Ian H. Hutchinson
Professor of Nuclear Science and Engineering
Thesis Reader

Accepted by .....
Jacquelyn C. Yanch
Chair, Department Committee on Graduate Theses

Plasma Flows in the Alcator C-Mod Scrape-Off Layer

by

Noah M. Smick

Submitted to the Department of Nuclear Science and Engineering
on December 4, 2009, in partial fulfillment of the
requirements for the degree of
Doctor of Philosophy, Applied Plasma Physics

Abstract

Near-sonic parallel plasma flows are persistently observed in the scrape-off layer (SOL) of tokamaks, at locations far from material surfaces. Ballooning-like transport asymmetries are thought to be a principal driver for the strong parallel flows, a hypothesis supported by the observation of steep high-field side pressure profiles in double-null discharges. Yet parallel flow can also arise as a result of toroidal plasma rotation and/or neoclassical Pfirsch-Schlüter currents. In addition, the mechanism that closes the mass-flow loop back onto itself has remained elusive. To investigate these phenomena, a novel magnetically-actuated scanning probe has been deployed on the high-field side in Alcator C-Mod. This probe, along with two other scanning probes on the low-field side, measure the total plasma flow vector at these locations: parallel flows, perpendicular $E_r \times B$ drifts and radial fluctuation-induced particle fluxes.

Boundary layer flows have been systematically examined as magnetic topology (upper versus lower-null) and plasma density were changed. It is found that the plasma flow pattern can be decomposed into two principal parts: (1) a drift-driven component, which lies within a magnetic flux surface and is divergence-free and (2) a transport-driven component which gives rise to parallel flows on the high-field side scrape-off layer. Toroidal rotation, Pfirsch-Schlüter and transport-driven contributions are unambiguously identified. Parallel flows are found to dominate the high-field particle fluxes; the total poloidally-directed flow carries one half of the particle flux arriving on the inner divertor. As a result, convection is also found to be an important player in high-field side heat transport. In contrast, $E_r \times B$ plus parallel flows yield a mostly-toroidal flow component in the low-field SOL.

The magnitude of the transport-driven flow component is found to be quantitatively consistent with radial fluctuation-induced particle fluxes measured on the low-field side, identifying this as the primary driver. In contrast, fluctuation-induced flux measurements on the high-field side midplane are found to be essentially zero, thereby excluding an 'inward pinch' effect as the mechanism that closes the mass-flow loop in this region.

Thesis Supervisor: Brian LaBombard
Title: Principal Research Scientist, Plasma Science and Fusion Center

Thesis Reader: Ian H. Hutchinson
Title: Professor of Nuclear Science and Engineering

Acknowledgments

Thanks to my advisor Brian, my thesis reader Ian, and all the scientists, staff and students at the PSFC for their help in conducting this research. Thanks to my friends and family, especially my wife Micki, for their love and support throughout the process.

Contents

List of Figures

List of Tables

List of Symbols

B_t, B_p	Toroidal, poloidal magnetic field
c_s	Speed of sound
d	Distance between adjacent probe electrodes, perpendicular to B
E_r E_θ	Radial, poloidal electric field
I_p	Plasma current
I_{sat}, I_s	Ion saturation current
J	Current density
m_e, m_i, m_D	Electron, ion, deuterium mass
M	Mach number
n, n_e, n_z	Density, electron density, impurity density
n_{20}	Density in units of 1×10^{20} m^{-3}
$\bar{n}_e$	Central line-averaged density from two-color interferometry
NL04	Central line-integrated density from two-color interferometry
n_g	Empirical tokamak density limit (Greenwald density)
q	Tokamak safety factor
$q_\parallel$, $q_\perp$	Parallel and perpendicular heat flux
R	Major radius
r	Minor radius
S	Normalized parallel distance, inner divertor to outer divertor
T_e, T_i, T_z	Electron, ion, impurity temperature
V_f	Floating potential
v	Velocity
$v_{\tilde{r}\tilde{n}\tilde{\phi}}$	Fluctuation-induced radial velocity
Z_{eff}	Plasma effective ion charge
α	Sheath transmission factor
α	Angle between probe surface and B field
β	Angle between probe surface and flux surface
$\Gamma_{\tilde{r}\tilde{n}\tilde{\phi}}$	Fluctuation-induced particle flux

Γ_θ	Poloidal particle flux
δ	Secondary electron emission coefficient
ε	Inverse aspect ratio
η	Plasma resistivity
θ	Angle between probe surface and B field within a flux surface
$\kappa_\parallel^e$	Plasma thermal conductivity
$\ln \Lambda$	Coulomb logarithm
λ_n	Neutral mean-free path
μ	Ratio of electron mass to ion mass
ν_b	Ideal ballooning mode growth rate
ρ	Depth into SOL from LCFS mapped to outer midplane
Φ_p	Plasma potential
Φ_e	Effective plasma potential, accounting for $\nabla_\parallel T_e$
χ	Thermal diffusivity
ψ	Poloidal magnetic flux

Chapter 1

Introduction

1.1 Background

1.1.1 Magnetic Confinement Fusion

Nuclear fusion has the potential to provide inexhaustible energy without heavy environmental impact, nuclear materials proliferation, or long-lived nuclear waste. Magnetic confinement of deuterium/tritium plasmas heated to high temperatures is the most advanced and promising method of achieving economical fusion energy production. Of the various magnetic confinement schemes that have been investigated, the tokamak has achieved the highest power production. Alcator C-Mod [1] is a compact, high-field, high-density tokamak which has been operated by MIT's Plasma Science and Fusion center since 1992. The operational parameters are as follows: toroidal magnetic field $B_t \leq 8$ T, plasma current $I_p \leq 2$ MA, central electron density $n_e \leq 10^{22}$ m^{-3}, and central ion and electron temperatures T_i, $T_e \leq 5$ keV.

1.1.2 Edge Plasmas

The high field and high power density present in C-Mod give it edge conditions that are the closest among current devices to those that would be found on a fusion power reactor. Studies of edge conditions on C-Mod therefore provide insight into the operation of future devices. C-Mod is has a diverted magnetic configuration, in

which the plasma-wall interface is localized far from the confined plasma by means of a poloidal field null, typically located below the main plasma. The area of plasma wall interaction is called the divertor. This is where the power and particle exhaust in a power reactor would have to be handled. The expected heat flux is very large ($\sim$ 10 MWm^{-2}) and is at the limits of what can be handled by current technology. Spatial or temporal asymmetry in the power or particle exhaust could cause major operational difficulties. It is therefore of great interest to understand how particles and energy are passed from the confined plasma, through the edge or 'scrape-off layer' (SOL) to the divertor.

1.1.3 Plasma Flow/Rotation

A critical parameter influencing divertor power and particle flux is the presence of bulk flows of plasma in the SOL. These flows are often observed [2] and can affect divertor loading in a number of ways. The flows can directly affect the spatial distribution of heat and particles on divertor surface, but flow shear can also affect the source of particles and heat to the SOL by determining the size of turbulent eddies present in the plasma edge [3]. The flows in the SOL also represent a boundary condition on the confined plasma, perhaps affecting its rotation velocity. This in turn can have stabilizing effects on the macroscopic equilibrium of the plasma, for instance: the suppression of error field instabilities [4].

Flows in the boundary can be both parallel to the field, as particles and heat drain along the field lines to the divertor surface, and perpendicular to the field lines as spatially varying potentials, temperatures, densities and magnetic field strength lead to the the drift of particles across the field .

A theoretical prescription for flows in the boundary is extremely challenging to produce. The sources are driven by largely anomalous cross-field transport, and the sink is the interaction of the plasma with solid surfaces and neutral gases, involving many different types of physics over a large range of plasma conditions. For these reasons, much of our understanding of the edge flows comes from empirical sources. However, direct measurements of plasma flows in the edge are challenging as well.

The temperature and density here are typically too low to use standard spectroscopic techniques to measure plasma properties, particularly in the presence of the large amount of 'background' radiation emanating from the core. The difficulties are exacerbated by the high spatial resolution required in the edge, further limiting the available signal. Luckily, the reduced temperature and density in the edge allows Langmuir probes to be used to measure edge flows. This technique has its challenges as well, primarily due the the strong perturbations that are inherent in plunging a physical object into the plasma. Nonetheless, this is the technique we have used in this thesis to study edge flows in Alcator C-Mod.

1.2 Goals and Thesis Outline

The primary goal of this thesis is to design and operate a scanning Mach probe to operate in the high-field side scrape-off layer (HFS SOL) on Alcator C-Mod. This probe should be equipped with multiple electrodes to allow the measurement of temperature, density, floating potential and plasma flows from the inner wall the the last closed flux surface (LCFS) and beyond. This probe is to be used in conjunction with the scanning probes which are in place on the low-field side (LFS) and the arrays of embedded probes in the C-Mod divertors to explore the SOL phenomenology in detail, including ballooning transport-driven flows and their dependence on discharge configuration. Specific goals to be addressed include:

1. Measure the perpendicular component of the plasma flow.
2. Examine momentum coupling between the edge and core.
3. Make contact with published 2-D modeling of the C-Mod Edge, including results from UEDGE and B2-EIRENE.
4. Test the transport-driven flow hypothesis that has been proposed based on existing measurements of parallel flows on the HFS.

5. Measure fluctuation-induced particle fluxes, and check for consistency with the observed poloidal flow pattern.

6. Understand the mechanism by which the particles flowing towards the inner divertor return to the core.

7. Examine the dependence of the observed flows, heat and particle fluxes on discharge density and magnetic topology.

In order to address these issues, the thesis is arranged as follows. Chapter 2 describes the types of measurements we have made with the probes and the details of the physical construction of the instruments that were used. In chapter 3, an outline of the experimental program which produced our results is presented. In chapter 4, we attempt to validate the measurements we have taken by benchmarking them against previous data, and trying to identify and resolve any sources of error or uncertainty. Chapter 5 deals specifically with the problem of the Gundestrup probe, which has not previously been used in the capacity that we attempting to use it. We will attempt to understand how to interpret the data from this diagnostic. Chapter 6 describes the results a number of minor experiments that address some of the goals stated above, including transport-driven flows and momentum coupling. Chapter 7 compares our results to results from simulations, to those from other experiments and to those from other C-Mod diagnostics. In chapter 8, we explore the poloidal flux of particles and energy based on measurements of the total flow vector.

Chapter 2

Hardware

2.1 Langmuir Probes

The Langmuir probe is one of the earliest and simplest diagnostics to be used to measure a plasma. It takes advantage of the fact that solid surfaces represent a very good sink for all charged particles incident on them. These particles recombine and become neutrals. If a conducting surface is used, it can be biased to preferentially collect ions or electrons, and the current collected can be measured as a function of voltage. From this I-V characteristic, a simple Langmuir probe can determine the electron temperature and density, as well as the electric potential of a plasma. Sampling the data at a high frequency can also provide information about turbulence and transport through an analysis of the fluctuations in density and potential. Arrangements of multiple probes can measure bulk plasma flows by comparing the currents collected from different directions. The primary limitation of the Langmuir probe is its inability to operate for extended periods in hot dense plasmas. For this reason, its usefulness in fusion devices is limited to the edge plasma. This section contains an overview of Langmuir probe theory for the special case of a strongly magnetized plasma.

2.1.1 Basic Theory

Strong magnetic fields hinder the transport of particles across the field lines. We therefore expect a probe with dimensions that are large compared to the ion Larmor radius to collect particles only in the direction parallel to the field. In general, this is equivalent to taking the area of the probe to be the area projected along the field lines. The plasma being sampled is a long flux tube which is populated by some diffusive or drift mechanism. The dynamics of strongly magnetized Langmuir probes is then essentially a one-dimensional problem, with a source term that is governed by the perpendicular dynamics.

It is instructive to proceed with a heuristic discussion of probe theory before the more rigorous derivation. We begin by considering an electrically 'floating' probe, which is equivalent to any unbiased plasma bounding surface. A surface collecting no current 'floats' at a potential that is less than the plasma potential by several times the electron temperature. This is because most of the highly mobile electrons must be reflected to maintain an electron current equal to the collected ion current. The region near the probe surface where a substantial number of electrons are reflected and quasineutrality is violated is called the sheath. Since this is a shielding phenomenon, the thickness of this sheath is of order the Debye length. Outside the sheath, a potential drop exists that accelerates ions towards the sheath. This region is called the pre-sheath. Since quasi-neutrality must be maintained in the pre-sheath, the potential drop is somewhat less than the electron temperature. Therefore, most of the potential drop must occur across the sheath. We can use Poisson's equation and the ion continuity equation to write a self-consistent expression for the potential and the velocity of the ions. [5] This equation can be expanded near the sheath edge and coupled with the plasma solution (outside the sheath) in which the charge density is taken to be zero. This procedure produces the condition that ions arrive at the sheath edge at the sound speed. This can be intuitively understood as free expansion of the ions in the presence of a perfect sink.

We now extend the discussion to a probe whose potential can be specified by

an external power supply. If the voltage is raised above the floating potential, the probe samples more of the electron distribution function. Since the electrons have a Maxwellian velocity distribution, the electron current increases exponentially as the probe voltage is raised. Provided the probe is still substantially below the plasma potential, nearly all of the ions are still collected. The electron temperature can be determined simply by the e-folding voltage of this exponential. If, on the other hand, the voltage is decreased below the floating potential, nearly all of the electrons are reflected and the probe only collects ions as fast as they arrive at the sheath (the sound speed). This is known as "ion saturation." Since the temperature is known from fitting the shape of the $I-V$ characteristic, the sound speed is known as well. This means that the ion saturation current can be used to infer the plasma density. This heuristic explanation omits many order-unity corrections but captures the basic concepts of traditional Langmuir probes which measure temperature, density and plasma potential.

A more careful analysis [5] produces the following formula for probes biased below the plasma potential:

$$I_{probe} \cong \frac{1}{2} e A_p n_e \left(\frac{T_e}{m_i}\right)^{\frac{1}{2}} \left(-1 + \sqrt{\frac{2m_i}{\pi m_e}} \exp\left(\frac{eV_{probe}}{T_e}\right)\right) \tag{2.1}$$

$$\cong \frac{1}{\sqrt{8}} e A_p n_e c_s \left(-1 + 48 \exp\left(\frac{eV_{probe}}{T_e}\right)\right) \tag{2.2}$$

Where A_p is the projected area of the probe electrode along the field. The factor of 48 is dependent on the ion mass and is calculated here for deuterium. This factor is not important for the interpretation of the $I-V$ characteristic in any case, because only the saturation current value, the e-folding voltage and the floating voltage are needed to extract the quantities of interest. It should be noted that errors of $10-20\%$ [5] are inherent in this derivation, due to the approximations required for sheath analysis.

2.1.2 Mach Probes

As discussed in section 1.1.3, fusion edge plasmas often contain significant plasma flows that are important to the performance of the device. It would seem reasonable to expect that an electrode exposed to plasma on only one side would collect ions at a rate that depends on the direction of the plasma flow. Since ions normally arrive at the sound speed, we expect the probe sensitivity to be limited to flows at significant fractions of the sound speed (Mach numbers which are $\lesssim 1$). This concept is the basis of the Mach probe.

Plasma flow direction is predominantly parallel to the magnetic field. The simplest Mach probes measure this flow by comparing the ion saturation current on electrodes facing in opposite directions along the field lines. Ideally, the two electrodes are close together to produce a spatially localized measurement. In a steady state plasma, a single electrode may be rotated to view both directions in turn.

A simple analysis of the Mach probe can be accomplished using a fluid treatment that employs the ion and electron parallel momentum equations and the ion continuity equation under the assumption that electron and ion temperatures are constant everywhere. The resulting equations relate the parallel velocity to the logarithm of the density. Plasma is assumed to populate the field lines intercepted by the probe by either a diffusive or convective model. The diffusive treatment[5] produces Eqn. 2.3 for the ion saturation current collected by a probe in a plasma with a parallel flow of Mach number M away from the surface:

$$I_{sat} = eA_p n_e c_s \exp(-1 - 1.1M) \tag{2.3}$$

In order to obtain this result, the simplifying assumption is made that the particle diffusivity is equal to the momentum diffusivity. Note that for $M = 0$, this approach produces a nearly identical result to Eqn. 2.1 because $1/\sqrt{8} \cong \exp(-1)$. The convective treatment which closes the particle balance using drifts requires the presence of some non-zero perpendicular plasma fluid velocity, and will be addressed in section 2.1.3. However, the parallel Mach number obtained from that approach is very similar

to that found with the diffusive approach.

Since equation 2.3 adds a second unknown (M) to the ion saturation current equation, a single electrode is not sufficient to measure the density and parallel Mach number. For the simplest case of a Mach probe with identical electrodes facing in opposite directions along the field, the parallel Mach number can be obtained from the ratio of the ion saturation currents measured on the two electrodes, leading to the result:

$$M = 0.43 \ln \left(\frac{I_{sat,up}}{I_{sat,down}} \right) \tag{2.4}$$

With this result, the capabilities of the Langmuir probe are extended to the measurement of the parallel flow velocity.

2.1.3 Probe Measurements of Plasma Flows Perpendicular to the Magnetic Field

In order to measure the total flow vector in the edge plasma, and thereby determine the net poloidal particle transport, we require some measurement of the perpendicular component of the flow. Three methods of measuring the perpendicular flows are described: Measurement of E_r to infer $E_r \times B$ flow, use of multi-faceted Gundestrup probe tip geometries to measure total flow vector, and use of poloidally separated electrodes to measure the phase velocity of fluctuations.

ExB Velocity

The most straightforward way to infer bulk plasma drifts (flows perpendicular to the magnetic field) with Langmuir probes is the direct measurement of the radial variation of the plasma potential. The justification for this is that all bulk motions of plasmas which are not along the field occur concomitant with a perpendicular electric field which is zero in the frame of the plasma. Therefore, the measurement of the perpendicular electric field is equivalent to measuring the perpendicular velocity. Furthermore, the plasma potential is expected to be near constant on a magnetic flux

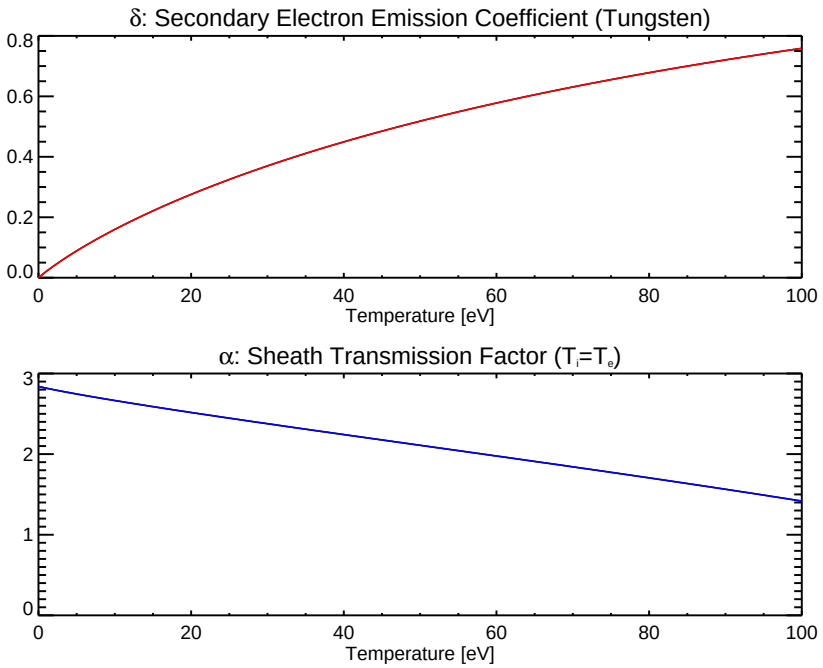

Figure 2-1: Typical values of the sheath transmission factor, α and the secondary electron emission coefficient, δ for tungsten electrodes.

surface since parallel electron conductivity is large. To first order then, the electric fields are predominantly radial and the drift is perpendicular to the field within a flux surface.

Section 2.1.1 describes the measurement of the floating potential and temperature of a plasma using a Langmuir probe. The determination of the plasma potential from thse quantities is accomplished using the relation $\Phi_p = V_f + \alpha T_e$, Where the factor $\alpha \lesssim 2.8$ is the sheath transmission factor [6]. The transmission factor is a function of the secondary electron emission coefficient of the electrode material, as given by [7]:

$$\alpha = \frac{1}{2}\ln[(2\pi\mu)(1+\frac{T_i}{T_e})(1-\delta)^{-2}] \tag{2.5}$$

Where δ is the secondary electron emission coefficient, averaged over a Maxwellian thermal distribution. The secondary electron emission coefficient itself is a function of temperature and has been empirically tabulated for tungsten [8]. Lacking measurements of T_i, we typically take $T_i = T_e$ and use these relations to calculate the appropriate value of α. Fig. 2-1 shows the values of δ and α for the range of

temperatures typically encountered by the probe.

Having obtained a radial profile of the plasma potential, we can calculate the perpendicular electrostatic drift velocity of the plasma by taking the radial gradient of the plasma potential and crossing it with the local magnetic field. Unfortunately, there are many sources of uncertainty in this measurement. We have already noted the uncertainty in the ion temperature used in Eqn. 2.5. This equation is based on measurements made in very controlled conditions and is expected to depend on the surface condition of the electrode, something which is not well-controlled in our experiments. Eqn. 2.5 is also derived with the assumption of Maxwellian energy distribution. These factors combine to create substantial uncertainty in the value of α. In addition, there can be thermionic electron emission from the electrode, which depends on the unknown electrode surface temperature. We routinely check for probe surface temperature effects by comparing ingoing and outgoing scans and discarding those that do not overlay well, but this effect could still cause error in less severe cases of overheating. We must also recognize that in the case of a flowing plasma, we often observe both temperature and potential differences between multiple electrodes exposed to the plasma in different directions. This variation is not described by theory, so it is not known how to treat it correctly. We use an arithmetic average of the value reported by the four electrodes. Additionally, the calculation of the plasma potential often amounts to the difference between two large terms (*i.e.* a highly negative floating potential plus the electron temperature). This magnifies any errors that are present in the measurement. Finally, taking a gradient of the resulting plasma potential to arrive at a perpendicular velocity magnifies the uncertainty further. We are left with a result that inspires a minimum level of confidence.

Gundestrup Probes

Because of the difficulties of measuring the perpendicular flows via the floating potential, a more reliable method of determining this quantity was sought. The Gundestrup probe [9] emerged as a potential solution. This type of probe features many electrodes, with their surfaces oriented at different angles to the magnetic field. A

rotating probe, with a continuously variable angle to the field, can produce similar measurements. These configurations are shown in Fig. 2-2. The purpose of this type of probe is to make measurements of perpendicular plasma flows. While this may seem like an intuitively obvious design, more careful consideration reveals that measuring perpendicular flows using inclined surfaces is not a problem which is simply described. In the strongly magnetized case, the perpendicular direction is ignorable and the problem is treated as essentially one dimensional, with a long pre-sheath extending along the field line. If a diffusive model is used, it is not obvious how drifts will affect the particle source in the pre-sheath. Fortunately, we can arrive at an intuitive understanding of the role played by the $E_r \times B$ drift in the collection of ions on an angled surface by performing a Galilean transformation [10]. We imagine the electrode to have infinite extent, and transform the problem to a reference frame moving along the surface at the velocity that eliminates the radial electric field. In the new Galilean frame, the problem returns to the drift-free case, but now with an external parallel Mach number of $M_{||} - M_{\perp} \cot(\theta)$, where θ is the angle of the surface with respect to the magnetic field. This verifies that $E_r \times B$ drifts do influence the collection on angled surfaces. However, the role of diamagnetic drifts or probe-induced perturbations is not addressed by this simple exercise. A recent paper by Hutchinson [11] addresses some of these issues with great success, while at the same time avoiding the need to make the heuristic diffusion assumptions of the original derivation of the parallel Mach probe. This two-dimensional approach assumes that the pre-sheath is populated exclusively by drifts and solves the fluid equations exactly. It includes diamagnetic effects and even considers the effect of facets which are angled in the radial direction (as the C-Mod high-heat flux probes are, see section 2.2.2) and derives appropriate corrections. The result of this calculation is summarized by equations 2.6.

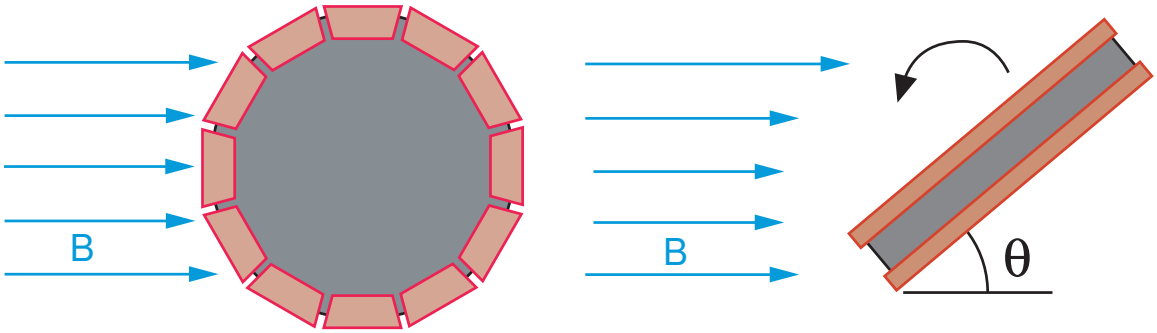

Figure 2-2: Two examples of probe configurations which can be used to measure perpendicular flows. The Gundestrup probe (left) has many electrodes oriented at different angles to the magnetic field. Alternatively, a rotating probe (right) can be used for a steady state, low heat flux plasma.

$$I_{sat} = eA_p n_e c_s \exp(-1 - M_{||} + M_{\perp} \cot(\theta)) \tag{2.6a}$$

$$M_{\perp} = (1 + M_{||}) M_{Te} + M_{Di} + M_{E\times B} - \left(\frac{1 - \sin\alpha}{1 + \sin\alpha}\right) M_D \tag{2.6b}$$

$$M_D = M_{Di} - M_{De} = (M_{ni} + M_{Ti}) - (M_{ne} + M_{Te}) \tag{2.6c}$$

Here, the various M's are drift velocities normalized to the sound speed, c_s. M_{Te}, M_{Ti}, M_{ne} and M_{ni} are diamagnetic drifts due to the electron and ion temperature gradients and the electron and ion density gradients respectively. α is the angle between the surface and the field, not to be confused with θ which is the angle between the surface and the field in the plane of a flux surface (see Fig. 5-2).

As can be seen in equation 2.6a, the full 2-D drift calculation produces a similar form to one which combines the 1-D diffusive Mach model (equation 2.3) with the result of the Galilean transformation discussed in this section. There are two differences: the elimination of the of the $M_{||}$ pre-factor of 1.1, and the identification of $M_{\perp}$ as a combination of the various drifts listed in Eqn. 2.6b. It is now clear that there is an implicit dependence of $M_{\perp}$ on $M_{||}$, which has the potential to complicate the analysis. This issue will be addressed in section 2.2.2.

In this thesis, the reported Gundestrup perpendicular Mach number is that which is calculated from Eqn. 2.6a (the LHS of Eqn. 2.6b).

Phase Velocity of Fluctuations

The C-Mod edge region is subject to drift-interchange fluctuations [12, 13], which are fairly ubiquitous. These modes are characterized by fluctuations in density and plasma potential. The density fluctuations are routinely measured by the probes on C-Mod during periods of ion saturation. The digitization rate of the probe signals allows a frequency range of 5 kHz to 500 kHz. These fluctuations are observed to be larger in amplitude on the low-field side (LFS) than they are on the high-field side (HFS). The closely spaced array of electrodes which comprise a Gundestrup probe can be used to track the poloidal propagation these fluctuations. Signals from adjacent electrodes are found to be roughly in phase parallel to the field, but show delays of several μs in the perpendicular direction. From a simple correlation analysis in the time domain, it is possible to use the probe spacing and the time delay to determine a perpendicular phase velocity of the fluctuations (see Fig. 2-3). The LFS probes produce the best data using this technique due to the large amplitude fluctuations at that location.

The phase velocity of fluctuations is not a direct measurement of the fluid velocity, since the drift-interchange waves propagate according to their dispersion relation added to the bulk fluid ($E_r \times B$) velocity. However, it has been suggested that shear in drift wave phase velocity could be as important to the suppression of turbulence as the shear in the fluid velocity. It is also possible that the $E_r \times B$ velocity is much larger than the inherent velocity of the fluctuations, in which case the phase velocity technique might provide a reasonably good measurement of the fluid velocity.

2.1.4 Fluctuation-Induced Particle Fluxes

Another important measurement which can be made with arrays of Langmuir probes is fluctuation-induced radial particle flux. Drift-interchange turbulence is responsible for particle and energy transport when the density and potential fluctuations are out of phase. Density fluctuations can be measured by a probe with a swept bias, routinely measuring the temperature, and inferring the density fluctuations with high time

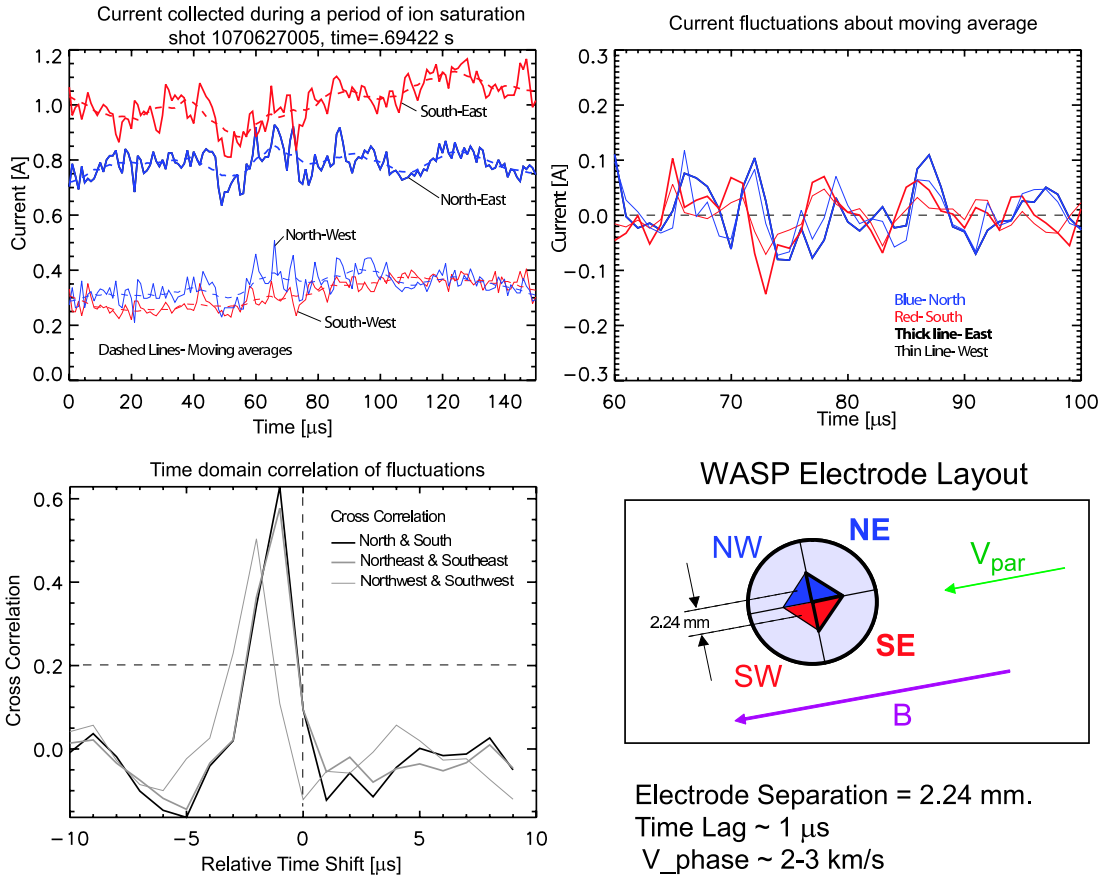

Figure 2-3: Illustration of the phase velocity fitting process. During periods of ion saturation, the currents on the four electrodes are scaled in amplitude so that their time-averaged values match. A cross-correlation analysis is then performed on poloidally adjacent electrodes. The maximum in the cross-correlation represents the time for the fluctuation to propagate from one electrode to another. The spatial separation of the median collection points of the electrodes provides the perpendicular distance used to calculate the phase velocity. Low-frequency trends are removed by subtracting a moving mean value, with a time window of 15 μs in this case.

resolution during periods of ion-saturation. Floating potential fluctuations can be inferred with high time resolution by a floating electrode. With a closely spaced array of electrodes, it is possible to use separate electrodes to infer density and potential fluctuations simultaneously and to look for correlations with the proper electrode arrangement. These can be used to calculate the magnitude of the outward particle flux.

This technique is complicated by the fact that the measurements must be made with separate electrodes which are not in exactly the same location. It is therefore necessary to correct for phase differences which are due to the finite wave-number of the mode rather than the phase shift between the density and potential fluctuations. Most importantly, this calculation assumes that the measured fluctuations in floating potential are a good proxy for fluctuations in plasma potential. In fact, the sheath drop depends on temperature, so temperature fluctuations could be important as well. Unfortunately, our current probes do not measure temperature with high temporal resolution, so this effect is not included in the measurement. Following [6], $\Gamma_{r\tilde{n}\tilde{\phi}}$ (the fluctuation-induced particle flux) is calculated as follows for the two types of electrode configurations used on C-Mod (see Fig. 2-5):

$$\Gamma_{r\tilde{n}\tilde{\phi}} = \frac{\langle \tilde{n}\tilde{E}_\theta \rangle}{B} = \left\langle \frac{\langle n \rangle (I_E + I_W)}{\langle I_E + I_W \rangle} \frac{V_S - V_N - \langle V_S - V_N \rangle}{Bd} \right\rangle \approx \langle \tilde{n}\tilde{v}_r \rangle \quad \text{(A)} \tag{2.7}$$

$$\Gamma_{r\tilde{n}\tilde{\phi}} \approx \left\langle \frac{\langle n \rangle (I_{SW} + I_{NW})}{\langle I_{SW} + I_{NW} \rangle} \frac{V_{SE} - V_{NE} - \langle V_{SE} - V_{NE} \rangle}{Bd} \right\rangle \approx \langle \tilde{n}\tilde{v}_r \rangle \quad \text{(B, C)} \tag{2.8}$$

Here, the $\sim$ denotes the fluctuating part of a quantity (zero average value). The form typically used for calculation is shown, where the I's and V's are current and voltage time series from the four probe electrodes. The averages are taken over a period of ion saturation (a few hundred μs) and the magnetic field B and the electrode separation d are taken -to be constants in time. In this formulation, the mean has been subtracted out of the electric field, but it could equivalently have been subtracted from the density or the both the density and field without affecting the result. Equation 2.8 (the one for the high-heat flux Gundestrup probe, see section 2.2.2) suffers from the

fact that the density and potential are measured in only one parallel direction or the other. The large parallel flow that is present on the HFS is known to affect both temperature and density measurements, and could affect floating potential as well. This asymmetry is addressed experimentally in section 8.2.6. Dividing out the density gives us an effective radial velocity, $v_{\tilde{r}\tilde{n}\tilde{\phi}} = \Gamma_{\tilde{r}\tilde{n}\tilde{\phi}}/\langle n \rangle$. Comparing this quantity at a variety of poloidal locations can help us measure poloidal tranpsort asymmetry and even search for the presence of an inward particle pinch on the HFS, which has been proposed by several theories [14, 15, 16, 17].

2.2 C-Mod Probe Diagnostics

Alcator C-Mod has a variety of Langmuir probe diagnostics positioned at multiple locations in the plasma boundary. These are capable of making the measurements described in section 2.1.4. There are arrays of embedded probes located in the inner divertor, the outer divertors and the ceiling tiles. There are also three scanning probes placed at different poloidal locations in the SOL. Fig. 2-4 shows a cross-section of Alcator C-Mod indicating the locations probe diagnostics and other diagnostics relevant to this thesis. Each of these systems will now be described in detail.

2.2.1 Divertor Probe Arrays

Alcator C-Mod is equipped with a number of Langmuir probes embedded in the divertor tiles. The original installations on the lower divertors (inner and outer) were called 'flush-mounted probes' (FMP's). They now include probes that extend from the surface to increase the angle of field incidence, but the FMP naming convention has been carried along. These probes are operated with swept voltage waveforms allowing the measurement of electron temperature and density, and floating potential in the upper and lower divertors. As shown in Fig. 2-4, a third array of probes has been added in the ceiling tiles below the new upper-divertor cryo-pump. This allows us to measure divertor profiles in USN magnetic topologies, in addition to the usual LSN topologies. Each of the three embedded probe arrays is arranged to provide

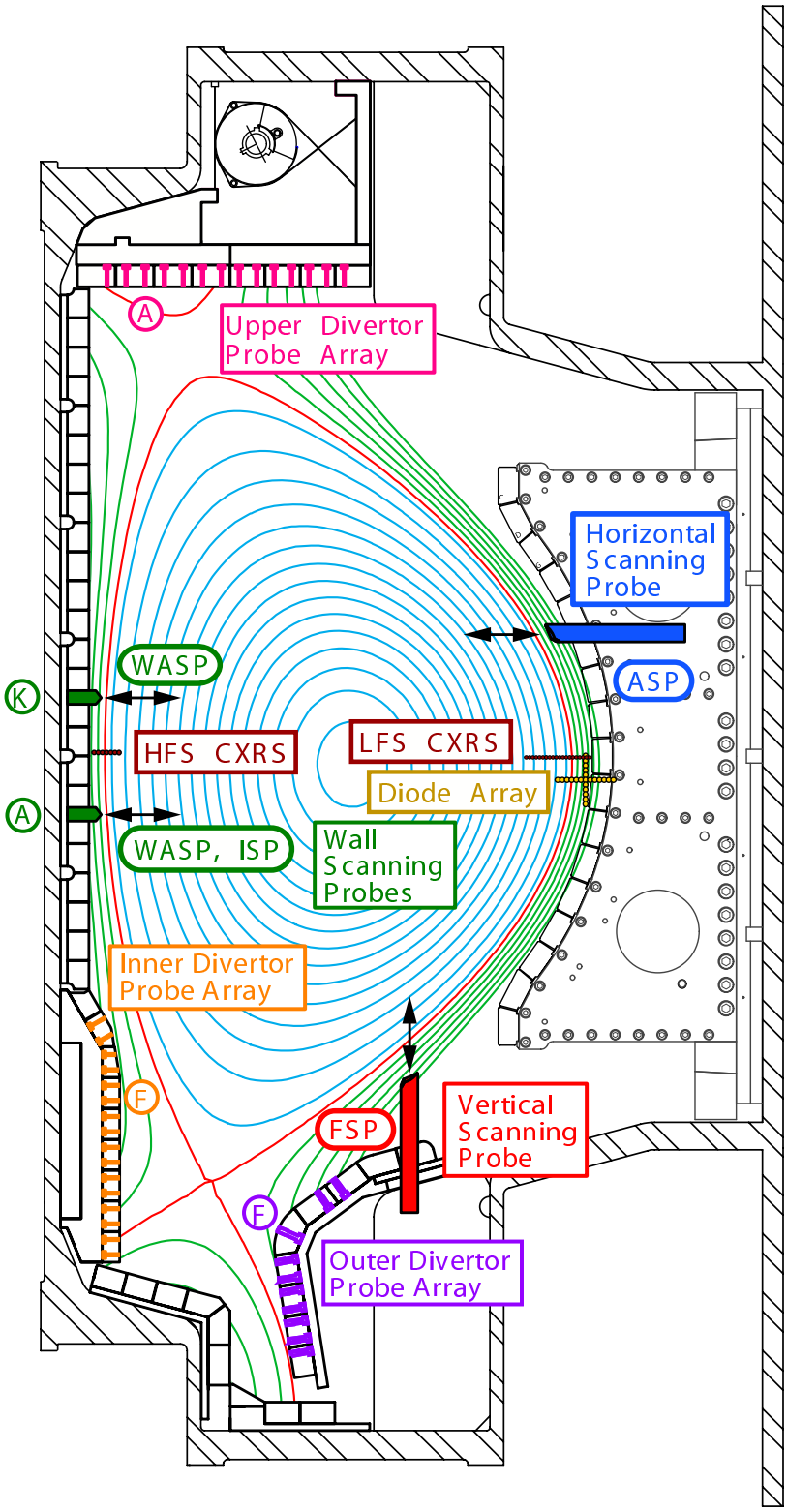

Figure 2-4: Poloidal cross-section of Alcator C-Mod showing the locations of the probe diagnostics discussed in this thesis. Other pertinent diagnostics are shown as well.

radial SOL profiles for comparison with the scanning probes.

2.2.2 High Heat Flux Probe-Tip Geometries

Before describing the individual scanning probe diagnostics, we now discuss probe tip geometries and electrode arrangements that are used on the C-Mod scanning probes. The usual strategy when designing scanning probes for C-Mod's high heat flux environment is to employ a pyramid shaped probe tip. This spreads the heat flux over a greater area than an electrode with normal field incidence. Electrodes placed on the sides of the pyramid look upstream or downstream, allowing the probe to function as a Mach probe. The original design, (A) in Fig. 2-5, had four electrodes placed on the edges of a pyramid with a steepness of 30°. The electrodes were labeled by the points of the compass when looking at the probe tip head-on. The East and West electrodes were operated in swept voltage mode (see section 2.4), functioning as a Mach probe and measuring temperature and density. The North and South electrodes were operated in a floating voltage mode to measure high-frequency potential fluctuations. The simplest method of converting such a design to a Gundestrup probe is to place the electrodes in the four faces of the pyramid, so that a flux-surface cross-section of the probe yields an angle of 45° between the surface of each electrode and the field lines. Our first generation Gundestrup probe, (B) in Fig. 2-5, was the most straightforward implementation of this plan: we simply moved the electrode pins to new locations on the faces of the pyramid, maintaining their spacing and diameter, and using the same pyramid geometry. This probe tip configuration was tested on the horizontal scanning probe at the end of the 2006 campaign.

The results were encouraging: we were able to measure what appeared to be a perpendicular flow velocity, which exhibited a large feature near the separatrix. The feature consisted of a hump in the perpendicular velocity, with a magnitude of 5-10 km/s in the electron diamagnetic direction (see section 6.2). This led us to quickly attempt to refine the Gundestrup design and place it on the vertical scanning probe, and the new WASP probe.

Several changes were made to the second generation Gundestrup probe, which

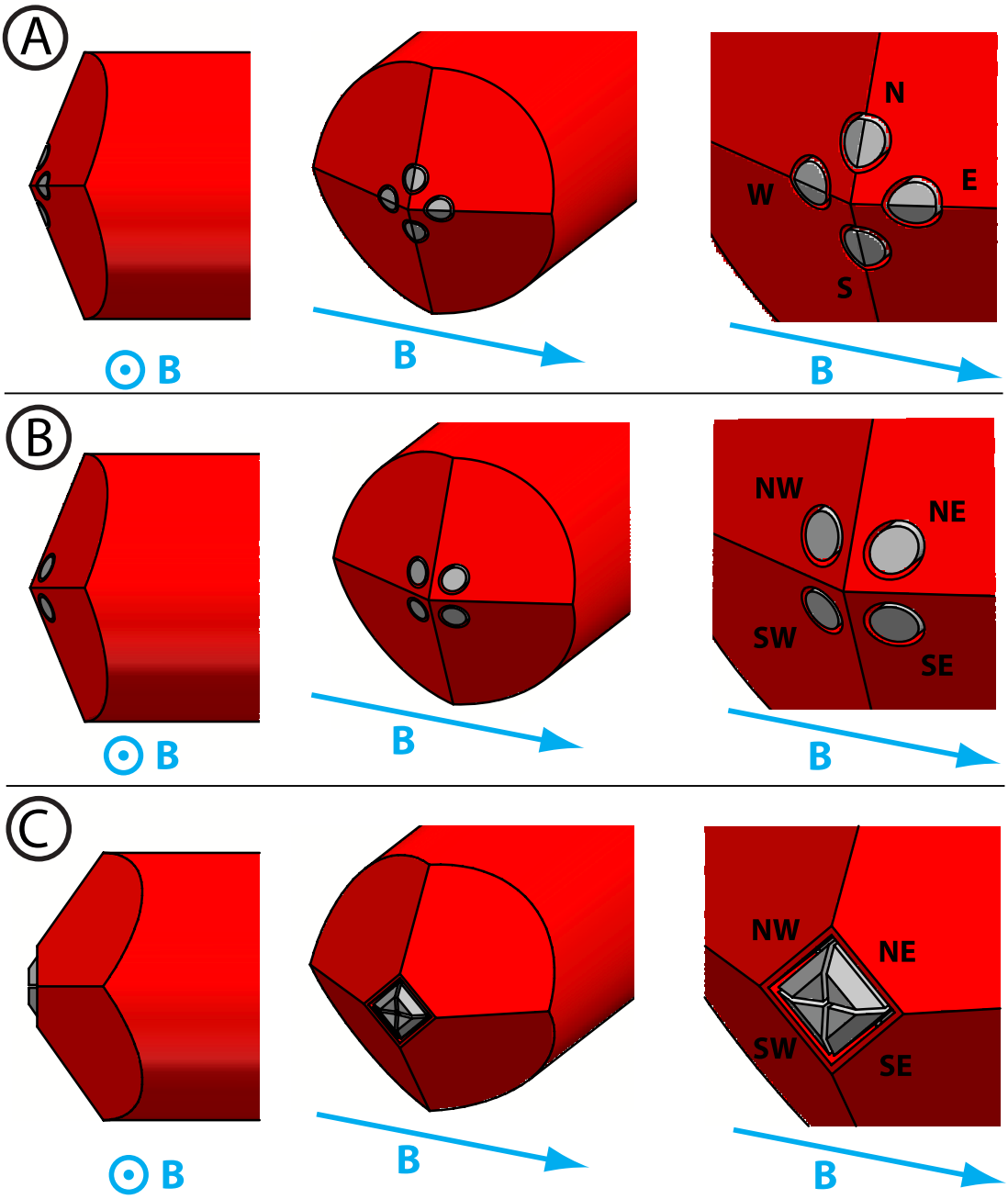

Figure 2-5: Illustration of the probe-tip geometries recently used on C-Mod: (A) Mach/float geometry, (B) trial Gundestrup geometry (C) refined Gundestrup geometry. Shown at left, the probes as they would appear looking in the parallel direction, along the field. The diameter of the shaft shown here is 19 mm (standard for pneumatic probes).

is shown in Fig. 2-5 (C). One concern was that the 30° pyramid steepness resulted in a small angle of incidence between the magnetic field and the electrode surface (22°). It seemed possible that such a small angle of incidence might corrupt the Gundestrup results, since the Gundesterup fluid model had only been and tested for two-dimensional probes (*i.e.* probes with geometry that is invariant in the radial direction). At the cost of a higher potential heat flux, the pyramid angle was steepened to 45° to avoid this problem. Another change was moving the electrodes to the very tip of the pyramid. This was motivated by the common failure mode of melting the probe tip. With the older designs (A and B), the very tip of the molybdenum probe body would melt and short out the electrodes. A proposed solution to make the entire probe body out of tungsten, which has a much higher melting temperature than molybdenum, was rejected because of the cost and expense of working with tungsten. Instead, the tungsten electrodes were moved to the very tip of the probe, exposing them to the highest heat fluxes rather than the molybdenum. In the new design, the maximum operational depth is not only up to, but beyond the maximum survivable depth for molybdenum. This modification also had the effect of reducing the inter-electrode spacing, producing a more localized measurement. Finally, it moved the electrodes out of the probe shadow, reducing the perturbative effects of the probe on the measurement. The new design required triangle shaped electrodes rather than the simple pins used in the past. These electrodes are quite small and fairly complex and therefore required electric discharge machining to achieve the necessary tolerances. Sharp corners were avoided, particularly in the molybdenum probe body, because exposure of these edges to the plasma rounds them and reduces the reliability of calculations of the projected area of the electrodes. The primary concern with the new design is that the less isolated electrodes could collect current from each others' flux tubes as a result of small misalignments.

The new electrode design forced us to develop a process for insulating the electrodes from the probe body. The insulating material had to withstand very high temperatures, but fit in a very small space. We considered using laser-cut mica sheets for this application, but the requred small sizes and complex geometry would

have made assembly exceedingly difficult. Instead, we decided to use a flame-sprayed ceramic coating, ∼0.2 mm thick. Alumina was selected for its favorable electrical and mechanical properties and easy availability. Early trials suffered from gross inconsistency in the thickness of the ceramic layer at different points on the electrode. There was also a problem of inadvertently depositing the ceramic layer on the electrode surface. This layer could be filed off, but preserving the geometry of the electrode surface is critical to an accurate determination of its projected area. To address these problems, we created a fixture that supported the electrode without obscuring any surfaces which requires coating. At the same time, the electrode surface was carefully masked with Teflon (to which the ceramic does not stick) to keep any alumina from being deposited there. This technique produced more consistent results, although some variations were still present. In the end, we asked for a slightly thicker layer than needed and hand-filed each group of electrodes to custom fit into a probe tip.

To reduce the possibility of the electrodes collecting unwanted current on their back surfaces due to a misalignment of the probe with the field, the gap between adjacent electrodes was made as small as possible. Since the electrodes are normally biased to the same potential, they are less susceptible to arcing to each other as to the floating probe tip, which can differ in potential by several hundred volts. The gap between electrodes was set to 0.1 mm while the gap between the electrodes and the probe body is the standard 0.2 mm.

The second generation Gundestrup probe was installed on all three C-Mod scanning probes throughout the 2007 and 2008 campaigns. It has proved extremely robust, routinely surviving very high heat flux plasma events.

The goal of using a Gundestrup probe design is to measure perpendicular flows due to plasma drifts. The C-Mod Gundestrup probes are designed to make this measurement simple and reliable. The use of four facets with angles of 45° to the field (when measured in a flux surface) produces a simplified set of four equations with three unknowns: the density (n), and the parallel and perpendicular Mach numbers ($M_{||}, M_{\perp}$) [11] (note: this assumes there is negligible plasma flow in the radial direction).

$$\ln(n_1/n) = M_{||} + M_{\perp} - 1. \tag{2.9a}$$

$$\ln(n_2/n) = M_{||} - M_{\perp} - 1. \tag{2.9b}$$

$$\ln(n_3/n) = -M_{||} + M_{\perp} - 1. \tag{2.9c}$$

$$\ln(n_4/n) = -M_{||} - M_{\perp} - 1. \tag{2.9d}$$

Here, the electrode numbering is chosen so that the positive $M_{||}$ correspond to electrodes facing in one parallel direction and positive $M_{\perp}$ corresponds to electrodes facing in one perpendicular direction. Also, the 'density' at the Debye sheath-edge for a given electrode is calculated using the standard form:

$$n_i = \left(\frac{I_s}{q A_p c_s} \right)_i . \tag{2.10}$$

Where the I_s are the ion saturation currents on the four electrodes, the A_p are the projected areas of the electrodes along the field lines and the c_s are the sound speeds calculated from the local temperature measurements. Eqs. (2.9) can be solved in a least-squares sense, providing measurements for the three unknowns.

Slight modifications to the above formulation are required to apply corrections for the case where the field is not precisely aligned with the probe tip. The corrections involve dotting the surface normal into the field vector rather than using the assumption that $\theta = 45°$. This procedure is detailed in Ref. [18]. Such corrections are regularly applied during the analysis routines that are run on probe data. Since the misalignment in C-Mod is typically small, the corrections have a small effect. This formulation also glosses over the implicit dependence of $M_{\perp}$ on $M_{||}$ which was pointed out in section 2.1.3. It is possible to apply corrections to equations 2.9 to account for this dependence, but it will be shown in chapter 5 that the correction to $M_{\perp}$ is typically small and can be neglected.

2.2.3 Pneumatic Scanning Probes

The simplest and most robust method of implementing a scanning probe is to use an external pneumatic drive coupled into the vacuum vessel by means of a bellows. C-Mod contains both horizontal and vertical ports, allowing access to most of the low-field side of the tokamak. There are two pneumatic scanning probes installed on C-Mod, one in the upper part of the A-horizontal port and one in the F-bottom vertical port.

The A-port scanning probe (ASP) has the ability to be withdrawn completely from the vessel and isolated behind a gate valve, allowing for the replacement of a probe-tip during a campaign without breaking the tokamak vacuum. This feature enables continued operation after catastrophic probe-melting events, which unfortunately are fairly common. It also allows us to test different probe-tip designs during a campaign.

The F-port scanning probe (FSP) cannot be replaced mid-campaign, but otherwise has functionality similar to the ASP. Both probes support four electrodes and can scan three times per shot to a pre-specified depth. This depth can be adjusted remotely between shots by means of a stepping motor. The time response of the stepping motor is not sufficiently rapid to allow for targetting adjustments during a shot. Details about the design and operation of the pneumatic scanning probes can be found in Ref. [19].

2.2.4 The Inner-Wall Scanning Probe

While pneumatic scanning probes have been able to provide a wealth of data about the LFS SOL, the requirement of direct port access has limited their deployment to the low-field side of the tokamak. However, phenomena such as MARFES [20] (which occur on the HFS) and in-out divertor asymmetries [21] have motivated curiosity about edge conditions there. Preliminary investigations with gas puff imaging [22] revealed the presence of strong flows parallel to the magnetic field. This motivated the development of a scanning probe design which would be able to measure the HFS edge plasma.

Previous experiments on C-Mod aimed at the effects of divertor 'closedness' on tokamak operation led to the development of magnetically actuated divertor bypass flaps [23]. These flaps were opened and closed by an embedded coil, which when activated, interacted with the toroidal magnetic field to produce a torque on the flaps. This concept was applied to the problem of placing a scanning probe on the HFS, leading to the development of a magnetically-actuated, single-electrode 'swing probe' which was placed on C-Mod's inner wall. The inner-wall scanning probe (ISP) [24] consisted of a coil mounted on a vertical shaft with a single electrode protruding from the side (see Fig. 2-6). When the coil was actuated, the probe rotated out of the shadow of the wall tiles into the SOL, the electrode tracing an arc in a horizontal plane. By reversing the polarity of the coil just as the coil became aligned with the field, it was possible to continue driving the coil through 180°, allowing the electrode to 'look' in the opposite parallel direction. The saturation currents on the first and second half of the scan could be compared to produce a radial profile of the parallel Mach number.

The ISP was successful in measuring radial temperature, density, floating potential and parallel Mach number in the HFS SOL, but suffered from several drawbacks. The single electrode made it impossible to employ any of the probe techniques requiring an array of electrodes, such as the measurement of fluctuation-induced fluxes or the Gundestrup technique. There were other drawbacks to the swing probe, including fixed plunge depth and poorly defined collection area at full-plunge. The latter limited the useful data to a few mm outside the LCFS. These shortcomings motivated the development of the wall scanning probe (WASP) (see Sec. 2.3).

2.3 Wall Actuated Scanning Probe (WASP)

To address the shortcomings of the ISP, the wall scanning probe (WASP [25], Fig. 2-7) was designed. This probe makes use of the successful coil-drive of the ISP but couples the motion into a linear-plunge probe using the parallelogram linkage shown in Fig. 2-8. This design allows a linear plunge probe to operate in the confined space

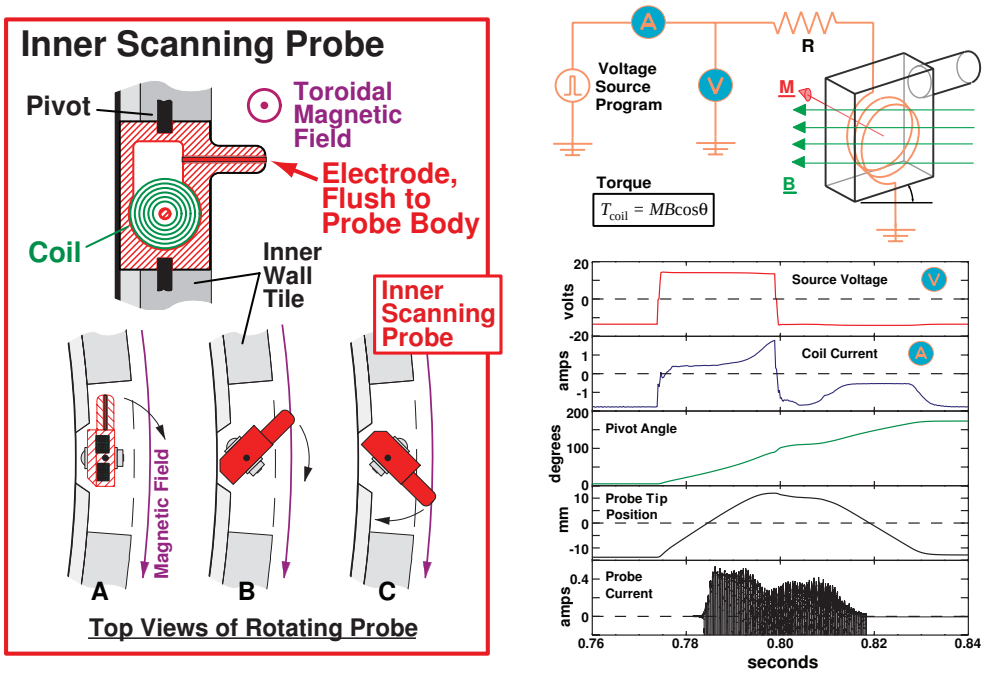

Figure 2-6: The Inner-wall scanning probe (ISP). The left panel illustrates the geometry of the probe. The top right shows schematically the circuit which operates the probe, while the bottom right shows typical wave forms during operation.

available on the inner wall. The probe is embedded in one of the standard inner wall tile modules, from which two of the 16 molybdenum tiles are removed and four more are modified to create the necessary space. The coil moves through an angular range of 0-45°, giving the stage a total linear plunge motion of ∼17 mm, in the major radial direction. The resultant linear range of the probe tip is roughly -2 mm to 15 mm beyond the tile surface.

2.3.1 WASP Components

The parts of the probe module are described as follows: The tile module, the coil housing, the stage and the probe-tip (see Fig. 2-7). They are described in turn.

Pivots and Drive Coil

The idea of using an embedded coil to drive mechanical motion using the ambient toroidal field was first implemented on C-Mod by C.S. Pitcher for the divertor bypass

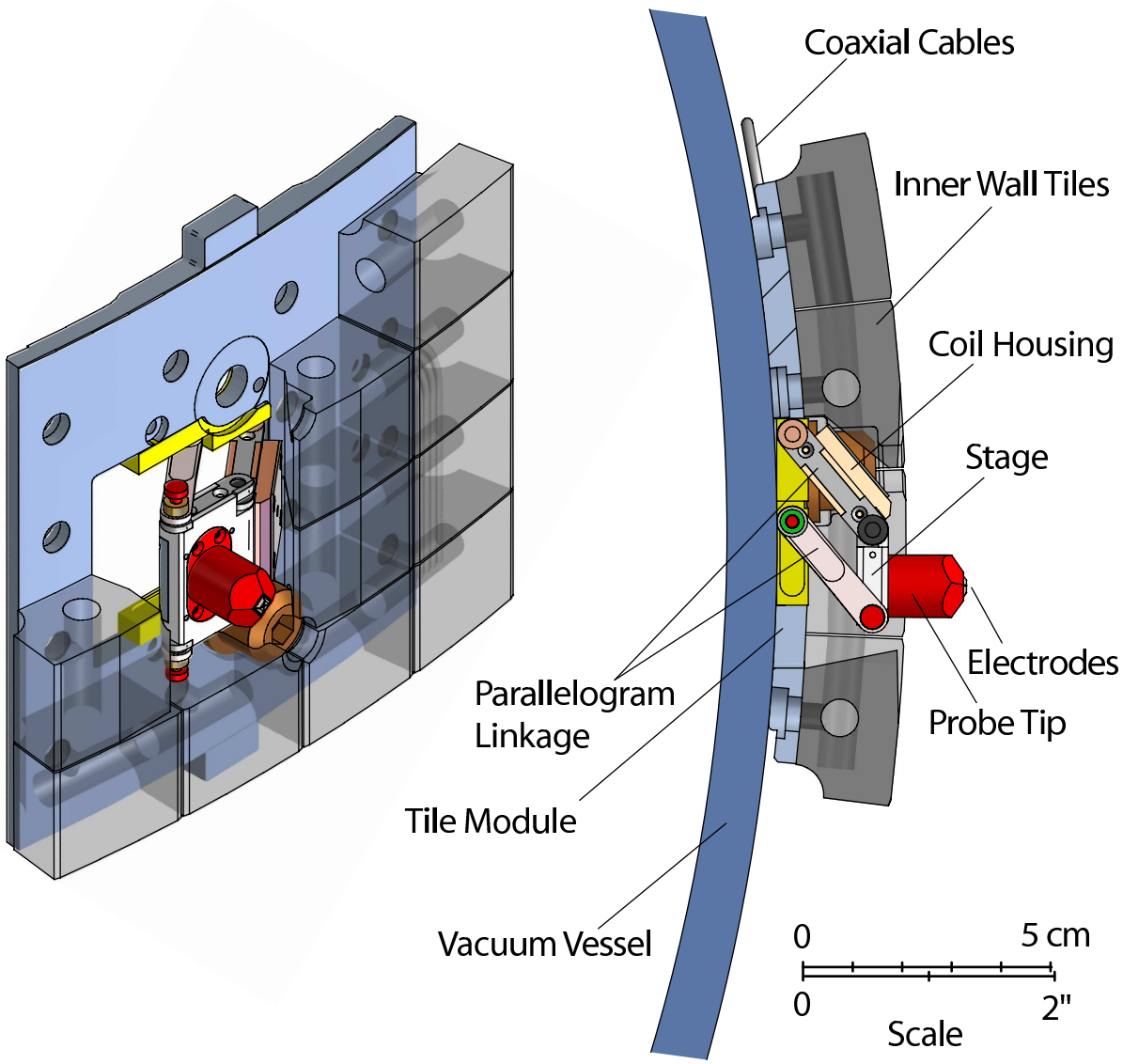

Figure 2-7: Wall-actuated scanning probe (WASP) assembly embedded in a C-Mod inner-wall tile module.

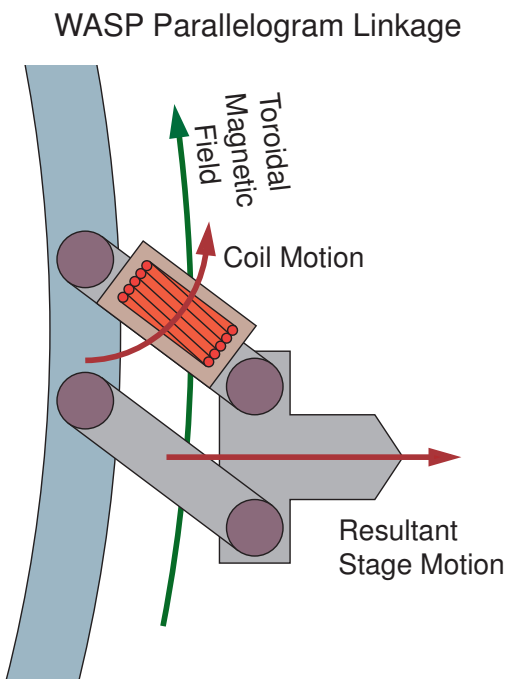

Figure 2-8: Illustration of the WASP coil drive linkage: When energized, the coil attempts to align its magnetic moment with the toroidal field. The parallelogram linkage maintains the orientation of the stage and probe tip with respect to the radial direction, reproducing the effect of linear radial motion.

'flappers' [23] and later used for the ISP [24]. The WASP is the first time such a coil has been mechanically arranged to drive linear motion. As a result, the WASP requires an array of eight pivots which must function in vacuum and survive high temperatures. They must also survive significant mechanical stress due to the inertial forces on the probe and should provide electrical insulation for the probe body. Otherwise it is possible that the probe body could draw a substantial current and increase the perturbation to the local plasma. One means of implementing these pivots is to use a shoulder bolt to secure the pivot assembly, but this solution occupies significant space and allows for the possibility of the bolt loosening and the probe failing. Since the WASP is inaccessible during a campaign, such a failure is highly undesirable. Our solution was to use compound bushings, which integrate a washer and axle into a single part, wherever possible (see Fig. 2-9). These bushings are captured in the structure during the assembly of the probe and module. They must endure the shear loads carried by the axle and require superior toughness. For this

application, we used zirconia, a ceramic with high fracture resistance. We were able to implement compound bushings in four of the eight pivot locations: two between the stage and coil and two between the coil and tile module. The other four pivots were implemented using a stainless steel shoulder-bolt locked against rotation by a set screw, with alumina washers providing electrical insulation and bearing surfaces. All of the ceramic bushings are captured by the structure as much as possible to prevent failure even in the event of a cracked bushing. Embedded torsion springs in two of the shoulder-bolt joints draw the probe back to the wall when the coil is not energized. This prevents the probe from accidentally being left in an extended position when not in use.

The coil is wound from 28 gage copper magnet wire with .025 mm thick polyamide-coating. The coil requires about 10 m of wire and has an inductance of about 50 μH. Its total effective area is roughly .03 m^2. The resistance of the coil is 2.3 Ω. Calculations indicate that the coil can survive being energized at the maximum power supply current of 6 A for 6.5 seconds without melting the polyamide coating. To prevent any shorting of the coil to the metal housing surrounding it, polyamide tape was wrapped around the mandrel of the coil and mica sheets were used to line the sides of the stainless spool. An extra coating of Teflon insulation was placed around the magnet wire where it exits the coil to prevent the coating from abrading over time and shorting the magnet wire to the housing.

Stage and Electrode Wires

The molybdenum probe tip extends from the 'stage'. The wiring for the four electrodes is routed through the stage (see Fig. 2-9). The current from each electrode is carried by a stranded, 28 gage copper wire with a 0.15 mm Teflon coating. The wire is routed from behind the tile module through the coil housing to the stage. Since the probe tip, and possibly the whole stage were expected to get hot, all electrical insulation in the stage and tip is done with ceramic parts. The electrode wires themselves can heat up both from carrying large currents and due to thermal conduction from the probe tip, so a ceramic heat sink cradles the wires where they enter the coil body.

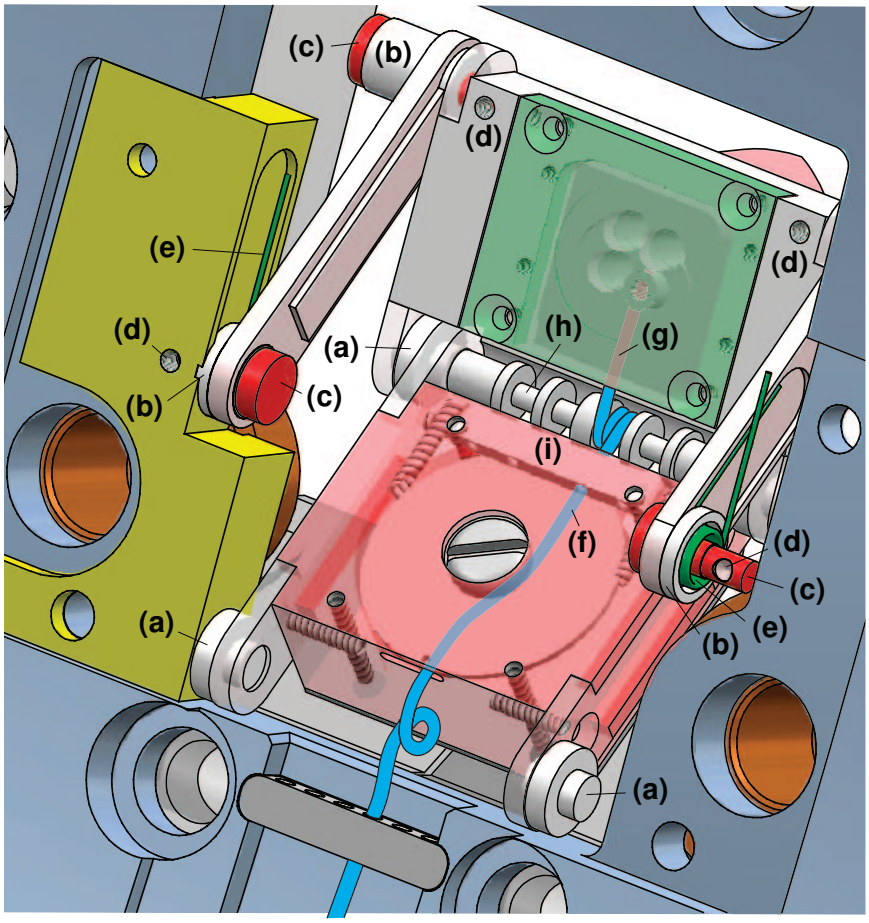

Figure 2-9: A back-view of the WASP: (a) 'compound' zirconia bushings, (b) alumina bushings, (c) shoulder bolts, (d) set screws, locking shoulder bolts against rotation, (e) return springs, (f) Teflon-coated electrode wire, (g) uncoated wire, terminating at the base of copper electrode contacts, secured by set screw, (h) alumina wire-support axle, and (i) alumina heat sink. Not shown for clarity: RHS mounting piece, three additional electrode wires and copper contacts, coil wires, limit springs, and small hardware.

Further from the plasma, we rely on the Teflon coating on the wires for electrical insulation. Calculations indicate that during an event where the probe is exposed to a sufficient heat flux to melt the molybdenum probe tip over 50 ms, the temperature change at the end of the wire closest to the electrode would be roughly 85°C. The ohmic heating of the wire is negligible in comparison. This result indicates that in a worst-case scenario, the Teflon ($T_m > 260$°C) is not likely to melt. Furthermore, we have inspected the Teflon after such events and found it intact. Care was taken that there be no direct line of sight from the plasma to the wires as the x-ray and UV light would quickly degrade the Teflon. To this end, shields were created out of shim stock and spot welded onto the coil structure.

There are two points where the wires must bend to follow the motion of the probe. It was feared that these points would be subject to fatigue failure of the wires. The problem is most pronounced at the joint between the coil and stage where space is the most limited. To mitigate this problem, the wires wrap twice around a rod that is coaxial with the pivot axis. In this way, the bending of the wires is distributed over a longer length, minimizing local strain. In addition, the Teflon coating was left on the wires in the area of the pivot even though all of the contact surfaces are ceramic or ceramic-coated. This maintains rigidity of the wire better than free metal strands. For the other pivot, located at the base of the coil, a single turn without a support shaft was used because the additional space reduced the bending requirement on the wires. In the stage, the wires terminate at the base of the copper spring contacts which connect to the electrodes. Behind the tile module, they are connected to co-axial cables with SMA pins.

Limit Springs

The motion of the WASP is limited by contact with the wall tiles at the maximum insertion, and contact with the vacuum vessel at maximum retraction. To reduce the inertial forces on the probe when colliding with these stops, finger-spring washers [26] were spot-welded to both the front and back surfaces of the coil housing and to the back surface of the stage (see Fig. 2-10). Originally, the springs were designed to

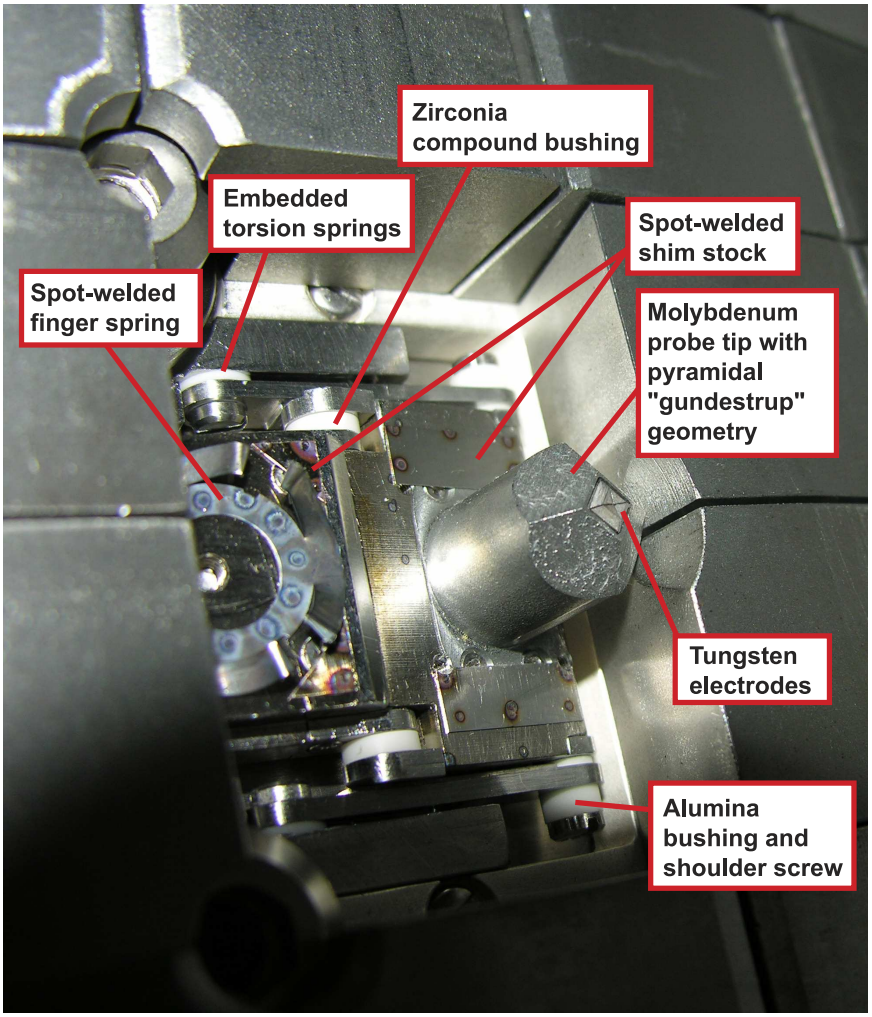

Figure 2-10: A WASP probe installed on the C-Mod inner wall.

assist the electro-mechanical drive in turning the probe around quickly at maximum plunge, but we discovered that the EM drive is quite capable of effecting a quick turn-around by itself.

Probe Tip

The probe tip is a molybdenum shaft, 12.7 mm in diameter, which extends $\sim$ 15 mm from the front of the stage, terminating in a high heat flux Gundestrup probe (section 2-5). The pyramid is rotated at 6.5° to align with the magnetic field for typical values of the edge safety factor.

A common failure mode for scanning probes is exposure to excess plasma heat flux.

This can happen during a plasma disruption in which control of the plasma is lost and it crashes towards the probe. Over-insertion of the probe can also lead to failure. Both of these events usually result in melting of the surface of the probe tip and/or the electrodes, which then become electrically shorted together. For this reason the probe tip and electrodes are designed so they can be removed easily as a unit and replaced. This modular design also allows the probe to be easily fit with alternate tip geometries if desired. Four screws hold the probe tip to the stage; they are accessible from the front of the unit. In Fig. 2-10 they are half-visible behind shim stock that has been spot-welded on the front of the stage to eliminate the possibility of the screws loosening during operation. The electrodes are held in place inside the probe tip with a threaded collar, and the electrical connection is made via a spring contact. Inside the stage, the electrode wires terminate in the base of the contacts (see Fig. 2-9). The wires are held in contact with a set screw. Solder was avoided at this location because we have found that exposure of the ceramic insulators to acid flux can lead to a current leakage path between electrodes. However, in retrospect it appears that this may have been the wrong decision. We have experienced occasional open-circuit electrodes during WASP operation which are most likely due to a loosening of the set screw that holds the wires in contact. This could be caused by either repeated motion or repeated thermal cycling of the probe. Prior to the 2009 installation, the wires were soldered to the connectors, and flux contamination was carefully avoided. Since this repair, no open-circuit failures have occurred.

Coaxial Cables

The electrical connections to the probe coil and electrodes are made via 50 Ω co-axial cables and vacuum feed-throughs. These provide the potential to sample plasma conditions at very high frequency, and to employ advanced signal processing methods such as the mirror Langmuir probe technique [27]. For the in-vessel sections, we selected a stainless steel jacket, SiO_2 insulated, 2.3 mm diameter cable from Meggitt Safety Systems. The small diameter was necessary due to space limitations behind the inner wall tiles. The 50 Ω cables terminate just before the actual probe, leaving

only about 70 mm of non-coaxial wire before the electrodes. To allow the entire probe module to be removed without re-routing all the cables, we installed SMA connectors [28] behind the wall tiles.

Electronics

The WASP electrodes use the standard set of electronics available to bias and record Langmuir probe data on C-Mod. Additional WASP-specific electronics have been developed to drive the coil (see Fig. 2-11). These include a series of logical interlocks, which require an active shot cycle and a manually set permissive to fire the probe. This allows us to disable the probe independent of the shot cycle, which can be very useful in a panic situation. These interlocks communicate with a relay which connects the coil to its power supply. An anticipated failure mode for the control system was that a large current might be driven for an extended period, potentially melting the coil windings. To avoid this, we employ a pair of 555 timers in the circuit which allow the coil to be energized for only a two-second window and then have it time out for about two minutes. This should never interfere with normal probe operations, but should prevent an over-current failure. The coil current is measured by adding a high-power, high accuracy 1 Ω resistor in series with the coil and measuring the voltage across it. (Note that this resistance is included in the R in Eq. (2.12)). The voltage and current signals are monitored via high-impedance op-amps and sent to CAMAC digitizers.

2.3.2 Electro-Mechanical Model

The WASP coil drive is based on those that were used for the ISP [24] and divertor bypass flappers [23]. The torque balance on the probe assembly is given by:

$$\begin{aligned} I_m \frac{\mathrm{d}^2\theta}{\mathrm{d}t^2} &= \tau_{coil} + \tau_{spring} + \tau_{eddy} \\ &= AIB\cos\theta - k(\theta - \theta_0) - \kappa B^2 \cos^2\theta \frac{\mathrm{d}\theta}{\mathrm{d}t}. \end{aligned} \tag{2.11}$$

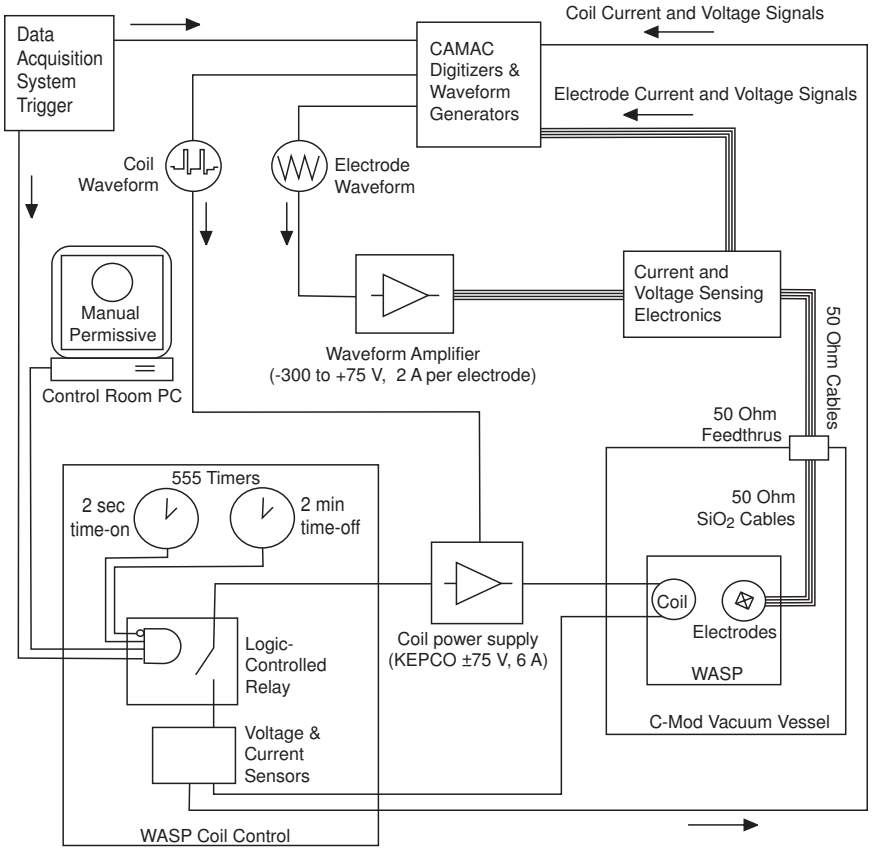

Figure 2-11: Block diagram of WASP control electronics and data acquisition system.

Where I_m is the effective moment of inertia of the probe assembly, θ is the angle of the coil from its rest position, A is the effective area of the coil, I is the current driven in the coil, B is the magnetic field, k is the spring constant of the return springs, θ_0 is the rest angle of the return springs, and κ is an eddy current coefficient. This model assumes the object is a rigid rotor, which is not strictly true for the WASP. As a result, both κ and I_m vary with θ due to the changing geometry as the coil rotates. A careful calculation of the moment of inertia shows that it varies by only about 6% over the coil's range of motion. This is small enough that it should not affect the accuracy of our model.

The primary challenge in making an accurate model is correctly calculating the magnitude of the eddy currents induced in the probe as a result of its motion. The eddy currents effectively set a terminal velocity for the probe. Because of the strong impact that this has on the dynamics of the probe scan, and in particular the amount of time it would spend in the plasma, it was decided that the WASP should be tested off-line in a high field environment. This would also provide the opportunity to evaluate the mechanical durability of the design.

To perform these tests, we made use of the 1-J Magnet, operated by the PTF group at the MIT Plasma Science and Fusion Center. This water-cooled copper magnet can achieve magnetic fields as high as 4.5 T for a few seconds, providing us a data set that we could extrapolate to the 5-12 T typically found at the inner wall of Alcator C-Mod. At the time of the test, ceramic bearings were not yet available, so a set of graphite bearings were used instead. The probe was outfitted with mechanical limit switches which could sense if the probe was at maximum plunge or if it was fully retracted. These data supplemented the results of the back-EMF integration, which is the means of measuring the probe position when it is operated on C-Mod. The back-EMF is calculated using the equation:

$$V = IR + ABcos\theta\frac{d\theta}{dt} + L\frac{dI}{dt}. \tag{2.12}$$

The self-inductance term (last term) has minimal effect on the result because the

field generated by the coil is always much less than the ambient field in the tokamak. The only time it could be important is when the current is rapidly changed in the coil (e.g., at maximum plunge when the polarity is reversed) but we find experimentally that including this term makes very little difference in the result. Therefore only a rough value of the coil inductance is required. The inductance of our coil is $\sim 50\mu$H. It should also be noted that by solving this equation, one implicitly assumes that R and B have no time dependence. This is generally well satisfied, but care must be taken in the case of a rapidly ramping field. Given steady R, B and small L we need only know the effective area of the coil and its resistance to calculate the trajectory of the WASP from the coil $I - V$ characteristic. A robust method of calculating the resistance is to apply a small reverse voltage to the coil throughout the shot, which holds the coil firmly against the wall (see Fig. 2-13). The current passed in the stationary coil is used to measure the resistance before and after each scan to provide a nearly continuous calibration, which can track changes in the resistance due to changing coil temperature. The effective area can then be calibrated by comparing the back-EMF output to the known range of motion of the WASP.

We conducted WASP tests using the 1-J Magnet over a period of two days. The back-EMF integration and the signals from the limit switches confirmed that the probe was able to scan through its entire range and back in a time of $\sim$30 ms. This was less than the 50 ms scan time of the ISP, minimizing the probe's dwell time in the plasma. We collected data at a variety of magnetic fields ranging from 1 to 4.5 Tesla. This allowed us to fit the data to a computer model of the probe motion based on Eq. (2.11). We were then able to extract various constants which could be used to predict the motion of the probe in C-Mod. Several traces of predicted motion compared to observed motion are shown in Fig. 2-12. Note that our model does not account for energy dissipation during the collision of the probe with the wall (which appears to be substantial) or from friction in the bearings. However, it is fairly accurate in predicting the free motion of the probe. While the model is not needed for the normal operation of the WASP, it can be helpful in predicting the response of the coil drive to new magnetic field conditions or new driving waveforms, which can

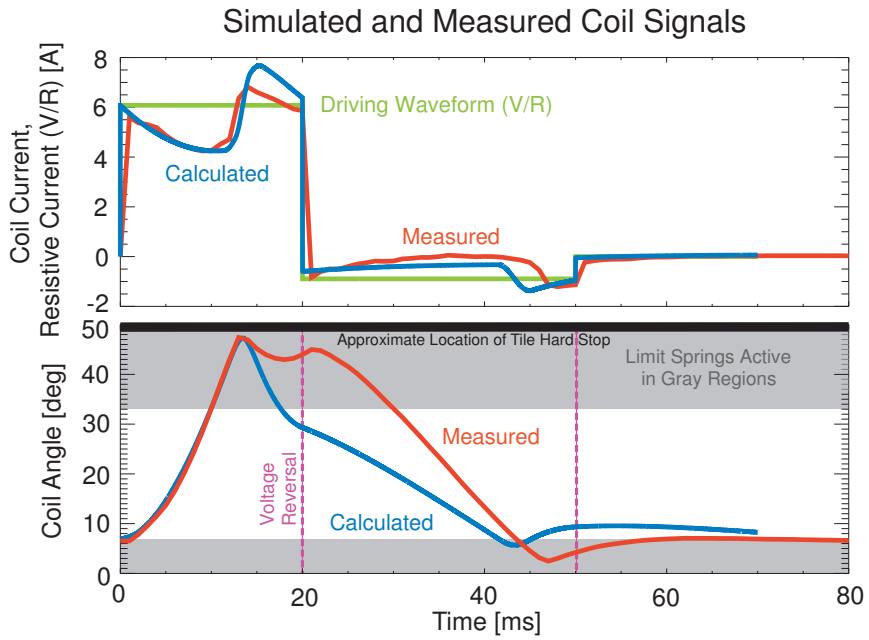

Figure 2-12: The model which predicts the coil motion can be used to roughly anticipate the response of the coil-drive to different field conditions and driving waveforms. The plunge depth measured by integrating the coil back-EMF provides the radial position measurements we report with our data.

be more convenient and less hazardous than a trial-and-error approach.

While testing the WASP on the 1-J magnet, we scanned the probe many times during a magnet pulse to evaluate its durability. A total of 100 scans were performed on the first day of testing, 400 on the second. Two of the graphite bearings fractured during the test, but this did not inhibit the operation of the probe. It did however confirm our suspicions that graphite would be an insufficient structural material for the bearings, motivating our use of ceramics. It is worth noting that very low fields result in more violent motions of the probe since the damping due to eddy currents is reduced. In the end we were satisfied that the probe would be sufficiently durable to survive operations inside C-Mod.

2.3.3 WASP operation

The WASP probe was operated for the first time in the spring of 2007. It was first tested during no-plasma, toroidal-field-only pulses at the beginning of the campaign.

This allowed us to verify that the probes were scanning and our back-EMF plunge calculation was functioning as expected. Throughout the '07 and '08 campaigns we operated the WASP without any problems affecting the coil drive or structural integrity.

On two occasions, we melted a probe tip. Once was due to an operator error: setting the plunge too deep. The other was the result of a disruption induced by another scanning probe plunging too deep. During the up-to-air between the '07 and '08 campaigns, we replaced the probe tip while the WASP coil and stage remained installed on the inner wall, a procedure that was quick and easy, as expected.

The WASP's EM drive affords us the ability to auto-target the probe based on the results of a previous shot. Using an identical program to control the magnetic flux surface shape and location of the plasma, we can reasonably expect the position of the last closed flux surface (LCFS) to follow a similar trajectory in time. The WASP has the ability to plunge to any specified depth depending on what driving waveform is used in the coil. This means that on repeat shots, a program can be written that targets the exact depth of the separatrix (or any specified flux surface) independently for several pulses at several different times (see Fig. 2-13 for an example). This is an extremely useful operational feature which removes all the anxiety and guess-work from the targeting process and greatly improves the efficiency of our experiments. This system was implemented for the WASP based on empirical measurements of the probe response to a variety of driving waveforms in a variety of fields. It typically hits the programmed target to within $\pm$ 1 mm.

2.4 Scanning Probe Interpretation

Fig. 2-14 shows an example of how probe data is typically processed on C-Mod. The top half of the figure shows data from the HFS WASP probe. The first two panels show the current and voltage on a single electrode for the duration of a single plunge. These data were digitized at 1 MHz. The voltage is externally controlled and attempts to trace a 2 kHz triangle wave. The negative voltage must be high enough to reach

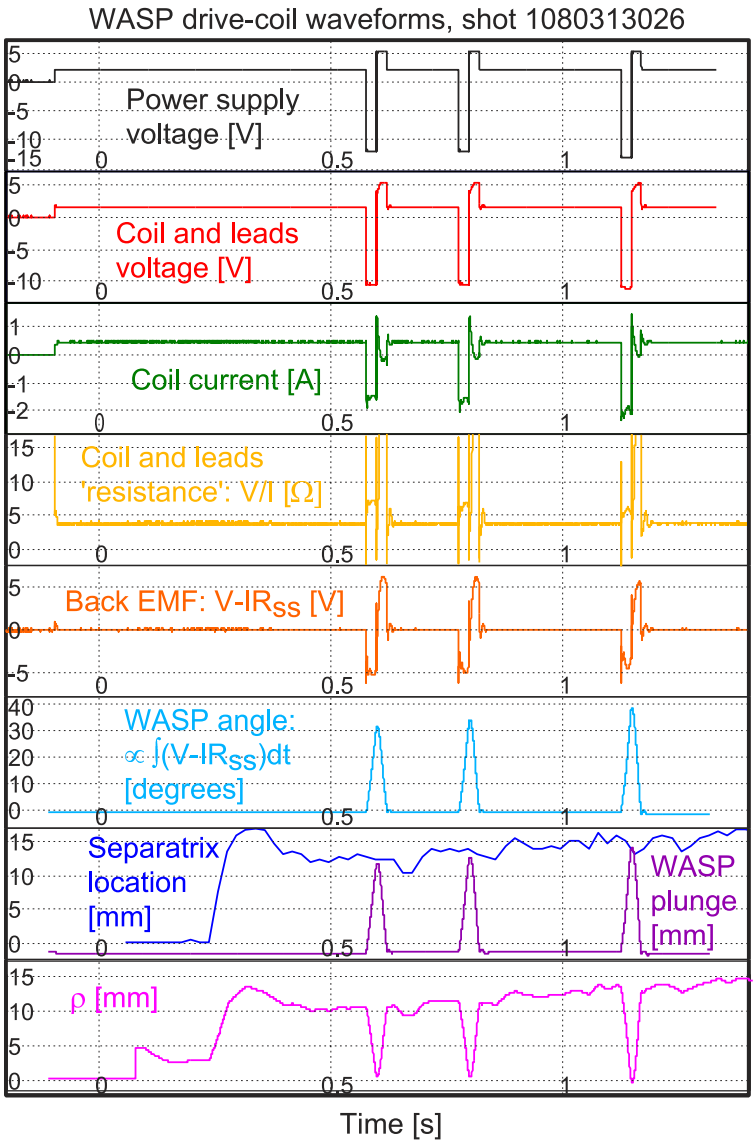

Figure 2-13: Typical waveforms for the WASP coil drive during a C-Mod discharge. Note that the 'resistance' calculated by V/R has a steady value between plunges when the coil is held against the wall with a reversed voltage. During this time, the coil is stationary and the current is constant. This provides the value of R_{ss} which is used in the back-EMF calculation. The final result, ρ, is the position of the probe in the SOL measured from the LCFS.

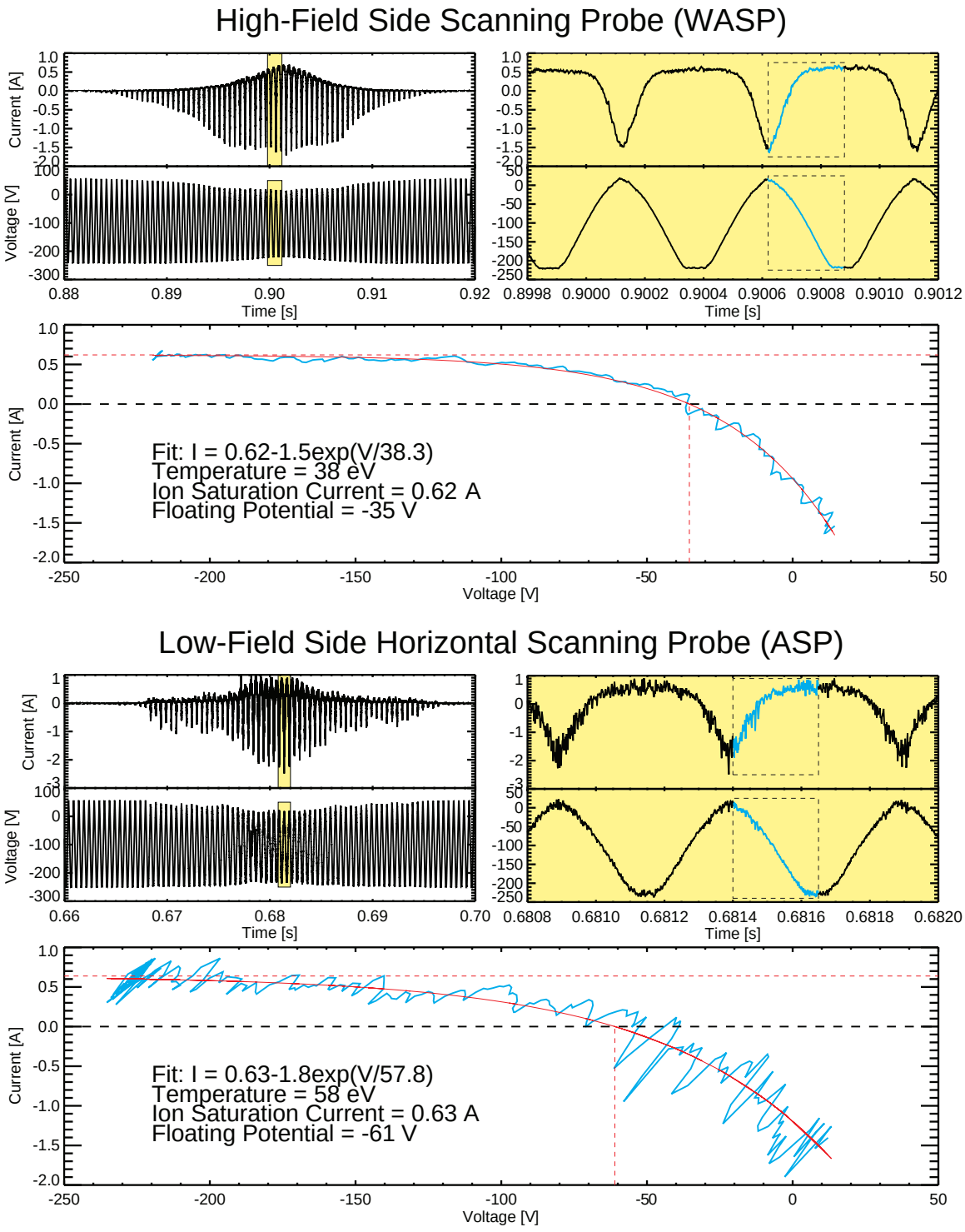

Figure 2-14: This figure shows time traces of the current and voltage on a scanning probe as a function of time during a single probe plunge. A roughly triangular voltage waveform with a frequency of 2 kHz is applied to the electrode. The upward and downward going $I - V$ sweeps are each fit with an exponential to provide 4 kHz measurements of electron temperature, density and floating potential. Examples are shown for a WASP and ASP $I - V$ fit. Note the smaller fluctuation levels in the high-field side data.

ion saturation (several times the electron temperature). The positive voltage limit is set relatively low because too much electron collection can damage the probe and electronics. The amplitude of the waveform is adjustable, with a typical example (-250 V to +50 V) shown in Fig. 2-14. Our electronics allow for a maximum bias of -300 V to +75 V, and have a current clamp at 2 A to limit the damage that can be caused by arcing. The positive current excursions (indicating current collected by the probe) define an 'envelope' which tracks the ion saturation current through time. The yellow boxes are magnified on the right, showing a few sweeps of the voltage and current. Each positive and negative going sweep provides an $I - V$ characteristic which can be fit to produce electron temperature, density and floating potential measurements. This provides 4 kHz measurement of these quantities. One sweep is selected and the fit is shown below, along with the extracted values of electron temperature, ion saturation current and floating potential.

The bottom half of Fig. 2-14 shows the same set of graphics for a typical scan with the LFS horizontal scanning probe (ASP). Notice the much higher levels of fluctuations that are present. It is generally observed that the fluctuation levels on the LFS are much higher than on the HFS. This is direct evidence of a ballooning-like poloidal asymmetry in turbulent transport.

Since the time to execute a single voltage sweep is very short (0.25 ms) we can generally assume the probe has moved very little ($\lesssim 0.25$ mm) during that time period and assign the measured value to a point in space which represents the average radial location of the probe during the sweep. In this way the data are mapped from a time series into a spatial trend. Of course the probe makes measurements on both the ingoing and outgoing scans, and generally the data overlay well. However, there are cases where the probe overheats and the outgoing scan is corrupted by thermionic electron emission. In this case the outgoing scan is discarded and the ingoing scan is treated as suspect.

Fig. 2-15 shows an example of plasma temperature mapped from time into ρ-space (flux-space) for a typical WASP plunge. In this thesis, data will always be presented as a function of radius, as shown in the right-hand panel of Fig. 2-15. The spline fit to

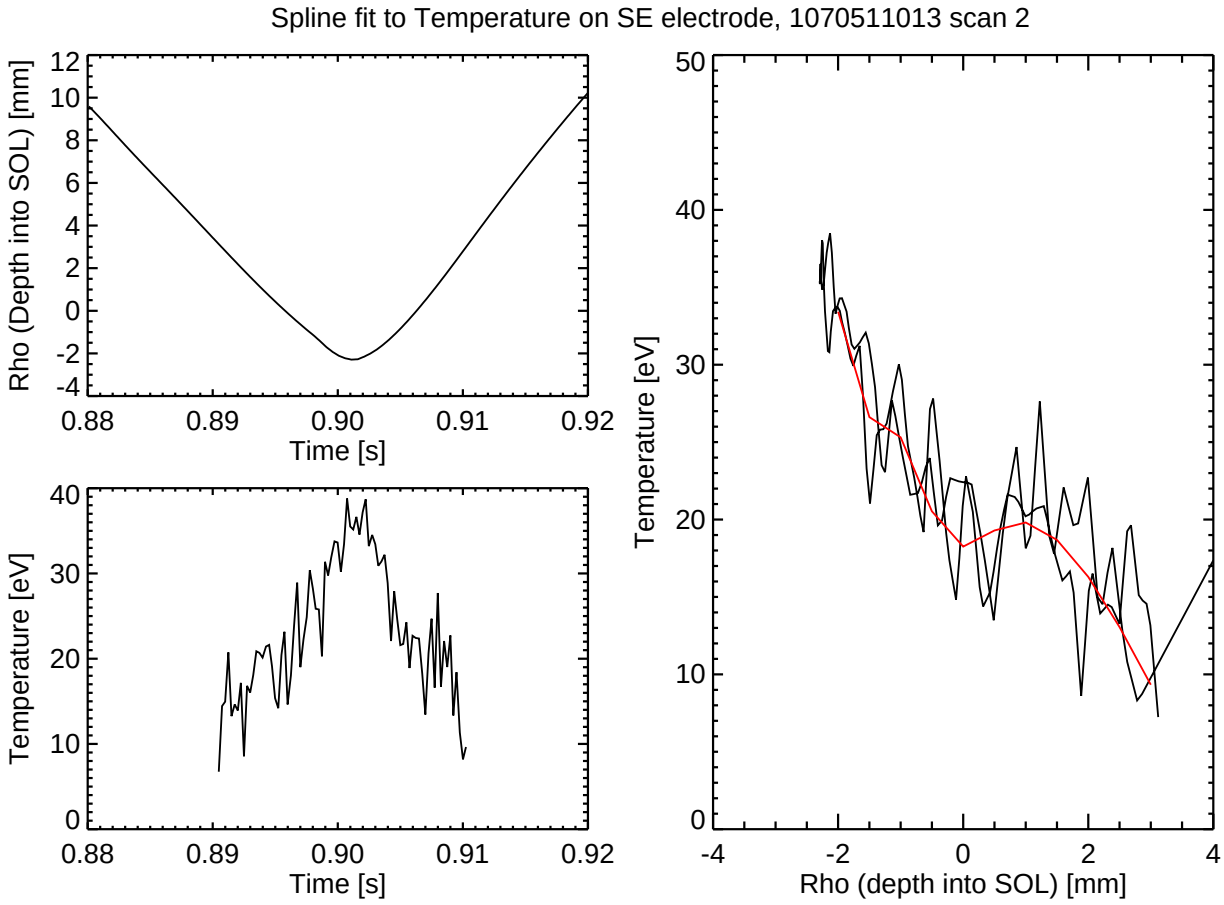

Figure 2-15: An example of a mapping of the temperature measurement on a single electrode during a single probe plunge from time space into ρ-space. The ingoing and outgoing traces overlay well, as is typically the case. The spline fit to the data is shown. The data in the remainder of the thesis will be presented in this format.

the data shown in red is the format in which data will be presented in the remainder of this thesis. The striking result from this plot is that the measured temperature attains a value of only 40 eV, though the EFIT reconstruction [29] shows a radial location of 2 mm inside the last closed flux surface. This is not realistic and can be attributed to uncertainties of 2-3 mm which are present in the EFIT reconstructions [30], and similar uncertainties in the probe position. In order to compare data from different scanning probes in a meaningful way, we routinely apply a shift to the ρ-location of a given probe scan. This is done based on power-balance considerations. The amount of power passing into the SOL is calculated as the ohmic input power minus the core radiated power deduced from bolometry. We then assume the SOL heat loss as dominated by parallel electron conduction. Following some further simplifying assumptions, the expected temperature at the LCFS at the LFS midplane can be calculated. This procedure is detailed in [31]. Once the midplane probe is adjusted to the correct ρ location, we shift the other probes to produce good alignment of the pressure profiles. In the case shown in Fig. 2-15, the WASP data were shifted outward in ρ space by ~ 3 mm.

Similar spline fits to the one shown in Fig. 2-15 are performed for density and floating potential for each electrode during each probe scan. Fig. 2-16 shows the traces from all four electrodes during a typical WASP plunge. While the Gundestrup formulation described in sections 2.1.3 and 2.2.2 can be used to interpret variation among ion saturation currents on the different electrodes, there is no established treatment for variations among temperatures and potentials measured by the different electrodes. Our standard procedure is to average the four values and report this as the local temperature measurement, but this is not justified by any theoretical considerations. Fig. 2-17 illustrates the typical variation of the three primary quantities between electrodes and shows the the final reported value.

Starting with the three quantities that are direct results of the $I-V$ fits (T_e, n_e and V_f) it is possible to derive many other quantities of interest. For instance, the Mach number is a ratio of saturation currents on upstream and downstream electrodes. The radial electric field requires a calculation of the plasma potential from the floating

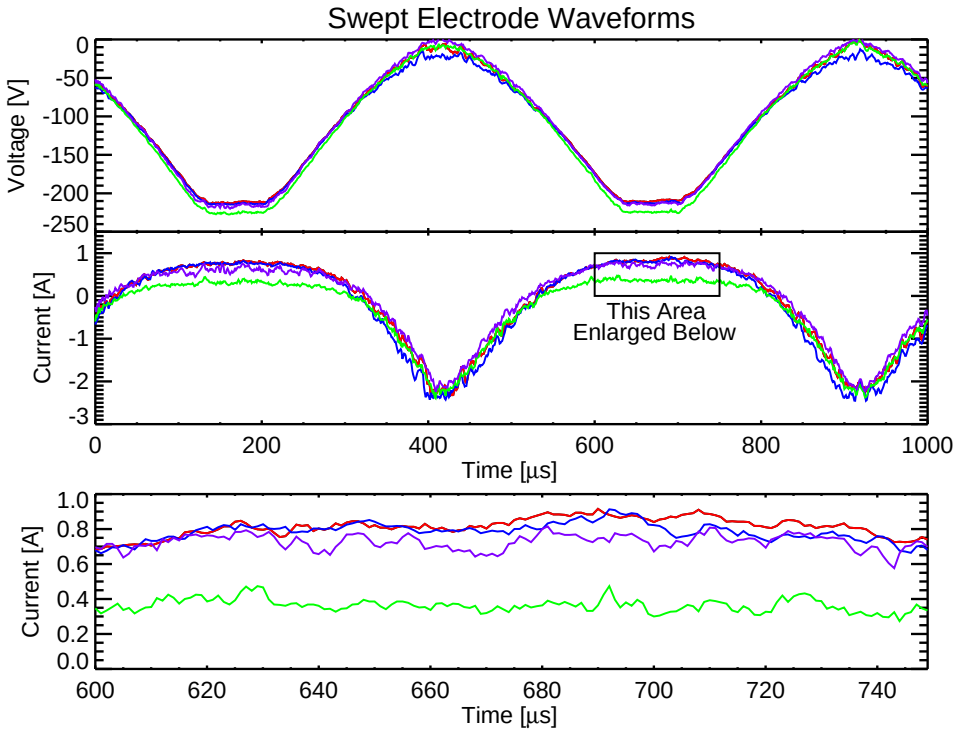

Figure 2-16: A 1 ms snapshot of the current and voltage traces from all four WASP electrodes. The bottom trace shows the currents from electrodes during a period of ion saturation. These currents are used to extract density and parallel and perpendicular Mach numbers. The signals are digitized at 1 MHz. Time-correlation of fluctuations can provide a measurement of the phase velocity of fluctuations propagating in the perpendicular direction.

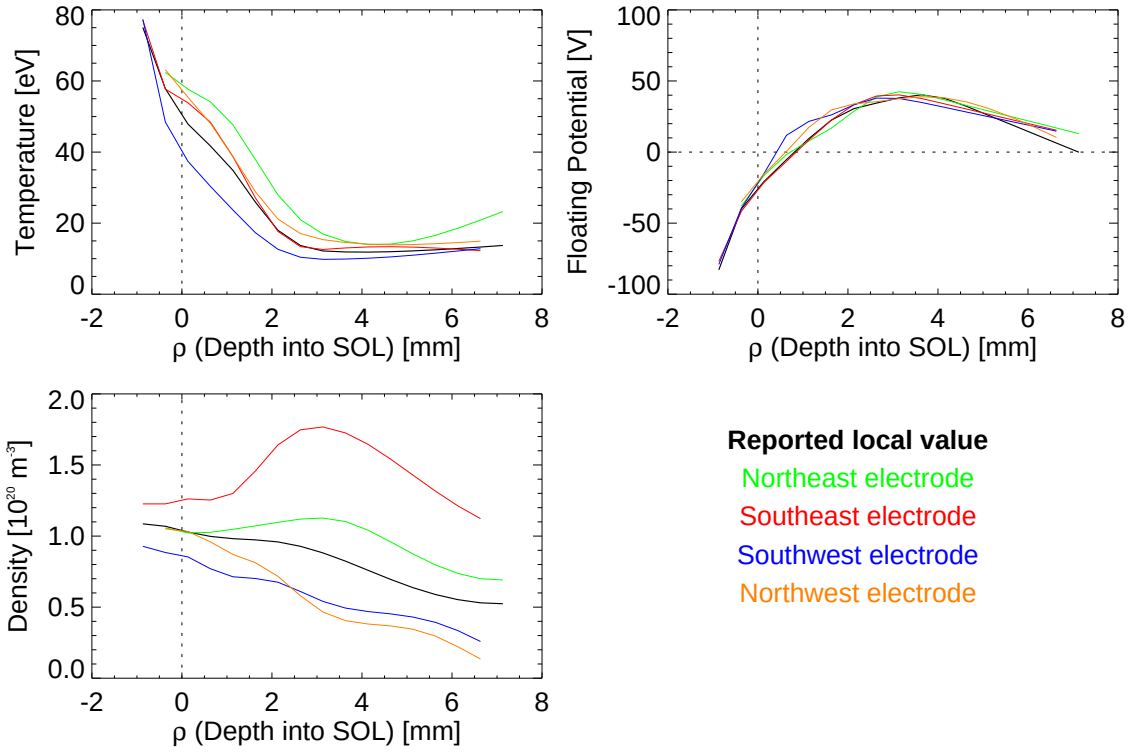

Figure 2-17: Variation of the primary probe measurements over the four electrodes for a typical WASP plunge. This is a LSN plasma with the dominant parallel flow from East to West, as is evident in the density data.

potential and electron temperature. E_r is then given by $\nabla_r \Phi_p$, as discussed in section 2.1.3. Of course, the most reliable measurements are those of the primary quantities.

High-frequency analysis is routinely conducted during periods of ion saturation. The bottom panel of Fig. 2-16 shows the WASP signals from the four electrodes during such a period. These are used to infer poloidal phase velocity of fluctuations by the time-delay correlation of the ion saturation currents on poloidally adjacent electrodes, as described in section 2.1.3.

When measurement of fluctuation-induced fluxes is desired, two of the electrodes are operated in the swept mode and two in 'floating mode'. Operating in floating mode involves simply setting the current to zero and recording the floating potential of the probe. This configuration allows us to calculate fluctuation-induced fluxes as described in section 2.1.4. The high heat flux probes are typically operated with the NE and SE electrodes floating and the NW and SW electrodes swept. When using this technique, we can still measure temperature, density and floating potential, but we cannot use any of the flow measurement techniques. However, in this case the temperature and density are measured in only one parallel direction, which can be misleading, particularly in the WASP location (see section 4.3).

2.5 Other C-Mod Diagnostics

Results from other diagnostic systems will be used in this thesis for comparison and benchmarking. They are briefly described in this section.

2.5.1 Charge Exchange Spectroscopy

Alcator C-Mod is equipped with charge exchange spectroscopy diagnostics to measure plasma conditions in the pedestal region. This technique can be used to measure impurity concentration, n_z, temperature, T_z and velocity v_z. There are two edge charge exchange systems, one measuring a region near the outboard midplane, with toroidal and poloidal viewing arrays, and the other trained on a region near the inboard midplane with a toroidally viewing array only [32, 33] (see Fig. 2-4). Both

systems measure line-emission from boron impurities in the plasma. Boron is present as a $\sim 1\%$ impurity due to the boron coatings routinely deposited on the first wall of the vessel. These coatings are intended to reduce contamination of the plasma by the high-Z materials comprising the plasma-facing components [34]. The spectrometer views line radiation from the $n = 7 \rightarrow 6$ transition in excited B^{4+} at 4944.67 Å. The pedestal region contains both B^{4+} and fully-stripped B^{5+}. In the absence of a source of charge exchange neutrals, there is still significant line emission due to electron-impact excitation of the B^{4+} ions, which the spectrometer sees integrated over a viewing chord. This is referred to as 'background' emission. This by itself can be used as a diagnostic technique, but suffers from both poor radial resolution of the region of interest, and low signal at high temperatures due to a reduced population of B^{4+}. However, in L-Mode plasmas, this method often produces good results.

When a neutral source is introduced, the signal is enhanced due to charge exchange recombination of B^{5+} to excited B^{4+} ions. If significant background is present before the introduction of the neutral source, it can be subtracted to produce a measurement that is localized to the neutral source region. This technique can be used to produce good radial resolution in the measurements. For the LFS system, the neutral deuterium atoms are provided by C-Mod's diagnostic neutral beam (DNB), while on the HFS they are provided by a gas capillary near the midplane that injects neutral deuterium.

An absolutely calibrated spectrometer provides a measurement of the velocity distribution function of the boron ions along the viewing chord. The first three moments of the distribution function (n_z, v_z, T_z) are of interest and are routinely measured. To calibrate the measurement of n_z, the neutral density must be known. The neutral density from the DNB on the LFS can be calculated with reasonably good accuracy. The same is much more difficult for the gas puff on the HFS and is not routinely done. Regular calibrations of the wavelength of the spectrometer using a known source allow a direct measurement of the impurity velocity; the temperature can be calculated without absolute calibration.

The measurements from the charge exchange systems usually suffer from very

low signal in the SOL, particularly in L-mode plasmas where we operate the probes. However, despite the lack of overlap, useful comparisons can be made of plasma parameters coupling across the LCFS. When comparing flow results from charge exchange diagnostics based on impurities to those from the probes, we must take care because plasma impurities are not necessarily expected to have the same distribution function as the bulk plasma. We can look for velocities which show similar trends, but in general, the most robust quantity for comparison is the radial electric field. On the LFS, this can be extracted from measurements of two impurity velocity components (toroidal and poloidal) combined with pressure gradient measurements and the radial force balance equation [33].

The comparison on the HFS is more difficult because we lack a poloidal view to extract that component of the velocity. However, during the '07 and '08 campaigns, an additional spectrometer was in use on Alcator C-Mod which made measurements of charge exchange not from an impurity, but from the bulk plasma [35]. This diagnostic monitored the deuterium Balmer beta emission line at 4860 Å, and is thus often referred to as 'CXRS D_β'. The neutral source was the HFS gas puff, as with the boron HFS charge exchange system. The resulting velocity distribution contained components from two distinct sources. The 'hot' component was identified as the bulk plasma while the 'cold' component signaled double charge exchange events of the injected neutrals. These two components can be extracted separately from the charge exchange spectra. This direct measurement of the main ion parallel flow is suitable for comparison with the probes. The spatial resolution of this technique is generally poor, but it can provide information about the gross features of the bulk plasma pedestal on the HFS. The flow profile spanning the LCFS can provide information about edge-core momentum transport. Results of this comparison are shown in section 7.3.2.

2.5.2 Midplane Diode Array

Alcator C-Mod is equipped with an array of photodiodes [36, 37], which view the LFS midplane horizontally (see Fig. 2-4). These diodes are sensitive to D_α light, the

emission of which is toroidally localized by a deuterium puff in the viewing region. The diode views are arranged into a horizontal and a vertical array. The vertical array is located at a major radius of 88.8 cm and can be used to measure the poloidal wave-number of plasma fluctuations at regular time intervals. This provides a dispersion relation of the turbulence in the poloidal direction over a frequency range up to 500 kHz and a wave number range of 40-800 m^{-1}. This can be used to calculate wave phase velocities for comparison to those measured by the probes. By scanning the location LCFS in front of these views, a data set can be assembled which covers a range of radii of $-10 < \rho$ [mm] < 10. Results from this technique are reported in section 7.3.1.

Chapter 3

Experimental Program

With the new WASP diagnostic and the Gundestrup probe tips in place, we began an experimental program designed to take advantage of their unique capabilities. This chapter will describe the operation of the probes during this experimental program, and the details of the experiments that were conducted.

3.1 Typical C-Mod Discharge for Probe Studies

The data presented in this thesis were collected exclusively from ohmically heated discharges, the majority of which were in L-mode. Fig. 3-1 shows some of the discharge parameters for a typical probe experiment. In this example, toroidal magnetic field and plasma current were maintained at typical C-Mod values of 5.4 T and 0.8 MA respectively. The systematically varied parameters in our experiments were the plasma density and the 'magnetic topology', which refers to divertor configuration (upper, lower or double null). Shown in Fig. 3-1 are the line-integrated density from the central chord of the two-color interferometry (TCI) system (known as 'NL04'), and the magnetic parameter SSEP, which is the radial distance between the primary and secondary separatricies at the outer mid-plane. This parameter is obtained from the EFIT [29] magnetic reconstruction code; it conveys detailed information about the magnetic topology: negative values are lower single null (LSN), positive values are upper single null (USN) and values near zero are double null (DN) configura-

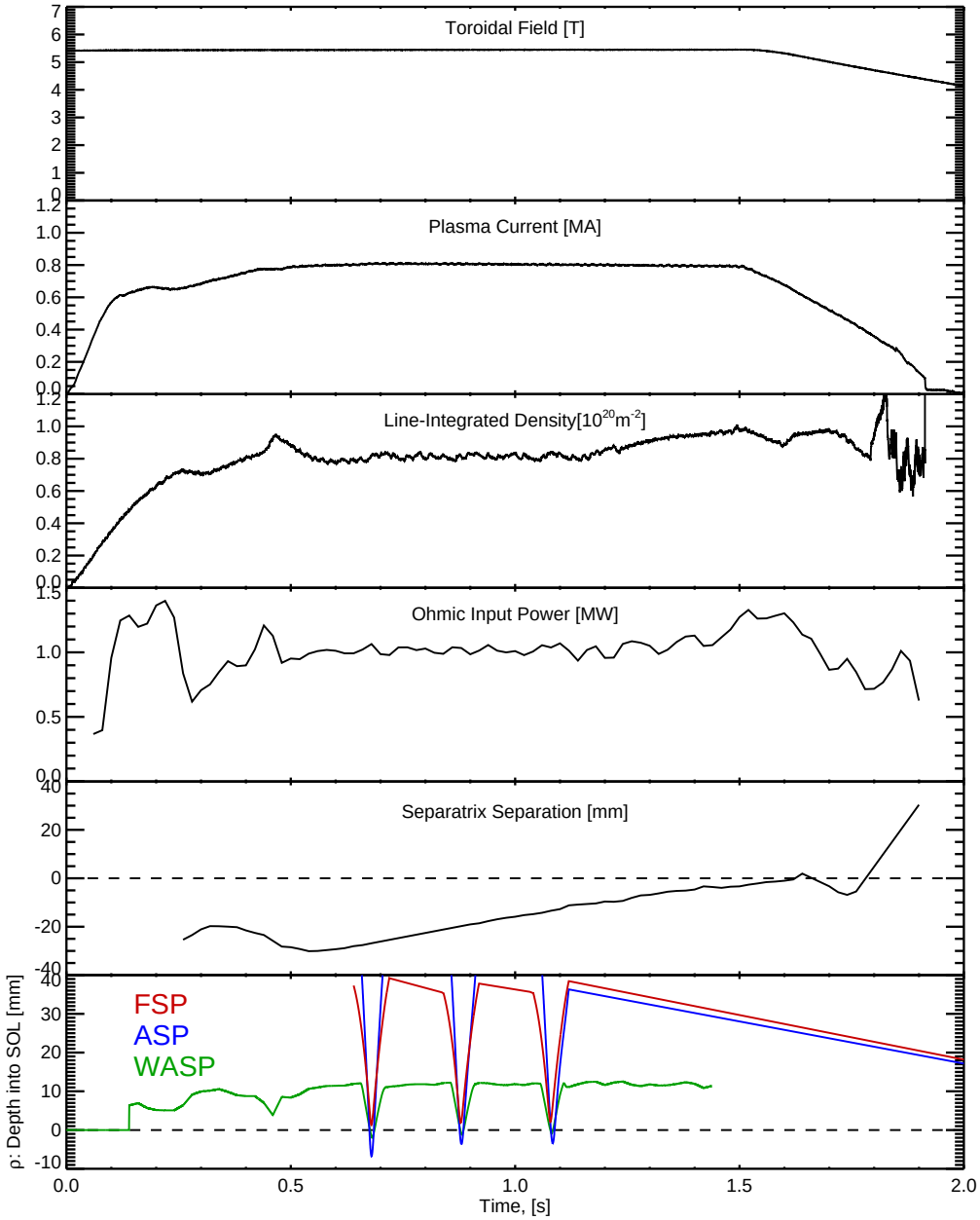

Figure 3-1: Typical traces of plasma parameters for an Alcator C-Mod L-Mode discharge. The separatrix separation (SSEP) is the distance between the primary and secondary separatricies at the outer midplane. Negative values indicate LSN while positive values indicate USN. The depth into the SOL (ρ) is the distance of the probe from the separatrix, also mapped to the outer midplane. The trajectories of each of the three scanning probes are shown.

tions. The density shown for this shot (NL04 $\sim 0.8 \times 10^{20}$ m^{-2}) is considered an intermediate value for probe experiments, which are usually conducted in the range of $0.4 <$ NL04 [10^{20} m^{-2}] < 1.2. Below this density range, it is difficult to operate the machine with normal field and current (0.8 MA, 5.4 T. Above this range, the discharge becomes increasingly susceptible to MARFEs [20]. MARFEs are plasma phenomena characterized by high recycling and very low temperatures on the HFS. Discharges in this state provide a minimum of interesting data at the WASP location; the pressures do not map from LFS to HFS and the HFS flows are suppressed. For these reasons, the MARFE was avoided in our experiments. In retrospect this may not have been wise, because the few shots where MARFEs did occur provided some interesting data (see section 8.2.5).

3.2 Mode of Scanning Probe Operation

The typical mode of operation for the scanning probes in our experiments was 3 plunges per shot. These were usually during the 'flat-top' portion of the discharge where the parameters are the most stable. The plunges were typically separated by $\sim$ 200 ms to keep the duty cycle reasonably low. The duration of a plunge was in the range of 50-80 ms. Figure 3-1 shows a plot of ρ (depth into the SOL) for the three scanning probes. The WASP's rest position is only about 10-15 mm in ρ-space. It therefore measures a somewhat smaller portion of ρ-space than the other two probes. This is limited by the 15 mm linear range of the WASP, and the slight flux expansion on the HFS. The three probes are synchronized so they reach maximum plunge at roughly the same time, and are targeted to reach the last closed flux surface. Each time a probe is scanned, the data are automatically mapped onto ρ-space. The resulting profiles are assigned a time stamp corresponding to the maximum probe plunge. This is referred to a time 'slice'. The processed data is stored in an edge database, which is organized by the shot number and the slice time in milliseconds.

The probes are not scanned in all discharges, mainly due to their need for constant monitoring and the possibility of overheating and melting the electrodes. This

can happen for many reasons, including over-insertion, unpredicted equilibrium fluctuations, and unlucky (or more likely, probe-induced) disruptions. Certain types of discharges are generally avoided for probe studies because of the increased chance of damage. High-density, high-current discharges present a hazard for the probes, so these are avoided if possible. H-mode discharges are characterized by reduced transport which makes the edge somewhat more hospitable, but care must be taken not to plunge too deeply into the pedestal where n_e and T_e increase dramatically. In addition, RF heated discharges have the additional problem of the creating RF sheaths which can damage the probes and complicate their interpretation [38, 39]. For this reason, when H-mode studies are undertaken, ohmic H-modes are created by ramping the toroidal magnetic field down during the discharge [40]. A final complication of probe studies is that we require careful control of the equilibrium location so it can be targeted by the probes. Ultimately, because of their fragility, the probes are operated cautiously and almost exclusively in discharges dedicated to probe experiments.

3.3 Experimental Investigations

Several experiments were carried out using the WASP and other probes during the '07 and '08 campaigns. These are listed chronologically in table 3.1. Experiments on C-Mod are distinguished by their 'mini-proposal' (MP) number. Other parameters shown in table 3.1 include the number of shots during which the WASP was able to take useful data, the wasp probe in use (A-port or K-port), and how many of the WASP electrodes were functioning normally (the WASPs suffered from intermittent open-circuit electrodes during these campaigns, as described in section 2.3.1). Also included are the range of toroidal field, plasma current and line-integrated density for each run day[1]. Four of the experiments (MPs 480, 510, 531, 547) were specifically aimed at utilizing the WASP probe, while others were more general probe experi-

[1]Run days are distinguished by a date in (y)yymmdd format where the year 0 corresponds to 1900. Using this system 1998 would be represented as '98' and 2005 would be represented as '105'. Individual shots are distinguished by adding an additional three-digit shot number onto the end (rarely larger than 035). For example: shot 1070627007 would be the 7th shot on June 27, 2007

ments. The experiments listed in table 3.1 provided the bulk of the data for this thesis. The following sections describe the WASP-specific experiments.

Topology effect on the SOL total flow vector (MP 480)

This experiment was a broad experiment designed at measuring the total flow vector with all three probes and its dependence on both magnetic topology (SSEP) and discharge density (NL04). This experiment was partially motivated by the results of 2-D simulations (Pigarov- UEDGE [14] and Bonnin- B2Eirene SOLPS5.0 [41]) which predicted the dependence of edge flows on topology and field (see chapter 7). Pigarov is among those who have invoked an inward pinch on the HFS to close the flow loop implied by the parallel flows observed there. To empirically address this hypothesis, a secondary goal of this experiment was the measurement of fluctuation-induced particle fluxes on the HFS. Two run days were allocated to this experiment (1070511 and 1070627) during which we had 36 discharges in which the WASP took good data, producing 97 time slices. 79 were in 'flow mode' while 18 were in 'fluctuation mode'. The on-axis toroidal magnetic field was held at its normal value of 5.4 T, as was the plasma current at 0.8 MA. Line-integrated discharge density was varied from 0.5 to 1.3 [10^{20} m^{-2}].

This experiment was revisited during the '09 campaign with the goal of collecting additional HFS fluctuation-induced flux measurements. In each discharge configuration, a shot was run with the probe in multiple different bias configurations. First, we ran a discharge with the probes in the standard flow mode. Then, two discharges were run with the probes in fluctuation mode; one with the East electrodes floating and the West electrodes swept and the other with the West electrodes floating and East electrodes swept. This was aimed at identifying any systematic errors which might be associated with the bias configuration. Finally, a few discharges were run with *all* the electrodes floating to look at the $\omega, \vec{k}$ power spectrum.

This run produced an additional 18 shots containing 50 slices with the WASP scanning to the LCFS. Field and current were held at standard values. The density was varied from 0.6 to 1.0 [10^{20} m^{-2}] in LSN, and a few discharges were run in USN

Experiment	Mini-Proposal	Run	Useful Shots	WASP in Use	Good WASP Electrodes	B_t [T]	I_p [MA]	NL04 [10^{20}m^{-2}]
2007 Campaign								
WASP Start-Up	465	1070404	10	A	4 - 3	5.4	0.8	0.60-0.7
Topology / Fluxes	480	1070511	25	K	4	5.4	0.8	0.48-1.3
B-Shear / Gradients	479	1070518	1	K	4	5.6	0.8	0.77
Topology / Fluxes	480	1070627	19	K	4	5.4	0.8	0.50-1.0
Ohmic H-Modes	493	1070710	0	K	4	2.9-4.4	0.8	0.64-1.6
Rev. B Topology Scan	510	1070725	15	A	1 - 3	5.4	0.8	0.35-1.4
2008 Campaign								
Wall Pumping	419	1071220	7	K	4	5.4	0.8	0.57-1.2
Wall Pumping	419	1071221	17	K	4 - 3	5.4	0.8	0.55-1.2
Ohmic H-Modes	493	1080124	14	K	3 - 4	2.7-5.9	0.6-1.2	0.48-0.9
Q-Scan	531	1080305	21	K	4 - 2	2.8-6.0	0.4-0.8	0.22-1.1
Ohmic H-Modes	493	1080313	23	A	3 - 4	2.5-5.9	0.6-1.2	0.58-2.0
Momentum Transport	537	1080314	2	A	3 - 4	5.4	0.8	0.78-0.9
Topology Scan	532	1080319	26	A	3 - 4	5.4	0.8	0.49-1.2
Momentum Coupling	547	1080411	8	A	3 - 4	5.4	0.8	0.82
Momentum Coupling	547	1080515	7	A	3	5.4	0.8	0.95
2009 Campaign								
Topology / Fluxes	480	1090721	18	A	4	5.4	0.8	0.61-1.0

Table 3.1: Probe runs on C-Mod during '07 and '08 campaigns. Highlighted runs are of particular importance to this thesis.

with NL04 $= 0.6 \times 10^{20}$ m^{-2}

Direct comparisons of the data from the density and topology scans with the results from edge codes are presented in section 7.1. The results of the fluctuation-induced particle flux measurements are reported in section 8.2.6.

Topology effect on the SOL total flow vector with reversed field (MP 510)

This experiment was aimed at verifying that the topology reversal is 'equivalent' to field and current reversal in the sense that reversing all three simultaneously is equivalent to turning the plasma upside-down with no other changes. This would allow us to eliminate up/down divertor asymmetries or probe asymmetries as a significant variable in our experiments. This experiment was conducted on 1070725 while the machine was configured for reversed field. Unfortunately, the WASP was suffering from multiple open-circuit electrodes at that late stage of the campaign, and very little flow data could be salvaged from the run. However, the data collected from the LFS probes show that the simultaneous reversal of field and current and mirroring of the flux surfaces about a horizontal plane also mirrors the measured flows about a horizontal plane. These results are presented in section 8.1.

Scaling of edge flow-shear profiles with plasma current and magnetic field (MP 531)

This experiment was intended to determine the sensitivity of the the edge profiles to changes in field and current. Of particular interest was the variation of the perpendicular flow shear layer that was observed in the near SOL. This experiment was carried out during the 1080305 run day. 21 shots with good WASP data were produced, containing 48 useful time slices. The field was varied over a range of 2.8-6.0 T and the current was varied from 0.4-0.8 MA. Though the density naturally tends to vary with both field and current, we also attempted to produce different densities in similar field and current configurations in order to observe independent shear layer trends with collisionality. We covered a wide range of NL04 from 0.2 to 1.1 [10^{20} m^{-2}]. No change was observed in the perpendicular phase velocity shear layer over a range

of edge q values from 3 to 10. However, we did observe a decrease in the shear layer with collisionality caused by changes in the perpendicular flow velocity in the far SOL. The perpendicular velocities measured in the far SOL were observed to scale like $1/B$, consistent with $E_r \times B$ drifts from a fixed $\nabla\Phi_p$.

Sensitivity of edge pressure gradients, toroidal rotation and flow-shear profiles to magnetic x-point topology (MP 532)

This experiment was similar to MP 480 but with emphasis on measurement of the perpendicular flow shear. The experiment was carried out during the 1080319 run day. 67 time slices were obtained over 26 good shots. Field and current were held constant at 5.4 T and 0.8 MA respectively, and topology was shifted from LSN to USN by incrementally changing the value of SSEP, allowing us to obtain data throughout the double-null transition. Line-integrated discharge density was also varied from 0.5 to 1.2 [10^{20} m^{-2}]. The flow shear was found to depend on topology, a result which is reported in section 6.2.3.

High-field side SOL momentum coupling experiments (MP 547)

This experiment set out to demonstrate whether the HFS flow was a the driving quantity in edge-core momentum coupling. This was done using a 'nose grazing equilibrium' which attempts to dramatically change the HFS parallel flows while maintaining a constant magnetic topology. Two run days were dedicated to this experiment (1080411 and 1080515). To minimize the number of variables in the data set, field, current and NL04 were held constant at 5.4 T, 0.8 MA and 0.8×10^{20} m^{-2} respectively. Difficulties with producing good discharges limited us to 15 useful shots comprising 43 slices. The results were consistent with the theory of the edge as a toroidal momentum source, but more data are necessary to draw a firm conclusion. These results are discussed in section 6.1.4.

The WASP was also scanned as an auxiliary diagnostic during several other experiments. Some of these were probe experiments, like those examining ohmic H-Modes,

while others were primarily serving other diagnostics. These produced a substantial amount of data which broadened the data set available for analysis. Some of these experiments are included in table 3.1, which add an additional 74 shots with good WASP data.

Chapter 4

Assessment of Measurement Techniques

Several of the measurement techniques carried out in this thesis are relatively new and must be subject to critical evaluation. The most important of these is the Gundestrup measurement of perpendicular flows, which will be dealt with separately in chapter 5. However, several other techniques stand to benefit by being bench marked against previous measurements. First, the WASP's general functionality should be bench marked against its predecessor, the ISP. We will then turn to the evaluation of the new high heat-flux Gundestrup probe tip geometry. This probe's ability to measure parallel flows must be verified by comparing its results to those from previous parallel Mach probe designs. It is also important to note that the parallel Mach formulation assumes that the electron temperature is similar upstream and downstream, something not borne out in probe measurements. We then turn to the measurement of perpendicular flows by methods other than the Gundestrup method. We will attempt to verify that we can trust the $E_r \times B$ method by using parallel Ohm's law to corroborate our measurements of the plasma potential. Finally, we will compare our measurements of perpendicular velocity from all three methods available to us: the Gundestrup, $E_r \times B$ and phase velocity measurements.

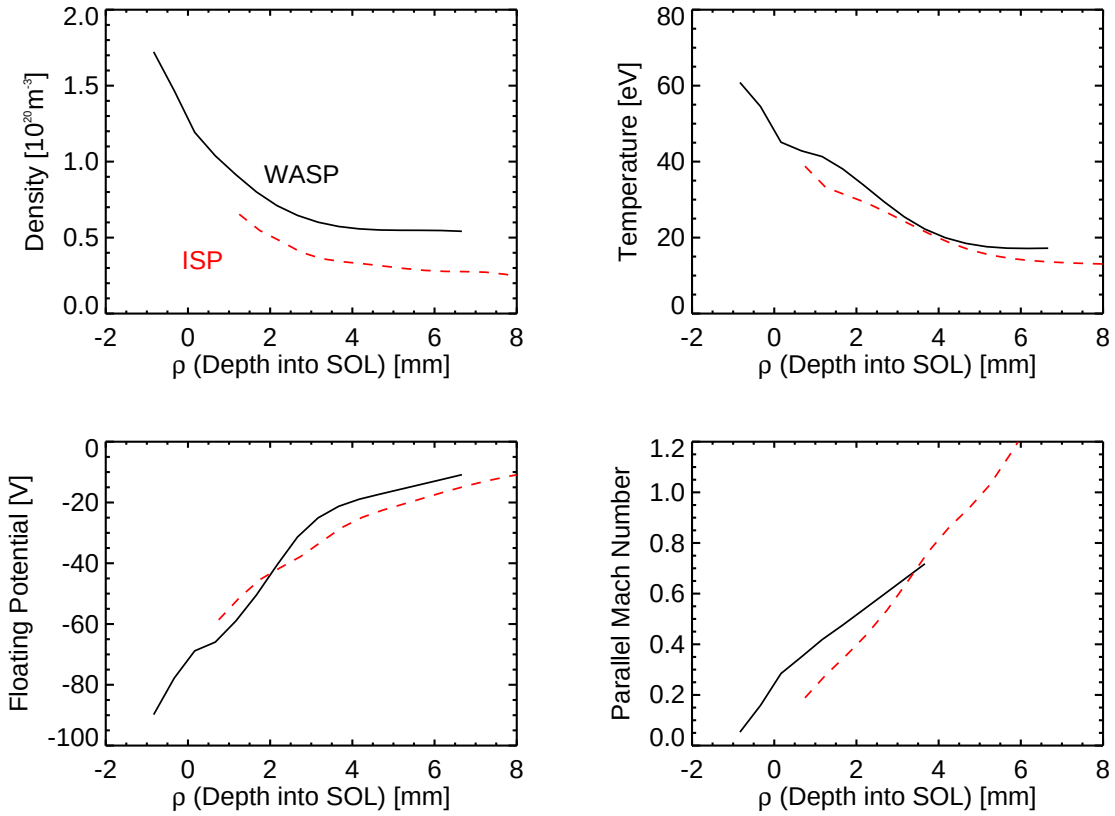

Figure 4-1: Comparison of results from the ISP (red dashed) and the WASP (black solid). Near-sonic flows are confirmed by WASP measurements. WASP data are from shot 1070627009 and ISP data are from 1050217014.

4.1 WASP Measurements Compared to ISP

The first benchmarking task for the WASP is a careful comparison to results from the ISP. A typical pair of matched discharges is shown in Fig. 4-1. These are typical 5.4 T, 0.8 MA, LSN, L-Mode discharges with line-integrated densities around $0.8-0.85\times10^{20}$ m^{-2}. The densities show a factor of $\lesssim 2$ difference, but this might be expected from the difficulty in determining the projected area of the ISP electrode. Otherwise, there is generally good agreement between the two probes, both measuring similar temperatures and potentials as well as parallel Mach numbers.

One study carried out with the ISP was a careful variation of the flux connection between the HFS and LFS SOLs [42]. This was done by varying the 'SSEP' parameter, which measures the flux spacing between the primary and secondary separatricies,

Probe	1	2	3	4
Type	Mach/Float	Mach/Float	Gundestrup	Gundestrup
Used for Campaigns	before '01	'01-'05	'05-'06	'07-'08
Electrode Spacing	3.2 mm	2.03 mm	2.03 mm	1.58 mm
Pyramid Angle	30°	30°	30°	45°
Electrode Placement	Edge	Edge	Face	Tip
Electrode Geometry	Circular Wire	Circular Wire	Circular Wire	EDM Trapezoid

Table 4.1: Properties of various C-Mod four-electrode Mach Probes. Electrode spacing here means the radial distance of the median electrode collection area from the axis of the probe. All probes are constructed with molybdenum bodies and tungsten electrodes.

mapped to the outer midplane. This can be thought of as the size of the flux tube connecting the HFS to the LFS. The ISP measurements showed that the HFS density tracked the LFS density in the connected region of flux space, but then dropped off in the unconnected region. This observation was explained by speculating that the HFS has reduced levels of transport, and the HFS SOL is mainly populated by parallel particle flux from the LFS. In regions where the flux connection is broken, the density drops off sharply. A similar experiment carried out with the WASP during the 2007 campaign (1070627 run, MP 480) confirms this trend. Fig. 4-2 shows the results of both experiments. The WASP has the added benefit of being able to measure the parallel plasma flows that are thought to be responsible for this re-distribution of particles. These results will be reported on in section 6.1.2.

4.2 Parallel Flows from Various Head Geometries

Since the high heat-flux Gundestrup probe was a new design, it was bench marked against previous probe geometries for parallel flow measurements. Table 4.1 and Fig. 4-3 summarize the various geometries operating in C-Mod.

A pyramid-shaped Mach-probe tip was standard on the C-Mod scanning probes

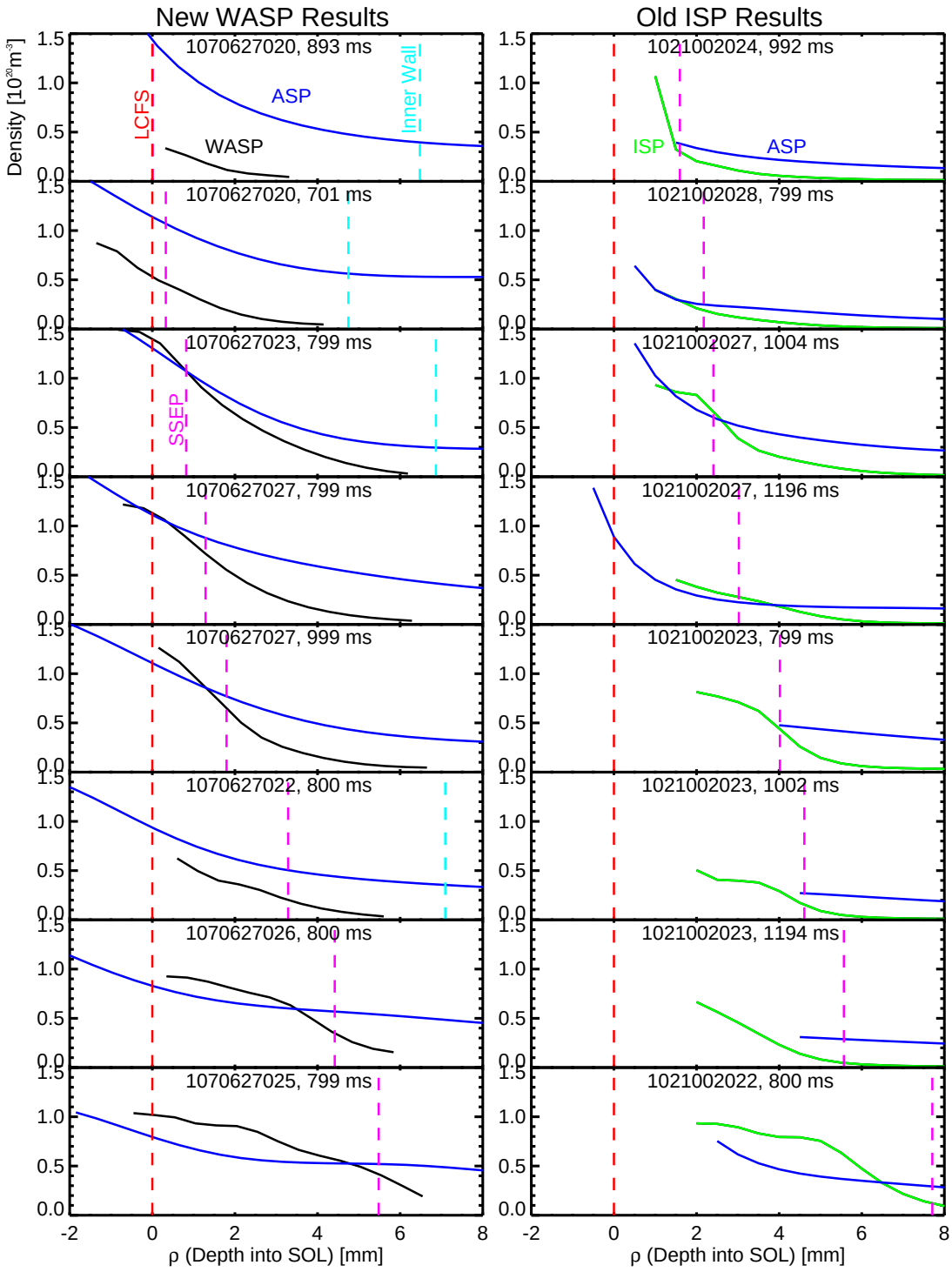

Figure 4-2: Density profiles from inner and outer scanning probes during scans of the secondary separatrix location. On the left, data is shown for the ASP (outer-midplane probe) and the WASP. On the right, the ASP is compared to the ISP. In both cases, the HFS data depart downward from the LFS data in the vicinity of the secondary separatrix.

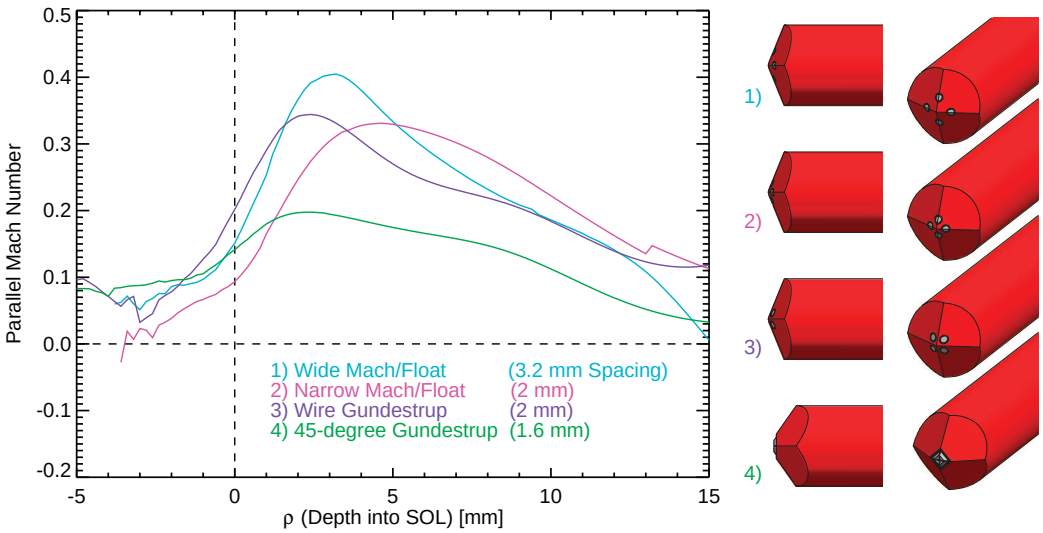

Figure 4-3: Parallel flow variation among different probe geometries: The four curves are composites of the data taken with each of the four geometries at low Greenwald fraction (when flows are the strongest) on the ASP. The data show variation in the magnitude of the measured Mach number by up to a factor of two, but generally similar radial structure.

through the end of the 2006 campaign. The slope of the pyramid face on these older probes was 30° rather than 45° but the design was otherwise similar, with the edges of the pyramid aligned with the magnetic field. The electrodes in this design were simple circular wires, inserted through holes in the pyramid and filed flush with the surface. A critical difference in the old design was that the electrodes were placed on the edges of the pyramid rather than in the face. This probe was designed as a parallel Mach probe supplemented with floating probes that viewed both directions along the field. Two versions of this probe were used, an early version with an electrode spacing of 3.2 mm and a later version with a spacing of 2.0 mm.

Before the implementation of the current high heat-flux Gundestrup probe, a transitional Gundestrup design was tested that was closely modeled after the probe described above. It maintained the same pyramid slope, electrode spacing and dimensions, but moved the electrodes from the edges of the pyramid to the faces.

Simple Mach probe theory 2.1.2 does not distinguish between the designs described above or that used in the '07-'08 campaigns; each should measure the same parallel Mach number when immersed a plasma with finite parallel fluid velocity. However,

this theory glosses over many practical differences between these probes that might lead to different measurements. Therefore, we will investigate the sensitivity of the measured parallel Mach numbers to probe tip geometry.

We compare the parallel velocities measured by the four different probe-tip designs when mounted on the horizontal scanning probe (ASP). Results from these experiments are shown in Fig. 4-3. These traces show an average parallel Mach number from many low density discharges for each of the four probe geometries. Discharges with line-averaged density below 20% of the density limit ($\bar{n}_e < 0.2\ n_g$) were selected because we observe the strongest flows at low density. These discharges cover a wide range of field and current, $2.2 < B_t$ [T] < 6, $0.4 < I_p$ [MA] < 1.4.

Similar trends are observed in the parallel flows measured with the four different electrode geometries, increasing our confidence in the ability of the Gundestrup probes to measure this quantity reliably. However, there is systematic variation in the amplitude of the measured Mach number. The most important variable appears to be the degree to which the electrodes are shadowed by the probe structure, with the most shadowed electrodes measuring the highest Mach number. This effect is parametrized by the electrode spacing, which reflects the distance of the electrodes down from the tip of the pyramid.

One possible cause of this discrepancy is the interruption of parallel heat flow by the probe itself, causing the downstream side to cool, and thus have a different temperature boundary condition far from the probe. This could result in errors in parallel flow because the Mach probe formulation assumes uniform temperature far from the probe in both directions. Based on a picture of diffusive heating of the downstream flux tube, we might imagine this effect to be more severe for electrodes farther into the probe shadow.

Another factor to consider is the sensitivity of the most recent design to misalignment. The orientation of the electrodes is optimized for a certain edge q, and relies on the electrodes themselves to shadow each other from collecting particles from the flux tube in the opposite direction. A small change in edge q, misalignment or manufacturing/assembly defect could cause this shadowing to be incomplete, allowing the

electrodes to collect particles from the opposite parallel direction. This would smear out the results, causing lower measured velocities.

We have identified possible sources of error due to both sheltered electrodes and protruding electrodes, so we cannot say which of the geometries is preferred for measuring parallel flow. The data show higher measured Mach number for more sheltered electrodes. We are encouraged that this error appears to be a fixed multiplier on the magnitude of the measured flow. While the magnitude of the flow varies by as much as a factor of two, we have confidence that we are able to make good measurements of the general parallel flow trends with all of the different geometries. It is also encouraging to note the close agreement between probes 2 and 3. These have identical probe-tip shape and degree of electrode shadowing, the only difference between them is that one is a Mach/float geometry while the other is a Gundestrup geometry. This bolsters our confidence in the Gundestrup probe's aptitude for measuring parallel flows.

4.3 Parallel Temperature Asymmetries

One of the basic assumptions of the Mach probe theory is that the plasma temperature is uniform. Even thorough derivations, such as Hutchinson's treatment of the Gundestrup problem [11] assume that the temperature is uniform in the parallel direction. However, the WASP probe observes clear parallel temperature asymmetries. This observation is evidence of a type of probe-induced perturbation not commonly observed. It is a concern, not only for the measurement of parallel flows, but for our measurements of temperature and perpendicular flow as well.

In Fig 2-17 we can see the variation among the measured quantities between electrodes on the same probe. We see the largest variation in 'densities' (meaning densities calculated for individual electrodes, without regard to flow), moderate variation in electron temperatures and very little variation in floating potentials. While the large variation of the 'density' on the four electrodes is expected for non-zero Mach-numbers, the variation in temperature is not described by Mach probe theory

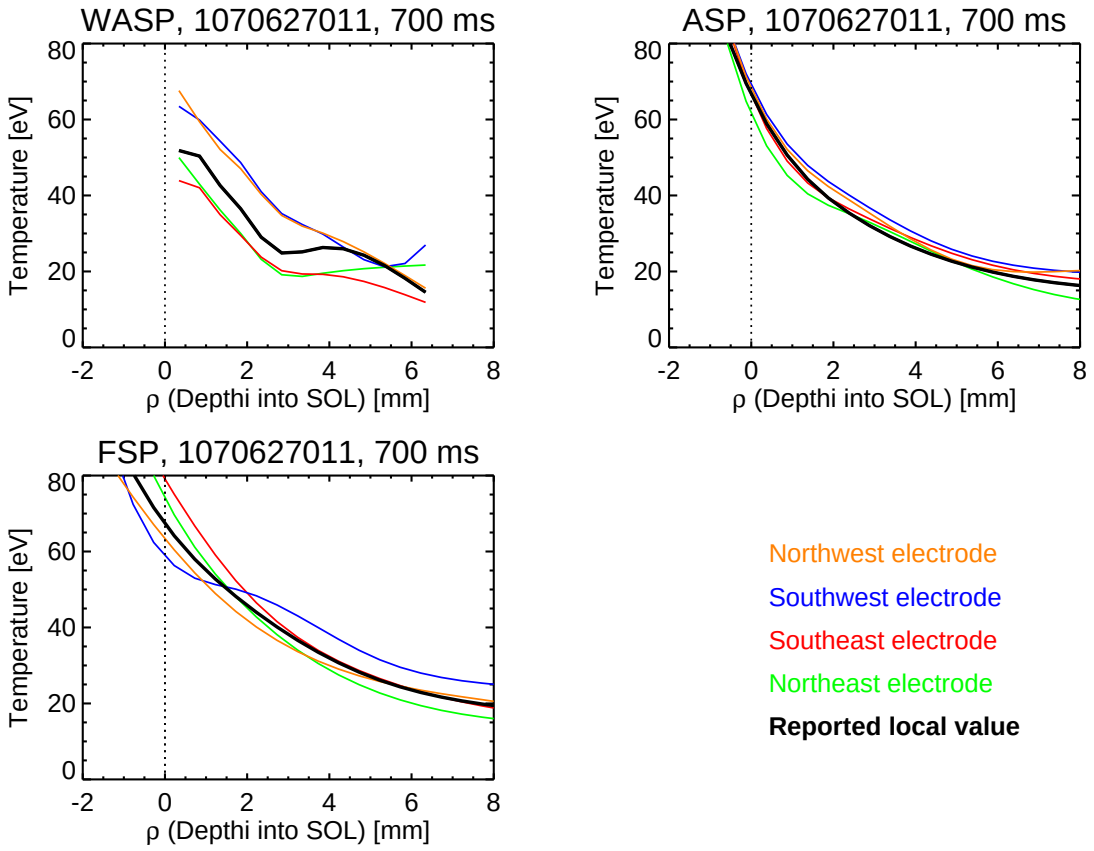

Figure 4-4: Temperatures measured on the four electrodes for each scanning probe. All data is from the same discharge at the same time. In this USN discharge, the parallel flow at the WASP is from West to East with a Mach number of $M_{\|} \sim 0.4$.

[5]. Fig. 4-4 shows temperature data from the four electrodes of all three scanning probes at the same time during a typical USN plasma shot. On the WASP, we notice that the temperature asymmetry in this case is almost entirely in the parallel (East/West) direction. The likely cause of this temperature asymmetry is that the probe is interrupting some conductive parallel heat flux, causing the entire pre-sheath on the 'cool side' to drop precipitously. Based on this model, we might expect the measured parallel temperature asymmetry to be proportional to the unperturbed parallel temperature gradient. Recent results from an RFA probe on Tore Supra support this hypothesis [43]. Experiments there where the parallel flow was systematically varied by changing the point of contact between the plasma and the limiter on the LFS showed that both ΔT_e and ΔT_i correlate with $M_{\|}$. It is sometimes observed that the WASP temperature measurements begin to return to agreement once the probe is inside the LCFS (see Fig. 2-17). This indicates that the directed heat flux is localized to the SOL, as expected.

While this is an interesting observation, we are left with a few concerns. First, what procedure should we use to calculate the local temperature? The simplest guess we can make is that the parallel variation of the temperature is linear, in which case we expect a simple average of the up and downstream temperatures to be a good approximation of the local temperature in the absence of the probe. This procedure is commonly employed and we have no reason to suspect it is inaccurate. A more serious concern regards the validity of the Gundestrup model, which assumes an infinite, homogeneous plasma parallel to the magnetic field. We have reasons to be suspicious of the Gundestrup measurement (see Chap. 5) and this temperature asymmetry adds to the difficulty. However, the temperature asymmetry generally appears on the HFS, meaning that this effect should not influence the LFS measurements. This limits its capacity to resolve our issues with Gundestrup measurements, since the Gundestrup inaccuracies appear on the LFS as well as the HFS (see chapter 5).

4.4 Assessment of Plasma Potential Measurements

While the parallel flows measured with the Gundestrup probe appear to be reliable, we will find in chapter 5 that the perpendicular flow measurement may not be. For this reason, we would like to validate our measurements of the plasma potential, so we can proceed using the $E_r \times B$ velocity to calculate total flow vector with confidence. The difficulties associated with probe measurements of the radial electric field are discussed in section 2.1.3. Because the magnitude of the uncertainty introduced by these difficulties is not well characterized, we will proceed by testing the measured plasma potentials to see if they are consistent with our understanding of edge physics.

Our array of scanning probes along with embedded probes at the inner and outer divertors allow us to compare the plasma potentials measured at each poloidal location on a flux surface. This comparison is shown in Fig. 4-5 for a typical LSN discharge. The density of this discharge is low (NL04 = 0.65 $\times 10^{20}$ m^{-2}) and the drift direction is favorable. Panels A and B in Fig. 4-5 show the temperature and floating potential data. These quantities vary substantially from one scanning probe to the next on the same flux surface, with the WASP reporting unusual *positive* values of floating potential. This can be understood however, if we calculate the plasma potential, $\Phi_p = V_f + \alpha T_e$ (see section 2.1.3). The plasma potential inferred from T_e and Φ_p (shown in panel C) *does* map fairly well between the scanning probes. We conclude that the high floating potential at the WASP is responding to the relatively low temperature at that location so as to make the plasma potential similar to that on the LFS. While Φ_p is expected to be roughly a flux function, we must use caution because we have already identified a possible driver of parallel potential gradients in panel A: parallel temperature gradients. This leads us to consider the full parallel Ohm's law before reaching a conclusion on the accuracy of our plasma potential measurements.

Parallel Ohm's law [44] can be stated as follows:

$$-\nabla_\parallel \Phi_p = \eta_\parallel J_\parallel - 0.71 \nabla_\parallel T_e - \frac{\nabla_\parallel n_e T_e}{ne} \tag{4.1}$$

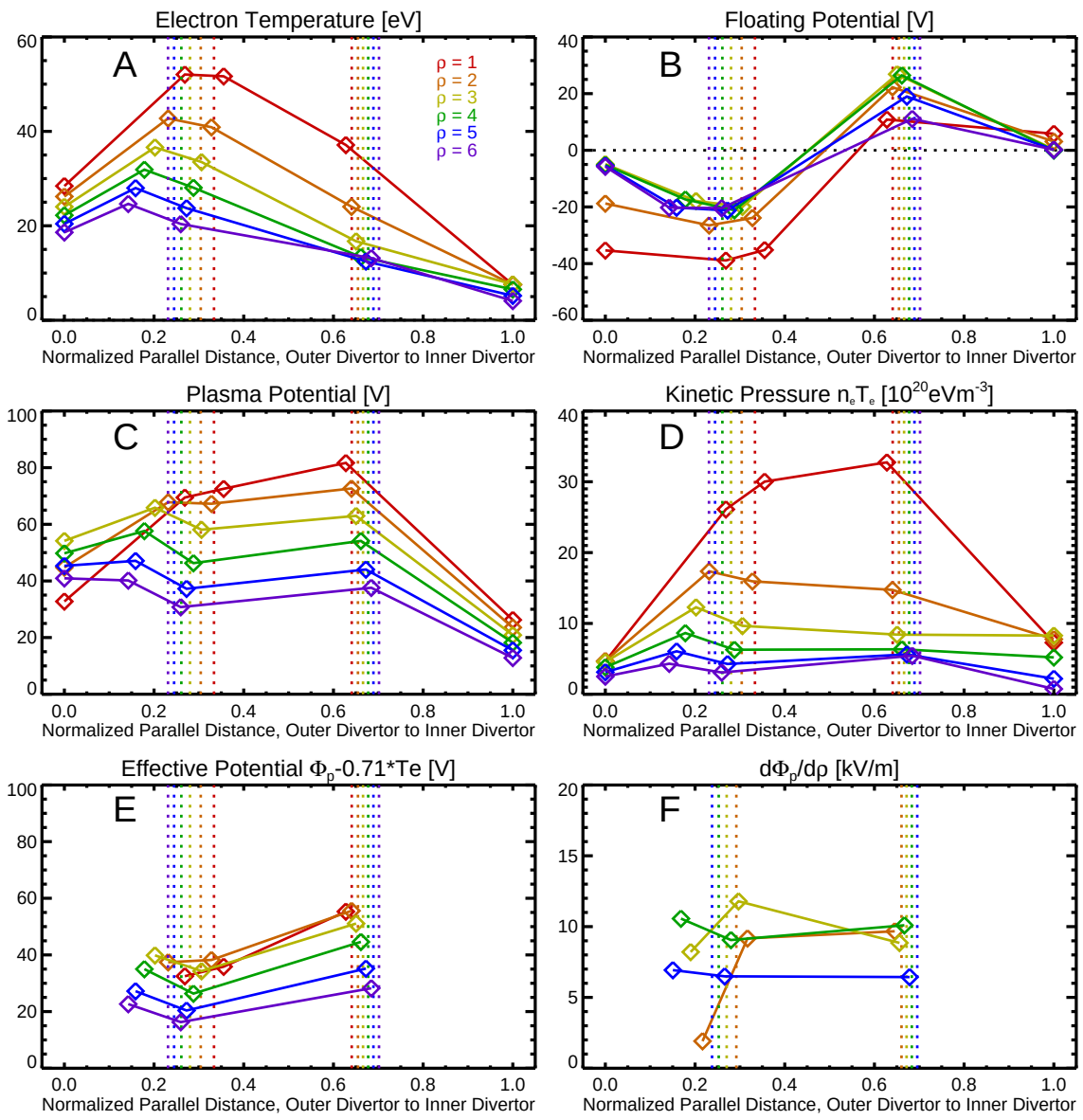

Figure 4-5: Plasma potential and related data are shown as a function of normalized parallel distance from outer divertor to inner divertor. The five points on each trace are the locations of the probe diagnostics in this space. from left to right these are the outer divertor embedded probes, the F-port vertical scanning probe, the A-port horizontal scanning probe, the wall scanning probe and the inner divertor embedded probes. The different color traces are data from different locations in ρ-space, red being very close to the LCFS and purple being 6 mm deep into the SOL. The dashed vertical lines show the locations of the LFS and HFS midplanes for each ρ location plotted.

This formulation makes the assumption that $Z_{eff} = 1$. Here, η is the electrical resistivity, and J is the current density. The second term on the RHS is the thermal gradient force which describes the tendency of mobile electrons to flow away from hotter regions of the plasma. The third term on the RHS is a parallel electron pressure gradient term. The pressures measured by the probes are shown in panel D of Fig. 4-5. These map well between the scanning probes with the exception of the very near SOL at $\rho = 1$ mm. Comparison of panels A and D shows that in this case, $(1/n_e)\nabla_\parallel n_e T_e$ is small compared to $\nabla_\parallel T_e$, and the last term in Eqn. 4.1 can be neglected. In doing so, we can express the current density as the gradient of an effective potential, $\Phi_e = \Phi_p - 0.71 T_e$ such that Eqn. 4.1 becomes:

$$\eta_\parallel J_\parallel = -\nabla_\parallel \Phi_e \tag{4.2}$$

It is the effective potential (Φ_e) that we would expect to be a flux function in the absence of parallel currents. This quantity is plotted in panel E of Fig. 4-5. We see that the parallel variation of Φ_e is larger than that of Φ_p. This cannot be explained by inductively driven currents because the parallel potential variation from the LFS to the HFS would be of order $(q/2)V_{loop}$ (only ~ 2 V). Furthermore, for the discharge shown, the loop voltage would lead to a higher potential on the LFS than the HFS, the opposite of what is observed. Pfirsch-Schlüter currents [4] do not result in a potential variation between the LFS and HFS midplanes, so this also cannot explain the gradient in Φ_e. We are forced to conclude that the absolute value of the inferred plasma potential is uncertain to roughly the observed poloidal variation in Φ_e among the scanning probes: ± 15 V.

While we have identified an uncertainty in the probe measurements of $\Phi_p(\rho)$, it is still possible that this uncertainty is due to a fixed radial offset in the ρ coordinate of each probe. Looking at panel E of Fig. 4-5, we can see that the flux mapping error needed to correct the observed disagreement in effective potential is typically of order 1 mm. This level of uncertainty could easily be due to flux-space mapping errors or probe position errors. However, we are actually interested in the gradients of the

plasma potential for the calculation of $v_{E_r \times B}$, which would not be greatly affected by small offsets in Φ_p. The flux-space derivative of the potential is shown in the panel F of Fig. 4-5. It is found to map between the scanning probes in the case shown despite the disagreement in Φ_p itself. If the Φ_p offset error is of a random nature, then the acquisition of sufficient statistics would still provide the correct result. To confirm that this flux-surface mapping of the plasma potential is consistently observed, binned and averaged profiles of $\partial\Phi_p/\partial\rho$ from a large number of LSN slices at low density are shown in Fig. 4-6. The error bars indicate the statistical scatter of the data. Despite the relatively large uncertainty in the value of $\partial\Phi_p/\partial\rho$ at the WASP location, the averaged data from the three probes appear to agree well across the measured profiles. We take this as evidence that despite possible errors in flux mapping, the radial electric fields deduced from the scanning probes can be trusted in a statistically deduced sense.

Another point can that can be addressed using the data in Fig. 4-5 is the question of whether the measured plasma potential in the SOL is consistent with simple models based on sheath physics. It is often argued [45, 46] that the SOL potential can be approximated as the plate potential plus the sheath drop:

$$\Phi_p \approx \Phi_d + \alpha T_e \tag{4.3}$$

Here, Φ_d is the divertor potential and α is the sheath potential drop, normally around 3. Thus, we would expect: $E_r \approx 3\nabla_r T_e$. While our observations support the expectation that the radial electric field is typically outward in the SOL, we do not observe E_r magnitudes that are consistent with Eqn. 4.3. In the example shown, $E_r \lesssim \nabla_r \Phi_p$, which is substantially less than $\nabla_r T_e$. This discrepancy is most pronounced in the near SOL. The cause of this disagreement is that the other terms in Eqn. 4.1 are not generally negligible. There are in general thermoelectric currents in the SOL and finite pressure gradients approaching the divertor. Thus, even in low density, sheath-limited cases such as the one shown here, finite potential gradients exist outside the sheath. Thus the simple sheath models do not accurately describe the observed SOL

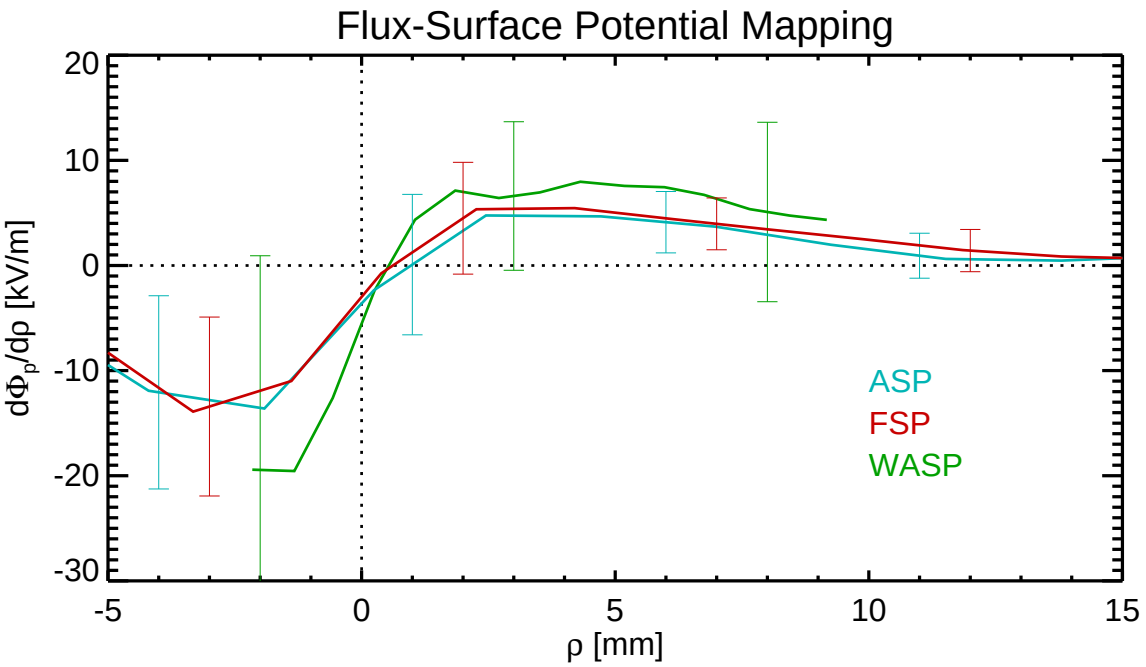

Figure 4-6: binned and averaged profiles of $\partial\Phi_p/\partial\rho$ measured by the three scanning probes over many time slices. The discharges that are included are those with normal field and current (5.4 T, 0.8 MA) with normal field direction and LSN magnetic topology. This plot shows data with line averaged discharge densities of NL04 $< 0.7 \times 10^{20}$ m^{-2}. The error bars show the statistical scatter in the profiles.

potentials, though the observed E_r is usually outward.

4.5 Perpendicular Velocity Comparison from Gundestrup, $E_r \times B$ and Phase Velocity

Section 2.1.3 describes three different measurements of plasma velocities perpendicular to the magnetic field: the $E_r \times B$ measurement, the Gundestrup measurement and the fluctuation phase velocity measurement. The new high heat flux Gundestrup probes on Alcator C-Mod have the ability to make all three measurements simultaneously. This allows us to directly compare the results from the different methods. Fig. 4-7 shows a comparison of the measurements from a representative probe scan.

Several typical features of the these measurements are shown in the figure. A strong shear layer is often present in the vicinity of the LCFS with velocities inside

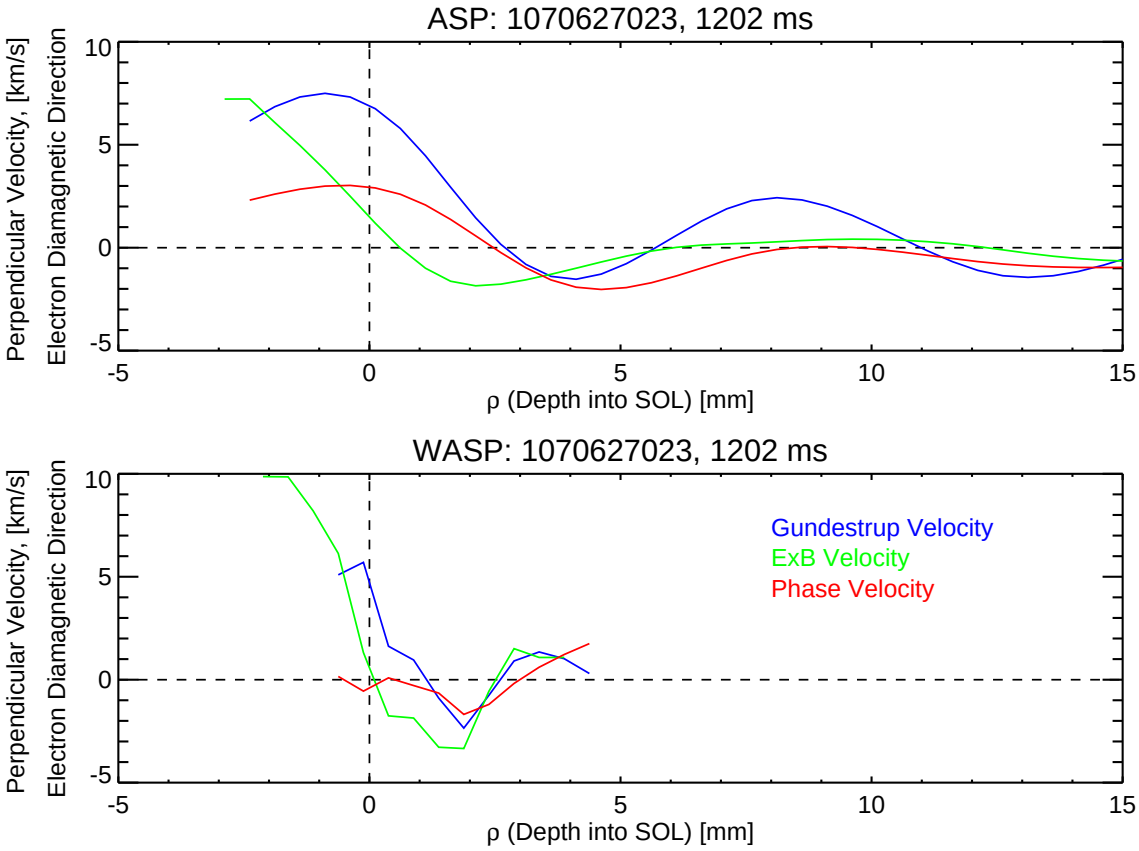

Figure 4-7: Comparison of perpendicular flow velocity measured with three different techniques. Examples are shown from a discharge with standard field and current, in a double-null magnetic topology.

the confined plasma being directed in the electron diamagnetic direction. The location of the shear layer is usually a few mm outside the LCFS according to the Gundestrup and phase velocity measurements, but at or inside the LCFS according to the $E_r \times B$ measurement. In fact, the $E_r \times B$ profile often crosses zero very close to the LCFS, which might be expected due to the different physics governing the sign of E_r on either side of the LCFS[1]. The shearing rate is often comparable for the Gundestrup and $E_r \times B$ measurements, but reduced by about a factor of two for the phase velocity measurement on the LFS. The phase velocity measurement on the HFS suffers from the lack of large amplitude fluctuations at that location. As a result, it is often difficult to make any measurement there at all. In this case, there is no recognizable shear layer in the WASP phase velocity measurement.

While these results are encouraging, we would like to be able to account for the differences in the Gundestrup and $E_r \times B$ measurements which are made simultaneously with the same probe at the same location, and should presumably be measuring the same thing. Several candidates for this discrepancy, including diamagnetic contributions to the Gundestrup measurements and non-linear averaging of fluctuations will be addressed in chapter 5.

4.6 Flux Mapping

One way to test what physics is at work driving the perpendicular flows is to examine how they map in flux space from one probe to another. The phase velocity measurements in particular display a striking linear relationship between the value measured at the outer midplane with the ASP and that measured on the same flux surface near the outer divertor with the FSP. The FSP phase velocities are typically about 60% of the ASP phase velocities, a relationship that appears to be repeatable even for different values of plasma current and edge q. This relationship is displayed in the top panel of Fig. 4-8. This scaling between the velocities can be explained straight-

[1]Radially outward electric fields are normally expected in the SOL as a result of divertor sheath drops responding to the radial temperature gradient. Inside the LCFS, one would typically expect a radially inward electric field, such that the $E_r \times B$ and ion diamagnetic drifts cancel.

forwardly if the measured velocity is the gradient of a flux function. The ratio should correspond to the flux expansion between the two locations. The flux expansion factor can be calculated as follows using the major radii and poloidal magnetic field values at the two probe locations:

$$C_F = \frac{R_F^2}{R_A^2}\frac{B_{pF}}{B_{pA}} \approx \frac{(0.73\text{ m})^2}{(0.88\text{ m})^2}\frac{0.5\text{ T}}{0.65\text{ T}} \approx 0.6 \tag{4.4}$$

where typical values have been used as an example. This is convincing evidence that the phase velocity is measuring a perpendicular flow that is responding to the gradient of a flux function.

This experiment can be repeated for the Gundestrup and $E_r \times B$ perpendicular velocity measurements. These data are shown in the second and third panels of Fig. 4-8 respectively. The $E_r \times B$ velocity shows reasonably good agreement with the expected flux mapping. This is equivalent to stating that the measured potentials are similar on the same flux surface (that is, they are roughly a flux function, as expected). However, the Gundestrup perpendicular velocity measurement shows poor agreement between the two probes. The velocities measured at the FSP are offset in the electron diamagnetic direction by ~ 4 km/s relative to the velocities measured with the ASP. This is disappointing because it was hoped that the Gundestrup probe would provide a direct measurement of the drift velocities. This offset indicates that whatever effect is causing the electron-diamagnetic offset seen with the Gundestrup probe, it is much stronger at the FSP location than at the ASP location.

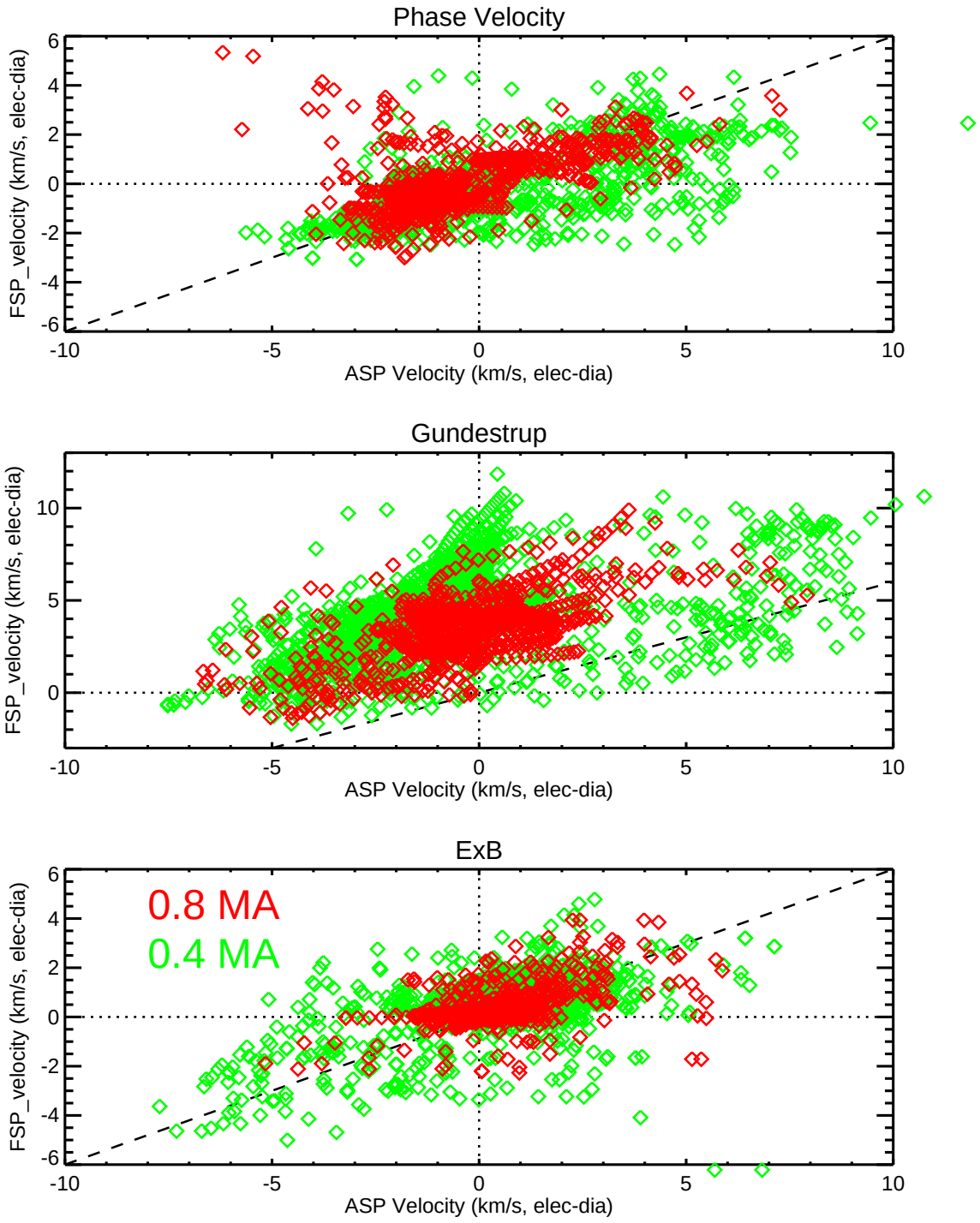

Figure 4-8: Velocities measured with the LFS midplane ASP are compared to those measured with the LFS divertor FSP. The three panels show the comparison for the three perpendicular velocity measurements. Two values of plasma current ares shown, both with toroidal magnetic field of 5.4 T. The flux expansion factor between the two probe locations of 0.6:1 is also plotted. Agreement indicates that the measured velocity is consistent with the gradient of a quantity which is constant of flux surfaces.

Chapter 5

Assessment of Gundestrup Perpendicular Flow Measurements

As described in section 4.5 (Fig. 4-7), the results of the Gundestrup perpendicular flow measurement are in systematic disagreement with the $E_r \times B$ perpendicular flow measurement. While it was uncertainty about the $E_r \times B$ method that led to the development of the high heat-flux Gundestrup probe, the accuracy of this new method has not been demonstrated. In fact, several observations suggest that we do not fully understand the Gundestrup perpendicular flow data. The Gundestrup perpendicular velocity measurements in the far SOL routinely show relatively high values (typically 2-10 km/s) which persist all the way to the limiter location and beyond (see Fig. 5-1). These flows are consistently in the electron diamagnetic direction. This is in contrast with the $E_r \times B$ measurements which show roughly zero velocity in the far SOL. These anomalous Gundestrup flows are a concern on two fronts: first, it seems unlikely that such high perpendicular velocities would be seen outside the steep gradient region, and in such close proximity to a solid surface. Second, the far SOL is where the $E_r \times B$ method is thought to be the most reliable because the temperatures are low, reducing both secondary and thermionic electron emission. Also, the temperature and floating potential do not change rapidly with radius in the far SOL, making the resulting E_r approximately zero, independent of the estimated sheath potential drop. We therefore believe the $E_r \times B$ measurements of small perpendicular velocity in the far

SOL to be accurate and the Gundestrup offset in the electron diamagnetic direction to be puzzling. This offset persists into the near SOL, which suggests it is a general property of the Gundestrup measurement which we do not fully understand. Thus we approach this chapter under the assumption that the Gundestrup perpendicular flow measurements are in error, and explore the potential causes of this error.

A close look at some perpendicular flow data can help illustrate the trends described above. Fig. 5-1 shows binned and averaged data for all three scanning probes with C-Mod operating in different configurations. Positive velocity corresponds to the electron-diamagnetic direction. ASP data are available in both forward and reversed field cases, shown in the upper two quadrants of Fig. 5-1. The WASP data are in the lower left and the FSP data in the lower right. The data from each of the four cases are shown for USN and LSN, and for two density ranges, greater or less than NL04 $= 0.7 \times 10^{20}$ m^{-2}. The Gundestrup flow data are nearly always offset significantly in the electron diamagnetic direction relative to the $E_r \times B$ data. The offset is present independent of probe, topology, field direction or density. While the offset is greater in some cases than others, the universality of the offset in the electron diamagnetic direction allows us to eliminate any geometric errors as the cause. That is, there is no random machining or assembly error that could produce an offset of the flow measurement which is in the *electron diamagnetic* direction despite field and current reversals, and which is reproduced using at least ten different probe tips mounted on four different scanning probes. These factors may contribute to the variation in the magnitude of the offset, but cannot explain the offset itself. We must therefore restrict our search to something systematic, which is a general property of the plasma-probe interaction.

We will begin with a careful characterization of the range of applicability of the Gundestrup model. We will then proceed to consider several plasma effects that may be capable of causing the observed disagreement.

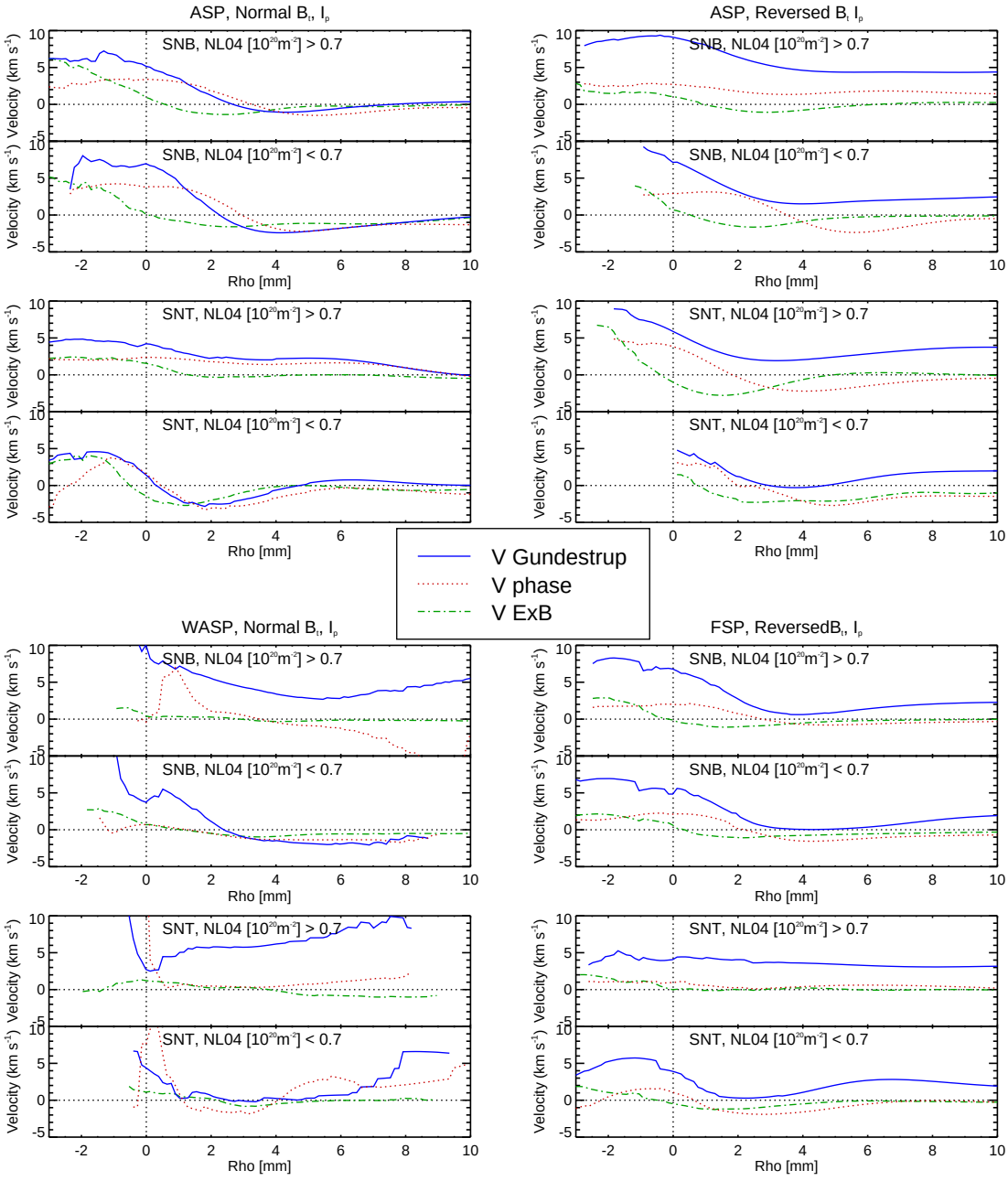

Figure 5-1: Plots showing binned and averaged traces of the three perpendicular velocity measurements. The solid curves show the fluid velocity measurements, and the dashed curve the phase velocity measurement. All the cases shown are for 0.8 MA, 5.4 T discharges. Normal (reversed) field and current direction is clockwise (counterclockwise) when viewed from the top of the machine. The magnetic topology is identified as 'Single-Null Top' (SNT) or 'Single-Null Bottom' (SNB). Each pair of plots has a low density case at bottom and high density at top. Reversed field data are from 2007 while WASP and FSP data are from 2008-2009. The ASP normal field data comes from all three campaigns.

5.1 Range of Validity of Gundestrup Model

The Gundestrup fluid model (section 2.1.3) predicts ion-saturation current as a function of the angle of incidence of the magnetic field onto the probe surface. The result can be summarized by Eqn. 2.6b, which is repeated here:

$$I_{sat} = eA_p n_e c_s \exp(-1 - M_{||} + M_{\perp} \cot(\theta)) \tag{5.1}$$

Eqn. 5.1 diverges when θ, the angle of field incidence, becomes small. Since we do not expect the probe to collect infinite current in this grazing-field condition, there must be a critical angle where the fluid model no longer accurately predicts the measured ion saturation current. It is essential to avoid the region of disagreement if we are to trust the flows calculated by inverting Eqn. 5.1. The angular range of applicability of the Gundestrup fluid model has been investigated empirically [47] on the Castor tokamak. That investigation found good agreement for $\theta \gtrsim 30°$. However, this was a conservative estimate and the study did not attempt to parametrize the angular range of disagreement as a function of the ambient flow velocities. The published results showed a single fit to data with $M_{\perp} = 0.5$ and $M_{||} = 0.17$. Such a high perpendicular Mach number is likely to be an extreme case. It is also unclear from an experimental perspective whether the grazing angle in question is the angle of field incidence in the plane defined by the field and the total flow vector (here called θ), or the plane defined by the field and the surface normal (here called α), see Fig. 5-2. This is because the Gundestrup probes that were used on Castor had their electrode surfaces oriented at right angles to the flux surfaces, so that α and θ were equivalent. On C-Mod's pyramidal Gundestrup probes, the electrode surface is inclined with respect to the flux surface and α and θ are *not* equivalent.

Lacking the results of a methodical experimental characterization of the angular range of applicability, we will let ourselves be guided by heuristic arguments. The discussion of the Gundestrup probe in section 2.1.3 made reference to the Galilean transformation [10] which produces a result essentially in agreement with the more rigorous fluid model. When considering Eqn. 5.1 in this framework, we realize that

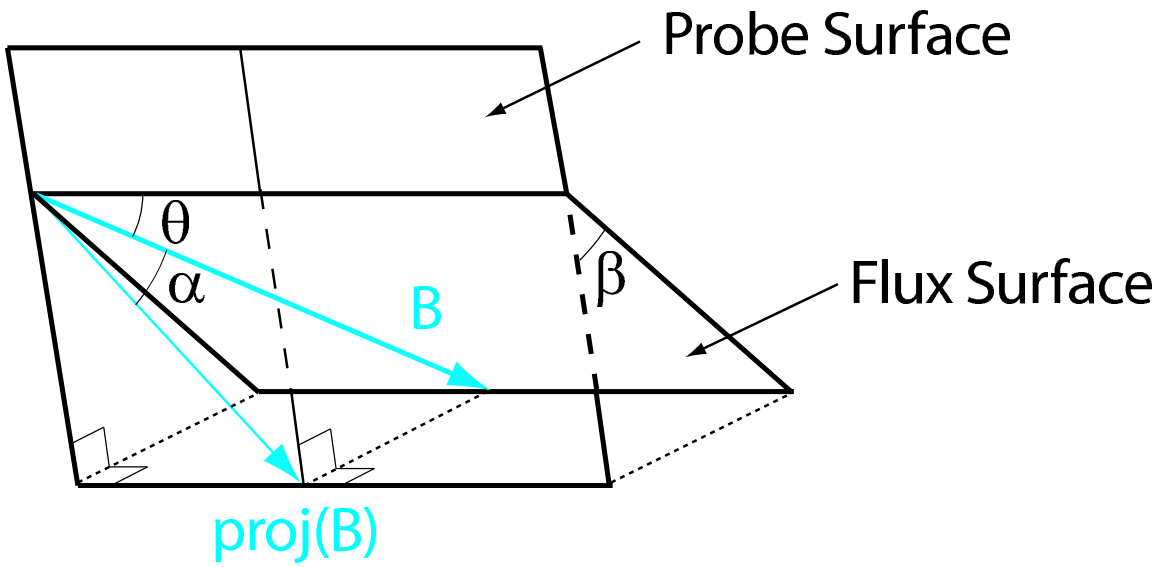

Figure 5-2: An illustration of the various angles discussed in this section. The angle β is the angle between the flux surface and the probe surface. This is equivalent to the 'pyramid steepness' and is 45° on the C-Mod high-heat flux Gundestrup probes. For most previous Gundestrup experiments, this angle has been 90°. The angle θ between the field and the probe surface *within a flux surface* is the primary quantity used in the Gundestrup formulation. On the C-Mod probes, this angle is also $\sim 45°$. The angle α is the simple angle between the field and the surface, that is, the angle between the field and its projection onto the surface. For probes with $\beta = 90°$, $\alpha = \theta$. On C-Mod, $\alpha \approx 30°$.

the reason for the failure of the fluid model near grazing field incidence is due to the divergence of the 'corrected parallel Mach number,' $M_{||} - M_{\perp}\cot(\theta)$. Since the fluid model is not intended to apply to the case of supersonic flows, we can define the likely range of validity of the model using the condition that the magnitude of the corrected parallel Mach number does not exceed unity.

Fig. 5-3 shows the results of the fluid model for a variety of different parallel and perpendicular flow conditions. The current collected by an electrode of constant area is shown as a function of its angle with the magnetic field in a flux surface (θ). If there is no flow, the curve is a symmetric figure-eight with the lobes aligned to the field. The black curves show the progression from $M_{\|} = 0$ to $M_{\|} = 1$, with $M_{\perp} = 0$. The lobes become more asymmetric as the flow increases. The red curves show cases with $M_{\perp}$ varying from 0 to 1 at an intermediate parallel Mach number of $M_{\|} = 0.5$. The divergence on the right side of the plot for finite perpendicular drift is where the fluid model breaks down. This occurs when the perpendicular flow velocity is large and the angle of field incidence is small. The dotted line shows the point where the corrected parallel Mach number exceeds unity. This line shows satisfying agreement with the location of the 'knee' in the curves of ion saturation current where the fluid model qualitatively begins to diverge.

The C-Mod high-heat flux Gundestrup probes have $\theta \sim 45^{\circ}$ so the condition for violation of the fluid model simplifies to: $|M_{||} - M_{\perp}| > 1$. Since all four electrodes must satisfy this requirement, it must be true for all sign combinations of $M_{\|}$ and $M_{\perp}$. Thus the condition for voilation becomes $|M_{||}| + |M_{\perp}| > 1$ This condition is occasionally realized on the WASP, but rarely and only just. Therefore we can be satisfied that the C-Mod probes usually stay well within the range of validity with regard to the angle θ. To address the range of validity of the angle α, we can refer to previous work addressing the validity of the standard sheath model at grazing field incidence [48]. This empirical analysis was aimed at embedded probes in divertor tiles, which can be subject to very small angles of incidence. It was found that the results of Langmuir probe measurements agree with the theoretical predictions for angles of $\alpha \gtrsim 5^{\circ}$. C-Mod's current Gundestrup probes have an incidence angle of

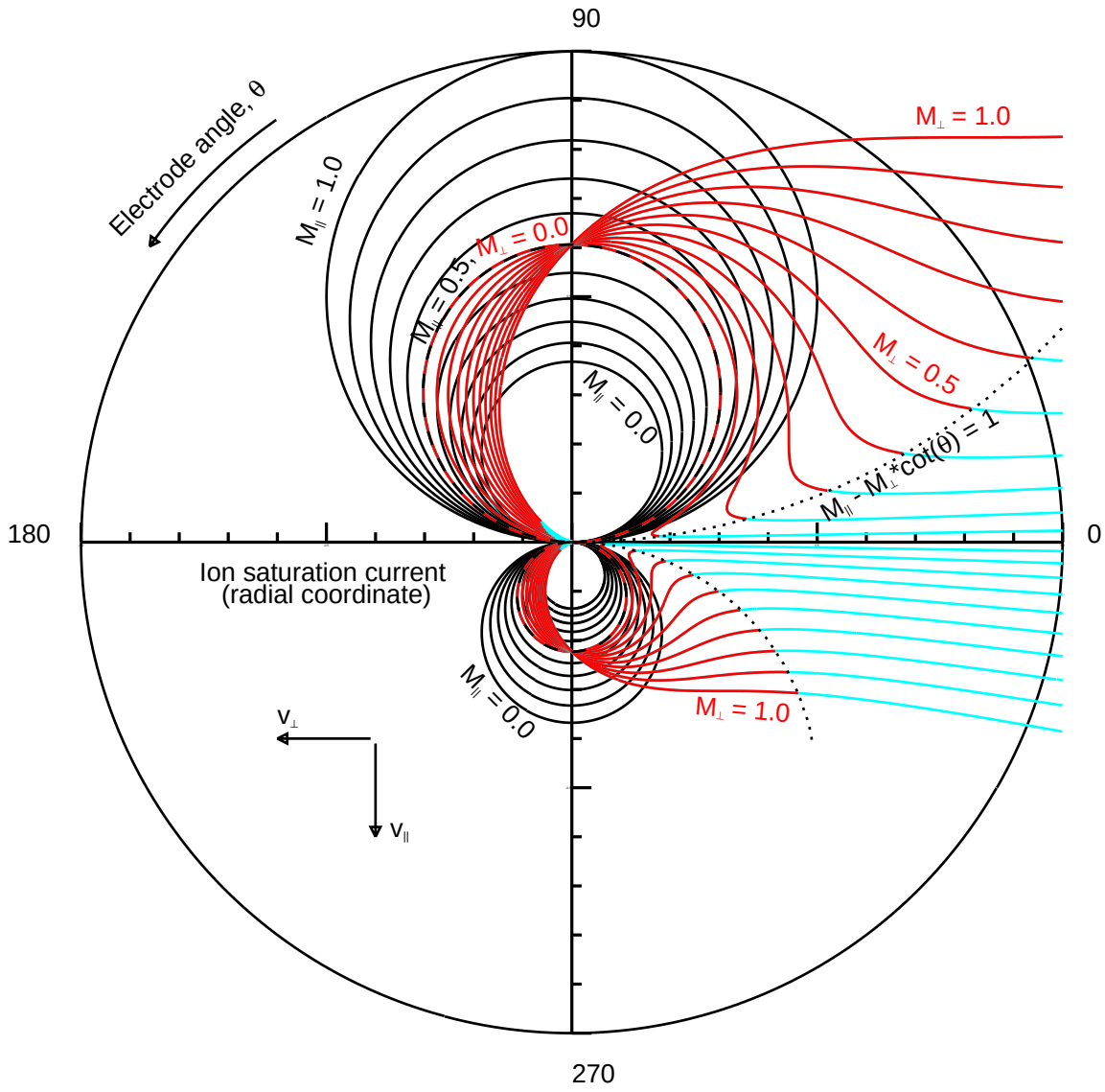

Figure 5-3: The results of the fluid model Gundestrup calculation. Here, the radial direction is the ion saturation current collected on a probe of constant area rotating relative to the magnetic field. 90° corresponds to the case when the probe is normal to the field, facing the parallel flow. 0° corresponds to the case where the probe is facing the perpendicular drift. The black curves all have $M_\perp = 0$, the red curves have $M_\parallel = 0.5$. Note that for finite drift velocity, the model diverges near 0°. The dotted line and cyan curves show the area where the 'corrected parallel Mach number' $M_\parallel - M_\perp \cot(\theta)$ is larger than 1.

$\alpha \sim 30°$, and even the earlier version had an angle of $\alpha \sim 22°$, both of which are well within the range of validity. Based on these considerations we will proceed under the assumption that the Gundestrup fluid model can safely be applied to the C-Mod probes, and grazing field incidence is not likely to be responsible for any corruption of the resulting data.

5.2 Flux Surface Misalignment

C-Mod's probes are designed to be oriented normally to the flux surfaces. However, due to the variation in the shape of the discharge equilibria, it is possible for the alignment to be imperfect. The WASP probes in particular have a systematic flux surface misalignment. This is because the probe tips are oriented normal to the inner wall (to simplify construction and allow the parts of the two probes to be interchangable), but the two probes are actually located slightly above and below the HFS midplane. The curvature of the flux surfaces results in a small systematic misalignment which is opposite for the two probes. The misalignment is not much larger than those commonly present on all the scanning probes due variations in equilibrium shape, but systematic nature of this misalignment makes the WASP probes ideal for testing the sensitivity of the Gundestrup measurement to flux surface misalignments. We can calculate the expected effect of the mislignment on the measured Mach number, and compare this with data from the two WASP locations.

Fig. 5-4 shows (a) an exaggerated diagram of the misalignment, and (b) an illustration of the geometric parameters we will use for calculating the effect on the Gundestrup measurement. The separation between the North and South electrodes is $d = 2.24$ mm. As a result of an angular misalignment of θ, the North electrodes will sample plasma from a different flux surface than the South electrodes. The spacing of these two flux surfaces is given by:

$$\delta\rho = d \sin\theta \approx \theta d \tag{5.2}$$

Here, we can neglect the sine because these misalignments are never greater than

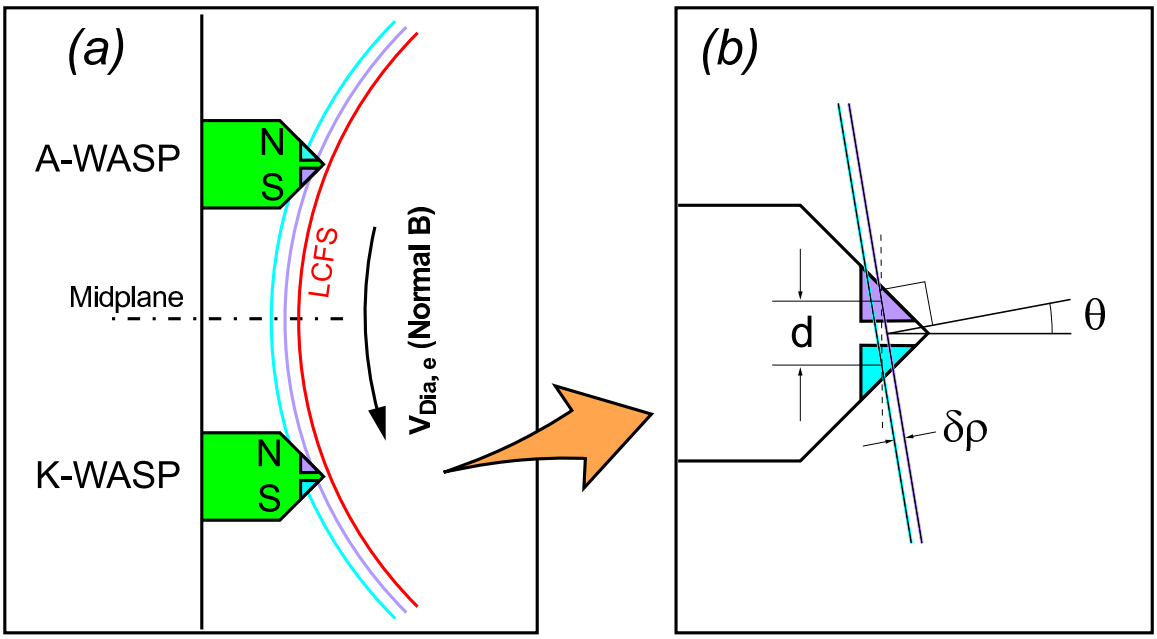

Figure 5-4: Diagram illustrating the effect of probe misalignment with a flux surface.

a few degrees. The difference in ion saturation current collected on the North and South electrodes that would result from this misalignment is:

$$\delta J_s = \delta\rho \frac{dJ_s}{d\rho} = \frac{\theta d J_s}{L_{J_s}} \tag{5.3}$$

Here, L_{J_s} is the scale length of variation of the ion saturation current. Because L_{J_s} is not routinely calculated, it is convenient to express it in terms of the density and temperature gradient scale lengths:

$$J_s \sim n c_s \sim n\sqrt{T_e} \quad \therefore \quad L_{J_s} = \frac{1}{\frac{1}{L_n} + \frac{1}{2L_{T_e}}} \tag{5.4}$$

The difference in ion saturation currents from Eqn. 5.3 would be interpreted by the Gundestrup formula as a Mach number:

$$\delta M_\perp = 0.43 \ln\left(\frac{J_s + \delta J_s}{J_s}\right) = 0.43 \ln\left[1 + \theta d\left(\frac{1}{L_n} + \frac{1}{2L_{T_e}}\right)\right] \tag{5.5}$$

Because the $E_r \times B$ method of measuring $v_\perp$ uses an averaged potential from the four electrodes to calculate E_r, it should not be greatly affected by the flux sur-

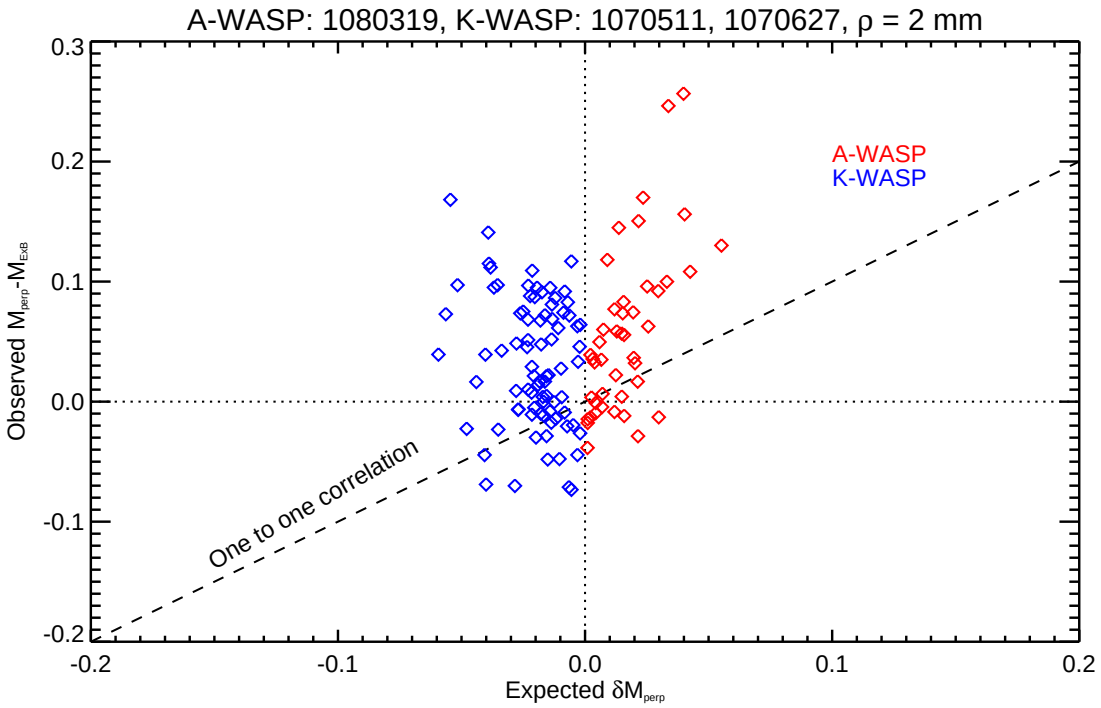

Figure 5-5: Comparison of the calculated flux surface misalignment effect to measured discrepancy between the Gundestrup and $E \times B$ perpendicular velocity. This data is from three similar run days, which consisted of density and topology scans. The K-WASP was operated during 1070511 and 1070627, while the A-WASP was operated on 1080319.

face misalignment. We can then compare the disagreement between the Gundestrup measurement and the $E_r \times B$ measurement with the calculated $\delta M_\perp$ to see if this effect accounts for the observed discrepancy between the two measurements. The result of this comparison is shown in Fig. 5-5. The data confirms that the two probes experience systematic misalignments in opposite directions. However, the observed discrepancy does not correlate with the prediction. In addition, the observed discrepancy is often substantially larger than the expected offset due to the misalignment. We conclude that this effect is not a primary cause of the Gundestrup offset.

5.3 Diamagnetic Corrections

A question that is often asked about Gundestrup measurements is whether or not the result should be interpreted as including diamagnetic flows. Since the diamagnetic drift does not result in motion of the guiding centers, it is not intuitively obvious whether particles should be collected by the probe as a result of this drift. Regardless of the answer to this question, it is difficult to explain the empirical fact that Gundestrup probe, which derives flows from measurements of *ion* saturation current, generally measures perpendicular velocities which are offset in the *electron* diamagnetic direction relative to $E_r \times B$ velocities. It is interesting to note that it is not merely the direction of the offset which suggests electron diamagnetic effects, but the magnitude as well. The Gundestrup perpendicular flow measurement often agrees well with the sum $E_r \times B$ and electron diamagnetic drifts, except in the far SOL at high density. (see Fig. 5-6).

Fortunately, a recent paper by Hutchinson [11] directly addressed the role of diamagnetic drifts in the Gundestrup measurement of perpendicular flows. The result is that diamagnetic drifts *are* measured by the Gundestrup probe. More specifically, the perpendicular Mach number measured with the Gundestrup probe can be expressed as a sum of several terms, including contributions due to both $E_r \times B$ and diamagnetic effects. The complete result was shown in Eqns. 2.6 and is repeated here:

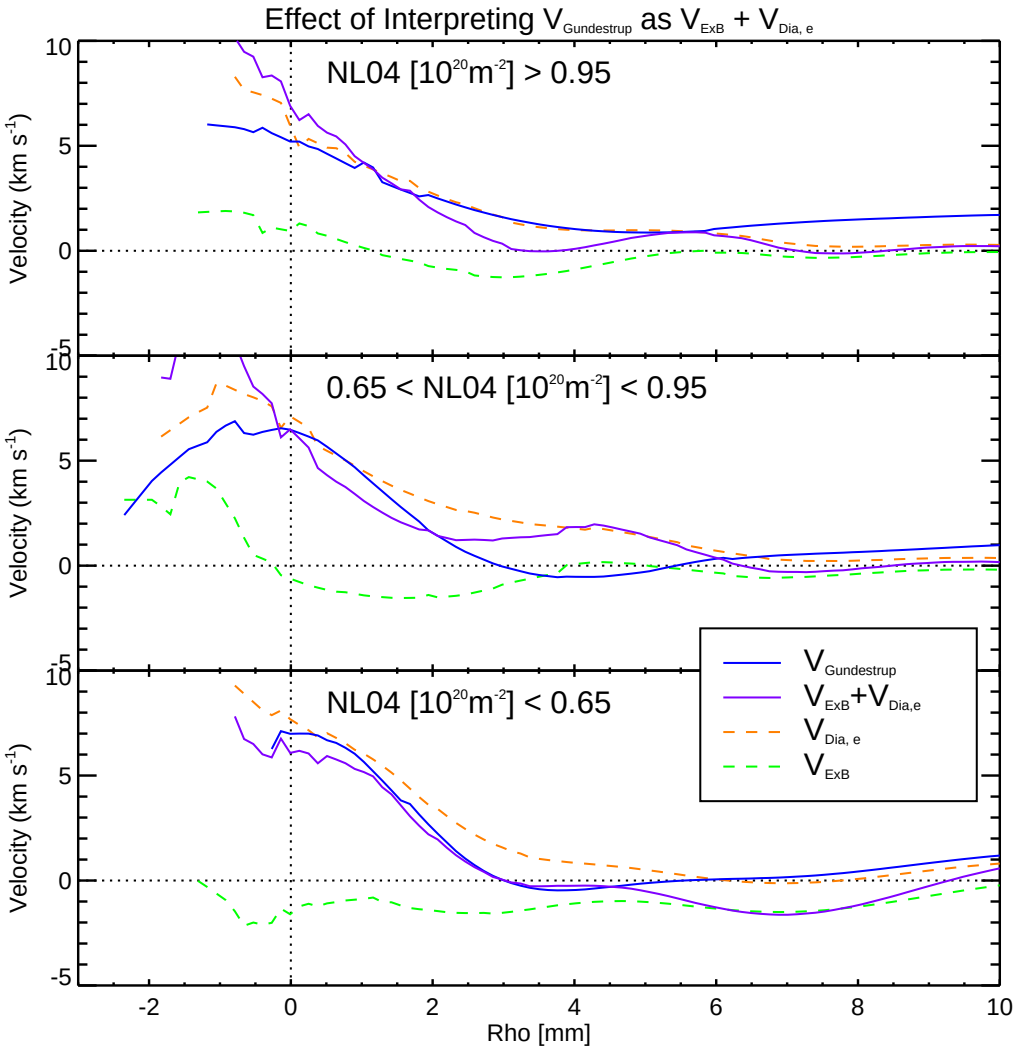

Figure 5-6: A comparison of the Gundestrup measured perpendicular velocity to the sum of the $E_r \times B$ velocity and the *electron* diamagnetic velocity inferred from the pressure gradient. The curves shown are averages of many slices during the 1070627 run day, binned according to discharge density. The surprisingly good agreement in all density cases leads to speculation that Gundestrup probe might somehow be sensitive to electron diamagnetic flows.

$$M_\perp = (1 + M_{||})M_{Te} + M_{Di} + M_{E\times B} - \left(\frac{1-\sin\alpha}{1+\sin\alpha}\right) M_D \tag{5.6a}$$

$$M_D = M_{Di} - M_{De} = (M_{ni} + M_{Ti}) - (M_{ne} + M_{Te}) \tag{5.6b}$$

The ion diamagnetic drift, M_{Di}, is included straightforwardly as a term in the Gundestrup result for perpendicular flow. Surprisingly, electron diamagnetic effects appear as well. An electron temperature gradient term is included which is dependent on the parallel Mach number. As mentioned in section 2.2.2, this can add a slight complication to the interpretation of the Gundestrup flows, which will be addressed shortly. Another diamagnetic term is included which is dependent on the angle α. For the case of $\alpha = 90°$, this term is zero, but as α becomes very small, this term results in the replacement of the ion diamagnetic velocity with the electron diamagnetic velocity. For the case of the C-Mod high-heat flux Gundestrup probes, $\alpha \approx 30°$ and equation 5.6a simplifies to:

$$M_\perp = (1 + M_{||})M_{Te} + M_{E\times B} + \frac{2}{3}M_{Di} + \frac{1}{3}M_{De} \tag{5.7}$$

At this angle the ion diamagnetic contribution is still larger than the electron diamagnetic contribution. Because we measure the pressure profiles with the probes, we are in a position to empirically address the question of whether these corrections can account for our observed disagreement. Each of the terms in Eqn. 5.7 is easily derived from quantities measured by the probes with the exception of M_{Di}. This term requires the ion temperature, which is not directly measured. It is generally expected that the ions and electrons are thermally well coupled in the C-Mod edge due to the high collisionality. However, this cannot be empirically verified. It is therefore necessary to make this comparison for a variety of assumptions about T_i.

Fig. 5-7 shows a comparison of the predicted Gundestrup result from equation 5.7 and the empirical Gundestrup data. The solid lines are the Gundestrup measurement of $V_\perp$ (blue) and the theoretical formulation according to Hutchinson (cyan). The

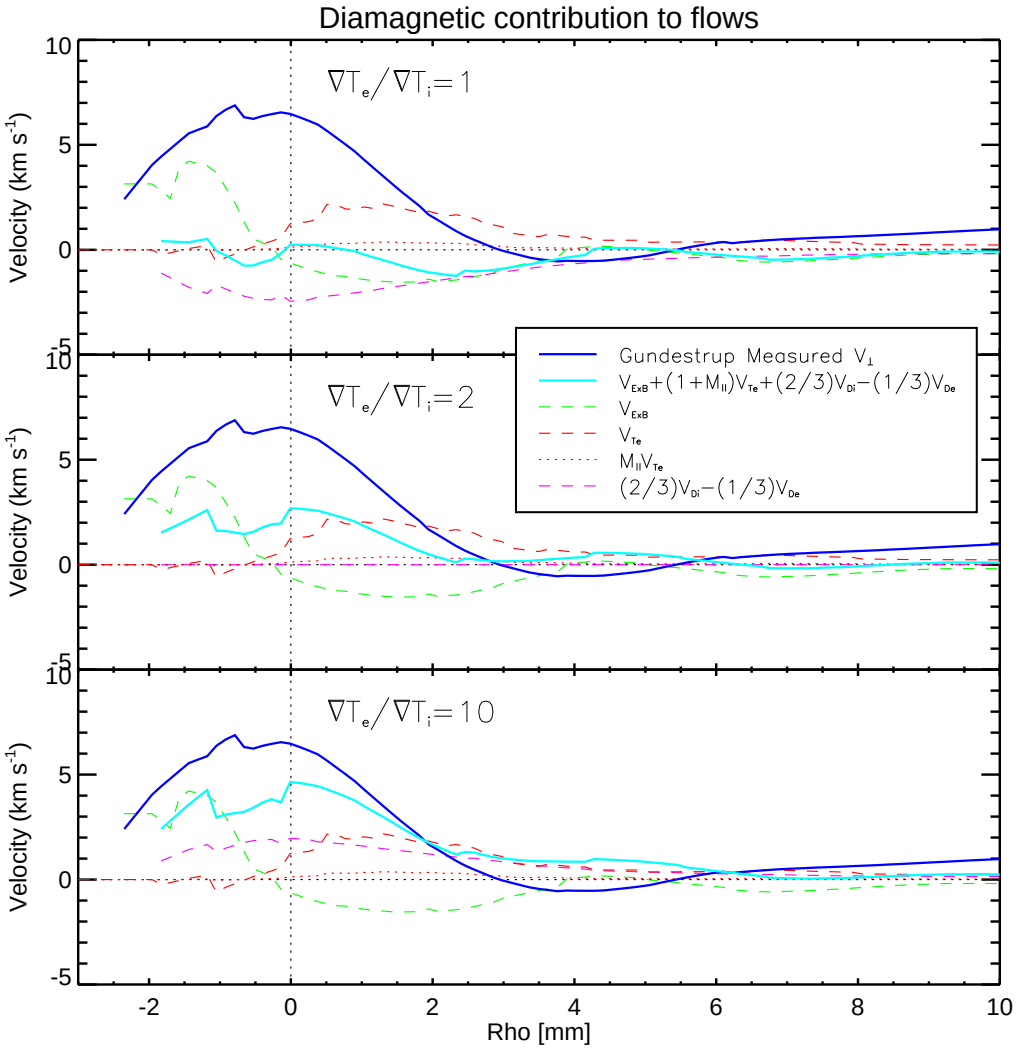

Figure 5-7: A comparison of Hutchinson's model for Gundestrup perpendicular flow measurements with the experimental results. The three panels show the Gundestrup $V_\perp$ measurement along with Hutchinson's prediction for different assumptions about the ion temperature gradient. The different terms of Hutchinson's formula are also shown. The data are from the ASP during medium density discharges ($1.04 < \overline{n}_e < 1.52$ [10^{20} m^{-3}]) on the 1070627 run day.

various terms in equation 5.7 are shown with dashed and dotted lines. The green dashed curve is the $E_r \times B$ velocity which is derived from the floating potential and electron temperature (see section 2.1.3). The red curves are the diamagnetic velocity due to the electron temperature gradient, which is routinely measured. This has been split into two parts, to show the relative magnitude of the contribution to $M_\perp$ that is dependent on $M_\parallel$ (see discussion, section 2.2.2). It is very small, and can be neglected in the initial determination of the parallel and perpendicular flow components. The magenta curve is the remaining diamagnetic velocity contribution, which contains terms due to both the ion and electron pressure gradients.

Fig. 5-7 is divided into three panels each of which shows the comparison of derived and measured Gundestrup velocities for a different assumption about the ratio of the electron and ion pressure gradients. The first panel shows the result when we assume the ions and electrons are thermally well equilibrated and the temperature gradients are equal for both species. The result is that the diamagnetic terms in the equation tend to cancel each other and very little change is seen in the result when compared to the simple $E_r \times B$ formulation. Inside the separatrix, the correction actually produces worse agreement than the $E_r \times B$ term alone. The second and third panels show the result for other assumptions about temperature gradient with $|\nabla_\perp T_i| < |\nabla_\perp T_e|$. This assumption is reasonable because electrons are preferentially cooled in the far SOL by parallel conduction. As we increase $\nabla T_e / \nabla T_i$, the theoretical result gets closer to agreement with the measured result. However, even assuming a $\nabla T_i \ll \nabla T_e$, as in the third panel, we cannot quite produce agreement. This indicates that some important effect is still missing from the Gundestrup theory.

5.4 Non-Linear Effects Due to Drift Waves

It was noted in section 4.5 that the Gundestrup measurement has similar structure to the measured phase velocity. Both are often slightly in the ion-diamagnetic direction in the far SOL and begin to ramp strongly into the electron-diamagnetic direction within a few mm of the LCFS. Though a similar ramp occurs in the $E_r \times B$ data,

it is typically seen at a few mm smaller minor radius and crosses zero roughly at the location of the LCFS. These trends can be observed in Figs. 4-7 and 5-1. The similarity between the Gundestrup measurement and the phase-velocity measurement hints that the Gundestrup probe could somehow be corrupted by the presence of drift-interchange fluctuations with a perpendicular phase velocity. The probe, being a perturbative object, could be absorbing the waves as they pass, so that they are 'crashing' on one side of the probe and dissipating before reaching the other side. Alternatively, one could picture the probe depleting the peaks of the ripple as it passes in the perpendicular direction so that the amplitude of the fluctuation is reduced by the time it reaches the electrodes on the other side of the probe. While we are not aware of any simulation that has demonstrated this effect, the observed similarity between Gundestrup and phase velocity measurements is suggestive.

In an attempt to determine whether there is a 'wave-breaking' phenomenon in action, we have carried out Gundestrup and phase velocity calculations for very short time windows. We find that the correlation between the two measurements is present at the shortest time scale (12 μs), which is similar to the period of the typical drift-interchange fluctuations . Furthermore, we note that in a region a few mm outside the LCFS, the phase velocity measurements often see fluctuations moving in opposite perpendicular directions during a single period of ion saturation. When this occurs, the Gundestrup-measured perpendicular velocities change in agreement with the general trend. Thus, the Gundestrup and phase velocity measurements are correlated even on a time scale of order the fluctuation period. It is not clear whether the alternating wave phase velocity is due to bulk fluid velocity (that is, E_r) fluctuations, which carry the drift-interchange perturbations with them, or is simply reflective of the distribution of the fluctuation phase velocities. Therefore this observation does not prove that the Gundestrup is incorrectly measuring fluid velocity. However, the fact the $E_r \times B$ method does not see any offset due to these fluctuations favors the explanation that they are purely a wave phenomenon.

If a wave-breaking phenomenon is causing the Gundestrup probe to measure phase velocity rather than (or in addition to) fluid velocity, the mechanism for this is not

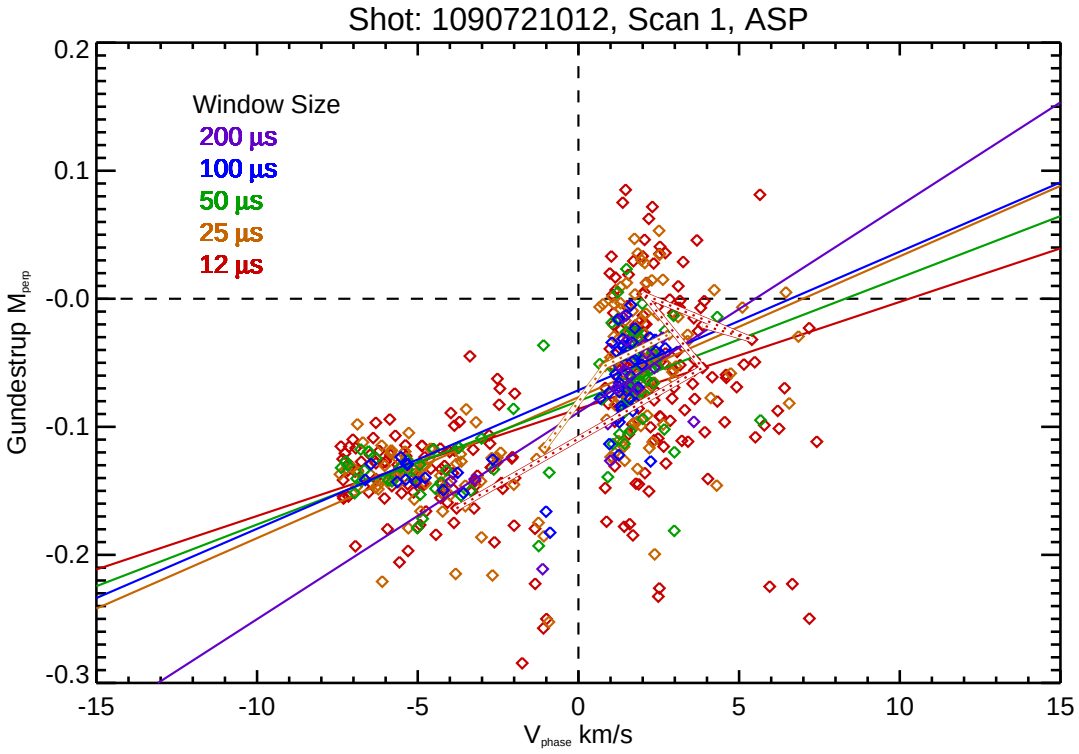

Figure 5-8: The correlation between measured Gundestrup perpendicular Mach number and fluctuation phase velocity is shown for a single ASP probe scan. Different colors represent the measurements derived with sampling windows of various durations. The shortest windows (shown in red) are not much longer than the period of the drift-interchange fluctuations. The dotted lines connect points from single periods of ion saturation, in which the measured phase velocity reverses direction. It can be seen that the Gundestrup perpendicular flow velocity responds in agreement with the general trend even at the level of individual fluctuations during a single period of ion saturation.

clear and is beyond the scope of this thesis to investigate. However, this explanation fails to explain why the electron diamagnetic offset often extends all the way into the far SOL where the turbulence generally becomes blobby, and is often seen to propagate in the ion diamagnetic direction [49].

5.5 Probe-Induced Perturbations

The issue of probe-induced perturbations is not a new one. In fact, probe theory is largely concerned with extracting the properties of the unperturbed plasma from the data collected at the necessarily highly perturbed location of the probe surface. This means that when using the standard formulations, we are automatically taking many probe-induced perturbations into account. Simple sheath theory addresses parallel potential and density gradients due to the probe. Also, Hutchinson has shown in his recent work [11] that probe-induced density variations are self-consistently accounted for by the standard Gundestrup formulation. However, there are perturbations which are not addressed by the standard theories. These include temperature perturbations due to the probe, and probe-induced flow patterns due to local injections of recycling neutrals.

5.5.1 Perturbation Due to Probe-Tip Recycling

The phenomenon of local flow perturbations has been addressed recently by S. Gangadhara [50, 51]. His experiments with impurity plumes injected from the probe tip revealed the presence of 'plasma jets' in the vicinity of the probe tip. These jets consist of strong plasma flow along the field lines away from a region just above the tip of the probe. These flows are likely the result of a recycling loop set up by the neutrals emitted from the probe tip. The concern with the Gundestrup probe is that probe-induced flows could be corrupting our measurements of flows in the background plasma.

Because we believe the jets are fed by recycling neutrals, the intensity of the jets should depend on the neutral mean free path. This means the effect on the

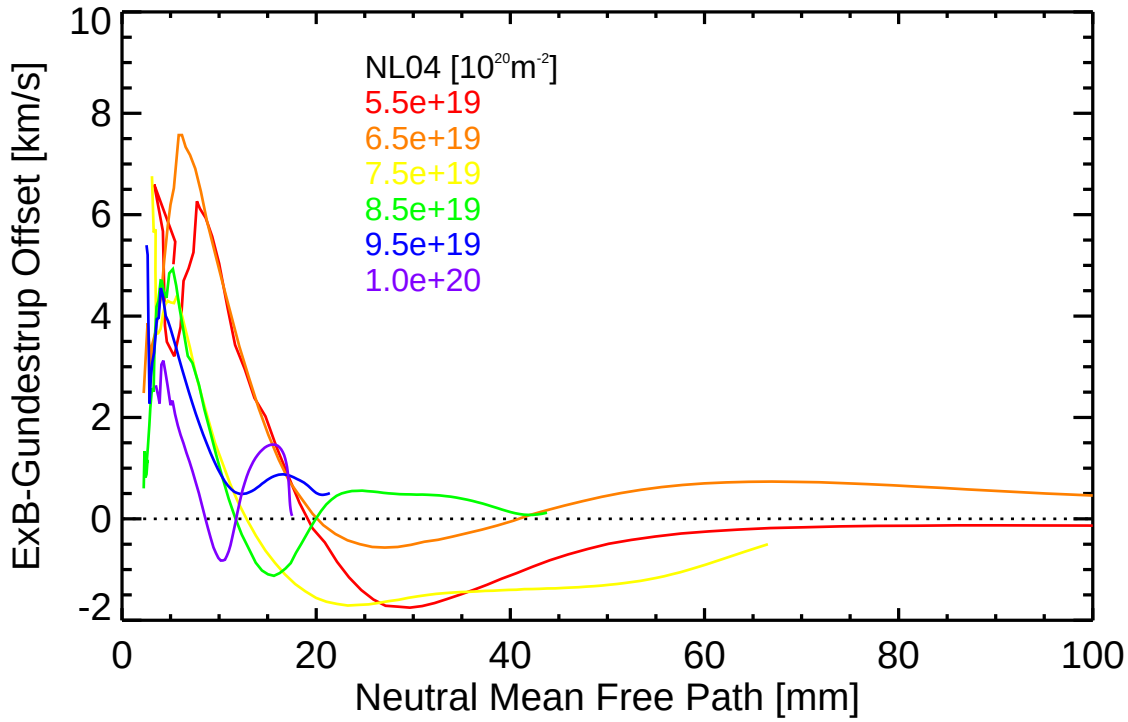

Figure 5-9: An investigation of the relationship between the difference in velocities inferred from Gundestrup and $E_r \times B$ methods and the neutral mean free path. This attempts to identify the potential role of recycling jets in corrupting the Gundestrup measurement. The different colored traces represent binned data from various line-integrated density ranges.

Gundestrup probe should vary with depth in the SOL, because the neutral mean free path is dependent on plasma temperature and density. It seems plausible that this effect could be capable of significantly corrupting the Gundestrup measurement.

To search for evidence of Gundestrup probe corruption due to jets, we can calculate the discrepancy between the $E_r \times B$ and Gundestrup measurements of perpendicular flow velocity and see if it correlates with the neutral mean free path. The neutral mean free path can be calculated using the expression of ionization rate in a Maxwellian plasma [52].

$$\langle \sigma v \rangle = 10^{-11} \frac{(T_e/E_\infty^Z)^{1/2}}{(E_\infty^Z)^{3/2}(6.0 + T_e/E_\infty^Z)} \exp\left(-\frac{E_\infty^Z}{T_e}\right) \quad [\mathrm{m}^3/\mathrm{s}] \tag{5.8}$$

where $E_\infty^Z = 13.6$ eV is the ionization energy for deuterium. The neutral mean free

path is then:

$$\lambda_n = \sqrt{\frac{2E_d}{m_D}} \frac{1}{n\langle\sigma v\rangle} \tag{5.9}$$

where $E_d \approx 3$ eV is the dissociation energy of deuterium molecules and m_D is the mass of the deuterium atom. The result is shown in Fig. 5-9. Here, data have been binned by discharge density for a large number of shots at normal field and current. The probe covers a different range of λ_n for different discharge densities, yet the large flow discrepancies occur only for values of $\lambda_n \lesssim 20$ mm. This is roughly the dimension of the probe itself, lending some credibility to the recycling theory. This result is circumstantial evidence that probe-tip recycling could be influencing the Gundestrup measurement, yet it is clear that there is additional systematic density dependence of the discrepancy. The Gundestrup flow offsets have smaller magnitude and are suppressed at lower λ_n for the higher density discharges.

It is important to remember that λ_n is not the only quantity that varies radially in the SOL. In fact, many plasma properties do, including diamagnetic velocity and turbulence properties. Thus, it is be difficult to extract the root cause of the discrepancy by looking at its correlation with quantities that vary with SOL depth or plasma density. The present lack of any theoretical mechanism by which probe-tip recycling could produce an offset in the electron diamagnetic direction leads us to look for other possible causes.

5.5.2 Electrostatic Perturbations due to probe shadow

An inserted scanning probe acts as a limiter for the local plasma. While the perturbative effect of the probe can be minimized at the electrodes, it can be large in the shadow of the extended probe body. Hutchinson's recent work [11] has shown that probe-induced density perturbations are self-consistently accounted for by the Gundestrup formulation. Temperature perturbations however, were not included. It is therefore possible that these could lead to the observed Gundestrup offset. The high-collisionality of the C-Mod edge can cause the probe shadow to be in a conduc-

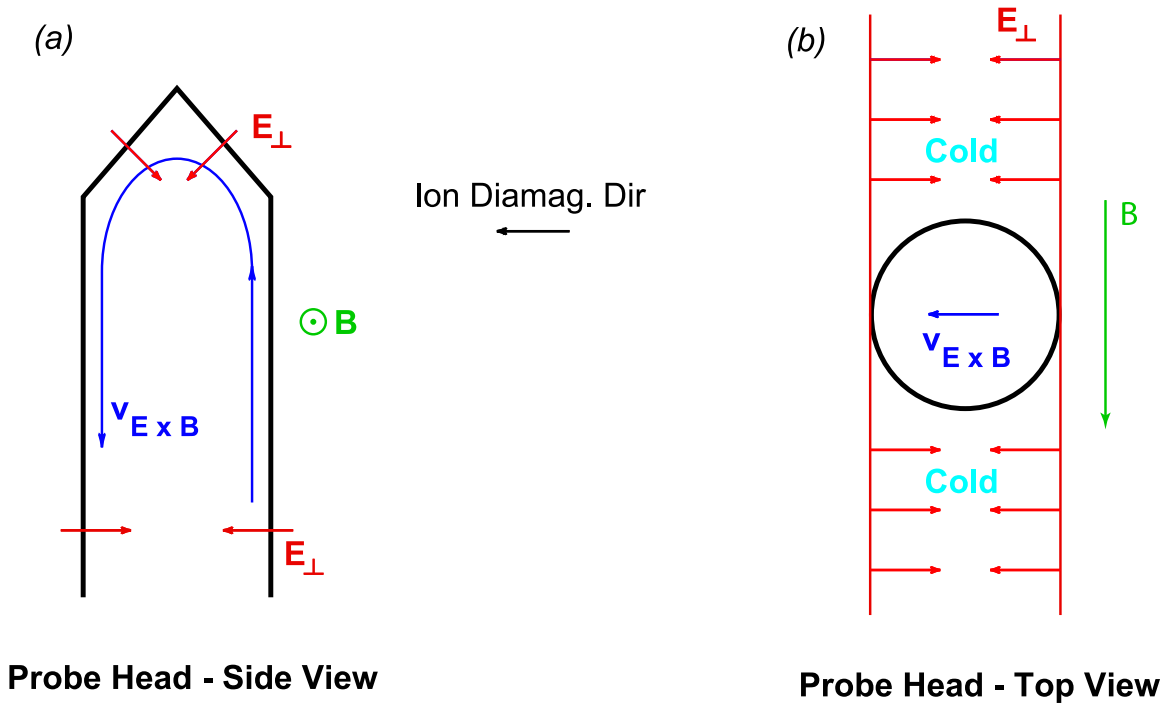

Figure 5-10: Flows due to probe-induced temperature perturbations.

tion limited regime, where the temperature of the entire pre-sheath can be depressed due to the heat absorbed by the probe body. Temperature perturbations affect the sheath boundary condition at the probe surface ($\Phi_p = V_f + \alpha T_e$, see section 2.1.3), leading to lower local plasma potentials. This in turn leads to electric fields pointing into the probe shadow, and an $E \times B$ drift which circulates the probe shadow. Such an effect has been investigated before [51] as a possible mechanism for transporting impurities down the probe shaft. The resulting pattern of electric fields is shown in Fig. 5-10.

Inspection of panel (a) in Fig. 5-10 reveals that $E \times B$ flow resulting from depressed pre-sheath temperatures is along the surface of the perturbing object, and should not affect the current collected by the probe electrodes. However, while the flow itself may not cause a perturbation, it is possible that the resulting density and temperature perturbations could. The flow pattern set up by the probe shadow temperature perturbation tends to draw hot, dense plasma down the ion diamagnetic side of the probe, and drive, cool, less dense plasma up the electron diamagnetic side. This could cause the electrodes on the ion diamagnetic side to collect enhanced current,

which would be interpreted as a flow in the electron diamagnetic direction. This effect would be the strongest on the down-stream side of the probe where the temperature perturbation is the largest.

It is possible that pre-sheath temperature depressions are a limiting factor on the use of Gundestrup probes in high-collisionality plasma environments. We are not equipped to look for direct evidence that it is affecting our measurements, but this hypothesis is consistent with the observation that the Gundestrup perpendicular velocity offset is in the electron diamagnetic direction and is often large at high density.

5.5.3 Non-Uniform Temperature Effects

Parallel temperature asymmetries have been noted in section 4.3. The likely cause of this observation is the interruption of parallel heat flux by the probe. This causes the boundary condition on the downstream flux tube to change dramatically, and the the temperature to be artificially depressed from the probe to the downstream limiter or divertor surface. This effect is expected to be particularly strong at the WASP location where there is minimum transport to fill in the probe shadow.

One possible solution to this problem would be to ignore the downstream electrodes when computing the perpendicular velocity, since we expect the perturbative effect to be greatest in the downstream direction. Fig. 5-11 shows the results of this exercise. In some cases, taking the perpendicular velocity from the upstream electrodes improves the agreement with $E_r \times B$ inferred velocities, but in other cases the disagreement is exacerbated. We are forced to recognize that parallel heat flux is not included in the Gundestrup models, and we do not know how it will affect the downstream or upstream electrodes with any confidence.

Non-uniform temperature effects cannot explain anomalous Gundestrup offsets on the LFS where reduced parallel heat flux should lead to reduced parallel temperature asymmetries. Moreover, radial ballooning-like transport is abundant, which should allow the pre-sheath to be equilibrated easily. However, this may be one of the factors folded into the difficulty of interpreting the Gundestrup perpendicular velocities.

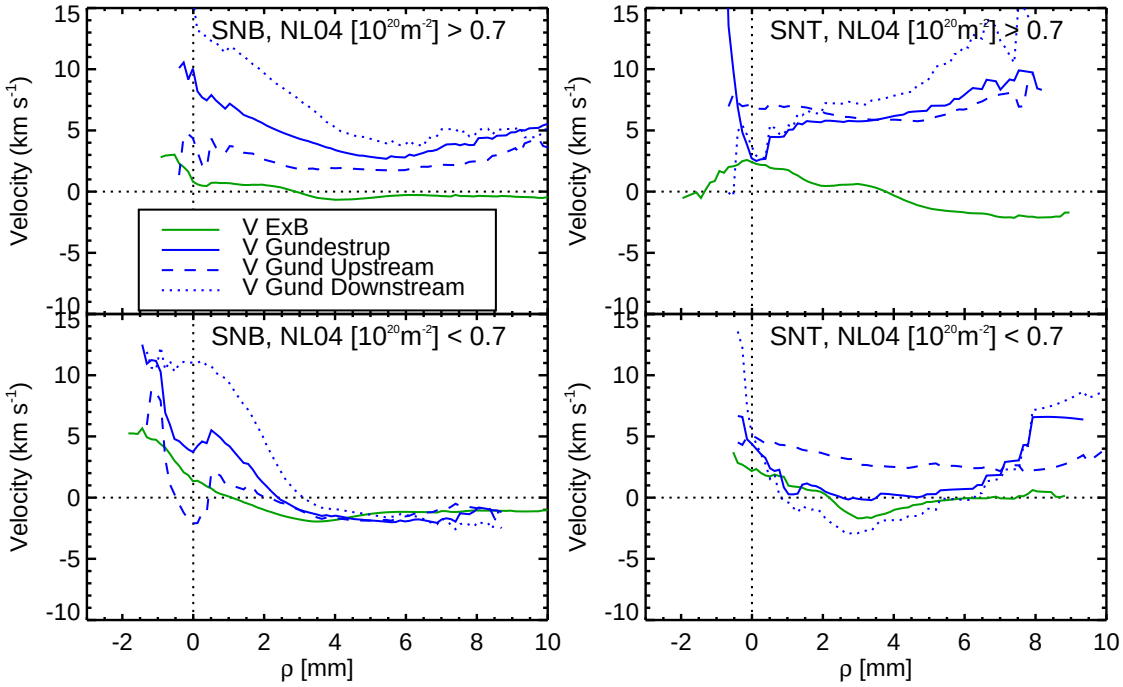

Figure 5-11: Comparison of WASP measurements of Gundestrup and $E_r \times B$ perpendicular velocities with Gundestrup velocities derived from only the upstream or downstream electrodes. A variety of cases are shown, each binning and averaging data from the '07-'09 campaigns. The upstream velocities are not generally a better match to the $E_r \times B$ velocities than the Gundestrup velocities computed using all four electrodes.

Despite our inability to determine the exact cause of the discrepancy, there is substantial circumstantial evidence that the Gundestrup model does not accurately describe our data. Therefore we will proceed using the $E_r \times B$ method to measure perpendicular fluid flows for the remainder of this thesis, unless otherwise stated. The large variability of this measurement will have to be managed by acquiring sufficient statistics to reduce the error to a reasonable level.

Chapter 6

Flow Observations

A variety of interesting flow observations were made with the scanning probes since the installation of the WASP. The first set of observations were made using parallel flow measurements alone. They address the question of which driving mechanisms dominate at various poloidal locations, as well as the issue of toroidal momentum coupling between the edge and the core. These observations are presented in section 6.1. When the perpendicular flow measurements became available on C-Mod, the most striking feature was an observed 'shear layer' in the vicinity of the LCFS. The variation of the shear layer with poloidal location and discharge conditions is examined in section 6.2

6.1 Topology Dependent, Transport-Driven Parallel Flows

One of the key findings of HFS Langmuir probes is that there are high parallel flow velocities that are persistently directed towards the active divertor along field lines. In many cases these flows approach Mach 1 despite being far from a limiter or divertor surface in the parallel direction. The HFS flow pattern is in contrast with observations on the LFS where parallel flows are generally reduced in magnitude and persistently directed in the co-current direction. The emerging theory to describe the

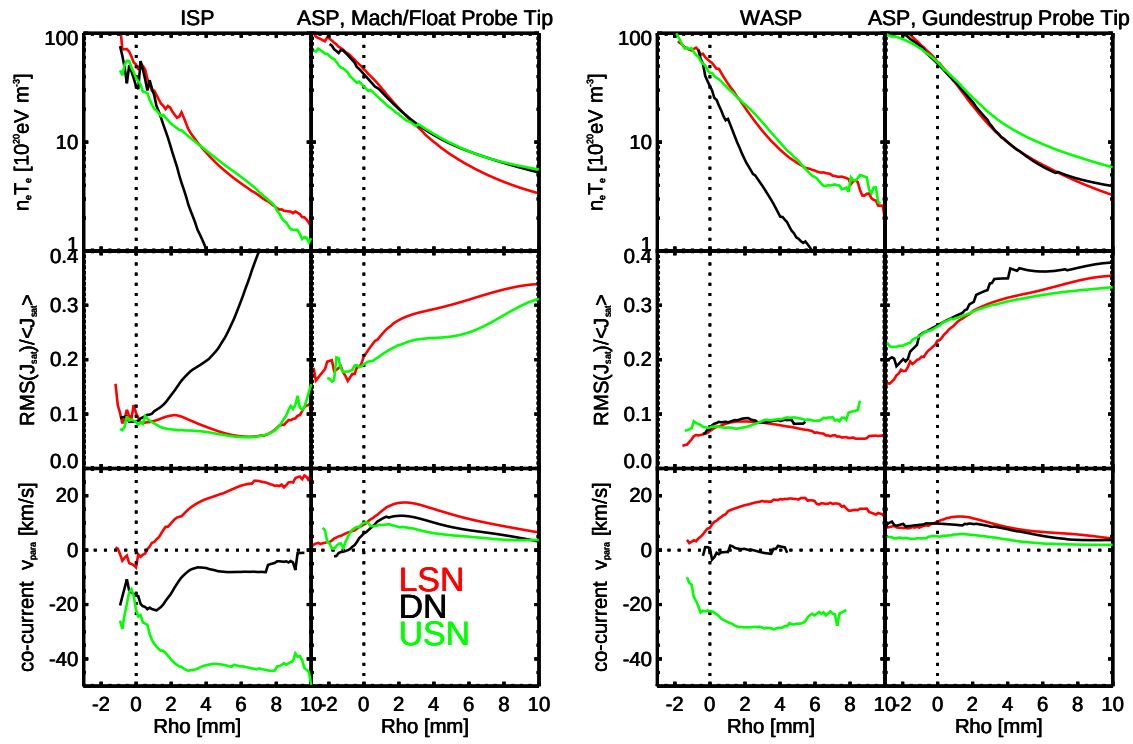

(a) (b)

Figure 6-1: HFS/LFS comparison of pressure, fluctuation intensity and parallel flow using data from different diagnostic sets: (a) Data collected prior to the start of the '07 campaign, using the ASP and ISP and (b) Data collected from '07 onward, using the ASP and WASP with high-heat flux Gundestrup probe tips. These traces represent averages of many profiles from 5.4 T, 0.8 MA discharges with normal field direction and NL04 $\leq 0.85\times10^{20}$.

HFS observations is that these flows are driven by poloidally asymmetric cross-field particle and energy transport.

6.1.1 The Transport-Drive Hypothesis

Parallel flows towards the divertor on the HFS were first observed on C-Mod by observing injected impurity plumes with digital cameras [53]. The transport-driven flow hypothesis immediately emerged as a potential explanation for these flows. The theory is that the cross-field transport of particles and energy is 'ballooning' in nature, meaning it is highly localized to the LFS of the plasma. The resulting pressure gradients drive rapid flow along the open field lines from the LFS midplane to the HFS divertor. The ISP [19, 24] confirmed that these flows are near sonic, often with

Mach numbers approaching 1. This picture is supported by several other observations:

1. The normalized levels of fluctuations are greatly reduced on the HFS, indicating a lower level of turbulent transport[1].

2. The parallel flows nearly disappear in well-balanced double-null magnetic topologies, when the magnetic connection to the LFS is severed.

3. Plasma density and temperature in the HFS SOL are greatly reduced in well-balanced double null, indicating that the plasma that exists there arrives from the LFS and not from local cross-field transport.

These observations can be seen in the data shown in Fig. 6-1 (a). The WASP has been able to reproduce these observations as seen in Fig. 6-1 (b), and add new information as well.

6.1.2 WASP Results for Parallel flows

In section 4.1 we saw results which showed that the HFS plasma density is reduced outside the secondary separatrix, where the magnetic field lines do not connect the LFS SOL to the HFS SOL. The same set of experiments provided data on the parallel flow velocity as well. Fig. 6-2 shows the results. The strong parallel flows are also reduced outside of the secondary separatrix, in agreement with the transport-drive hypothesis.

Another new WASP observation can be seen in Fig. 6-2. The parallel velocity at the separatrix is often near zero for LSN discharges, but maintains a counter-current velocity at the separatrix for USN discharges. One possible explanation is that the SOL flows are coupling to some independent, intrinsic rotation in the core that is in the counter-current direction. Such intrinsic rotation has been observed on C-Mod during L-mode discharges using x-ray spectroscopy [54, 55, 56]. This asymmetry in the flow pattern is reversed when the direction of the field and current are reversed,

[1]Fluctuation-induced radial particle flux is investigated in detail in section 8.2.6, and is found to be nearly zero

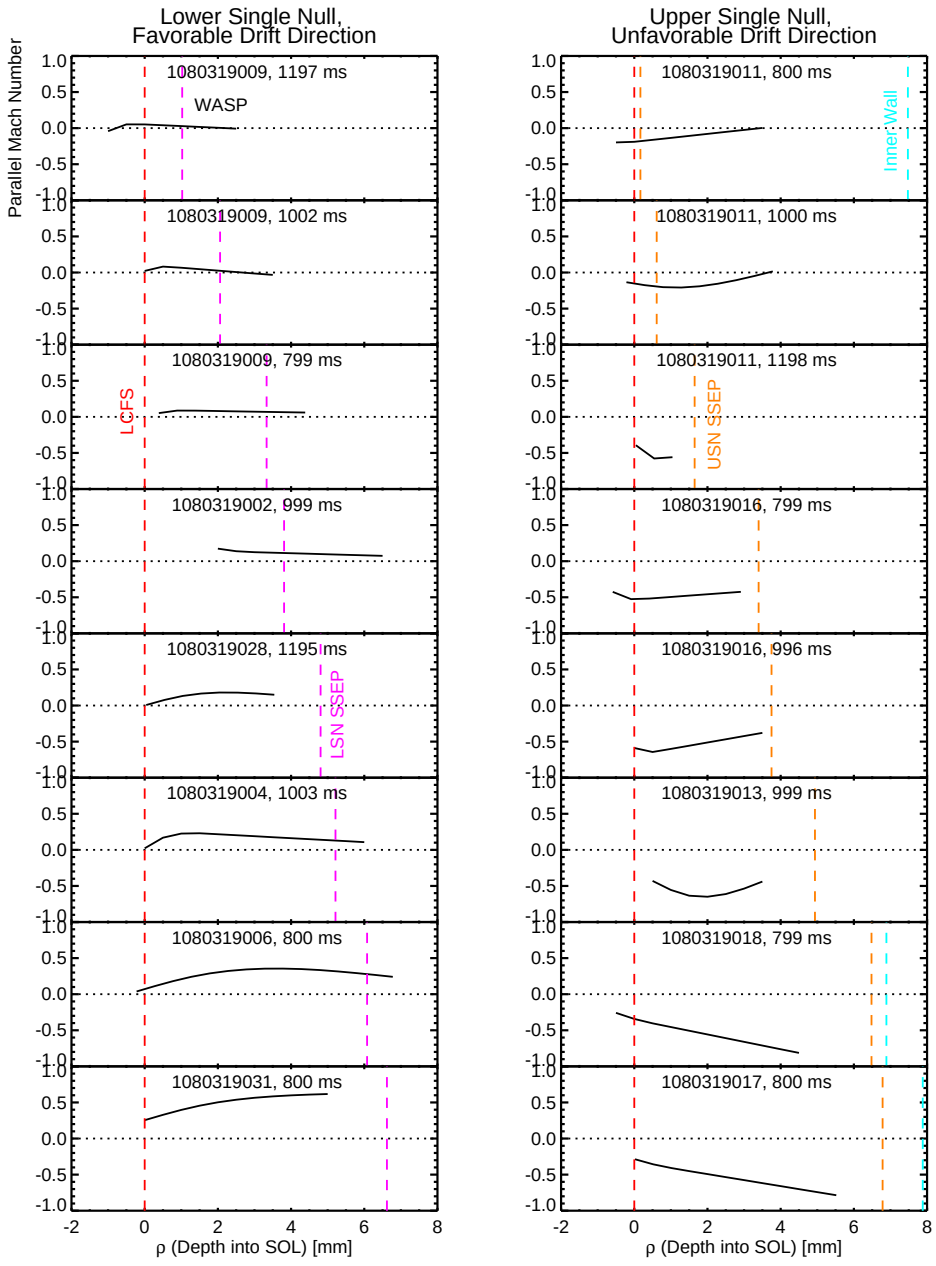

Figure 6-2: Parallel flows measured by the WASP probe during an SSEP scan. Positive is the co-current direction. The flow reverses direction when magnetic topology is changed from lower null dominant to upper null dominant. The flow is suppressed in near balanced double null, and shows signs of being more stagnant outside the secondary separatrix.

so it is not due to divertor geometry asymmetry, but to the direction of the toroidal field and current (see, for example, Fig. 7-6).

While the explanation of near-sonic flows rushing toward the inner divertor is tempting, the parallel flow measurement alone is is insufficient to reach conclusions about the net poloidal particle motion. The slight angle of the field line means that the poloidal particle flux can be strongly influenced by the presence of finite cross-field drifts. Therefore, a firm conclusion about the poloidal particle flux requires a measurement of perpendicular flow velocity, which will be addressed in section 6.2.

6.1.3 LFS Parallel Flow Observations

The parallel flows on the LFS do not reverse direction when the magnetic topology is changed from LSN to USN (see Fig. 6-1). Instead the parallel flows are persistently in the co-current direction. Therefore the LFS flow is influenced primarily by physics that is not dependent on topology. The controlling physics may include Pfirsch-Schlüter flows, or toroidal rotation in response to radial electric fields. These effects are dependent on field direction rather than the magnetic topology. However, there is a *modulation* in the parallel flow due to the topology, such that during a scan of the secondary separatrix we observe a step (but not a reversal) in the parallel flow as the topology passes through double-null. This change in the LFS parallel flow may be due in part to the fact that the ASP is not located exactly at the midplane. If the particle source due to transport is highly localized near the midplane, and evolves quickly as one moves poloidally towards either divertor, then we would expect a modulation in the parallel flow with topology reversal. It is also possible that the near-sonic parallel flows that circulate the plasma impose a different flow 'boundary condition' on the confined plasma, resulting in a modulation of parallel flows even on the LFS [19]. One possible scenario is that the HFS SOL flow couples its momentum across the LCFS via viscous drag, or a radially inward particle flux.

6.1.4 Toroidal Momentum Coupling with HFS flows

Several experimental observations of core rotation have reported the presence of an angular momentum pulse diffusing inward from the edge during L-H transitions. [57, 58]. Significant changes in toroidal rotation between LSN and USN topologies have also been observed [59, 55]. The presence of fast parallel flows in the HFS SOL which reverse with topology suggest that these flows may be setting a flow boundary condition on the core toroidal rotation. The possibility of viscous coupling between the edge and the core which is localized to the HFS seems plausible since these are the highest velocities in the edge. A recent experiment on C-Mod used a rapid shift in the magnetic topology from USN to LSN to produce a momentum pulse which moved inwards. The pulse was observed first by the HFS main ion charge-exchange diagnostic, and later by core x-ray spectrometer [35]. Unfortunately, the scanning probes cannot be used to observe this phenomenon because the probe cannot provide continuous data at a fixed location for a momentum transport time-scale ($\sim$ 35 ms [60]). Nonetheless, we would like to whether the source of the momentum pulse is the HFS transport-driven parallel flows.

Nose Grazing Experiments

While it seems likely that the parallel flows on the HFS are the agent by which magnetic topology reversal modulates core rotation, there are other possible explanations. It could be argued that some property of the magnetic topology itself causes the core rotation change, independent of the flows. To test the hypothesis that the HFS flows play a direct role, we conducted a series of experiments in which we maintained an USN magnetic topology, but interrupted the magnetic connection between the LFS and the HFS by brushing the LCFS against the inner divertor nose. This is referred to as a 'nose-grazing topology.' If we continue to 'crush' the equilibrium against the inner divertor nose, it becomes 'nose-limited' and a flux connection appears at the top of the plasma. This progression (illustrated in Fig. 6-3) is intended to reverse the direction of the HFS transport-driven flows. If the core rotation undergoes its usual

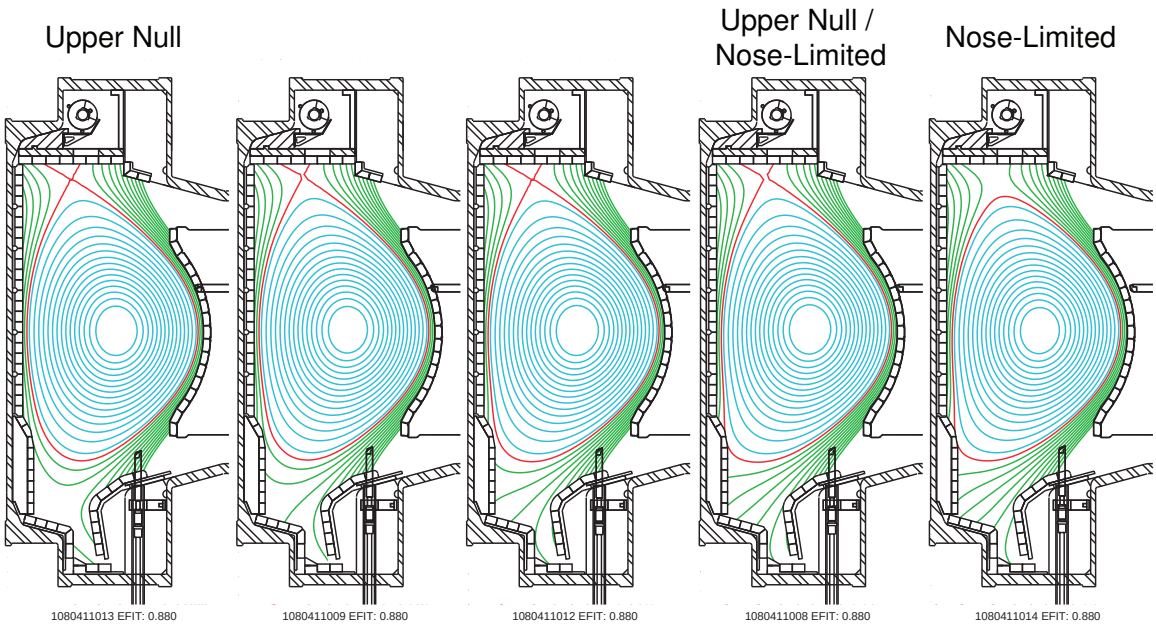

Figure 6-3: Equilibria showing the progression from USN diverted discharges to 'nose-limited' discharges. Both are USN dominant magnetic topologies, but the equilibrium on the RHS which is 'crushed' against the inner divertor nose have a SOL flow channel over the top of the plasma, similar to a LSN diverted equilibrium.

USN to LSN velocity shift in response to the HFS flow reversal, then the HFS flows are identified as the likely cause of the shift. If the core rotation does not change, then the magnetic topology change itself is responsible for the shift. These experiments were carried out during the 1080411 and 1080515 run days

The results of the nose grazing experiments are summarized in figure 6-4. The x-axis of the plots is the 'flow-gap'. This is the width of the flux channel connecting the low and high field sides, mapped to the outer midplane. This gap is the critical parameter if the HFS flow is due to LFS transport and requires a flux connection. In a normal diverted discharge, the flow gap is determined only by the position of the secondary separatrix (SSEP) in ρ-space. For diverted discharges in the nose grazing

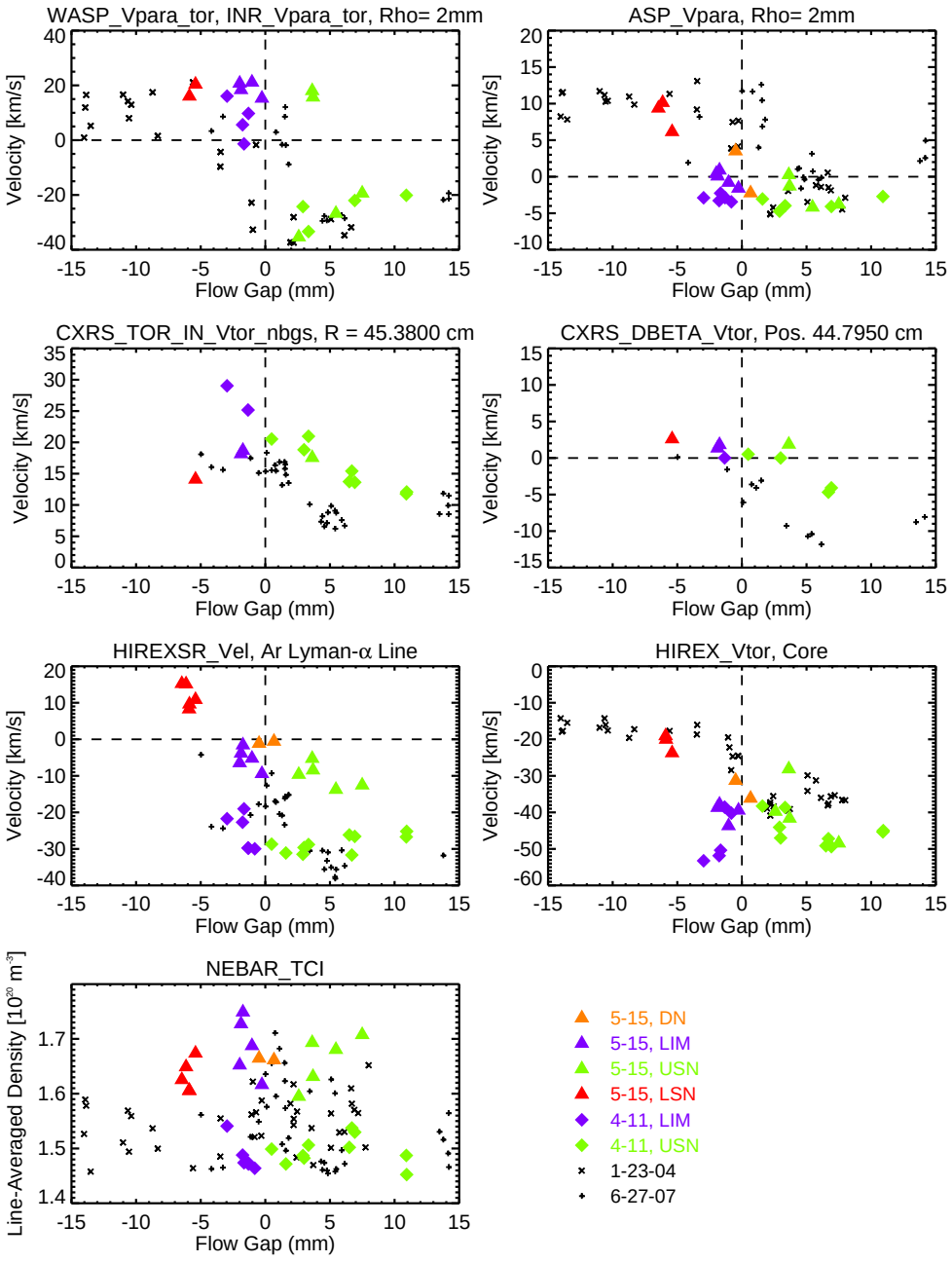

Figure 6-4: Results of the 'nose-grazing experiment'. The velocities at various locations in the plasma core and edge are plotted against the size of the flux connection between the LFS and HFS, or 'flow gap'. Black x's and crosses are reference data from normal diverted discharges, while colored solid symbols show data from the two days dedicated to nose-grazing experiments. These include a normal diverted topologies (LSN and DN), to make contact with the previous results, and a scan from USN to nose limited topologies which are still upper-null dominant. The last panel shows the discharge density for all the shots, which shows they are evenly distributed in density space, but also identifies the different densities that were used for the two run days. This density offset is the cause of the offset in the density-sensitive HIREX Sr. x-ray spectrometer between the two days.

experiment, the flow gap is determined by the position of the inner divertor nose in flux space if the nose reaches inside the secondary separatrix. For limited topologies, the flow gap is the distance from the limited flux surface to the primary separatrix in ρ-space.

The black points in Fig. 6-4 show results from previous SSEP scans without nose limited topologies (1040123 and 1070627). The flow gap for all of these cases is the distance in flux space from primary to secondary separatrix. For the edge and core diagnostics shown, there is a step on the order of a few tens of km/s near the point of topology reversal. The data from the nose grazing experiments are shown in color, with various topological conditions shown in different colors. The green points are USN, with the flow gap determined by the inner nose and the purple points are those with the LCFS defined by the inner nose and the flow gap determined by the primary separatrix. For reference, we also ran discharges in LSN and DN to make contact with the previous data (here flow gap is again determined by the secondary separatrix). The different run days are distinguished by different symbols. The last figure shows the density range which is spanned by this data set. We have included only data with line-averaged densities between 1.45×10^{20} and 1.75×10^{20} m^{-3} to reduce the influcence of density on the result. This plot shows that there is no correlation between density and flow gap built into the data. However, it also shows that the second day of the nose-grazing experiments was at higher density than the first. The core diagnostics are very sensitive to density, and a systematic offset can be observed in the HIREX data between the two days. This must be borne in mind when interpreting the data.

The WASP results show that the parallel flow reversal observed in USN to LSN topology scans is repeated for the flow gap scan in nose-grazing discharges. The boron charge exchange system located just inside the separatrix on the HFS (CXRS_TOR_IN) also shows evidence of a step in the toroidal rotation as it normally does in a topology scan. The deuterium charge exchange however (CXRS_DBETA) does not. Further difficulty comes from the core (HIREXSR, HIREX) and low field side (ASP) diagnostics, which do not show their typical velocity increment in the limited configurations. We are forced to conclude that the core rotation does not follow the trend from the

earlier topology scans.

The conclusion of this experiment is that the HFS flow boundary condition is not the sole cause of the core velocity increment. The fact that the ASP velocity increment is also suppressed suggests that the LFS SOL responds to the core velocity. This could be due to particles arriving from the core via transport, and carrying momentum with them into the LFS SOL.

We know from previous data [61] that LSN-dominant nose-limited discharges have LFS and HFS flows similar to normal LSN discharges. Thus, if we were to maintain a nose-limited topology and slowly change the discharge from upper to lower x-point dominant, we should at some point observe the co-current velocity increment on the LFS, and presumably in the core as well. Unfortunately, this experiment would be very difficult to conduct from an operational standpoint.

It should be noted that we were only able to achieve a small flow gap at the top of the plasma in nose-limited topologies. The gap was typically only a few mm. In this condition, the density e-folding length on the HFS is greatly reduced, and the total momentum contained in the HFS plasma is much smaller than in a normal LSN. This seems to a be moot point since we imagine the edge-core coupling mechanisms to be viscous momentum transport across the LCFS. If so, the only important influence on core rotation should be the momentum density in the near SOL, which is similar in the nose-limited cases to a normal LSN discharge. However, if the HFS SOL were able to couple all its toroidal momentum into the core, then it is still possible that the HFS flows determine the intrinsic toroidal velocity. Such a scenario might be possible since the HFS divertor region is often characterized by high levels of volume recombination and neutral penetration to the core. This possibility will be discussed in section 8.2.4. Another possibility is that something about the magnetic topology itself, rather than the flows, has a dominant influence on core rotation.

6.2 Sheared Perpendicular Flows

Regardless of which technique is used to measure perpendicular flows, a 'shear layer' is often observed near the LCFS with the LFS scanning probes. This shear layer is characterized by a region several mm wide in which the perpendicular velocity changes rapidly. Bacause $E_r \times B$ flow shear is often invoked as a potential mechanism for suppressing or regulating turbulence [62], the presence of this feature in the vicinity of the LCFS is interesting. We will present data showing the shear layer, and investigate the role it plays in SOL transport.

6.2.1 Role of Shear Layer in Regulating Edge Transport

The role of electromagnetic fluid drift turbulence in setting edge gradients has been investigated in detail [12, 63, 64]. The resulting picture is not one of diffusive transport, where the heat and particle fluxes are determined by the gradients according to $\Gamma_\perp = D\nabla_\perp n$, $q_\perp = \chi\nabla_\perp T$. Rather, the gradients are fixed at a 'critical' value, perhaps determined by electromagnetic shear. Plasma turbulence the adjusts the transport according to input power, always maintaining the critical gradient. In this picture, electromagnetic shear sets the gradients and determines access to high-confinement modes of operation. Recent work by LaBombard [65] has shown the gradients to be largely independent of magnetic shear, through an experiment that carefully varied magnetic shear by incrementally shifting from a diverted, high-elongation magnetic topology to a limited, low-elongation topology. The edge gradients observed with the ASP were insensitive to this scan, indicating that magnetic shear does not play a primary role in setting the gradients. The remaining candidate is 'electric shear' (sheared flows caused by $\partial E_r/\partial r$). Sheared $E_r \times B$ flows can arise due to the different physics setting potentials on the open and closed flux surfaces. On closed field lines, the potential adjusts itself to balance the local pressure gradient force, resulting in inwardly directed electric fields. On open field lines, potentials are strongly tied to the local temperature by the required potential drop across the sheath at the divertor or limiter. This leads to outward radial electric fields in the SOL. The

resulting $E_r \times B$ shear leads to perpendicular flows, which determine the gradients by regulating the size of turbulent eddies. The critical gradients are expected to be sensitive to parameters that set flows and potentials in the edge, including edge collisionality and magnetic topology. Our ability to measure the perpendicular flows directly allows us to test these ideas.

6.2.2 Probe Flow Shear Observations

Fig. 6-5 shows the three perpendicular velocity measurements for the three scanning probes. Each plot shows the shear layer in three magnetic topologies: LSN, DN and USN. A shear layer is present in all cases, with the exception of the Gundestrup and phase velocity data from the WASP. Because we are interested in the role of the shear layer in regulating transport, we will focus on the LFS data, where we know most of the transport occurs (see section 8.2.6). However, it is interesting to note the presence of the shear layer in the HFS $E_r \times B$ perpendicular flow data.

The shear layer displays several general characteristics that are independent of the diagnostic technique and fairly robust to changes in the plasma configuration. The perpendicular flow velocity is usually close to zero or slightly in the ion diamagnetic direction throughout the far SOL and rapidly ramps toward the electron diamagnetic direction in the near SOL or at the LCFS. The shear layer has a typical radial extent of around 5 mm. The measured velocities at the deepest locations (several mm inside the LCFS) are typically in the range of 0-6 km/s in the electron diamagnetic direction. The measurements in the far SOL agree with gas-puff imaging of blobs, which are usually observed to travel in the ion diamagnetic direction, and carry with them the bulk of the density at these locations. The electron-diamagnetic directed feature appears to be a more coherent fluctuation localized near the last closed flux surface. Similar structures have been seen in simulations of edge turbulence using the BOUT code [66].

One feature of the shear layers displayed in Fig. 6-5 is a dependence on magnetic topology. The velocity gradients are the highest in LSN and the lowest in USN magnetic topologies. Reversed field data show that this feature is a function of the

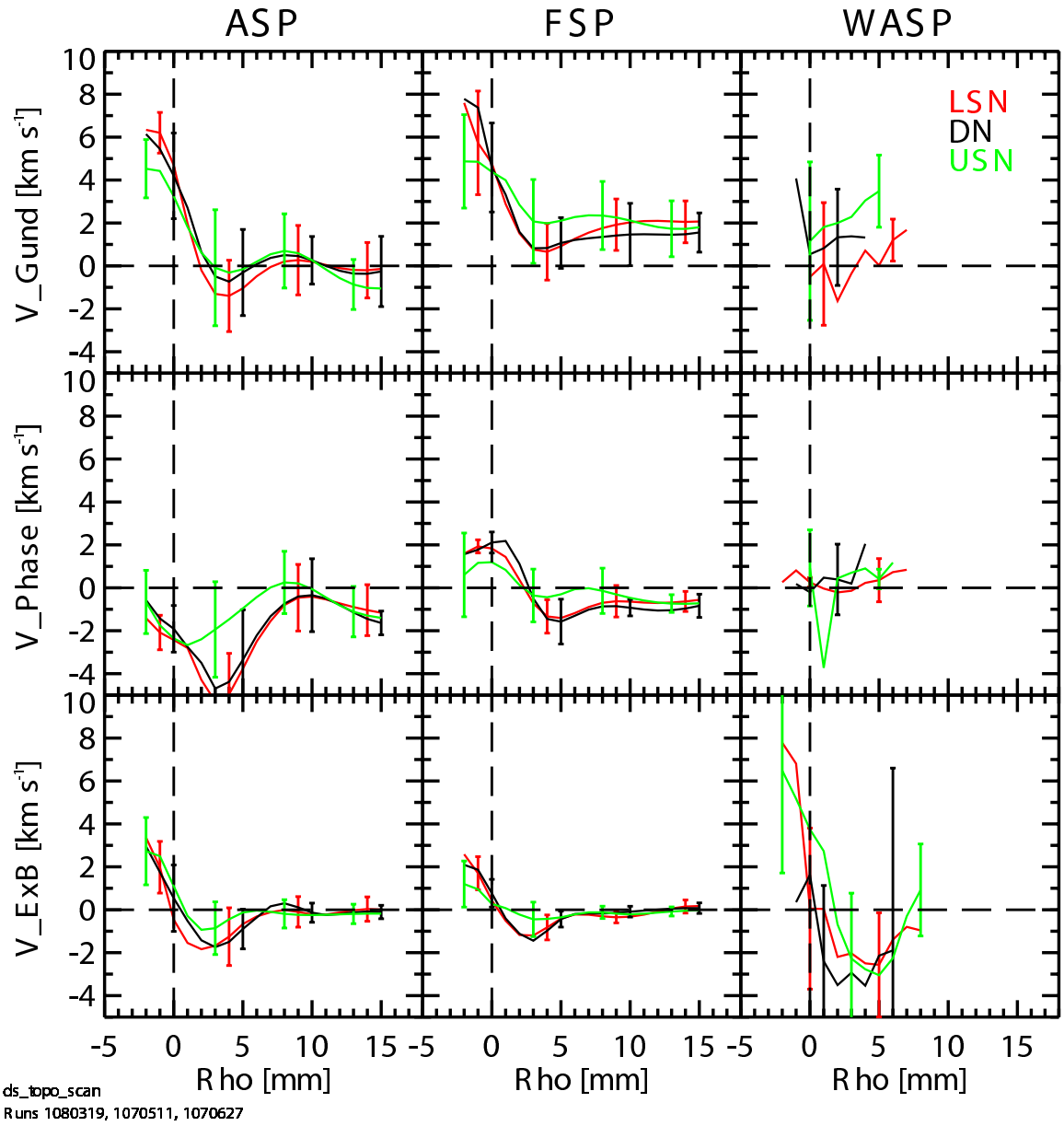

Figure 6-5: Perpendicular velocities measured with the three techniques on the thee scanning probes. Each plot shows data from three magnetic topologies. The data is binned over three run days: 1070511, 1070627 and 1080319, all with normal field and current (5.4T, 0,8MA). Error bars show the standard deviation of the binned data. The density range of this dataset is $0.1 < \bar{n}_e/n_g < 0.3$

$B \times \nabla B$ drift direction relative to the active x-point [67]. 'Favorable' topologies (those with $B \times \nabla B$ toward the x-point) show larger gradients. This result indicates that $B \times \nabla B$ drifts may interact with some topology-dependent edge flow effect to enhance or reduce the shearing rate. Attempts to connect the topology dependence of edge flow shear to the topology dependence of the L-H transition power threshold using ohmic H-modes have not been successful. In these experiments, no change in shear layer was observed, nor was any change observed in the L-H transition power threshold (in contrast with normal RF heated discharges). This indicates that the physics of ohmic H-mode transitions may be different from RF heated transitions.

6.2.3 Shearing Rate

Fig. 6-6 shows the shearing rates derived from the LFS midplane probe (ASP). It also shows the pressure gradient and the ideal ballooning mode growth rates. The ballooning mode growth rate is estimated from the temperature and density profiles following [68]:

$$\nu_b \approx c_s \left(\frac{2\nabla(n_e T_e)}{R n_e T_e} \right)^{1/2} \tag{6.1}$$

Here, c_s is the sound speed. To investigate the importance of collisionality, the data are shown at two different edge densities. The low collisionality case shows binned slices from discharges with densities between 10% and 20% of the Greenwald limit, while the high collisionality case contains discharges between 20% and 30% of the Greenwald limit. A number of observations emerge:

1. The shearing rates are comparable to the ideal ballooning growth rate, indicating that these flows may be the dominant mechanism regulating transport

2. The increased shearing rate at high collisionality in LSN corresponds to an increased ballooning growth rate and increased pressure gradient.

3. The topology dependence of the shearing rate, ballooning growth rate and pressure gradient is not present at low collisionality.

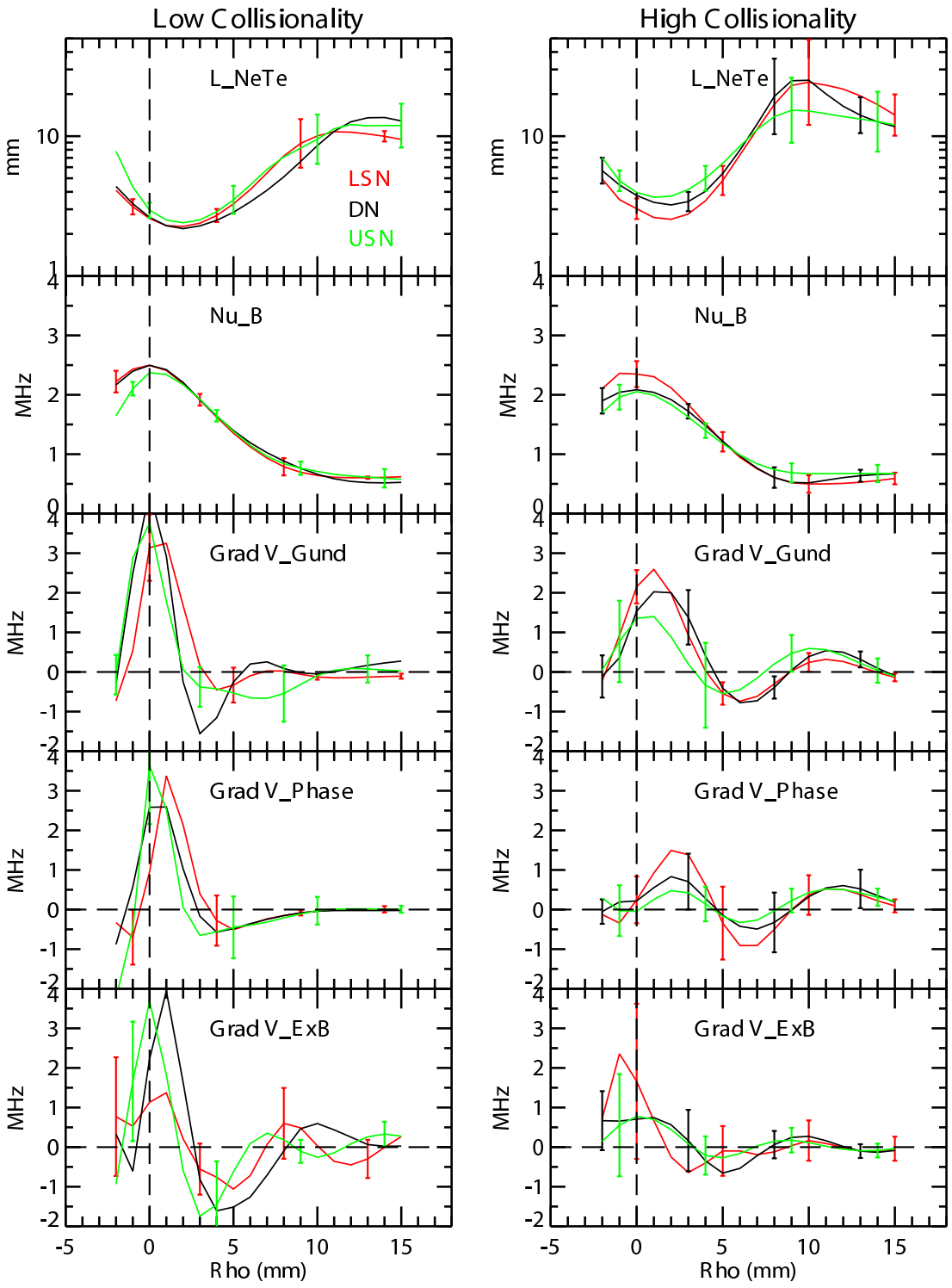

Figure 6-6: Pressure gradient scale lengths (first row) and inferred ideal ballooning mode growth rates (second row) are compared with shearing rates from ASP perpendicular velocity measurements. The data were obtained during the 1080319 run day with normal field and current (5.4 T, 0.8 MA). The left (right) column shows binned data from low (high) collisionality discharges: $0.1 < n/n_g < 0.2$ ($0.2 < n/n_g < 0.3$).

4. The observed shearing rates are slightly higher at low collisionality, as are ballooning growth rates and pressure gradients.

These observations support the connection between flow shear and edge gradients. The requirement of high collisionality for topology dependence to be observed is interesting and suggests that divertor physics may play a role. Whether the divertor is in a sheath limited or conduction limited regime could affect the edge plasma potentials and $E_r \times B$ flows. The divertor state and its relationship to edge flows will be addressed in section 8.2.4

Chapter 7

Comparison of Flow Measurements with Simulations and other Diagnostic Techniques

7.1 Comparisons of Measured Flows With Simulation

Two-dimensional edge transport codes have been used to simulate edge plasma flows. The new HFS WASP measurements allow better direct comparison of experimental data with the results of these simulations than has been possible in the past. In particular, the HFS location of the WASP allows us to make contact with the poloidal variations predicted by the models. Measurements of perpendicular flows are also important, since the models have often found perpendicular drifts to be an important player in the SOL flow picture. The following authors have used two different 2-D codes to model the Alcator C-Mod edge plasma: Xavier Bonnin (B2-Eirene SOLPS5.0) [41] and Alexander Pigarov (UEDGE) [14]. Our data are compared with their findings in the following subsections.

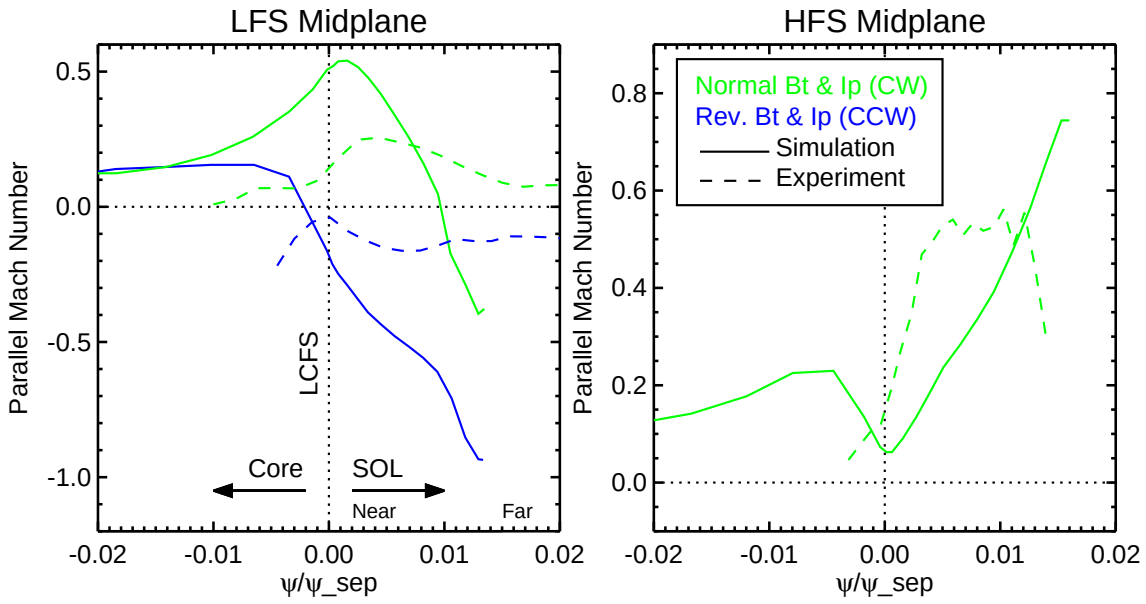

Figure 7-1: Comparison of parallel flows measured with inner and outer midplane probes to those simulated with the B2Eirene SOLPS5.0 code. The left (right)panel shows results for the LFS (HFS). The right panel shows results for forward field only, because no WASP data is available in reversed field. The sign convention labels the clockwise toroidal direction as positive (towards the inner divertor along the field). This corresponds to co-current for normal field and counter-current for reversed field.

7.1.1 Comparison With B2-Eirene SOLPS5.0 Simulation

B2 Eirene SOLPS5.0 is a plasma fluid code following Braginskii [44] (B2) coupled to a Monte-Carlo neutral code (EIRENE). X. Bonnin *et al.* carried out detailed simulations of the Alcator C-Mod edge and published parallel and poloidal flow profiles for the HFS and LFS midplanes for LSN plasmas with both forward and reversed field directions [41, 69]. These simulations included Pfirsch-Schlüter flows and currents and $E_r \times B$ drifts. They were run at low plasma densities ($n_e^{core} = 0.4 - 0.6 \times 10^{20}$ m^{-3}). Interpreting n_e^{core} as the core-side boundary condition imposed on the edge plasma simulation (that is, the density at the LCFS), the density range of the simulation corresponds roughly to $\overline{n}_e$ [10^{20} m^{-3}] = 0.83-1.0 or NL04 [10^{20} m^{-2}] = 0.4-0.6. For the following comparisons, the simulation results with $n_e^{core} = 0.6 \times 10^{20}$ m^{-3} have been used, and C-Mod data has been binned and averaged from discharges with NL04 $\lesssim 0.6 \times 10^{20}$ m^{-2}.

The results of the simulation for parallel flows at the LFS and HFS midplanes are shown in Fig. 7-1 along with the low density data from the WASP and ASP Mach probes. The LFS data shows agreement to within a factor of 2 in the near SOL, but generally poor agreement elsewhere. In the near SOL, both simulation and experiment show flow towards the inner divertor for normal field direction, and towards the outer divertor in reversed field. These parallel flows are co-current and co-field for both field/current directions, perhaps indicating some coupling to core physics, or that the Pfirsch-Schlüter flows (which are co-current on the LFS) are dominant in this region. There is quantitative disagreement between the results in the near SOL, with the simulation showing Mach numbers of $M \sim 0.5$, while the experimental data shows $M \sim 0.2$.

The far SOL shows disagreement between simulation and experiment. The simulation results are strongly towards the outer divertor for both field directions, changing sign for normal field case and reaching near $M \sim 1.0$ for reversed field. The experimental data show the same co-current trend that was observed in the near SOL with slightly reduced Mach number ($M \sim 0.1$).

The simulation and experiment agree better on the HFS, showing high Mach-number parallel flows towards the inner divertor, which become stagnant near the LCFS. However, there is a great deal of evidence (see sections 6.1.1 and 8.1) that the experimentally observed HFS flows are caused by a strong ballooning-like transport asymmetry, a feature that was not implemented in the simulation ($D_\perp$ and $\chi_\perp$ were taken to be poloidally invariant). The agreement in this case may therefore be fortuitous.

The simulation also produced results for the poloidal flow, including contributions due to the poloidal projection of the parallel flow and the $E_r \times B$ flow. These simulations were carried out in plasmas with $n_e^{core} = 4 \times 10^{19}$ m^{-3}. They found that the contribution from diamagnetic effects at these low densities was small and can be ignored. Fig. 7-2 shows the poloidal flow results from the simulation, along with binned, low-density data from the scanning probes.

The poloidal projections of parallel flows are derived from the parallel flows shown

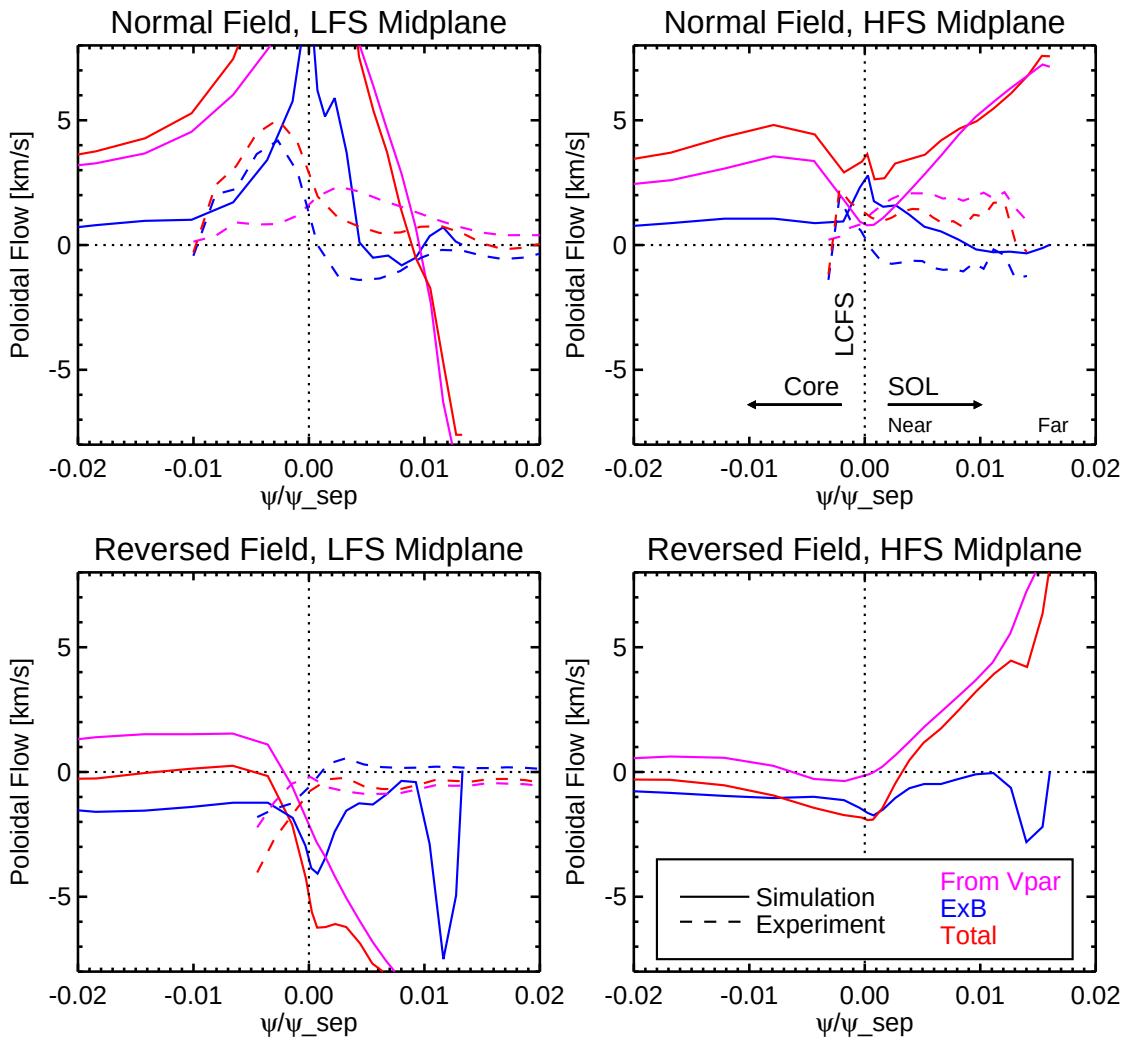

Figure 7-2: Comparison of poloidal flows measured with inner and outer midplane probes to those simulated with the B2Eirene SOLPS5.0 code. Results are shown for four cases: normal and reversed field direction on both the HFS and LFS (no experimental WASP data is available in reversed field). The sign convention is that positive flow is towards the inner divertor. This corresponds to the electron-diamagnetic direction in normal field and the ion-diamagnetic direction in reversed field.

Fig. 7-1. It is therefore surprising to see that the discrepancy between the simulation and experiment is larger for the poloidal projections than for the parallel flows themselves. This indicates one of two things: either the code was run with a different edge q than the experiment, and must therefore have had different field and current values than our standard 5.4 T, 0.8 MA discharges, or more likely, the SOL temperature profiles resulting from the simulation disagree with those measured in the experiment, changing the sound speed and affecting the conversion from Mach number to velocity. Unfortunately, Bonnin *et al.* do not report the field, current or temperature of the simulations, so the cause for this discrepancy is unresolved.

The other flow component is the $E_r \times B$ drift. For the experimental case, this is deduced using the $E_r \times B$ method, described in section 2.1.3. Here we see repeatable *disagreement* between the experimental and simulated results. There is some agreement a few mm inside the LCFS where both data sets show a flow towards the inner divertor in normal field and the outer divertor in reversed field (persistently in the electron diamagnetic direction). While this tendency is maintained in the simulation results into the SOL, the experimental data show a transition to ion-diamagnetic directed flows in the near SOL for all available data sets. There are similarities in the flow shear seen by experiment and simulation. Both show a region of strongly negative slope in the $E_r \times B$ velocity in the vicinity of the LCFS. The experimental shear layer is typically located very close to the LCFS, while the shear layer in the simulated results are is few mm into the SOL.

The simulation results do not show flows consistent with radially outward electric fields in the SOL, as would be expected from a simple sheath model for plasma potentials resulting from an equipotential divertor (see section 4.3). Instead, the simulation results show $E \times B$ flows consistent with radially inward electric fields in the SOL, as in the core. This result disagrees with our measurements.

Our data allow us to address a few points made by Bonnin *et al.* First, it is suggested that the poloidal stagnation point is generally at or below the outer midplane in normal field LSN (favorable $B \times \nabla B$ direction), but is near the 'crown' of the plasma in reversed field LSN (unfavorable $B \times \nabla B$ direction). This is in agree-

ment with our experimental measurements. We do not see the radial variation of the stagnation point that is present in the simulated results; in fact, we do not generally measure flow reversal in the far SOL.

Bonnin *et al.* point to two underlying causes of the simulated flow patterns. These are neutral recycling patterns and $E_r \times B$ effects. The neutral recycling pattern is different on the HFS and LFS, contributing to the strong parallel flows observed at the HFS midplane. The particles carried by these flows return to the core via strong neutral penetration into the confined plasma near at the HFS divertor. This penetration is due to the proximity of the x-point to the inner wall and the tendency of the inner divertor to readily enter a detached state. This is consistent with frequent experimental observations of a detached inner divertor on C-Mod (see section 8.2.4).

7.1.2 Comparison with UEDGE Results

A. Pigarov *et al.* have carried out simulations with Alcator C-Mod specific conditions [14] using UEDGE, a multi-fluid edge plasma transport code. Under normal conditions, these simulations produce a 'zonal flow' pattern to close the convective flow loop on the HFS (shown in the left panel of Fig. 7-3). This flow pattern includes a flow reversal on the HFS, similar to that which is frequently observed experimentally near the outer divertor [70]. The 'zonal flow' in the simulation is characterized by a strong variation in parallel flow velocity with depth into the HFS SOL. Near-sonic parallel flow velocity toward the inner divertor in the far SOL give way to parallel flows away from the inner divertor in the near SOL. The far SOL flows are thought to be transport-driven, while the near SOL 'reversed flows' arise to maintain particle continuity in the inner divertor region. In the simulated plasma, the mutual annihilation of these counter streams produces a density peak in the SOL and causes diffusive particle transport *into* the confined plasma on the HFS. Inclusion of particle drifts in the simulation enhances the backflow, because the $E_r \times B$ and $\nabla B \times B$ drifts compete with the transport-driven flow on the HFS in favorable drift topologies.

It was recognized by Pigarov *et al.* that the zonal flow pattern pattern did not agree with the HFS measurements from C-Mod, since neither the back-flow nor the

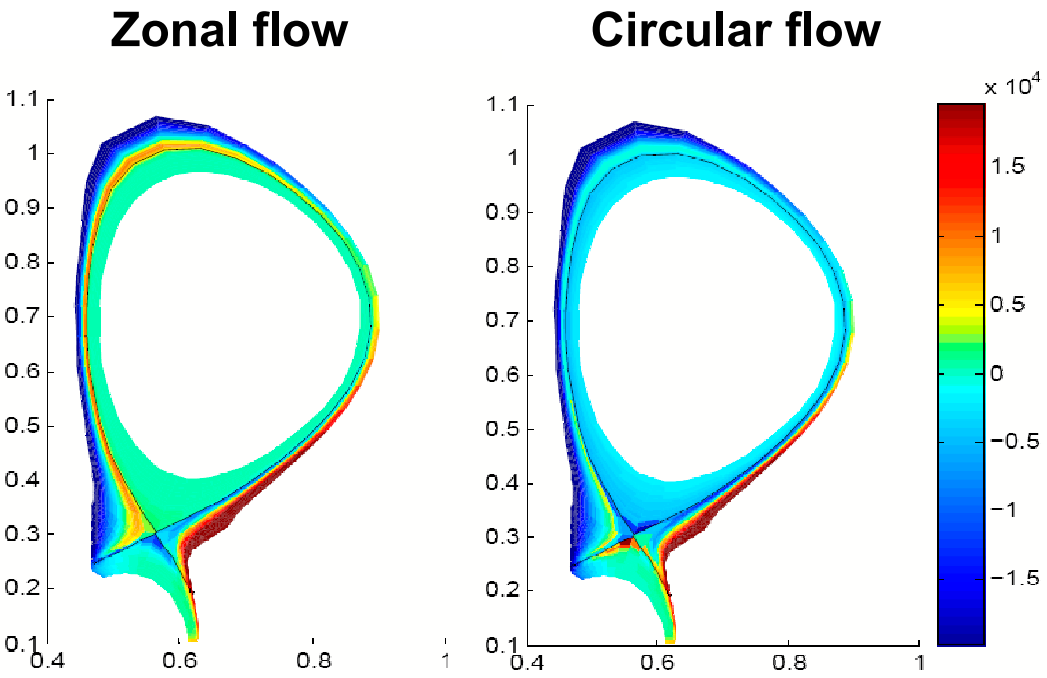

Figure 7-3: Flow patterns produced by UEDGE for Alcator C-Mod specific runs. The color contours show the flow velocity throughout the SOL with the positive velocities (red colors) indicating clockwise flow and the negative velocities (blue colors) indicating counter-clockwise flow in the poloidal cross-sections shown. The 'zonal flow' pattern on the left is characterized by flow reversal in both divertors and a density peak near the HFS midplane leading to radially inward diffusive flux. The 'circular flow' pattern on the right requires an imposed anomalous flux from the inner divertor into the private flux region with an effective velocity of 20 m/s to close the particle loop. The circular flow pattern agrees better with experimental data.

density peaking are observed experimentally. What we observe experimentally in C-Mod is a 'circular flow pattern' (shown in the right panel of Fig. 7-3), in which the parallel flow in the HFS is toward the inner divertor throughout the radial extent of the SOL. In order to change the simulated flow pattern from zonal to circular, an anomalous convective term was added which transports particles from the HFS divertor into the private flux region. The authors hypothesized that blobs similar to those observed on the LFS could be responsible for this anomalous transport. It was found in the simulation that an inward velocity of 20 m/s combined with a suppression of the drifts to 1/3 of their nominal value was required to close the particle flux loop and prevent back-flows. The reduction of the drift amplitude was justified by proposing that intermittent transport in the SOL could disrupt the normal drift mechanisms. Additionally, anomalous radial transport on the HFS was reduced to zero in the simulation to produce the desired circular flow pattern. Although this flow pattern is in good agreement with experimental measurements, there is no experimental justification for either the imposed transport from the inner divertor to private flux region or the suppression of the particle drifts, both of which were necessary to produce this agreement.

7.2 Comparison with Edge Flows Measured on Other Devices

Though no other tokamaks have installed scanning probes at the HFS midplane, scanning probes have been placed at some unique poloidal locations. JT-60U operated a scanning probe in the HFS divertor region [71], while JET has a scanning probe located near the crown of the plasma [72]. Both of these probes provide interesting cases for comparison. Each machine has the capability of measuring parallel flows using a Mach probe. In the case of JET, the probe in use was a retarding field analyzer (RFA) [73]. Both machines have carried out forward and reversed field experiments, allowing us to compare the parallel flows for favorable and unfavorable $B \times \nabla B$ drift

directions. Combining the poloidal locations available on C-Mod with those from JT60-U and JET, and assuming the SOL flow patterns in the three devices to be similar, we can construct a fairly complete poloidal picture of the parallel flows. The results are displayed in Fig. 7-4.

The first row of figure Fig. 7-4 shows the parallel flow results for favorable and unfavorable $B \times \nabla B$ drift direction for each poloidal probe location (three from C-Mod, one from JET and one from JT60-U). All of the favorable drift data are from forward field, LSN plasmas. All of the unfavorable drift data are from reversed field, LSN discharges, with the exception of the data from the WASP. There was no data available from the WASP in this condition, so the unfavorable WASP data presented in the figure come from a discharge with forward field in USN. The midplane location of the WASP allows us to make this symmetric reversal. This procedure ignores the possibility of effects due to different divertor geometries in the top and bottom of the machine, but we are comparing with devices with significantly different divertor geometries in any case.

The trend of high parallel Mach numbers towards the inner divertor on the HFS is clear, especially in the favorable drift direction. However, there are differences between the favorable and unfavorable drift cases that are not easy to unravel. In order to help us see the trends more clearly, it is useful to decompose the flows into two components. One which changes with field and current reversal and one which does not. The part that is independent of the reversal is termed the 'transport-driven' flow component based on the idea that it is caused by a pressure asymmetry driven by ballooning-like transport. It should be noted that this term is somewhat misleading, in that there could be transport which is *itself* dependent on the drift direction. Flows resulting from drift-dependent transport would not appear in the transport-driven flow component. Any flows that depend on the field direction, including those resulting from drift-dependent transport and those caused by drifts themselves are included in the 'drift-driven' flow component. This component reverses direction when the field and current are reversed.

Operating under the assumption that the transport and drift-driven flow com-

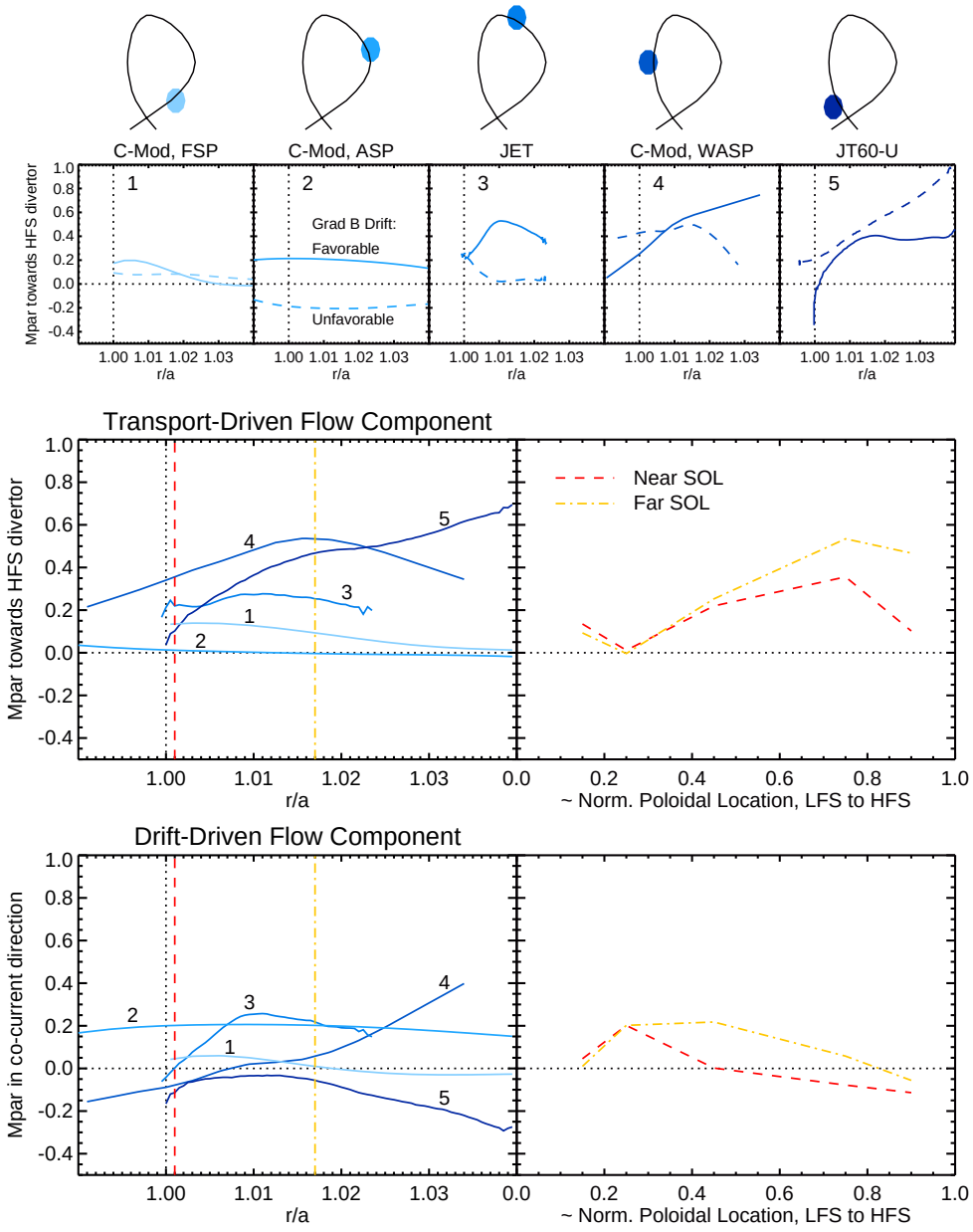

Figure 7-4: A comparison of parallel flows measured on Alcator C-Mod, JET and JT60-U at a variety of poloidal locations. The top panels show the measurements from each location for forward and reversed field. The second row, left-hand panel shows measurements from each location averaged for favorable and unfavorable drift direction, or 'transport-driven flow component'. The right-hand panel shows this flow component as a function of poloidal distance at the r/a locations indicated in the left-hand panel. The last row shows half the difference between the favorable and unfavorable parallel flow measurements, or the 'drift-driven flow component'.

ponents are linearly independent, we can compute them straightforwardly. The transport-driven component is the average of the favorable and unfavorable measurements, while the drift-driven component is half of the difference. Our convention is that the sign of the transport-driven part is positive when towards the HFS divertor, while the sign of the drift-driven part is positive when in co-current in the toroidal plane.

As expected, the transport-driven part generally increases moving from the LFS to the HFS. This trend is stronger in the far SOL. The drift-driven part decreases on the HFS, reversing sign from electron to the ion diamagnetic direction. This is consistent with a Pfirsch-Schlüter flow which compensates for ions drifting across the LCFS. Here again, the results from the FSP are in disagreement with the general trend. It has been suggested [2] that the transport-driven component may dominate the flow pattern in the far SOL while the drift-driven component dominates the near SOL. This is not consistent with the data we have assembled here.

7.3 Comparisons with Results from Other C-Mod Diagnostics

There are a few cases where the measurement capabilities of the scanning probes overlap with those of other C-Mod diagnostics. These cases provide the opportunity to bench-mark some of our results. They are explored in the following subsections.

7.3.1 Midplane Diode Array Measurements of V_{phase}

The perpendicular phase velocity measured with the probes can be compared directly to measurements taken with the midplane diode array [36] (section 2.5.2). This comparison is very appropriate since the two diagnostics look at the same radial range in the same poloidal location. This comparison verifies that our simple time-delay correlation is valid by comparing to an independent measurement. Fig. 7-5 shows the result of this comparison. The probe shows very good agreement with the diode data,

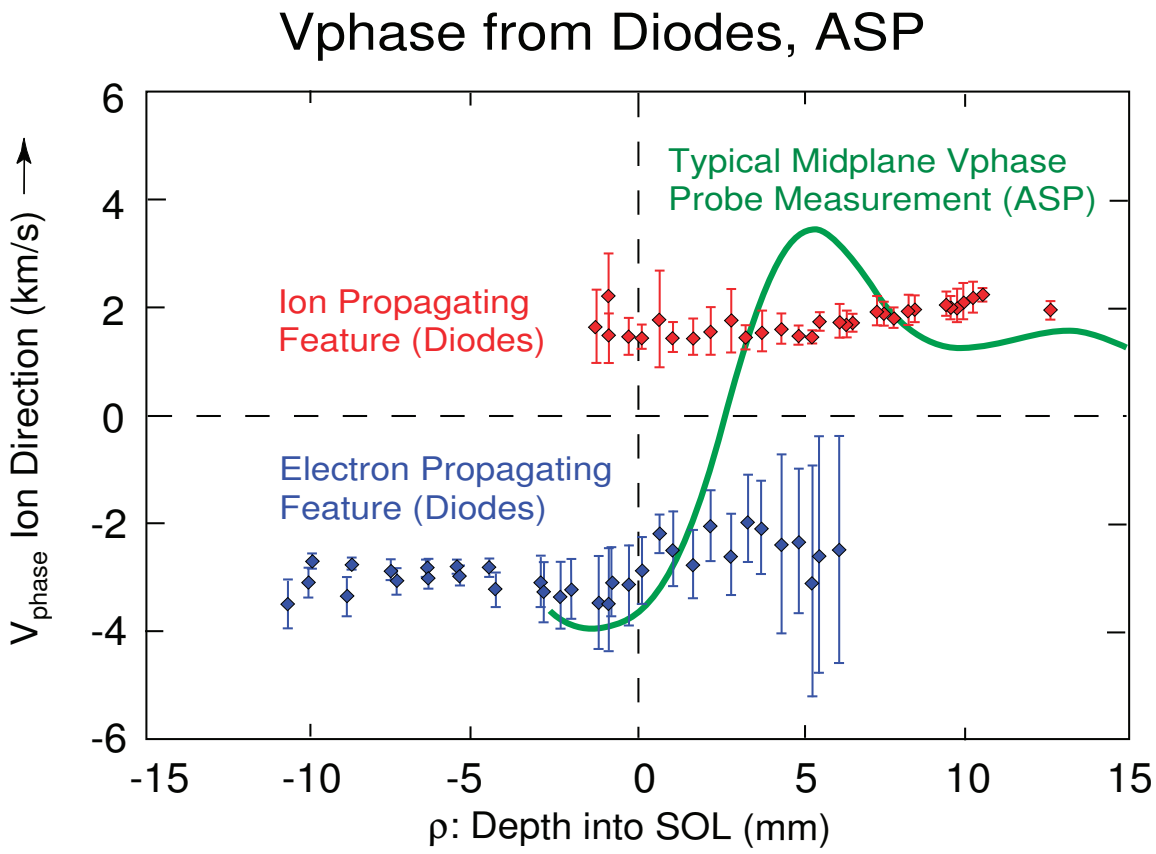

Figure 7-5: A comparison of the phase velocity measured by the probes to that measured by the midplane diode array.

reproducing the ion propagating feature in the far SOL and the electron propagating feature in the vicinity of the separatrix. However, the data illustrate the tendency of the probe's data-fitting routines to 'smear out' the features of the phase velocity profile. The probe data show a smooth transition from ion to electron direction, while the diodes measure one distinct feature slowly replacing the other, and coexisting over a range of several mm. Despite this smearing tendency of the probe analysis, we can proceed with confidence that we are able to measure the *average* phase velocity that is present in the LFS plasma with reasonable accuracy. On the HFS, where the fluctuations are much smaller and we have no direct comparison available, we must be more cautious.

7.3.2 HFS Charge Exchange Measurements of V_{tor}

The HFS 'D-β' charge exchange system [35] described in section 2.5.1 provides an ideal means to verify whether the flows observed in the HFS SOL are coupled across the separatrix into the core plasma. This diagnostic measures the distribution function of the main ions, providing temperature and velocity measurements in the HFS pedestal region. Though the radial range accessible to the CXRS system does not overlap with that of the WASP they do sample radially adjacent regions of the HFS plasma. This allows us to investigate whether the two measurements are radially continuous. Fig. 7-6 shows a comparison between WASP and CXRS measurements taken during the same discharges. The data from several shots are shown, including both forward and reversed field cases in LSN and USN.

The data show remarkable continuity across the LCFS, with the two measurements forming a nearly continuous profile of toroidal velocity. This agreement enhances our confidence in the accuracy of both diagnostic techniques. The flow reversal observed by the WASP is clearly reproduced inside the LCFS as well, where the direction of the parallel velocity has the same dependence on magnetic topology, although with reduced magnitude. This suggests that the SOL flows are the driver in this system, with momentum diffusing inward across the LCFS. It is interesting to note that unfavorable drift topologies (green and blue in Fig. 7-6) have higher observed parallel

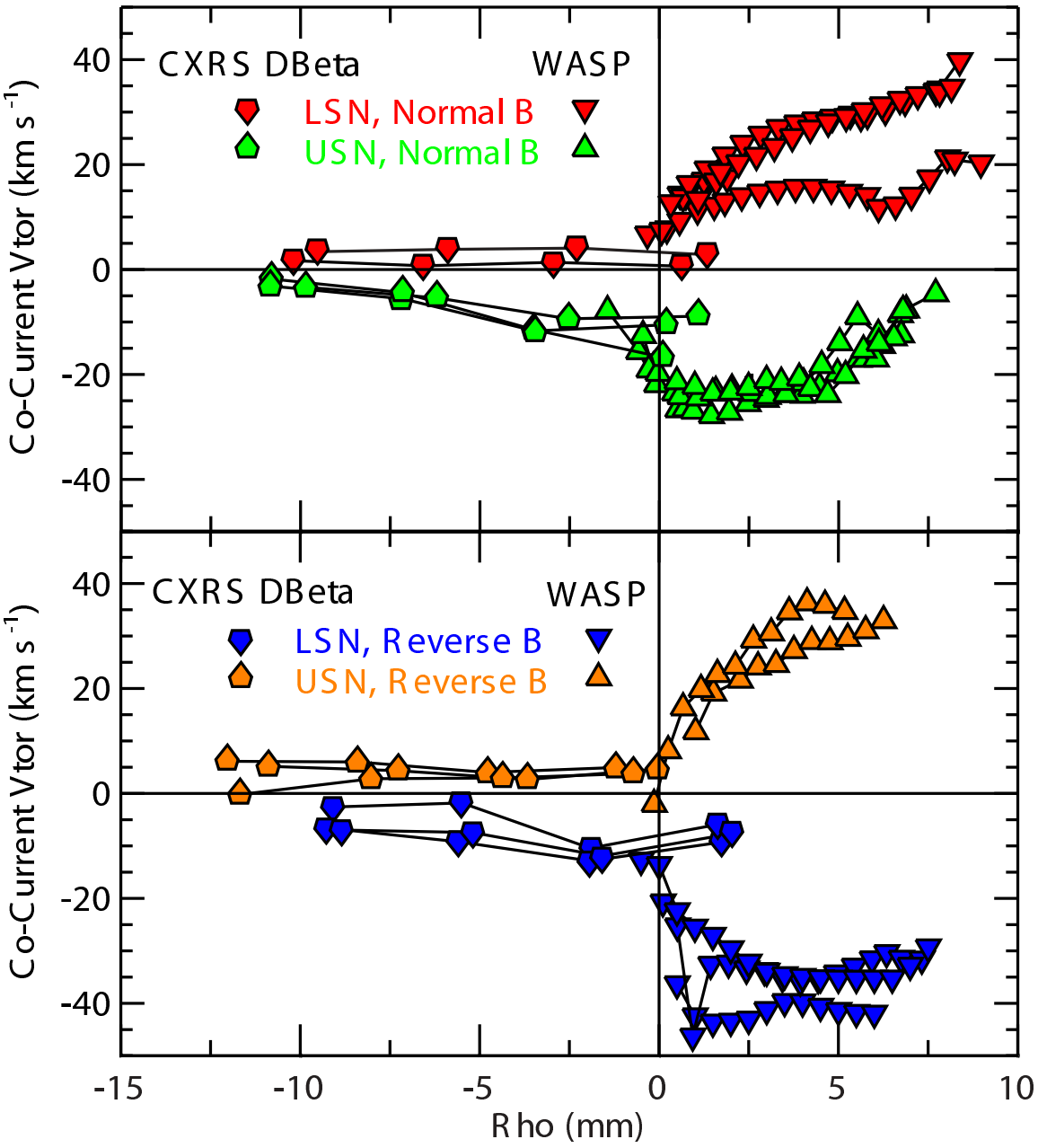

Figure 7-6: A comparison of the parallel velocity measured by the WASP to that measured with the HFS main-ion (D-β) charge exchange system for a selection of typical discharges. Based on the sign convention (co-current parallel flows = positive), the positive direction changes with field/current reversal. Thus, the two cases with favorable drift direction (red and orange) can be directly compared, as can the cases with unfavorable drift direction (green and blue).

velocity at the separatrix than for favorable topologies (red and orange in Fig. 7-6). This is observed by both the WASP and CXRS diagnostics.

Chapter 8

2-D Structure of Heat and Particle Transport

Our array of scanning probes at three poloidal locations, each measuring parallel and perpendicular flows as well as radial particle fluxes allows us to assemble a complete picture of the bulk particle motion in the edge. We can investigate how this picture changes with discharge density and topology in an attempt to address some of the unexplained sensitivity of tokamak plasmas to these variables. Because these probes also measure the plasma temperature at each poloidal location, this type of investigation can be extended to the question of edge heat flux as well. This chapter organizes this inquiry into three sections. We begin by constructing total flow vectors and identifying their symmetry with respect to field and current reversal. This allows us to identify the physics mechanisms responsible for the observed flows, and check their consistency with theoretical predictions. In the second section, we construct the net poloidal particle flux and attempt to identify the mechanism by which the particles incident on the inner divertor are returned to the core. In the third section, we model the poloidal heat flux, identifying the relative importance of convection and exploring the cause of observed in/out temperature asymmetries.

8.1 Total Flow Vector

While the toroidal velocity is generally well characterized by measurements of parallel flow alone, techniques for the measurement of the cross-field flow component are required for a complete understanding of the poloidal flow picture. As discussed in chapter 5, it seems that the $E_r \times B$ method of measuring perpendicular flows is more reliable than the Gundestrup method. We will therefore use the measurements of the plasma potential to provide the perpendicular components of our poloidal flow picture.

8.1.1 Net Poloidal Flow

Fig 8-1 shows the poloidal components of both the parallel and perpendicular flow velocities, and the resulting net poloidal flow velocity. These data are shown for both the HFS and LFS midplane scanning probes in favorable and unfavorable $B \times \nabla B$ drift directions. Since there are two ways to get favorable topologies (LSN, normal field and USN, reversed field) and two ways to get unfavorable topologies (USN, normal field and LSN, reversed field), there are four different possible favorable/unfavorable comparisons which could be made. Note that without external momentum input and with the exception of differences in divertor geometry, the two favorable cases are theoretically equivalent, as are the two unfavorable cases. Displayed in this plot are the favorable and unfavorable cases with the most available data (those in normal field). The sign convention used is that positive flows are directed towards the inner divertor. These curves were produced by averaging data from many discharges over the '05-'08 run campaigns, all with standard field ($\sim$5.4 T) and current ($\sim$0.8 MA), for discharges with a range of line-integrated densities; $0.5 <$ NL04 $[10^{20}\ \mathrm{m}^{-2}] < 1.0$. We see a complex behavior, which is different for the two poloidal locations and different for the two drift directions. In order to understand this picture, we will examine the symmetries in the data to sort out the controlling physics.

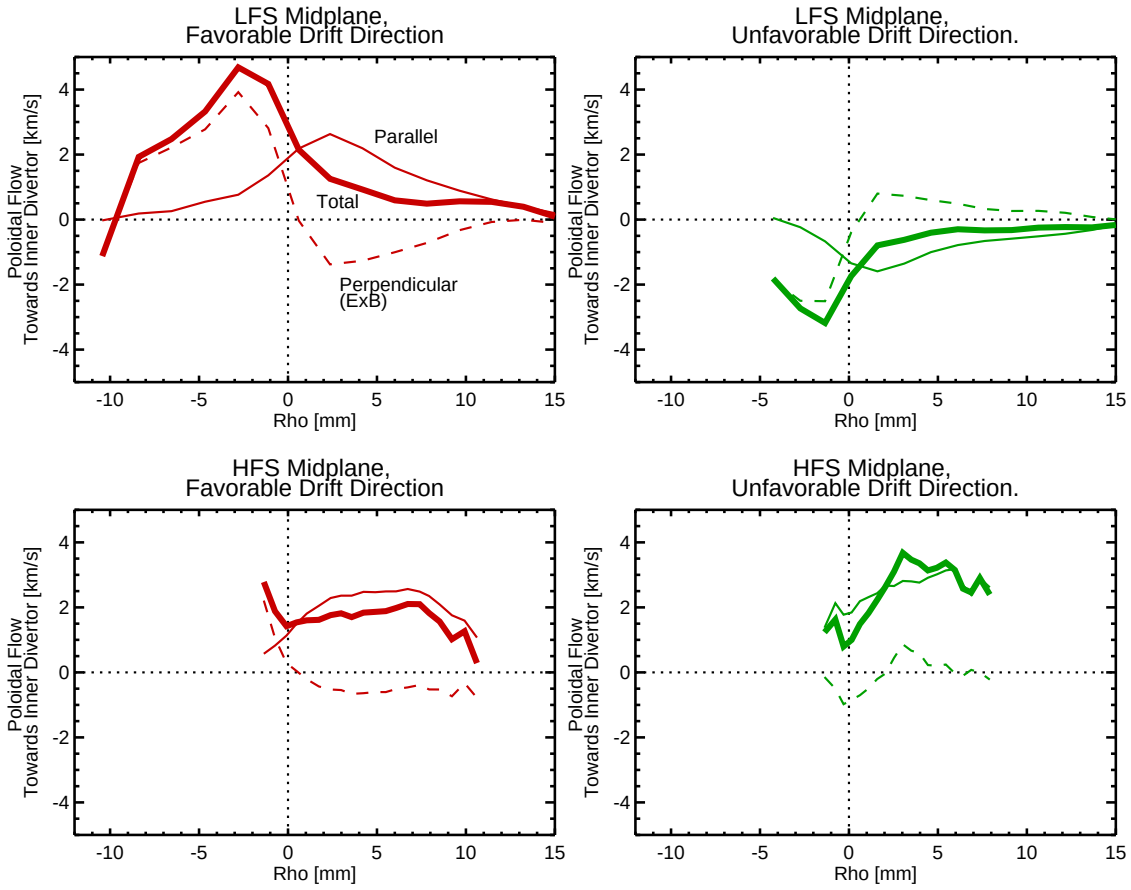

Figure 8-1: Net poloidal flow velocity. The top row shows the measurements made with the ASP near the LFS midplane. The bottom row shows data taken with the WASP on the HFS. The left column is data from LSN in normal field (favorable $B \times \nabla B$ direction) while the right column is from USN in normal field (unfavorable $B \times \nabla B$ direction). The thick lines show the total poloidal velocity which is the sum of the poloidal components of the parallel (thin line) and perpendicular (thin, dashed line) flow measurements.

	Parallel	Perpendicular
Symmetric	Pfirsch-Schlüter Flow $E_r \times B$ Rotation	$E_r \times B$ Drift Diamagnetic Drift
Asymmetric	Transport-Driven $\nabla_{\|} P$	Transport-Driven Toroidal Rotation?

Table 8.1: Summary of the types of physics that might lead to various measured flow components

8.1.2 Transport and Drift-Driven Components

Measurements of both the parallel and perpendicular flows allow us to determine the relative roles played by different physics mechanisms in the poloidal redistribution of particles and energy. So-called 'transport-driven' flows are thought to be the result of poloidal transport asymmetries causing poloidal pressure gradients, which in turn drive parallel flows. These should be dependent only on which divertor is in use, that is, whether the magnetic topology is LSN or USN. This effect is not expected to drive perpendicular flows. In contrast to the transport-driven flows, 'drift-driven' flows depend only on the direction of B and therefore change with field direction, and not with magnetic topology. Perpendicular drift-driven flows include diamagnetic flows and $E_r \times B$ flows. Drift-driven flows in the parallel direction can arise due to Pfirsch-Schlüter effects [74] (see section 8.1.3). Drift-driven parallel flows can also arise from the tendency of the plasma to flow in the parallel direction such that the poloidal component of the $E_r \times B$ drift is canceled, resulting in pure toroidal rotation. In a toroidal reference frame rotating with the plasma, the radial electric field is zero. These physics mechanisms and their expected symmetry properties are summarized in table 8.1.

Using the parallel and perpendicular flow measurements made during field and topology reversal experiments, we can uniquely identify flows resulting from the four quadrants of table 8.1. This technique has been used in [61] in the *parallel* direction to distinguish between transport-driven flows and drift-driven flows, but has not previously been applied to both parallel and perpendicular components.

Fig. 8-2 shows the projections of the the measured parallel and perpendicular flows

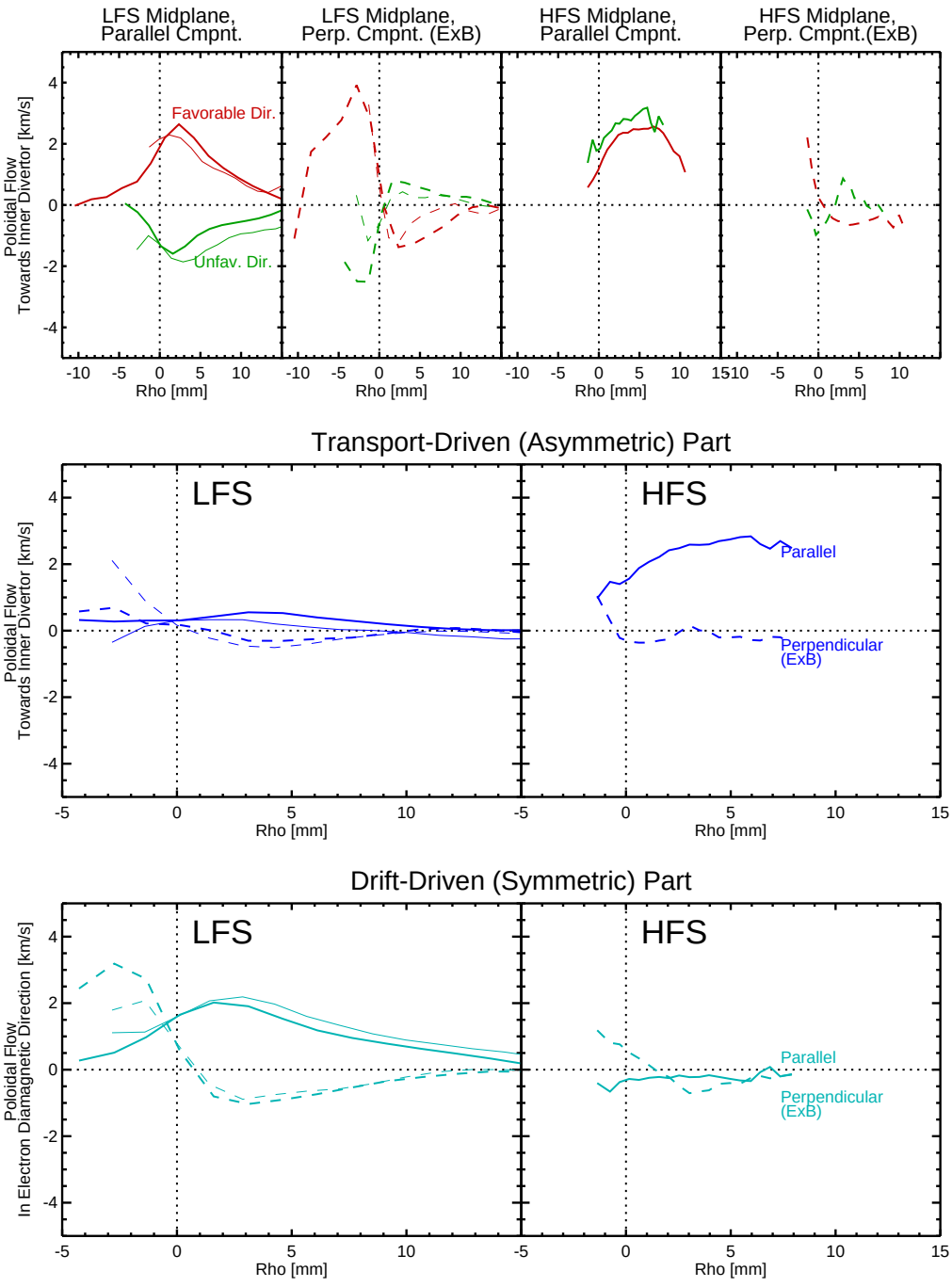

Figure 8-2: Measured parallel and perpendicular components of the poloidal flow are shown in the first row. Each plot shows the data for favorable (red) and unfavorable (green) $B \times \nabla B$ direction. On the LFS, thick lines (thin) lines show data from normal (reversed) field. The second and third rows show the symmetric and asymmetric components of the flow according to Eqn. 8.2. Here, solid (dashed) lines represent the parallel (perpendicular) components of the flow. Thick (thin) lines show data from topology reversal in normal field direction (field reversal in LSN)

in the poloidal direction. Here, unlike in Fig. 8-1 we have isolated the parallel and perpendicular components onto separate plots, and shown traces for the favorable and unfavorable drift directions together. Again, we show favorable/unfavorable results based on LSN/USN magnetic topologies in normal field (thick curves) but now also show those based on USN/LSN topologies in reversed field (thin curves). These results are shown for both the LFS and HFS scanning probes in the first row of plots in Fig. 8-2. We again use a the sign convention that positive flow is towards the inner divertor. This means that the coordinate system flips along with the x-point when we compare USN vs. LSN. Following Catto and Simakov [75, 76], the measured flows can be decomposed into 'symmetric' and 'asymmetric' parts. Since our coordinate system is reversed with the magnetic topology, our situation is equivalent to case i) from [75, 76] (field reversal). This is the most convenient case to work with because it neatly isolates the symmetric and asymmetric flow components, and does not require the decomposition of the poloidal field into symmetric and asymmetric components. It can also be directly compared to constant-topology field and current reversal experiments. In this case, the symmetric (field-dependent) part corresponds to a flow which is drift-driven, while the asymmetric (field-independent) part corresponds to a flow which is transport-driven.

In this space, the symmetric and asymmetric components are given by:

$$v_{asym} = (v_{fav} + v_{unfav})/2 \tag{8.1}$$

$$v_{sym} = (v_{fav} - v_{unfav})/2 \tag{8.2}$$

These are shown in the second and third rows of Fig. 8-2 respectively. These two components can be produced from any pair of favorable and unfavorable conditions from the first row. Displayed in the second and third rows for the LFS are the results of two pairings: the thick curves show the result of topology reversal in normal field, while the thin curves show the result of field reversal in LSN. On the HFS, no reversed field data are available, so only the topology reversal in normal field is shown.

The asymmetric component is plotted in the same space as the first row (with the positive direction towards the inner divertor), but the symmetric component changes direction in unfavorable conditions so that the parallel component is always in the electron diamagnetic direction. It is therefore plotted in a space with the diamagnetic direction positive. This is the same direction as the asymmetric component for the favorable cases, but opposite for the unfavorable cases. Therefore, the favorable (unfavorable) traces in the first row can be obtained by taking $v_{asym} + (-)\ v_{sym}$ from the second and third rows.

We can immediately see that the thick and thin LFS curves overlay very well, which proves the rough equivalence of the field and topology reversal experiments. That is, we cannot detect any effects due to asymmetric divertor geometries or magnetic topologies or the fact that the probes are not located precisely on the midplane. The only significant difference appears between favorable and unfavorable drift direction.

The result of these manipulations is that we have extracted the symmetric and asymmetric parts of the parallel and perpendicular contributions to the poloidal flow. These components are due to the different physics mechanisms summarized in table 8.1. We can now directly compare their magnitudes. The zeroth order result on the LFS is that the dominant term in the SOL is a symmetric, parallel (drift-driven) component in the electron diamagnetic direction. On the HFS, the largest contributor to the poloidal flow is an asymmetric, parallel (transport-driven) flow component towards the inner divertor. Since the perpendicular contributions are smaller, these findings are in agreement with the understanding that was arrived at from measuring parallel flows. However, the perpendicular contributions, while smaller, are not negligible.

We notice that in the LFS SOL, for both the parallel and perpendicular components, the drift-driven and transport-driven components sum constructively for favorable drift direction and destructively for unfavorable drift direction. This results in the generally larger poloidal flow magnitudes and shears measured in favorable drift direction compared to unfavorable drift direction, and may be a factor influencing

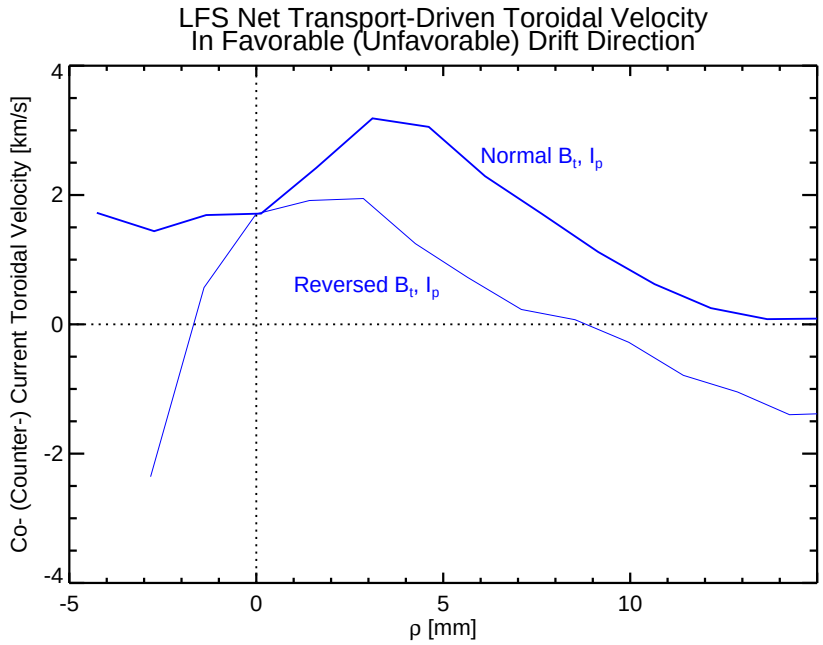

Figure 8-3: Transport driven component of toroidal rotation. The LFS transport-driven flow consists of a nearly purely toroidal velocity. Its magnitude is shown as a function of the flux-coordinate ρ (depth into the SOL at the LFS midplane). The thick (thin) curve is obtained from discharges with normal (reversed) field and current direction. The transport-driven rotation is in the co-current (counter-current) direction in discharges with favorable (unfavorable) $B \times \nabla B$ drift direction.

transport levels through flow shear.

It is interesting to note that the transport-driven flows measured on the LFS, though small, amount to a nearly perfect toroidal rotation. This can be seen by noticing that the poloidal components are approximately equal and opposite, resulting in a net transport-driven poloidal flow which is zero. The corresponding net transport-driven toroidal velocity has a maximum of about 3 km/s and is co-current in favorable drift direction and counter-current in unfavorable drift direction (see Fig. 8-3). This toroidal flow is consistent with the edge-core momentum coupling theory that has emerged and was explored in section 6.1.4. In this scenario, core rotation is caused by transport-driven flows on the HFS, and then couples back to the LFS SOL through ballooning transport; the particles pass into the LFS SOL with a memory of their core toroidal rotation.

Measurements inside the LCFS on the LFS indicate that symmetric (drift-driven)

perpendicular flows are the dominant contributor to poloidal flows there. Moreover, this flow component reverses direction from ion to electron diamagnetic direction near the LCFS. This agrees with the simple picture of the dominant physics mechanisms on open vs. closed field lines. Radially outward electric fields are normally expected in the SOL as a result of sheath drops responding to the radial temperature gradient. Inside the LCFS, there are different physics setting the plasma potentials. At this location, the equilibrium plasma must have a radially inward E_r such that $E_r \times B$ flows balance the ion diamagnetic drift. Under these conditions, the Pfirsch-Schlüter ion flow goes to zero, minimizing ion pressure variations from appearing on a flux surface, which would otherwise drive current across the LCFS. The necessary Pfirsch-Schlüter currents are then carried only by electrons. Our probe measurements support these simple theories.

The WASP results show the asymmetric (transport-driven) parallel flow component to be the dominant contributor to poloidal flow on the HFS. All of the other poloidal flow components are significantly smaller. The symmetric (drift-driven) perpendicular component shows a slight tendency toward the electron diamagnetic direction in the vicinity of the separatrix and is slightly ion diamagnetic directed elsewhere. This is reminiscent of the behavior on the LFS but much weaker.

The transport-driven parallel flows on the HFS are observed to decrease in magnitude as the LCFS is approached. This is consistent with the theory because we expect the LFS transport to be able to build up stronger parallel pressure gradients in the far SOL where the difference between the the 'natural' HFS pressure (that observed in balanced double-null) and the 'filled in' pressure is the greatest (see Fig. 6-1).

8.1.3 $E_r \times B$ Toroidal Rotation and Pfirsch-Schlüter Flows

Plasma drifts and drift-driven flows in the tokamak geometry are well described by theory. Having isolated the drift-driven flow components from the anomalous transport-driven components, we can now attempt to verify that our data are consistent with the theoretical prescription. If so, we can report the drift driven measurements in a simplified way. We can also proceed with confidence that our flow

measurements are reliable and that the transport-driven component is correctly characterized.

Before beginning, it is worth noting that these drifts under consideration are the result of gradients of flux functions: $p(\psi)$, $\Phi(\psi)$. This means that the expected drift direction is strictly within a flux surface. To avoid confusion, we generally use the term 'perpendicular' ($v_\perp$) to refer to vectors within a flux surface perpendicular to the field; radial (v_r) refers to vectors perpendicular to the flux surfaces. Drift-driven flows in the radial direction are taken to be negligible.

It is not intuitively obvious why particle drifts should lead to parallel flows. After all, particle drifts themselves constitute fluid motions perpendicular to the magnetic field. To explain how parallel flow can be connected to perpendicular drifts in toroidal geometry, we consider the source-free ion continuity equation: $\nabla \cdot n\vec{v} = 0$. By formulating this problem not in a parallel-perpendicular coordinate system, but in toroidal-poloidal system, the divergence of the flux density can be readily evaluated. We begin by neglecting radial drifts ($v_r = 0$), so the radial divergence of the drift-driven flow is zero. The toroidal divergence is zero by symmetry ($v_\phi = v_\phi(r, \theta)$). This means that the poloidal divergence of drift-driven flows must also be zero:

$$\nabla \cdot n\vec{v}_d = 0 = \nabla_r n v_r + \nabla_\phi n v_\phi + \nabla_\theta n v_\theta = \nabla_\theta n v_\theta \tag{8.3}$$

Since $\nabla \cdot \vec{B}_\theta = 0$, this can be expressed simply as:

$$\left.\frac{n v_\theta}{B_\theta}\right|_\rho = C(\rho) \tag{8.4}$$

Where C is a constant on a flux surface, labeled by its distance into the SOL at the outer midplane (ρ). Therefore, if the plasma drifts resulting from the local gradients cause poloidal flows that do not satisfy $nv_\theta/B_\theta = C$ then parallel flows (which have a finite poloidal component) must arise so that the *net* poloidal flow does satisfy $nv_\theta/B_\theta = C$. These parallel flows are generally referred to as Pfirsch-Schlüter flows after the original discoverers of parallel currents that arise in toroidal geometry [74]. The term 'Pfirsch-Schlüter' is often used to refer to special cases of parallel

currents or flows induced by toroidal geometry, so some clarification of our definition is appropriate.

The typical derivation [4] of Pfirsch-Schlüter effects is concerned with *current* continuity rather than ion fluid continuity. The derivation replaces nv_θ with J_θ in Eqn. 8.4. The Pfirsch-Schlüter current is defined as separate from inductively-driven parallel currents. The derivation next assumes that the parallel resistivity is a flux function and invokes Faraday's law in steady state, $\oint E \cdot d\theta = 0$. Taken together, these conditions mean that the average poloidal current is zero. Since B_θ is always finite, $\langle J_\theta \rangle = 0$ means $J_\theta / B_\theta = C$ can only be satisfied if J_θ vanishes identically and $C = 0$. Thus, the parallel and perpendicular components of J_θ must always have equal and opposite poloidal components. The perpendicular current is determined by the drifts, and the resulting $J_\parallel = J_\perp B_\phi / B_\theta$ is the Pfirsch-Schlüter current. For the case of *flows* however, there is no reason the flow pattern cannot have net circulation. Therefore, C is not generally zero and nv_θ and v_{PS} may have finite average values.

We can greatly simplify our treatment by making use of the assumption that ϕ is constant on a flux surface. In this case, it is always possible to move into a rotating reference frame where the electric field is zero:

$$\omega = \frac{v_{rot}}{R} = \frac{E_r}{RB_\theta} = \frac{-\frac{\partial \Phi_p}{\partial r}}{R\frac{1}{2\pi R}\frac{\partial \psi}{\partial r}} = -2\pi \frac{\partial \Phi_p}{\partial \psi} \tag{8.5}$$

Here, Φ_p is the plasma potential and ψ is the poloidal flux. ω, though independent of θ, can vary with flux surface. Having identified the $E_r \times B$ toroidal rotation, we can then calculate the Pfirsch-Schlüter flow in the rotating frame. The constant C is unchanged by this transformation. The Pfirsch-Schlüter flow is then clearly identified as the parallel flow as measured in the rotational frame. A vector illustration of this process is shown in Fig. 8-4.

Using our measurements of the drift-driven parallel flow, the drift-driven $E_r \times B$ flow and the pressure gradients, we can determine the total drift-driven fluid velocity at both the HFS and LFS midplanes. At each location, we can calculate the two constants: $C(\rho)$ and $\omega(\rho)$ as a function of flux surface coordinate. The constants

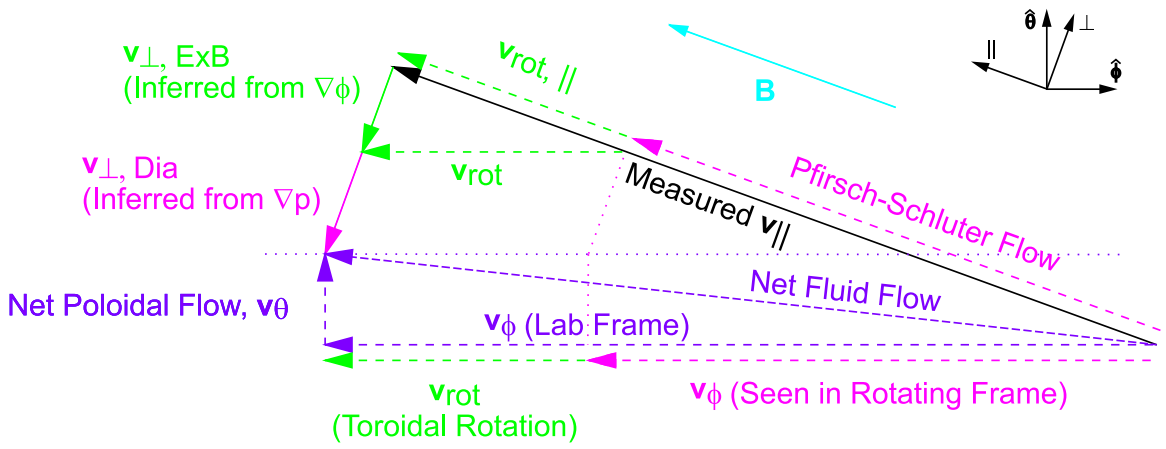

Figure 8-4: An illustration of the decomposition of flows into various components is shown. In particular, the components of the parallel flow identified as 'Pfirsch-Schlüter flows' and 'toroidal rotation' are identified.

should be independent of poloidal location, allowing us to perform a consistency check on our measurements. We can also unambiguously decompose the measured parallel flow into parts which represent the toroidal rotation and Pfirsch-Schlüter flow. The primary caveat in this calculation is that the pressure gradients are inferred from electron temperatures, not from ion temperatures. The calculation of the diamagnetic drift is thus incorrect to the extent which the electron and ion temperatures are not equilibrated. However, the disagreement in electron and ion temperatures is expected to be small due to the high collisionality of the C-Mod edge. This procedure is applied to the drift driven flow-components determined from topology reversal in normal field that were shown in Fig. 8-2. These discharges had $0.5 < \mathrm{NL04}\ [10^{20} m^{-2}] < 1.0$. The result is shown in Fig. 8-5.

Several important observations can be made from the data shown in Fig. 8-5.

1. ω is well matched between LFS and HFS data. This result shows that the measured potentials are flux functions. The observed $E_r \times B$ toroidal rotation peaks at ~10 km/s in the co-current direction near ρ = 3 mm in the SOL, reverses direction near the LCFS and reaches ~20 km/s in the counter-current direction near ρ = -2 mm in the confined plasma.

2. $C = nv_\theta/B_\theta$ is conserved between the LFS and HFS locations, indicating that

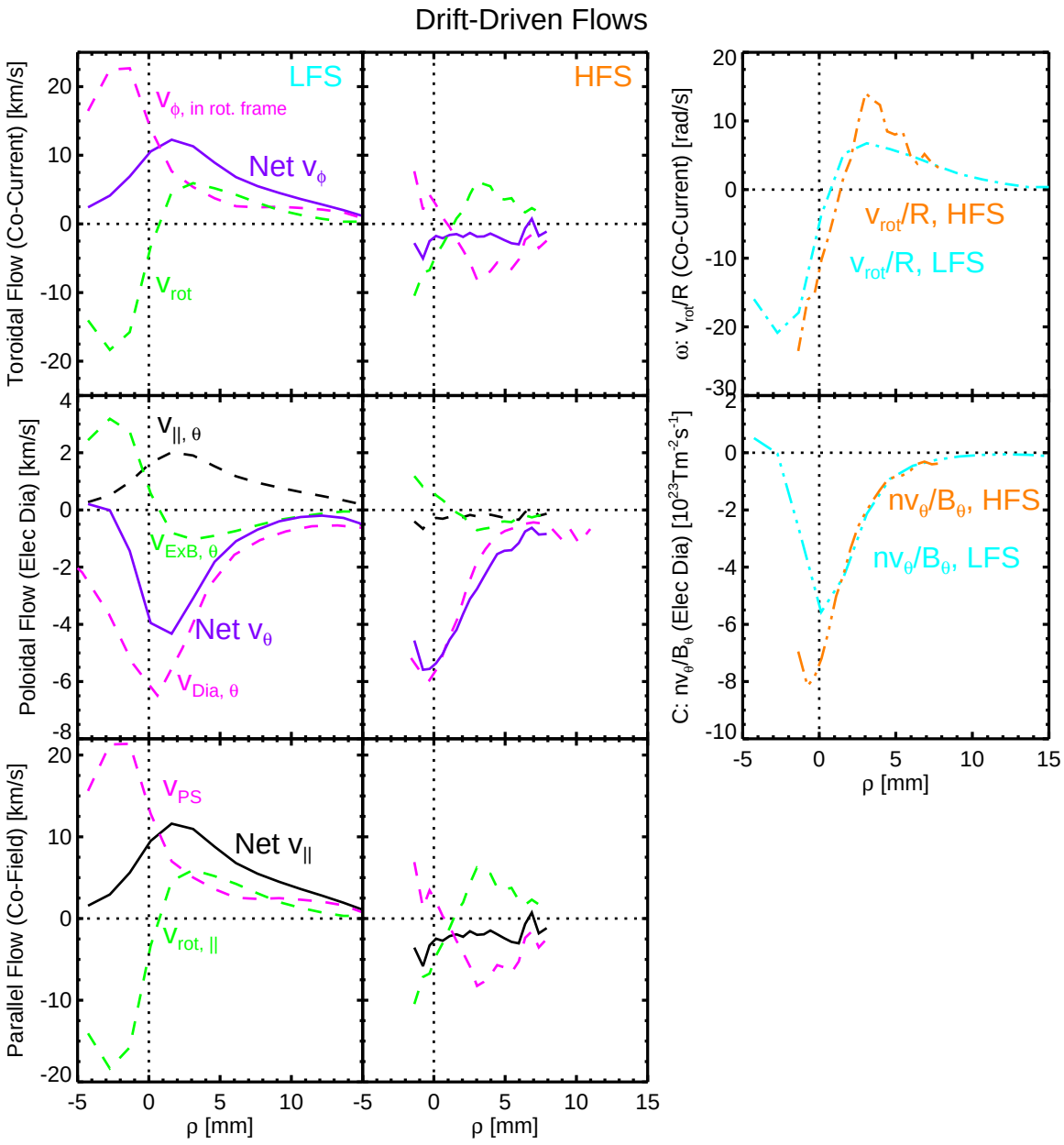

Figure 8-5: The toroidal and poloidal components of the drift-driven flows from Fig. 8-2 are shown in the top two rows of plots. The components are determined according the the vector manipulations illustrated in Fig. 8-4. The first column shows the LFS location and the second column shows the HFS location. The third column shows the constants ω and C at these two locations. Both are observed to be independent of poloidal location, as expected for a divergence-free flow with potential and pressure constant on a flux surface. The third row shows the components of measured parallel flow.

we do observe a divergence-free flow pattern. This is true despite different radial structure of the various components at the two poloidal locations. This result is an indication that the flow components are measured correctly with the methods used here.

3. The largest contributor to the net poloidal fluid velocity is the ion diamagnetic velocity, but the parallel flow and the $E_r \times B$ flow contribute significantly as well. The resultant v_θ is peaked near the LCFS in the ion diamagnetic direction and has a maximum value of $\sim$ 4 km/s. v_θ reaches zero in the core around $\rho = -3$ mm and in the far SOL around $\rho = 10$ mm. This is confirmation that the diamagnetic and $E_r \times B$ drifts cancel in the core, as expected.

4. The measured drift-driven $v_\parallel$ in the LFS SOL has similar contributions from Pfirsch-Schlüter flow and $E_r \times B$ toroidal rotation. In the core and the HFS SOL, the two components tend to cancel. Note that in the far SOL where the net v_θ is near zero, the familiar $\cos\theta$ behavior of the *current* is recovered; opposite flows are observed on the HFS and LFS. Near the LCFS however, where v_θ is finite, the Pfirsch-Schlüter flow is in the same direction at both locations.

Others have attempted to explain LFS parallel flow measurements in terms of drift-driven flows. Pitts *et al.* [77] measured parallel flow on TCV for forward and reversed field cases at the LFS midplane. They found the parallel flow was dominantly drift-driven, consistent with the data shown here. However, their measured drift-driven flows were consistent with a Pfirsch-Schlüter calculation that ignored the possibility of net poloidal circulation. These results were obtained from measurements 10 mm into the SOL. C-Mod has similar dimensions to TCV, so a comparison with our data at $\rho = 10$ mm is reasonable. Our results show very little poloidal circulation at that location, in agreement with the TCV data.

We have showed that the poloidal variation of the drift-driven flows is such that these flows are divergenceless, consistent with the expectation that drift-driven flows should not be driven by radial divergence. The magnitude of the various drift-driven

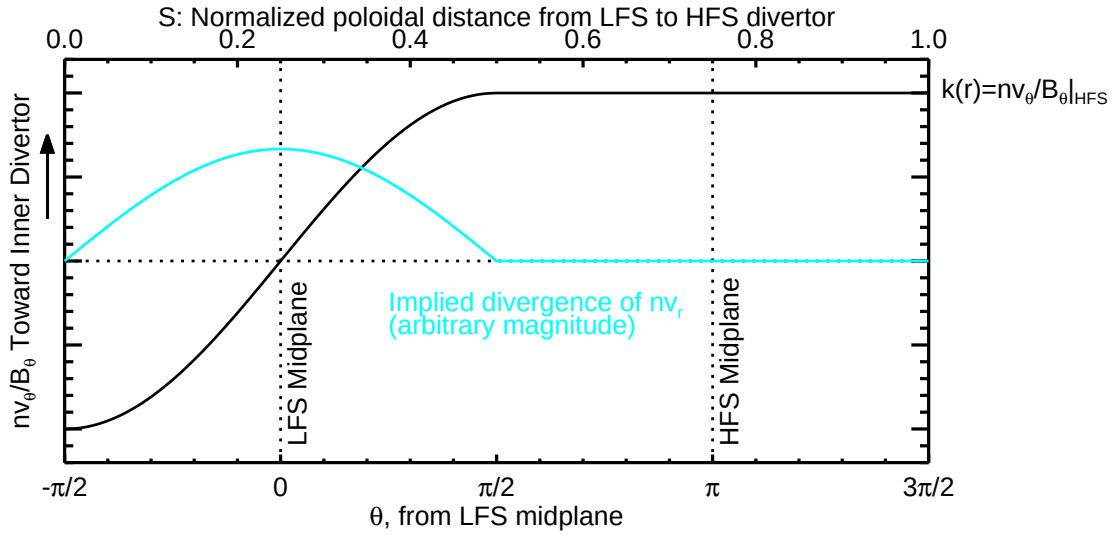

Figure 8-6: The assumed poloidal functional form of the transport-driven poloidal flows. The implied divergence of the radial transport is also shown.

components, including Pfirsch-Schlüter flows and toroidal rotation have been presented as a function of ρ. We next proceed to a discussion of the other half of the flow picture, that of transport-driven flows.

8.1.4 Transport-Driven Flow Observations

While we have now confirmed that the poloidal divergence of the drift-driven flow component is zero, this is not true of the transport-driven component. This is clear both by inspection of Fig. 8-2 (where approximately zero net poloidal flow is observed on the LFS compared to $\sim$ 2 km/s steady flow on the HFS) and by the definition of transport-driven flow; these flows are assumed to exist because of a finite divergence of the radial particle flux, which is equal and opposite to that of the poloidal flux. If we make some simplifying assumptions about the poloidal distribution of the radial transport, we can determine the form of the radial particle flux to within an integration constant.

We begin by assuming all of the transport is localized to the LFS. This assumption is based on our own observations indicating ballooning-like transport asymmetry (see section 6.1), as well as similar observations by others. Experiments on Tore Supra

by Gunn *et al.* [78] showed strong transport-driven parallel flows resulting from a ballooning-like particle source localized within a 30° sector at the LFS midplane. We therefore take the poloidal transport-driven particle flux, nv_θ/B_θ, to be a represented by a sine function on the LFS, and to be constant on the HFS, consistent with a source localized around the LFS midplane:

$$\frac{nv_\theta}{B_\theta} = \begin{cases} k(r)\sin\theta & (|\theta| < \frac{\pi}{2}) \\ k(r) & (|\theta| \geq \frac{\pi}{2}) \end{cases} \tag{8.6}$$

Here, r is the location in minor radius at the LFS midplane and θ is the poloidal angle measured from the LFS midplane. The choice of the sine function is consistent with the measurement of nearly zero poloidal particle flux near the LFS midplane. The amplitude of the sine, $k(r)$, is the value of nv_θ/B_θ measured at the HFS midplane. This situation is illustrated in Fig. 8-6.[1] Using this assumption for the form of the radial transport and a simplified geometry, we can express the LFS midplane radial particle flux as a function of the measured HFS midplane poloidal particle flux. This procedure is detailed in appendix A. The result for C-Mod is:

$$nv_r|_{LFS} = 2.7 \int_{wall}^{r} \mathrm{d}r \; nv_\theta|_{HFS} + nv_r|_{wall} \tag{8.7}$$

We have assumed in this calculation that the local particle source in the SOL is zero. This assumption is inconsistent with main chamber recycling given that the neutral mean free path in C-Mod is usually smaller than the SOL width. In reality, there is an additional divergence of the radial particle flux due to ionization of neutrals emitted from main chamber recycling. This balances the plasma flux to the wall $nv_r|_{wall}$. Therefore, we can ignore this local recycling loop, and justify our assumption of no local particle source by taking $nv_r|_{wall} = 0$. The result will be the part of the radial flux that is balanced by transport driven flows, and not the part balanced by local

[1] Note that there is a discontinutity at $\theta = -\pi/2$, where we place the x-point in this calculation. This requires that the particles are returned to the core by some divertor physics. In fact, our boundary conditions are at $\theta = 0$ and $\theta = \pi$ so the calculation is not valid outside this range in any case.

recycling. Unfortunately, our measurement of nv_θ on the HFS does not extend all the way to the LFS wall in ρ-space. Some extrapolation is necessary to determine what our integration constant should be at the maximum measured radius to produce zero flux to the LFS limiter.

Figure 8-7 shows the result of applying Eqn. 8.7 to the HFS data. The top row shows the transport-driven poloidal flow data from Fig. 8-2. The parallel and perpendicular components are added to produce the total poloidal velocity. On the LFS, we see that the net poloidal flow at the LFS is indeed very close to zero, especially in the SOL. On the HFS, the velocity is substantial with a value of ~ 2 km/s toward the inner divertor. The second row shows LFS and HFS density measurements, and the resultant poloidal particle on the HFS. Eqn. 8.7 is then applied to produce the plot in the bottom left panel. Three different results of the integration are shown, with different selections for the boundary condition at the maximum radius of the available data. The solid trace shows the result when a choice is made that extrapolates to zero radial flux at the location of the LFS limiter. This assumption is appropriate because the calculated flux *does not* include any radial particle flux due to local recycling, which would be added to the result shown in a complete accounting. The LFS density can then be divided out to produce a radial velocity, which is shown in the bottom right panel for the three boundary conditions. The solid curve and its extrapolation agree well with the results obtained from measurements of fluctuation-induced radial velocities (see section 8-19). Excess particle flux over the measured value could be accounted for by main-chamber recycling, as previously mentioned. It seems likely however, that much of the observed radial velocity at the LCFS on the LFS can be counted as necessary to supply the poloidal transport-driven flows on the HFS.

This result shows that our decomposition of measured flows into transport and drift-driven parts produces a story which is consistent with other observations. As with our analysis of the drift-driven flow components, the agreement observed here lends credibility both to the measurement and analysis techniques in use, and to the interpretation of the observed flow pattern as a sum of drift-driven and transport-

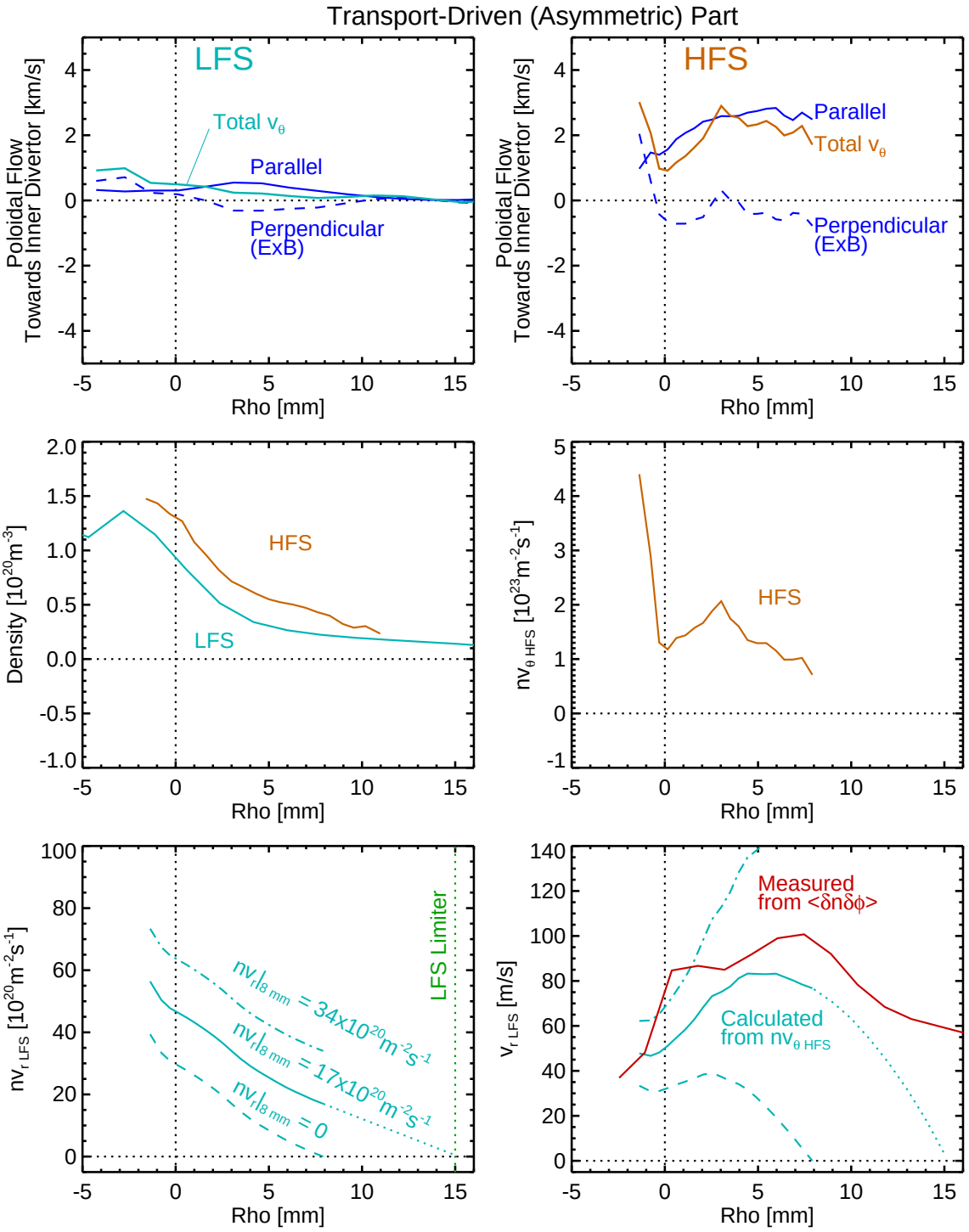

Figure 8-7: Calculation of the ballooning LFS particle flux from the observed HFS poloidal particle flux.

driven flow components. Having identified the likely source for the HFS poloidal particle fluxes, we next turn to the question of how this flux terminates near the HFS divertor, and by what mechanism the particles are returned to the core.

8.2 Poloidal Particle Balance

With regard to particle balance, the most important question to answer is the direction and magnitude of the net poloidal particle flux. This bears directly on questions of divertor erosion and redeposition as well as tritium co-deposition and tritium inventory in a power reactor. The analysis of section 8.1.4 has already hinted at the general answer to this question: there is net particle flow toward the inner divertor which is balanced on the LFS by a divergence of the radial particle flux due to ballooning transport. However, this only half of the picture. We must turn our attention to the question of what happens to the particles once they arrive at the inner divertor. In steady state, there must be a mechanism for returning these particles to the core, such that they can be lost again by ballooning transport on the LFS. Candidates for this mechanism are:

1. A substantial fraction of neutrals recycling from the inner divertor are able to penetrate directly into the core or private flux region without being ionized locally.

2. The inner divertor is detached, resulting in an area of volume recombination which allows many particles to return to the core without ever reaching the divertor.

3. There is a significant particle pinch between the HFS midplane and the inner divertor which transports particles from the HFS SOL into the core or private flux region.

We will have to examine the state of the inner divertor to be able to address the first two possibilities. We will also need to experimentally investigate the possibility of a

HFS pinch. However, our first task is to determine the particle flux approaching the inner divertor. This will establish the magnitude of the particle flux which must be accounted for by whatever mechanism closes the particle loop. A careful calculation of the net (transport *and* drift-driven) poloidal particle flux passing the WASP at the HFS midplane will frame the problem.

8.2.1 Computation of Poloidal Particle Flux

The net poloidal particle flux can be calculated at the location of each scanning probe using the parallel and perpendicular flow information and the local density measurement. In doing this calculation we must choose which of the poloidal flow mechanisms to include in our calculation. The question of whether diamagnetic drifts should be included is not trivial; while this drift does represent a fluid particle flux, the guiding centers of the particle orbits do not actually move. This question has been addressed previously by Chankin and Stangeby [79]. Their conclusion was that diamagnetic drifts are not actually collected at the divertor plate, but are identically divergence free and self terminating even in the vicinity of the divertor surfaces. The mechanism for this is parallel pressure gradients in the pre-sheath leading to diamagnetic drifts that encircle the poloidal cross section even when field lines strike solid surfaces. In contrast, the $E_r \times B$ drift was shown not to be divergence free, and to be capable of delivering particle flux to the divertor plate. Given that our ultimate goal is to determine the particle fluxes incident on the divertors, and to compare with particle fluxes measured by embedded divertor probes, we proceed by including $E_r \times B$ perpendicular drifts, but neglecting diamagnetic drifts in our computation of poloidal particle flux.

Our method for comparing poloidal particle fluxes at different poloidal locations is to integrate the measured local particle flux between two flux surfaces:

$$\Gamma_\theta = 2\pi \int_{r_1(\rho_1)}^{r_2(\rho_2)} \mathrm{d}r \; Rnv_\theta \tag{8.8}$$

Here, $v_\theta = v_{E\times B} B_\phi/B + v_\parallel B_\theta/B$. The flux surfaces ρ_1 and ρ_2 are chosen to cover as

much of the SOL as possible, while ensuring that there is still good data on all three scanning probes. The results in the following subsections have performed the integral over the first 7 mm of ρ-space ($\rho_1 = 0$ mm, $\rho_2 = 7$ mm). In real space, this typically covers about 7 mm at the ASP location, 8.5 mm at the WASP location and 10 mm at the FSP location.

8.2.2 Variation with Magnetic Topology

It has been established in the preceding sections that the magnetic topology is a critical player in the edge flow picture. The topology-sensitive interplay between transport and drift-driven flows may be connected with a host of interesting phenomena, including transport reduction via flow shear and edge-core toroidal momentum coupling to name a few. For this reason, we apply the results of section 8.2.1 to a scan of magnetic topology in order to observe how the poloidal particle flux depends on this critical parameter.

The first question to answer is whether the the poloidal flux picture is really well represented by the picture that has been developed using parallel flow data alone. Even a small perpendicular flow can have a large effect on the net poloidal flow pattern because of the small field angle. The dependence of *parallel* flows on magnetic topology has been investigated in some detail [61]. The result on the HFS is persistent parallel flow toward the active divertor. We would like to see if this picture holds when perpendicular flows are included. As has been done in the past, we will observe the variation of the flow quantities as a function of the parameter SSEP. This is the distance between the primary and secondary separatricies at the outboard midplane. It reflects the degree to which the plasma is in one magnetic topology or the other. By convention, negative SSEP corresponds to LSN and positive SSEP corresponds to USN. When the magnitude of SSEP is less than roughly the SOL e-folding lengths (SSEP $\lesssim$ 5 mm), the topology can be called double null (DN) a Fig. 8-8 shows the results of this investigation.

The well-established picture of HFS poloidal particle flux due to parallel flows is displayed by the plot in the upper left panel of Fig. 8-8. Negative values of SSEP

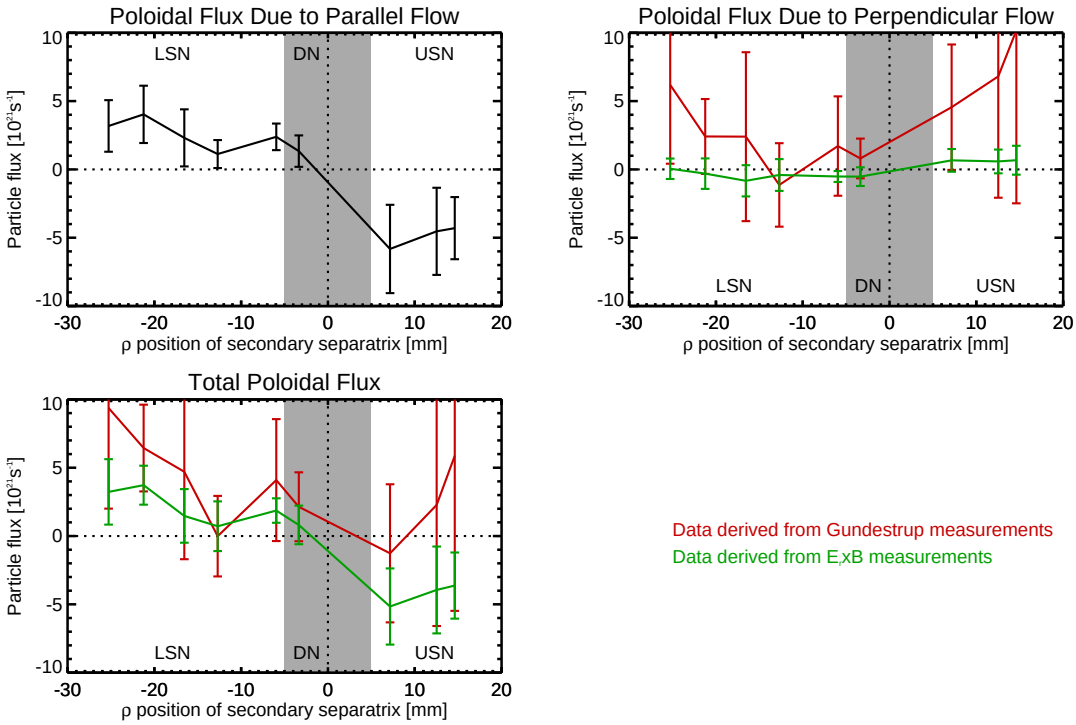

Figure 8-8: Poloidal flux of particles due to parallel and perpendicular flows at WASP location integrated to $\rho = 7$ mm. All data are at normal current and field (0.8 MA and 5.4 T clockwise, respectively). The data are binned over a large number of shots with a wide range of densities $0.5 \lesssim$ NL04 $[10^{20}$ m$^{-2}] \lesssim 1.2$. Negative values of the x-coordinate indicate LSN while positive values indicate USN. Positive values of the y-coordinate indicate poloidal particle flux in the electron diamagnetic direction (vertically downwards for these HFS, normal field measurements). Green data are the result of perpendicular flow measurements by the $E_r \times B$ method. The red data are the result of perpendicular flow measurements by the Gundestrup method. The first panel shows the contribution to poloidal flux from parallel flows. Here we see clearly the topology dependence of the data. The top right panel shows the contribution from perpendicular flows as calculated by both $E_r \times B$ and Gundestrup methods. The total poloidal particle flux shown in the last panel is the sum of the parallel and perpendicular contributions. Note that the inclusion of perpendicular flows does not change the general topology dependence for the case of the $E_r \times B$ method, but does for the Gundestrup method.

(indicating LSN) show a particle flux towards the lower divertor, while positive SSEP (USN) discharges have flux towards the upper divertor. Flux at balanced DN is approximately zero. The transition occurs for SSEP within ~ 5 mm of DN.

We next show the contribution of perpendicular flows to poloidal particle flux as a function of SSEP. This is shown in the upper right panel of Fig. 8-8 for both the $E_r \times B$ and Gundestrup perpendicular flow measurements. For the case of the perpendicular fluxes derived from the $E_r \times B$ method, the flux is roughly zero with similar spread in the data as seen for flux derived from parallel flows. There is not a strong dependence of the $E_r \times B$ poloidal flux component on topology. The flux derived from Gundestrup measurements of $v_\perp$ however is quite different. It shows a persistent trend in the electron diamagnetic direction and large uncertainty in the measured value.

We can put the parallel and perpendicular data together to produce a total poloidal flux measurement, as shown in the lower panel. We find that the trend observed from the parallel flows alone is not greatly altered by the addition of the $E_r \times B$ poloidal flux measurement. We still see the topology dependence of the poloidal particle flux; particles are moving towards the active divertor. Thus, using the $E_r \times B$ perpendicular flow data, our interpretation of the HFS particle flux picture is unchanged from that which came from parallel flow measurements; the net poloidal particle flux on the HFS is generally towards the active divertor, in agreement with the transport-driven flow hypothesis. The data from the Gundestrup measurement show a different story, with enhanced particle flux towards the lower divertor in LSN and approximately zero poloidal particle flux in USN.

The preceding analysis can be repeated for the ASP and the FSP, allowing us to observe the poloidal variation of the poloidal particle flux. Fig. 8-9 shows the parallel and perpendicular components of the poloidal flux for the ASP and Fig. 8-10 for the FSP. In both of these locations, the persistently co-current parallel flows result in poloidal fluxes in the electron diamagnetic direction. Unlike the HFS, there is only a small topology dependence of the flux components at the LFS locations. The poloidal flux due to parallel flow is slightly weaker in USN than in LSN. The poloidal

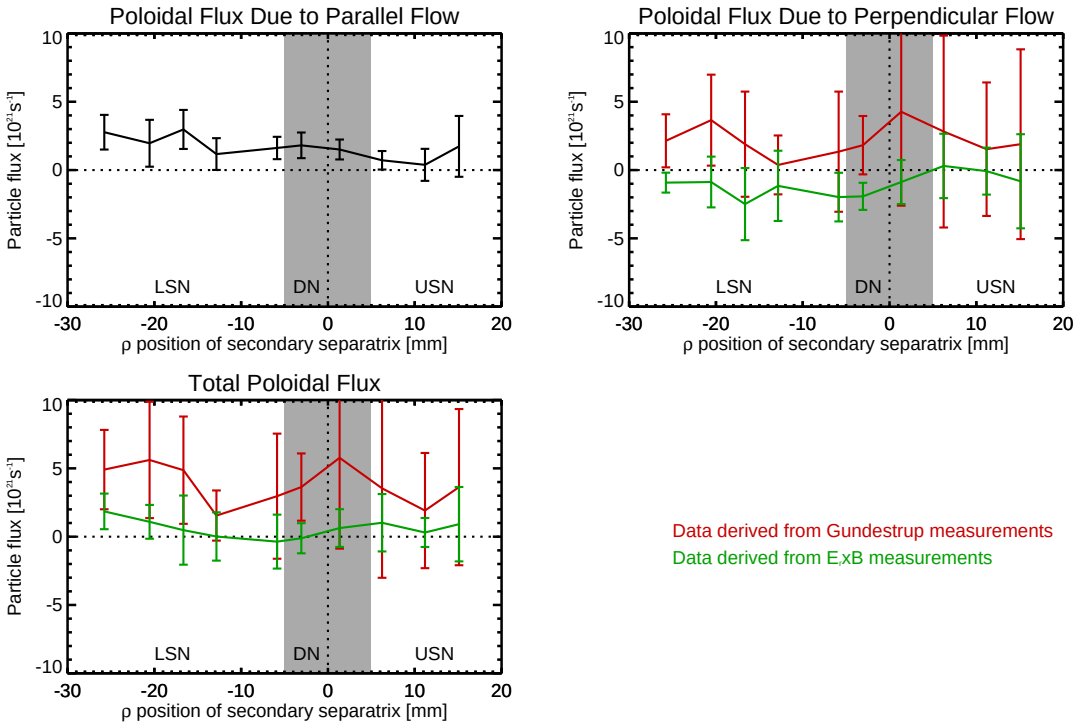

Figure 8-9: Poloidal flux of particles due to parallel and perpendicular flows at ASP location integrated to $\rho = 7$ mm. Positive values of the y-coordinate indicate poloidal particle flux in the electron diamagnetic direction (vertically upwards for these LFS, normal field measurements). Green data are the result of perpendicular flow measurements by the $E_r \times B$ method. The red data are the result of perpendicular flow measurements by the Gundestrup method.

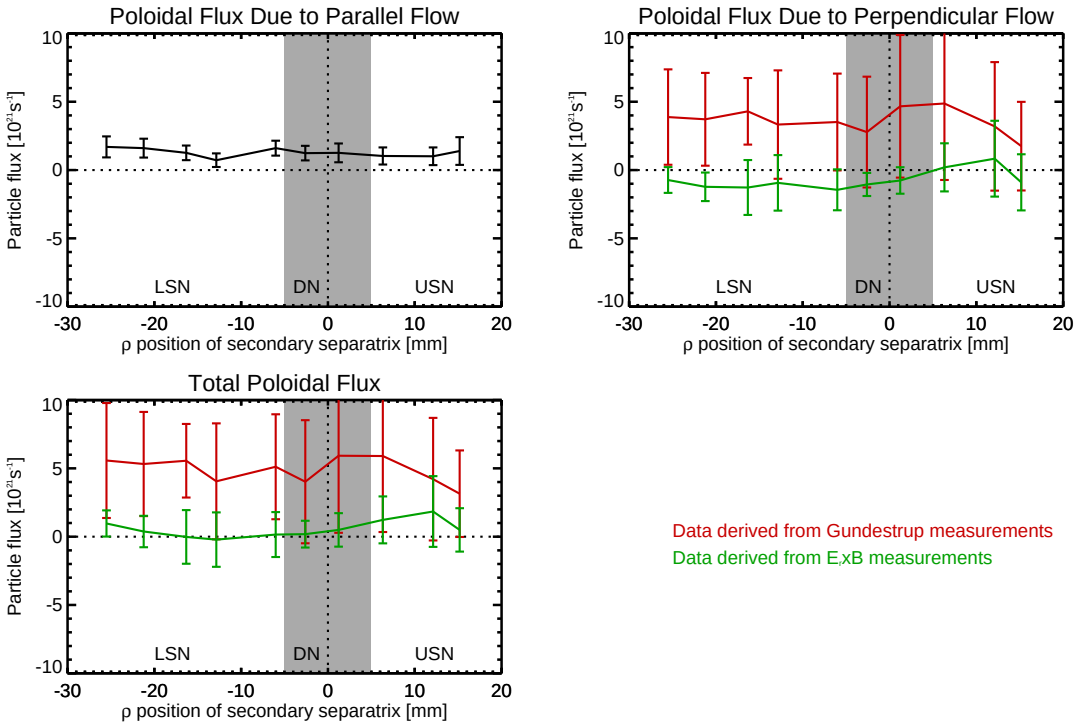

Figure 8-10: Poloidal flux of particles due to parallel and perpendicular flows at FSP location integrated to $\rho = 7$ mm. Positive values of the y-coordinate indicate poloidal particle flux in the electron diamagnetic direction (vertically upwards for these LFS, normal field measurements). Green data are the result of perpendicular flow measurements by the $E_r \times B$ method. The red data are the result of perpendicular flow measurements by the Gundestrup method.

flux due to $E_r \times B$ flow is slightly in the ion direction in LSN and nearly zero in USN at both LFS probe locations. The Gundestrup and $E_r \times B$ techniques measure clearly different signs of the poloidal flux, consistent with an offset in the Gundestrup measurement rather than a multiplicative factor. The Gundestrup measured flux of roughly 4×10^{21} s^{-1} in the electron direction contrasts with the $E_r \times B$ measured flux of $1 - 2 \times 10^{21}$ s^{-1} in the ion direction. The total poloidal fluxes obtained from adding parallel and perpendicular contributions are roughly zero at both locations for the $E_r \times B$ data, indicating a nearly pure toroidal flow. The total poloidal flux is strongly in the electron diamagnetic direction for the Gundestrup data.

As discussed in chapter 5, the Gundestrup is subject to an offset in the electron diamagnetic direction that is not well understood. The Gundestrup data has been included in this section for completeness, but we proceed using the $E_r \times B$ measurements of perpendicular velocity for the remainder of this chapter.

Combining the above measurements of particle flux, we can assemble the plot shown in Fig. 8-11. Here we show the total poloidal flux measurements (including contributions both from parallel flows and cross-field drifts) as a function of normalized parallel distance from the outer divertor, S. The S parameter is a proxy for poloidal location in the SOL. We have added data from the embedded divertor probes at either end of the SOL. To calculate particle flux to the divertor, we simply measure the current density collected by the probes when they are ion saturation, and integrate over the same portion of flux space as the scanning probes. The curves shown are averages of many shots, with the different colors indicating different density bins. The five points on each curve are the flush-mounted probes on both divertors, and the three scanning probes. $E_r \times B$ values for cross field flow velocity were used to generate these plots. The data are shown for both LSN and USN configurations, with the toroidal field and current in the normal (clockwise in plan view) direction.

Fig. 8-11 shows an asymmetry in the poloidal particle flux pattern between USN and LSN configurations. In LSN (favorable $B \times \nabla B$) the particle flux is towards the inner divertor for all locations other than the outer divertor. For USN however, the stagnation point is located near the 'crown' (bottom, in this case) of the plasma. This

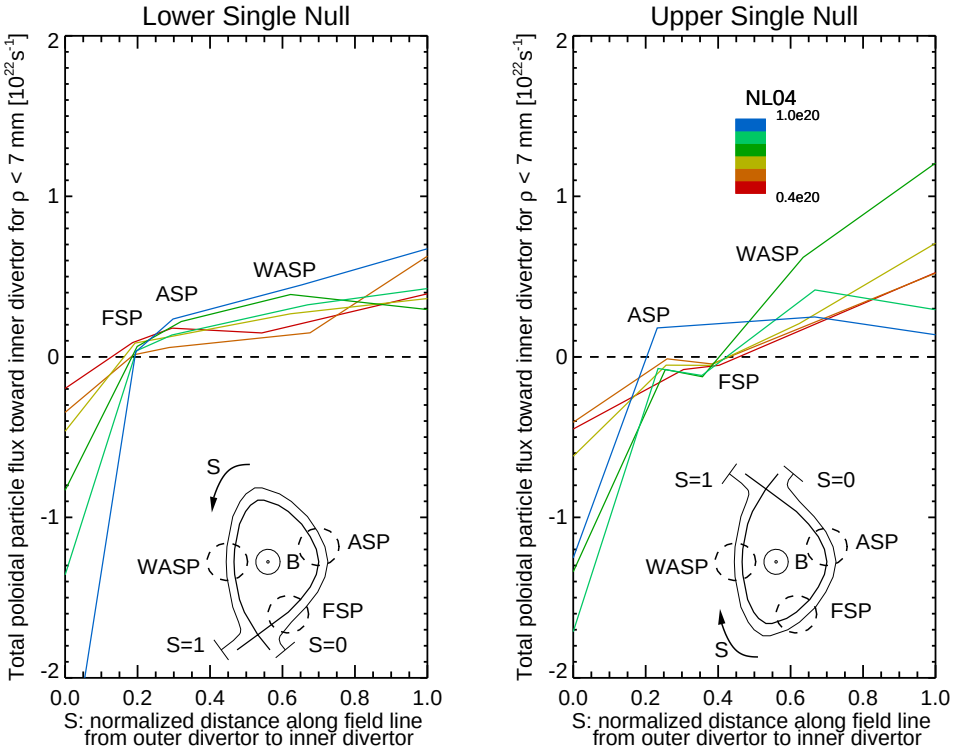

Figure 8-11: The total poloidal particle flux is plotted as a function of the normalized distance from outer divertor to inner divertor along the field line for normal field direction (clockwise). Positive fluxes are towards the inner divertor. The plot on the left shows the result for a lower single null topology, while the plot on the right is an upper single null. The data has been binned according to density as indicated by the color scale. Each line has five measurement corresponding to the two divertor probe arrays and the three scanning probes.

can be understood by looking back at our results for flow components on the LFS. Fig. 8-2 shows that the LFS transport-driven poloidal flow is very small. Fig. 8-7 shows that the drift-driven poloidal flows are composed of parallel Pfirsch-Schlüter flows in the electron diamagnetic direction, and perpendicular $E_r \times B$ flows in the ion diamagnetic direction. The Pfirsch-Schlüter is somewhat larger, leading to a net poloidal flow in the electron diamagnetic direction at the LFS midplane. Thus, the poloidal stagnation point is shifted in the electron diamagnetic direction from the LFS midplane, even though the poloidal distribution of the particle source due to transport remains centered roughly at the midplane.

The outer divertor displays the features we are accustomed to seeing there. Much higher fluxes are recorded to the divertor plate itself than at the upstream FSP location. This demonstrates that this is a 'high-recycling divertor', meaning that most of the neutrals produced at the surface are re-ionized locally and return to the divertor. As the plasma density increases, the particle flux to the outer divertor increases and the recycling flux is amplified. At the inner divertor we see a surprisingly different picture. In most cases the flux recorded at the divertor plate is a factor of two or less times that recorded at the WASP probe. This is observed at all densities and in both topologies. Clearly, a different physical picture from that at the outer divertor that will be required to explain these observations.

At high density in USN, the inner divertor flux is sometimes *less* than that recorded upstream at by the WASP. This indicates that the inner divertor is not in the same high recycling condition as the outer divertor. This may be due to the onset of detachment at the inner divertor. In this case, volume recombination could absorb particle flux and inject much of it into the core as neutrals. This suggests that different mechanisms for closing the HFS particle flux loop may dominate at different discharge densities and in different topologies. This possibility will be investigated in detail in section 8.2.3

The reversed field and current runs late in the '07 campaign allowed us to look at symmetric field reversal to eliminate any effects due to systematic asymmetries in the geometry of the probes or the divertor. The data set is sparse because we lack

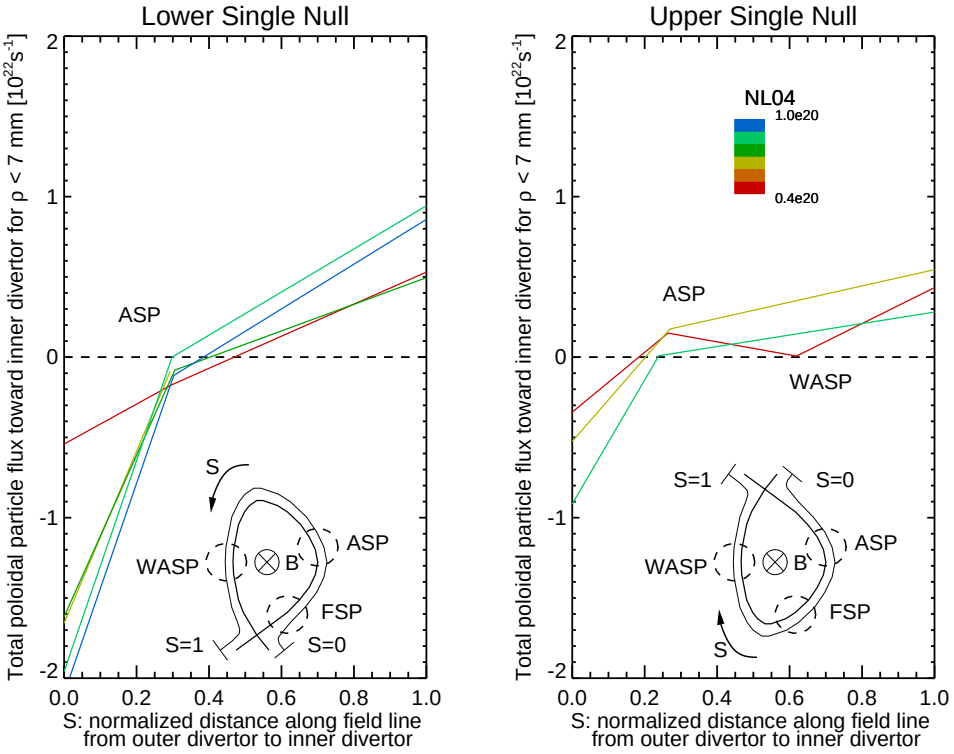

Figure 8-12: The total poloidal particle flux is plotted as a function of the normalized distance from outer divertor to inner divertor along the field line for reversed field direction (counter-clockwise). This data set is sparse, but the data we have indicates that the trends swap from USN to LSN in accordance with the reversal of the direction of the $B \times \nabla B$ drift.

good measurements from both the WASP and the FSP. However, in what data are available, we generally see the trends described for the normal field case repeated in the reversed field case, that is, the data from LSN reversed field looks similar to the data from USN in normal field, and vice-versa. This says that the difference between topologies in normal field direction is due to the direction of $B \times \nabla B$ relative to the active x-point and *not* due to some geometrical machine asymmetry.

8.2.3 Variation with Density

The observations of the preceding subsection suggest that the mechanism for closing the HFS particle flux loop may be different depending on the discharge density. In order to better characterize the particle flux trends with density, and identify the density ranges in which certain mechanisms may be dominant, we now recast the net poloidal particle flux trends as a function of discharge density.

Figs. 8-13 and 8-14 show the net poloidal particle flux data from each probe location as a function of the line-integrated density. We see that the inner and outer divertors have different behavior. The outer divertor particle flux increases steadily with density in LSN, while the inner divertor shows almost no change. In USN, the outer divertor shows even higher flux at low densities, but begins to decrease at NL04 $\sim 0.9 \times 10^{20}$ m^{-2}. The inner divertor also shows an increase in flux with density, up to NL04 $\sim 0.75 \times 10^{20}$ m^{-2} at which point it begins to decrease as well, perhaps due to the onset of detachment at the inner divertor, as discussed earlier. The inner divertor flux is almost eliminated at a line-integrated density of 0.95×10^{20} m^{-2}. The fluxes recorded by the scanning probes show little sensitivity to density, though their magnitudes increase slightly with density in LSN.

In reversed field, the USN (LSN) discharges behave like the LSN (USN) discharges in normal field. We now see larger divertor particle fluxes in the LSN topology than in USN. The exception is the divertor probes at high density. Here, we do not observe the decrease in poloidal particle flux that was observed for the unfavorable topology in normal field. Instead, they maintain their maximum value up to the highest densities measured (NL04 = 0.95×10^{20} m^{-2}). It appears that the physics

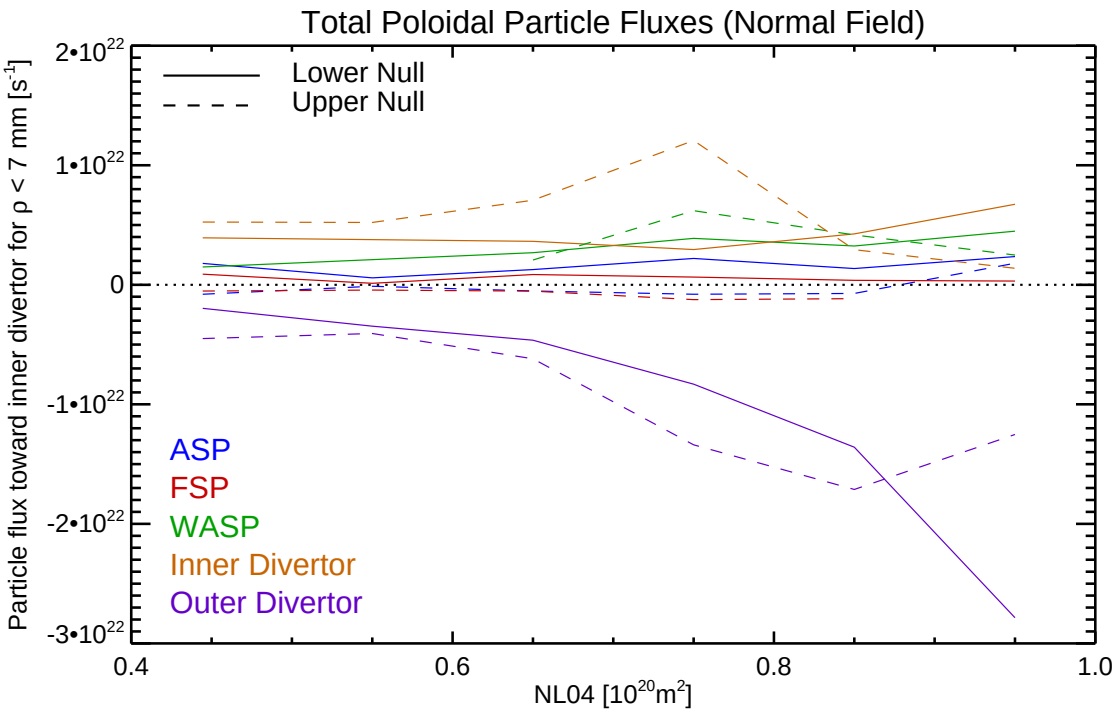

Figure 8-13: The data from Fig. 8-11 recast as a function of line-integrated density. Poloidal particle flux towards the inner divertor is plotted as a function of density for each probe. Solid lines show lower single null data while dashed lines show data from upper single null.

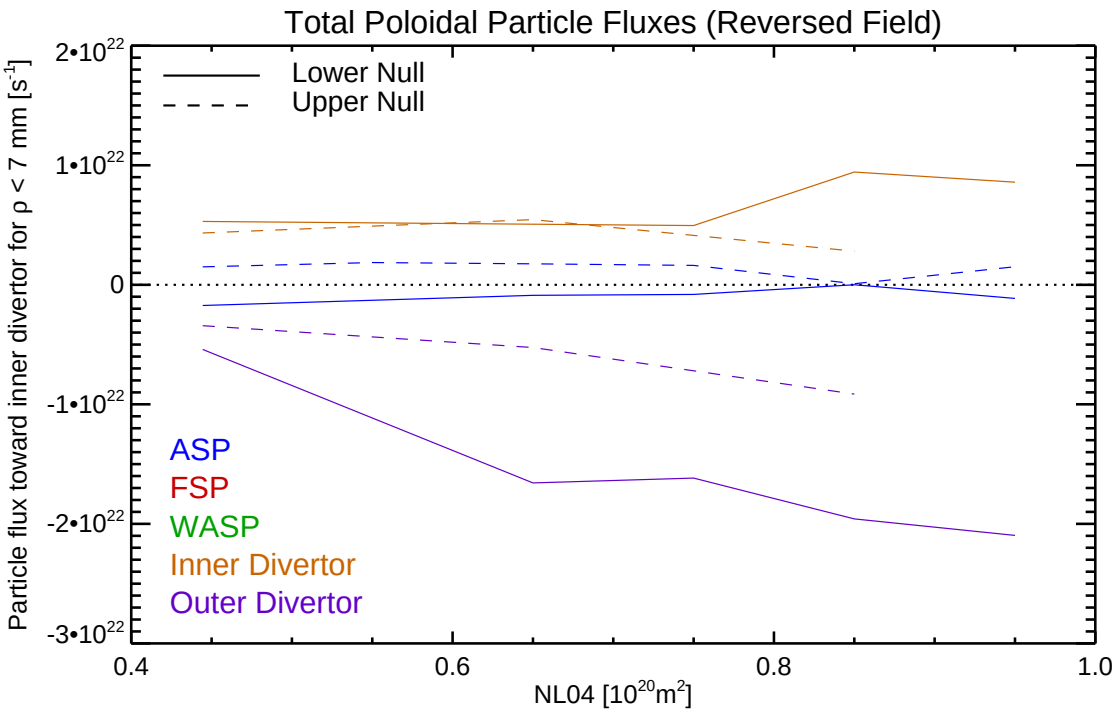

Figure 8-14: The data from Fig. 8-12 recast as a function of line-integrated density. Poloidal particle flux towards the inner divertor is plotted as a function of density for each probe. Solid lines show lower single null data while dashed lines show data from upper single null.

dominating these net particle fluxes through most of the SOL depends on the direction of the particle drifts with respect to the active divertor. However, the unfavorable divertor in reversed field (the lower divertor) resists detachment. This may be due to the very different geometries in upper and lower divertors. These differences may affect the detachment density threshold.

Returning to the normal field case at high density in USN where the HFS poloidal flux does not reach the divertor, our working hypothesis for the fate of these particles is that volume recombination allows much of the flux to return to the core without reaching the inner divertor. This must be verified by investigating the state of the inner divertor. If volume recombination is present in these discharges, we would not expect the pressure to map from upstream to the divertor plate. We would also expect the flush-mounted probes to measure electron temperatures of ~ 5 eV, where volume recombination becomes significant [70]. Examination of the inner divertor state will be undertaken in the next section. Once we have determined the influence of volume recombination, we will attempt to sort out which of the remaining proposed particle-flux closure mechanisms is at work at the lower densities.

8.2.4 Role of Divertor Conditions in SOL flows

SOL flows are intimately connected to the state of the divertors or limiters at either end of the open field lines which permeate the SOL region. When considering the global particle flux picture, we must consider the physics of the divertor region, because the divertor areas ultimately represent the sinks for these flows. The C-Mod divertor has been investigated in detail [70, 21, 46] and the standard range of divertor regimes have been identified. These are usually organized by discharge density. A 'sheath-limited' divertor occurs at the lowest density. In this case, the neutral mean-free path is long and neutrals emitted from the divertor target ionize far from the divertor itself. The plasma temperature is not depressed due to recycling and maps to the temperature upstream. Density maps to upstream values as well to balance pressure. The high plasma temperature means that the parallel thermal conductivity of the plasma is much larger than that of the sheath (thus the name sheath-limited).

If the discharge density is raised the neutrals emitted from the divertor are re-ionized locally. This causes the plasma density in the divertor to increase and the temperature to drop so that the pressure still balances the pressure upstream. The strong dependence of thermal conductivity on temperature causes the heat flux to become limited by the cool dense plasma near the target. This is called a 'high-recycling' regime. If the density is increased further, the temperature can drop low enough ($\lesssim 5$ eV) that there is significant volume recombination in the vicinity of the divertor. This state is referred to as 'detachment' and is characterized by plasma pressure which is not conserved along the field line and are balanced by neutral pressure in the divertor region. Detached divertors have very low incident heat flux. The power is radiated by the recombining plasma before it reaches the divertor. These regimes are routinely observed on the C-Mod outer divertor.

The inner divertor does not behave identically to the outer divertor, as detailed in [70]. This appears to be due to a combination of a drift asymmetry caused by the direction of the magnetic field and an fundamental in/out asymmetry, as demonstrated by the failure of the divertors to symmetrically change state when the field direction is changed. To determine whether the upper divertor is detached in the high-density USN case (as proposed in section 8.2.3), we must look at pressure mapping and divertor temperatures.

Fig. 8-15 shows temperature and total pressure ($(1 + M_{\|}^2) n_e T_e$) from the WASP and upper inner divertor for typical USN discharges with normal field and current. The left column is a lower density discharge and the right a higher density. The low density discharge is in the range where we observe higher net poloidal particle flux at the divertor than at the WASP. The higher density discharge on the right is from the range where the poloidal flux at the divertor is the same or less than that observed at the WASP. Fig. 8-15 shows that the low density case is in the high-recycling regime, with pressures mapping from the WASP to the divertor, but the temperature reduced at the divertor. The high-density case is clearly detached because of the very low pressure observed at the divertor plate. The divertor temperature in the high-density case is below 5 eV through most of the SOL, indicating that the plasma has a

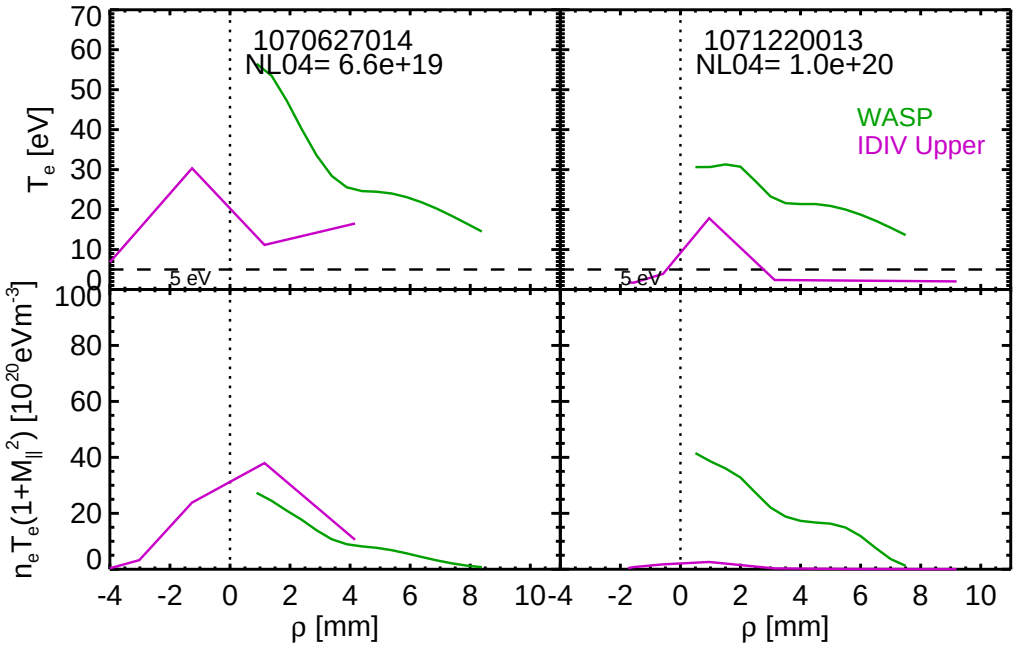

Figure 8-15: Temperature and total pressure (kinetic + ram pressure) measured during USN discharges at the HFS midplane and at the upper inner divertor. These discharges had normal field and current (5.4 T, 0.8 MA) and normal field direction. The left column shows a low density discharge where the net particle flux to the divertor is observed to exceed that passing the poloidal location of the WASP. The the right column shows a high density discharge where the flux passing the WASP exceeds that reaching the divertor. For dashed line shows $T_e = 5$ eV, below which volume recombination is expected to be significant.

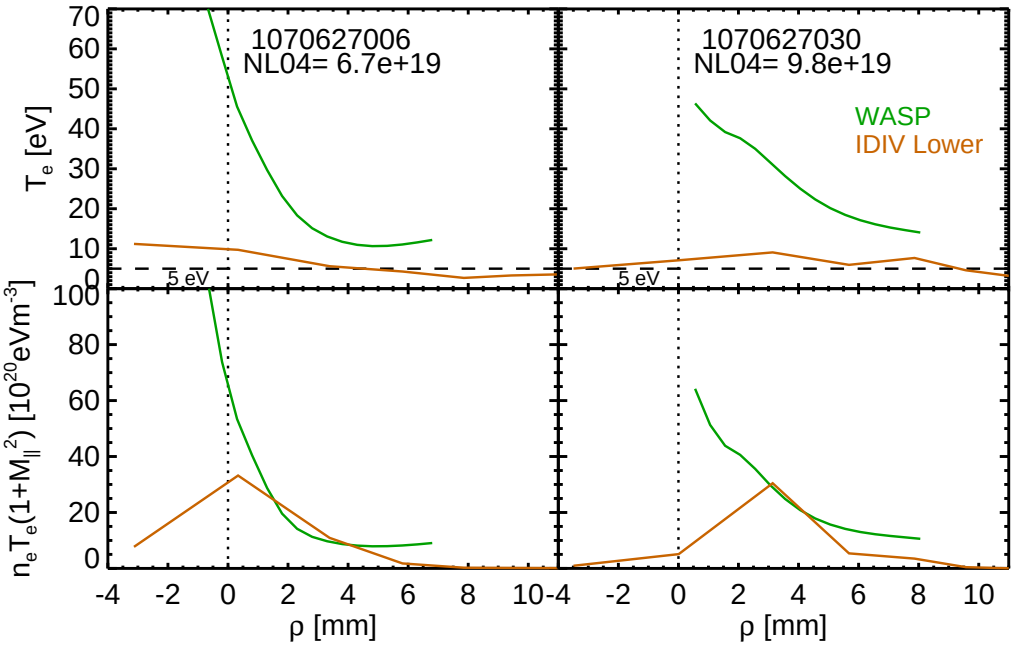

Figure 8-16: Temperature and pressure measured during LSN, normal field discharges at the HFS midplane and at the lower inner divertor. The left column shows a low density discharge and the the right column shows a high density discharge.

low enough temperature for a significant amount volume recombination. Therefore, it is possible that the some of the particle flux incident on the inner divertor in the USN, high-density case may be coupling into the core via neutrals emitted from a region of volume recombination. The roll-over in particle flux arriving at the inner divertor (USN) with increasing density seen in Fig. 8-13 is a consequence of this physics.

For comparison, Fig. 8-16 shows data from the WASP and *lower* inner divertor for typical LSN discharges. In contrast to the USN case, we observe little change in the divertor state over the same density range. The lower inner divertor maintains a high-recycling state in both high and low density cases, with divertor temperatures hovering slightly above the 5 eV level. If anything, the near SOL becomes slightly detached at high density, with pressure not mapping from WASP to divertor for $\rho \lesssim 3$ mm, but the effect is not nearly as strong as that observed in at the upper inner divertor at high density.

The idea that an area of volume recombination can return a large portion of the incident particle flux to the core without interacting with the divertor is reminiscent of the MARFE phenomenon, frequently observed in the HFS SOL. This has similar qualities to a detached divertor, but is located remotely from the divertor itself. MARFE observations can support the idea of an area of volume recombination absorbing incident plasma flux and injecting it into the core as neutrals.

8.2.5 MARFE

As mentioned previously, the presence of the MARFE has a major impact on the state of the HFS SOL and the inner divertor. Though this is not reported in the literature, it is found on C-Mod that the MARFE onset occurs at a lower discharge density in the unfavorable $B \times \nabla B$ drift direction than in the favorable direction. Because they greatly reduce the plasma density on the HFS and dramatically change the observed flows, MARFEs were avoided in WASP experiments. Yet, we did encounter a few MARFEs when trying to run unfavorable discharges with conditions matched to discharges with favorable drift direction. Fig. 8-17 shows examples of MARFEs observed during shots with the WASP scanning for unfavorable drift topologies in both forward and reversed field, along with slightly lower density cases where no MARFE is observed.

In the cases where the MARFE is present, nearly all of the plasma disappears from the HFS SOL between the location of the MARFE and the inner divertor. This can be seen by the greatly reduced pressures at the WASP and the inner divertor in the MARFEing cases (note, upper divertor data was not available due to the location of the upper x-point in the MARFE discharge). In addition, the rapid flow towards the divertor at the WASP location is halted, and in what little plasma remains, the flow is reversed, so that it is towards the MARFE instead of the inner divertor. Thus the MARFE is clearly an effective particle sink, able to absorb all of the incident plasma flux. The mechanism by which these particles are returned to the core is not known. One possibility is that the large temperature and density gradients in the vicinity of the MARFE lead to radial drifts, enhancing the mixing of edge and

core plasma. Another possibility is that the MARFE injects significant neutral flux into the confined plasma from volume recombination. This could be enabled by its proximity to the core. These observations support the hypothesis that a detached inner divertor could behave the same way.

8.2.6 HFS Particle Pinch

While we have proposed a mechanism by which the HFS poloidal particle flux can return to the core in the relatively rare case where the HFS midplane poloidal particle flux is not accounted for at the divertor, this solution does not apply to the majority of cases; those where the inner divertor is attached. In these cases, we must invoke some mechanism for removing particles from the SOL between the HFS midplane and the inner divertor. Candidate mechanism include strong core neutral penetration a low recycling inner divertor, and a particle pinch between the HFS midplane and the divertor strike point. The low temperatures observed at the inner divertors in section 8.2.4 are evidence against a low recycling state. We normally expect the upstream temperature to map to the plate in the low-recycling (sheath-limited) regime. Furthermore, many edge simulations have found neutral penetration to be insufficient to explain observed HFS flows [14, 15] and impurity deposition patterns [16, 17]. The authors of these studies have often proposed an inward particle flux to explain their results. We therefore have good reason to expect that there may be a pinch on the HFS and would like to characterize it experimentally. The HFS radial particle flux has not been directly measured in the past, but the WASP provides us with the capability of measuring the fluctuation-induced fluxes at the HFS midplane.

The experimental technique for measuring fluctuation-induced fluxes is described in section 2.1.4. It involves simultaneous measurement of density fluctuations and floating potential fluctuations. This requires operating two of the probe electrodes in a floating mode rather than a swept mode and therefore requires dedicated shots to make the measurement. This was done systematically on two occasions, once during the '07 campaign and once during the '09 campaign. These experiments are described in section 3.3. During the '09 run, new data acquisition systems allowed the data to

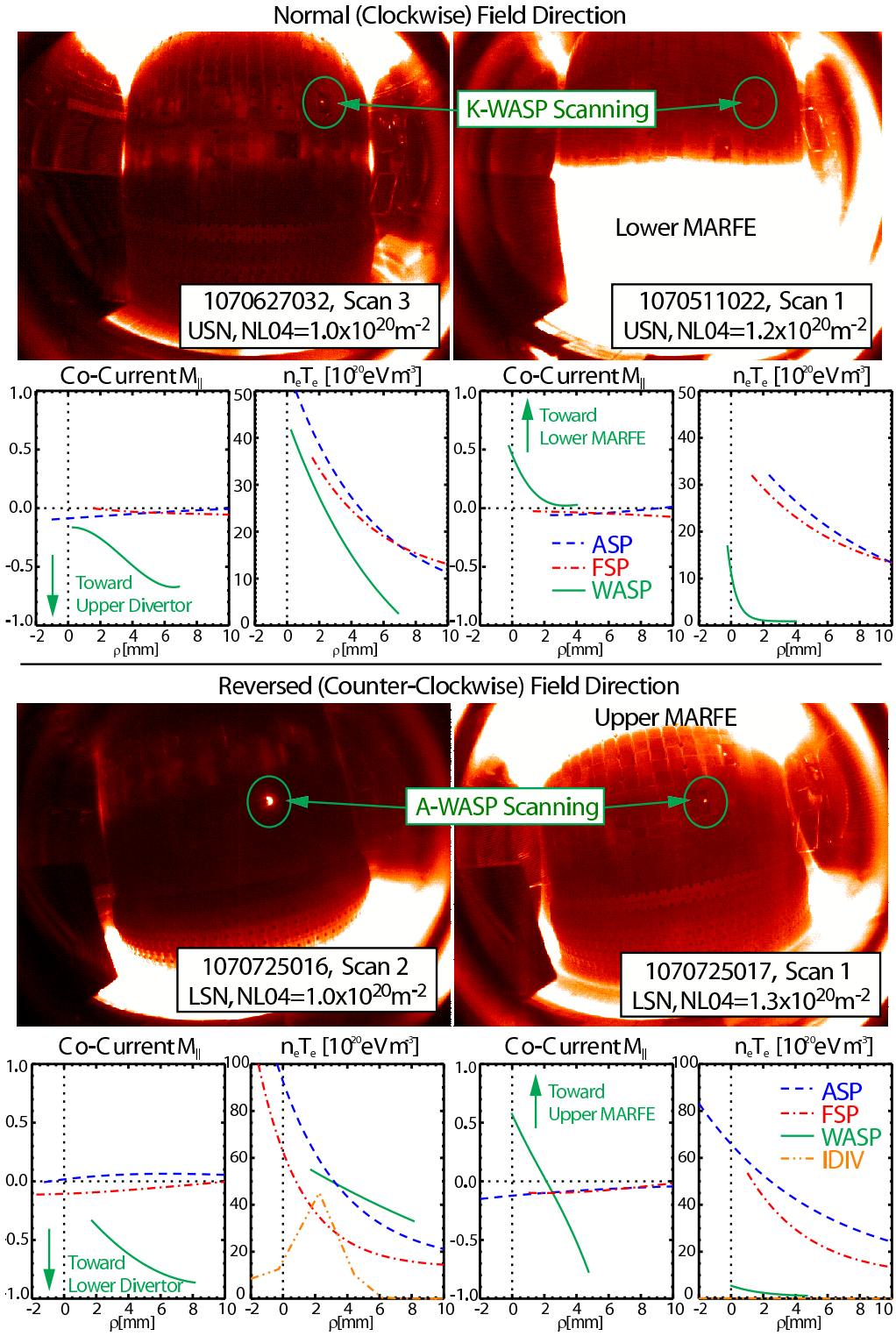

Figure 8-17: Comparison of discharges with and without HFS MARFEs in unfavorable $B \times \nabla B$ drift direction. The top half of the figure shows matched USN discharges in normal field, the left side without a MARFE and the right side with a MARFE. Below each picture is shown the measured parallel Mach numbers and pressures from the three scanning probes. The bottom half of the figure shows the same comparison for LSN discharges in reversed field, including lower inner divertor pressures.

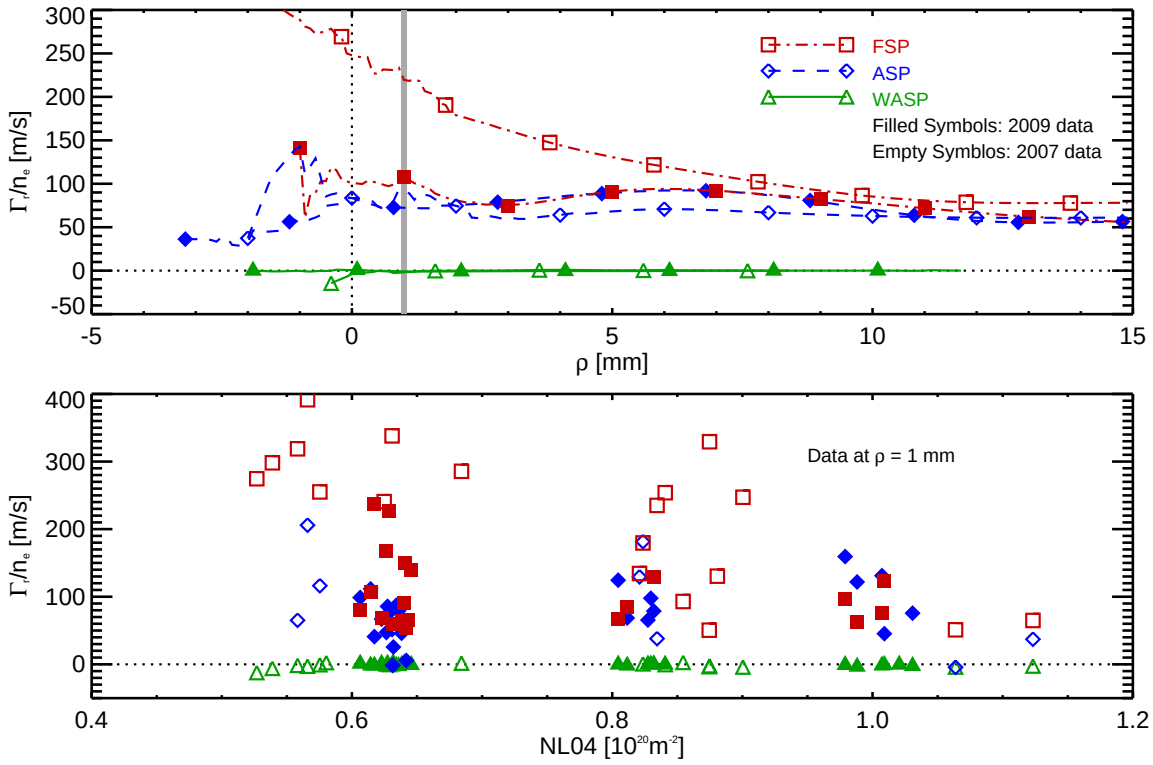

Figure 8-18: Fluctuation-incooduced fluxes normalized to local plasma density. The top panel shows the radial dependence of the fluctuation-induced fluxes measured by the three scanning probes. These data are averaged over the available density range. The dashed curves are the data from the '07 campaign, while the solid curves are from the '09 campaign. The bottom panel shows all the data as a function of density at ρ=1 mm, corresponding the the vertical gray line in the top panel. Triangles are from the '07 campaign while diamonds are from the '09 campaign.

be digitized at 5 MHz instead of the typical 1 MHz of previous campaigns. The higher digitization rate allows somewhat better characterization of the fluctuations, which have timescales of $\lesssim 10$ μs, but the results of the calculation appear to be insensitive to the change in digitization rate. Because the Gundestrup geometry forces the electrodes to be arranged asymmetrically with respect to the parallel direction, we tried bias combinations with both the East electrodes floating and with both the West electrodes floating during the '09 run day. This also did not affect the result. Altogether, about 85 plunges were run with the probes in fluctuation mode, across a variety of discharge densities in LSN and USN. All discharges had normal field (5 T) and current (0.8 MA) and normal field direction.

The top panel of Fig. 8-18 shows the radial dependence of the fluctuation-induced flux averaged over a range of line-integrated discharge densities with $0.5 <$ NL04 $[10^{20}\ \mathrm{m}^{-2}] < 1.2$. Here, Γ_r is the raw flux measurement. The flux is normalized to the local density so it is expressed as a radial velocity: $v_r = \Gamma_r/n_e$. The data from the two LFS probes overlay well with the exception of the FSP in the '07 campaign. This is likely due to the fact that the FSP was unintentionally operated with a probe tip intended for the ASP during '07. Thus the pyramid was not correctly aligned with the field and floating electrodes were measuring a radial component of the electric field, potentially corrupting the result. The WASP data from the different campaigns also overlay well, showing essentially zero radial flux. A hint of a pinch that appears near the separatrix from the '07 data but is shown by better statistics in the '09 data to be anomalous.

The bottom panel in Fig. 8-18 shows the dependence of the radial velocity on discharge density at $\rho = 1$ mm. There is very little density dependence observed, indicating that the density averaging in the top panel is reasonable. There is some indication that v_r may be reduced at line-integrated densities above $1 \times 10^{20}\ \mathrm{m}^{-2}$, possibly due to increased recycling and decreased SOL density gradients. However, much of the data which shows high velocity at low density is from the malfunctioning '07 FSP, limiting the credibility of this observation. The observed radial velocity at the WASP location is robustly zero throughout the SOL and regardless of density, compared to velocities that are 50 m/s near the separatrix on the LFS. These measured LFS fluxes are actually thought to be higher than the unperturbed values because the implied global particle balance exceeds that calculated by other methods [6]. The explanation for this disagreement is that the measured flux is influenced by the presence of the probe: that is, what is actually measured is the perturbed flux into the pre-sheath in addition to the background flux due to transport ($\Gamma_r = \Gamma_{plasma} + \Gamma_{probe}$). Because the WASP measures zero flux in the SOL, we must conclude that the flux in the absence of the probe would be at most zero (that is, could be inwards). However, it seems surprising that the perturbed flux would be precisely zero if it were the sum of two effects from independent phenomena. In addition, the calculation carried out

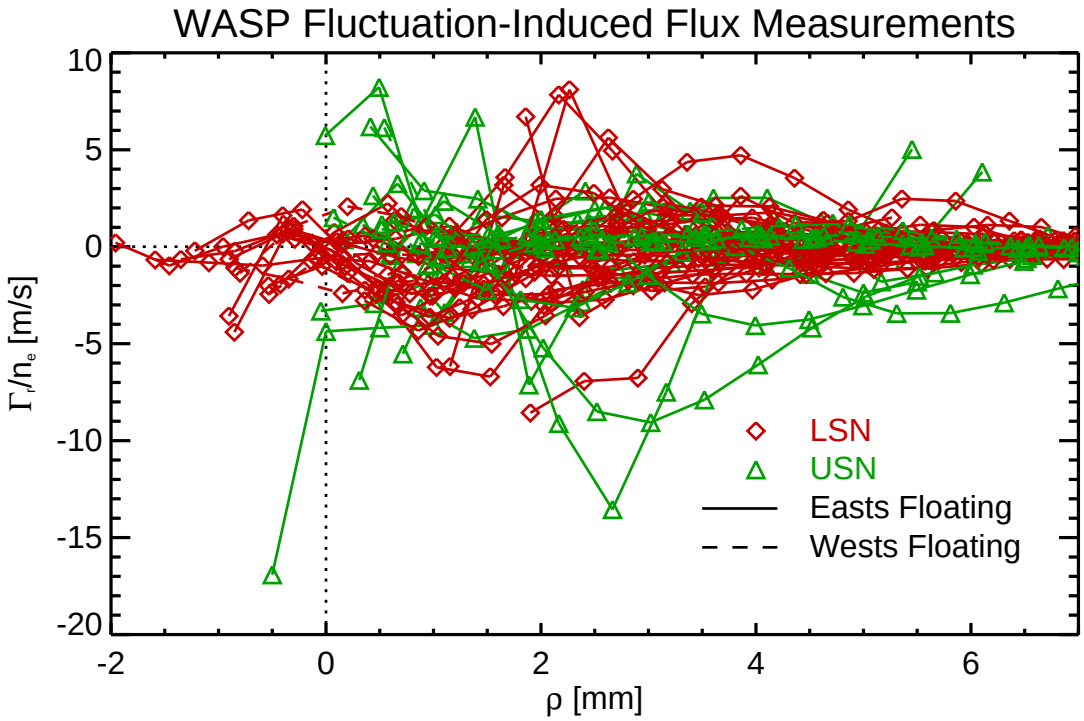

Figure 8-19: Profiles of fluctuation-induced fluxes measured by the WASP on individual scans.

in section 8.1.4 showed very good agreement between the radial fluxes measured by this technique and those calculated based on the transport-driven poloidal particle flux observed on the HFS. These observations hint that the probe perturbation to the fluctuation-induced flux measurement may actually be small.

The WASP data are shown in more detail in Fig. 8-19. Here, the data are distinguished by USN and LSN as well as by which group of electrodes was floating and which was swept. The result is insensitive to both of these parameters, as well as to

Author	Machine	Code	Pinch Velocity
Pigarov [14]	Alcator C-Mod	UEDGE	> 20 ms^{-1}
Elder [16]	DIII-D	OEDGE	$10 - 30$ ms^{-1}
Kirnev [15]	JET	EDGE2D	10 ms^{-1}

Table 8.2: Summary of HFS pinch velocities predicted by various tokamak edge simulations.

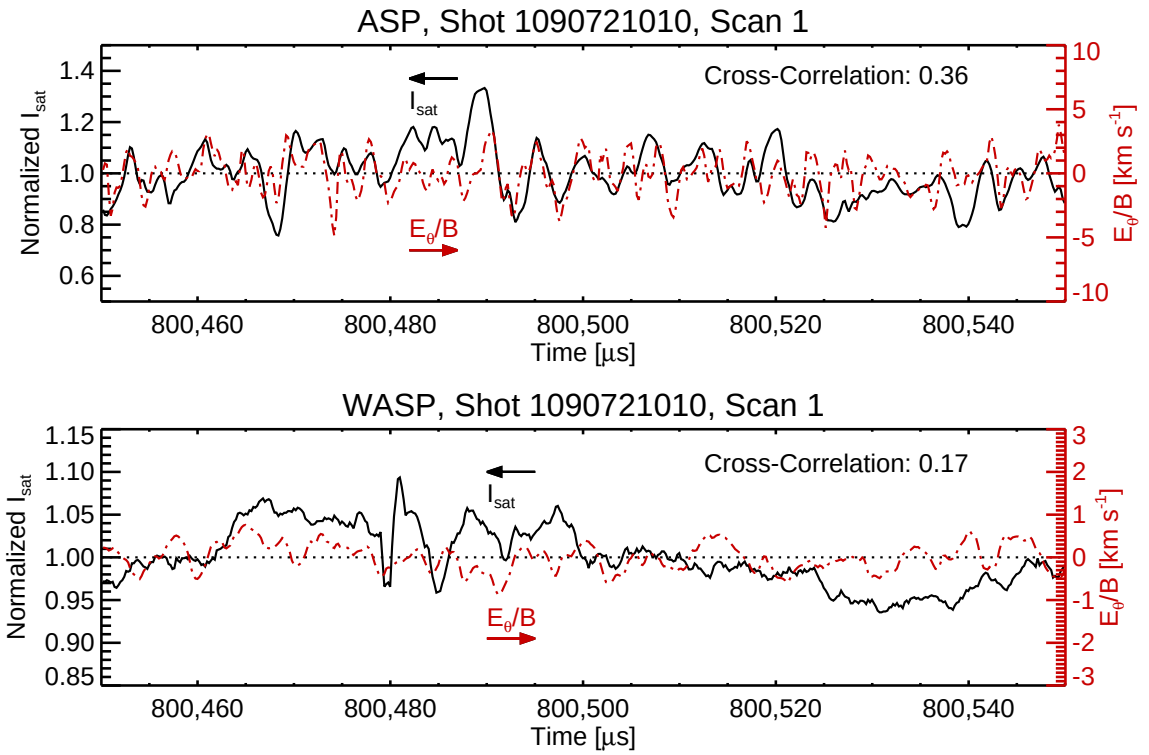

Figure 8-20: The magnitude and correlation of ion saturation current and perpendicular electric field are compared on the HFS and LFS for a typical shot with the probes operating in fluctuation mode.

density and radial position. It is always close to zero, rarely attaining a value as high as the 10-30 m/s required by simulations to produce agreement with the measured flows (see table 8.2), and never systematically showing a non-zero value. It should be noted that these simulations often impose the convective pinch on top of an assumed diffusion coefficient, so a net radial velocity of zero is not necessarily inconsistent.

Because the RMS fluctuation amplitude of ion saturation current and floating potential on the HFS are only about a factor of 2-3 lower than on the LFS (see Fig. 6-1), we cannot explain the difference in radial velocity by the difference in the magnitude of the fluctuations. The phase angle between the density and potential fluctuations on the HFS also contributes to the reduced radial particle flux. This can be seen in Fig. 8-20, which shows the normalized ion saturation current and perpendicular electric field signals during a snapshot of a probe scan during a period of ion saturation. The WASP signal has smaller amplitude fluctuations of both density

and electric field, which are less well correlated than those on the ASP. These effects combine to produce the very small measured fluctuation-induced particle fluxes.

It should be noted that we measure radial fluxes only due to fluctuations in n and E_θ, not due to their mean values. Finite $\bar{E}_\theta$ may be present and lead to radial particle motion, but this is not measured. Such effects might be localized near the divertor due to the poloidal temperature and potential gradients that can exist there.

From measurements of fluctuation-induced particle flux, we conclude that there is not a significant turbulent particle pinch at the HFS midplane of Alcator C-Mod. While we cannot rule out a pinch that is localized around the x-point, or a pinch from $\bar{n}\bar{E}_\theta$, our data does not show evidence of any fluctuation-induced particle flux crossing the LCFS near the HFS midplane.

8.2.7 Neutral Fueling from the HFS Divertor Region

Having eliminated a general HFS turbulent particle pinch as the mechanism responsible for returning the observed HFS midplane poloidal particle flux to the core, we next consider the possibility that neutral penetration from the inner divertor exhausts particles from the HFS SOL. The MARFE observations of section 8.2.5 lead to this hypothesis for detached inner divertor conditions. Yet the data in Figs. 8-13, 8-14 tell us that the return flow mechanism must also be present in attached divertor conditions. This effect has also been observed in some edge simulations [41]. Thus we need to consider neutral penetration and recycling under these conditions.

To address the degree of core penetration by neutrals in the region of an attached HFS divertor, we can make use of a simple slab model of neutral ionization. KN1D is 1-D space, 2-D velocity kinetic neutral code that was developed by B. LaBombard for the purpose of modeling plasma-neutral interactions in the SOL [80]. It takes input radial profiles of electron and ion temperature and electron density and computes distribution functions of molecular and neutral hydrogen in the limiter shadow, the SOL and the edge of the confined plasma. The 1-D geometry and neutral pressure far in the limiter shadow are also taken as inputs. Though it does not self-consistently account for the complexities of the inner divertor geometry, this simulation can pro-

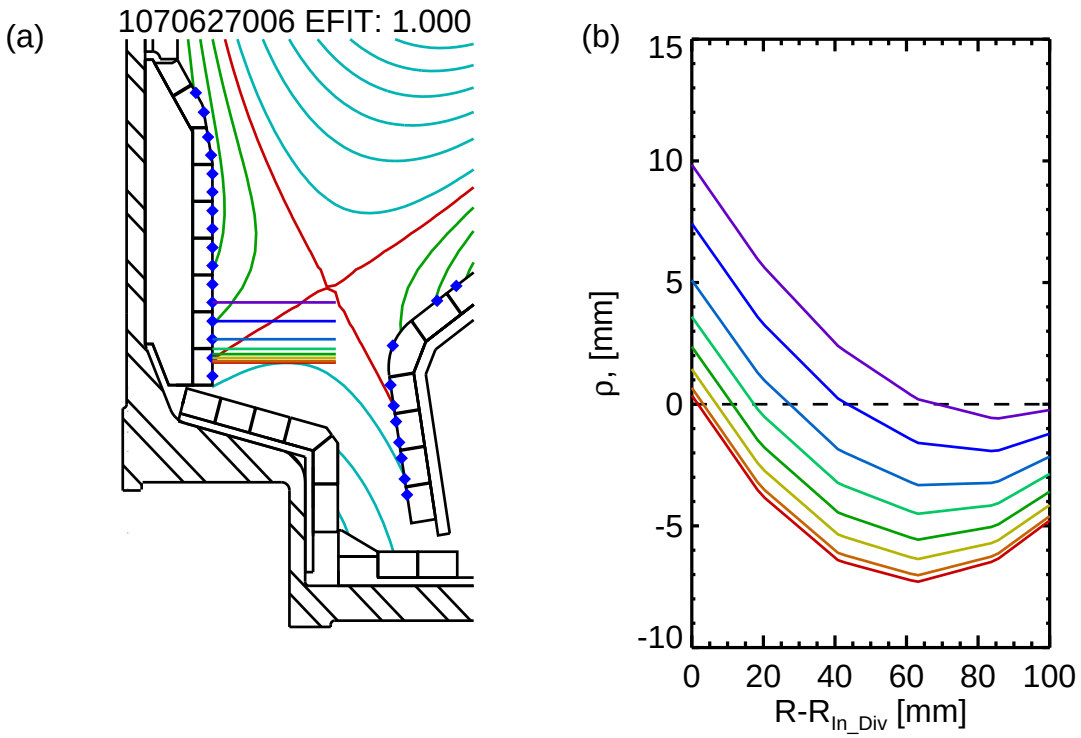

Figure 8-21: Geometry for KN1D simulations. The horizontal lines from the inner divertor shown in panel (a) are the domains of the 8 KN1D simulations that were conducted. The blue diamonds show the locations of the embedded divertor probes. Panel (b) shows the mapping of the ρ coordinate onto the chords. This is used to convert density and temperature data from the divertor probes to input profiles for the KN1D simulations.

vide a rough estimate of the fraction of the neutrals emitted from the inner divertor that penetrate directly into the private flux region without ionizing.

Fig. 8-21 shows the equilibrium chosen for our simulations. We use the magnetic equilibrium and divertor probe measurements from the discharge shown in Fig. 8-16, which has a line-integrated density of NL04 = 0.67×10^{20} m^{-2} and has a divertor profiles consistent with a high-recycling divertor state. At this density, we typically observe a net particle flux incident on inner divertor that is only about 150% of the poloidal flux passing the WASP (see Fig. 8-13). A KN1D simulation was carried out for each of the horizontal chords shown in panel (a) of Fig. 8-21, which covers the region of the inner divertor where a significant incident plasma flux is recorded with the embedded probes. We assume the density and temperature measured by the

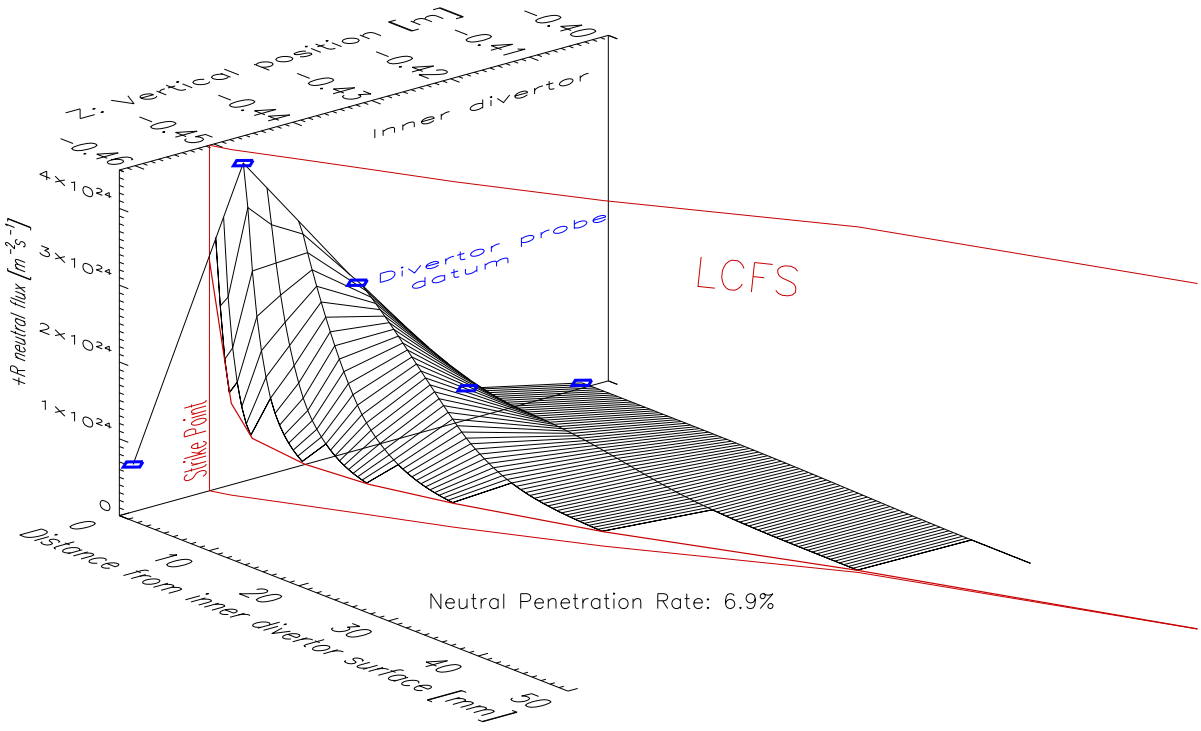

Figure 8-22: The results of the KN1D inner divertor simulations for shot 1070627006. The initial inward neutral flux from the inner divertor is shown, along with the outputs from the simulations which determine the inward neutral flux reaching the LCFS. By integrating over the region shown we find that the penetration fraction for neutrals born on the divertor surface is about 7%.

divertor probes is representative of that on the flux surfaces in the region simulated. A neutral flux equivalent to the incident plasma flux is launched from the divertor wall, and the simulation calculates the inward flux as a function of distance along the chord. Panel (b) shows the SOL outer midplane flux coordinate, ρ mapped onto the 8 chords that were simulated. This mapping was used to interpolate density and temperature measurements from the divertor probes onto the simulation chords.

Fig. 8-22 shows the result of the 8 KN1D simulations. Each one produces an inward neutral flux as a function of distance from the divertor surface based on the initial neutral flux launched from the divertor. The penetration of neutrals launched

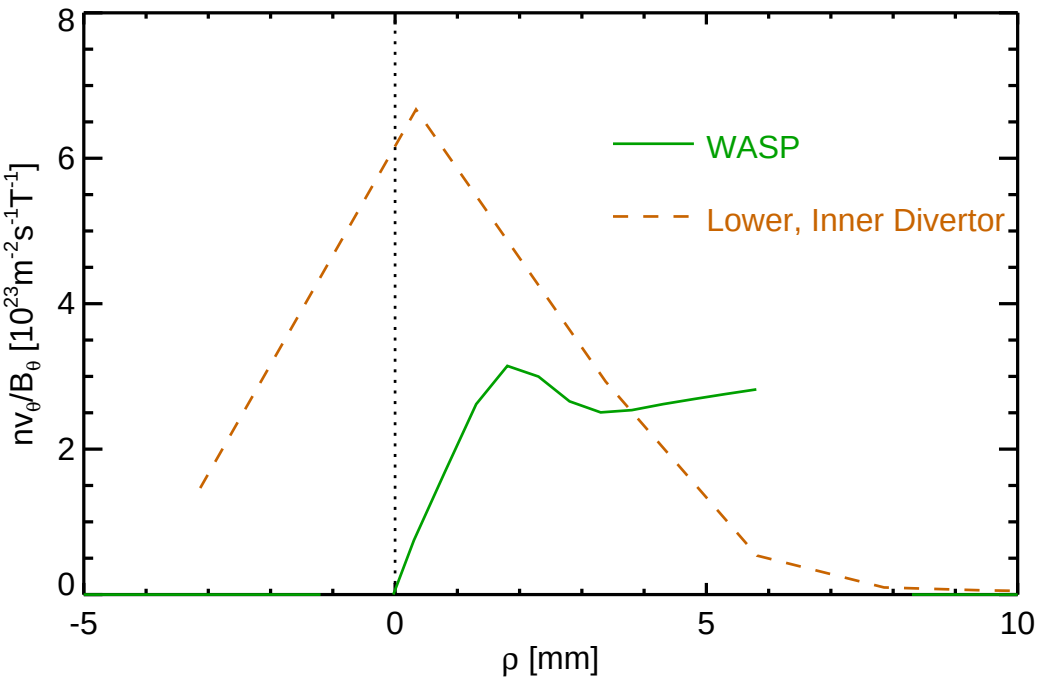

Figure 8-23: nv_θ/B_θ is the particle flux density normalized to the poloidal magnetic field. This quantity is constant flux surface for divergence-free flows. This allows us to compare flux densities measured at different poloidal locations. Here, we see that the particle flux density passing the WASP in the near SOL is much less than that arriving at the divertor, indicating a high-recycling state. In the far SOL, it is the opposite, with much higher flux densities at the WASP than the inner divertor. This is consistent with a region of volume recombination in the far SOL.

near the strike point is found to be small. We can determine the net neutral penetration rate by integrating the flux over the initial profile, compared to that reaching LCFS. We find that only 7% of the emitted neutrals reach the private flux region. Our modeling is consistent with a divertor that is in a high recycling state. This agrees with the temperature measurements and the results of other modeling. However, this result remains inconsistent with the observation that the flux incident of on the inner divertor is only 50% higher than that passing the HFS midplane. The high recycling level found in the KN1D simulations implies that the inner divertor flux should be greatly amplified over the upstream poloidal flux, as is consistently observed at the outer divertor.

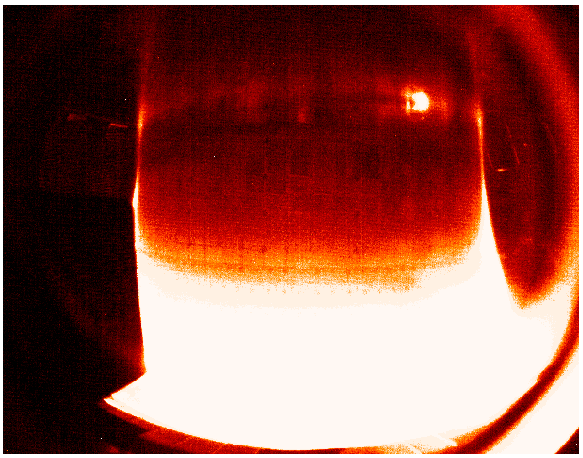

Figure 8-24: Recombination light from the inner divertor leg at the simulated time slice: 1070627006, $t = 0.91$ s. The K-WASP can be seen scanning. Note the difference between the intensity in the tangential view of the HFS SOL above and below the midplane. The volume recombination region appears to extend up the inner wall to approximately the midplane location.

Another possibility is suggested by a number of observations. The inner divertor is almost always observed to be 'partially detached' at low density. In Fig. 8-16, we can see that the temperature in the far SOL ($\rho \gtrsim 5$ mm) is below the 5eV detachment threshold, and the pressure does not map to the WASP data upstream. A comparison of the poloidal particle flux densities normalized to the poloidal magnetic field (nv_θ/B_θ) at the WASP and inner divertor is shown in Fig. 8-23. This quantity is poloidally invariant for the case of divergence-free flows. Much larger values of nv_θ/B_θ are observed at the divertor than the WASP in the near SOL, but smaller values of nv_θ/B_θ are observed at the divertor than at the WASP in the far SOL. This is consistent with detachment of the far SOL (where there is a sink due to volume recombination) and a high-recycling state in the near SOL (where there is a source due to ionization). Thus, the far SOL remains detached even in discharges with an 'attached' inner divertor. It is possible that this region contains an area of recombining plasma and neutrals. Substantial numbers of these neutrals might be able to penetrate the relatively thin, hot near SOL and reach the core (see Fig. 8-25). This region could span a very large area of the inner divertor leg ($2\pi R\Delta z \approx 2\pi \times 0.45$ m$\times 0.35$ m ≈ 1 m^2) and provide sufficient neutrals to return the observed WASP particle flux to the

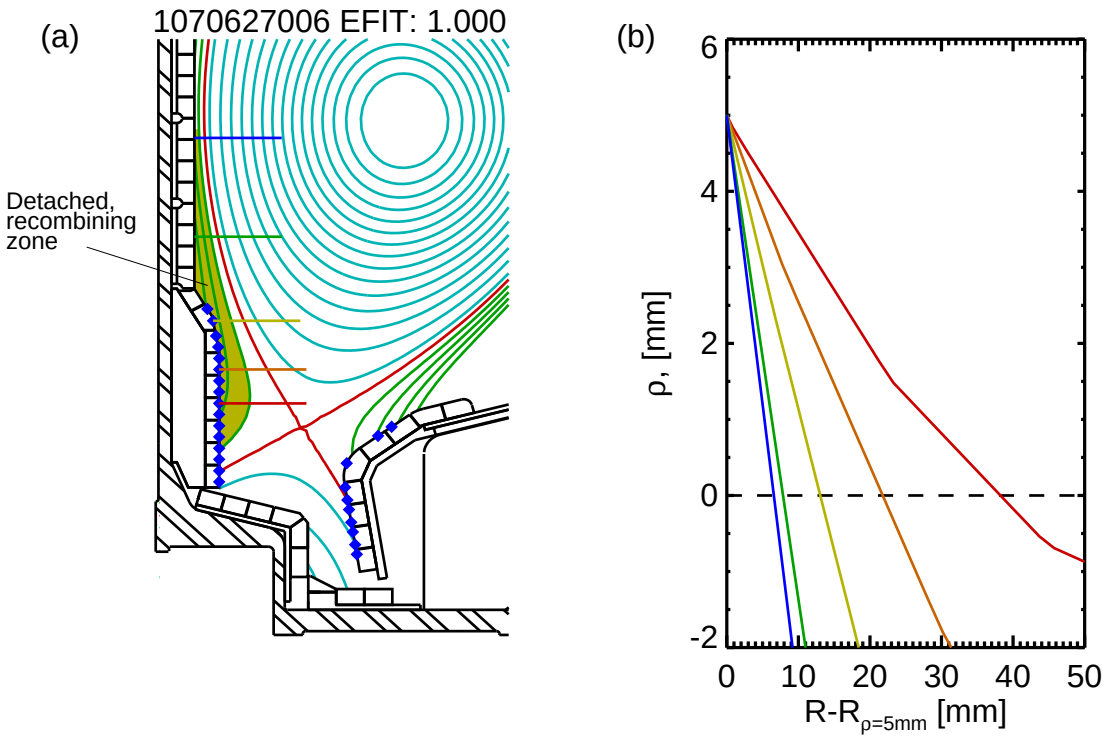

Figure 8-25: Partially detached divertor geometry. The shaded region in panel (a) below the HFS midplane at $\rho > 5$ mm is proposed to be a cold, detached volume recombination zone. We simulate the neutral penetration in this situation using the horizontal chords shown. The flux mapping onto these chords is shown in panel (b) for $\rho < 5$ mm.

core without extremely high penetration rates. Visible images of the HFS divertor region consistently show a very bright plasma region that envelops the entire divertor nose (see Fig. 8-24). This observation supports the idea that a large area of volume recombination is present at the inner divertor even at relatively low discharge density.

We can calculate the neutral penetration rate using KN1D. We assume that the temperature and density perturbations due to divertor recycling are localized near the divertor plate. We therefore use the WASP temperature and density profiles, mapped onto the chords shown in Fig. 8-25(a) using the flux mapping shown in Fig. 8-25(b). Because the HFS midplane has higher temperature and lower density than the divertor, this choice minimizes the collisionality of the plasma layer used in the simulation. Our result will therefore represent an upper bound on the neutral penetration rate, because closer to the divertor, we expect the plasma conditions

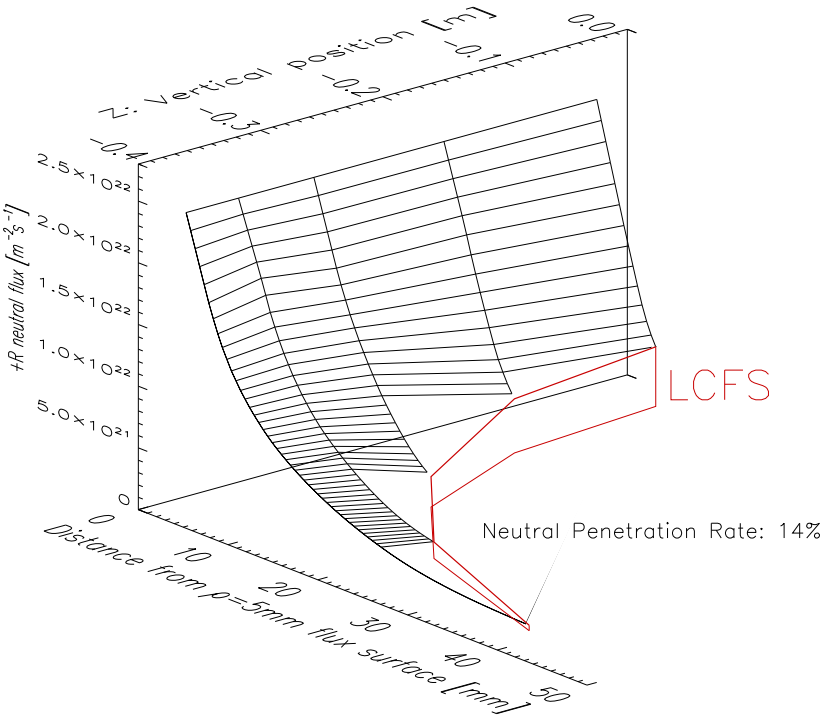

Figure 8-26: Results of KN1D simulation of neutral penetration from a region of recombining plasma in the far SOL. For simplicity, we assume that the entire HFS SOL below the midplane and for $\rho > 5$ mm is in a recombining state. The penetration fraction is then calculated on 5 chords from the 5 mm flux surface to the LCFS. The initial particle flux is adjusted so the total neutral flux reaching the LCFS exactly matches the total poloidal particle flux past the WASP toward the inner divertor.

to approach the divertor temperature and density. We begin the simulation at the $\rho = 5$ flux surface and determine the neutral penetration rate to the core assuming a constant neutral pressure in the recombining zone. We can then determine the neutral pressure required to cause a neutral penetration flux equal to the poloidal flux passing the WASP.

The result of the neutral penetration calculation from the volume recombination region is shown in Fig. 8-26. 14% of the neutrals launched from the 5 mm flux surface are found to penetrate to the core. This requires that the remainder be ionized in

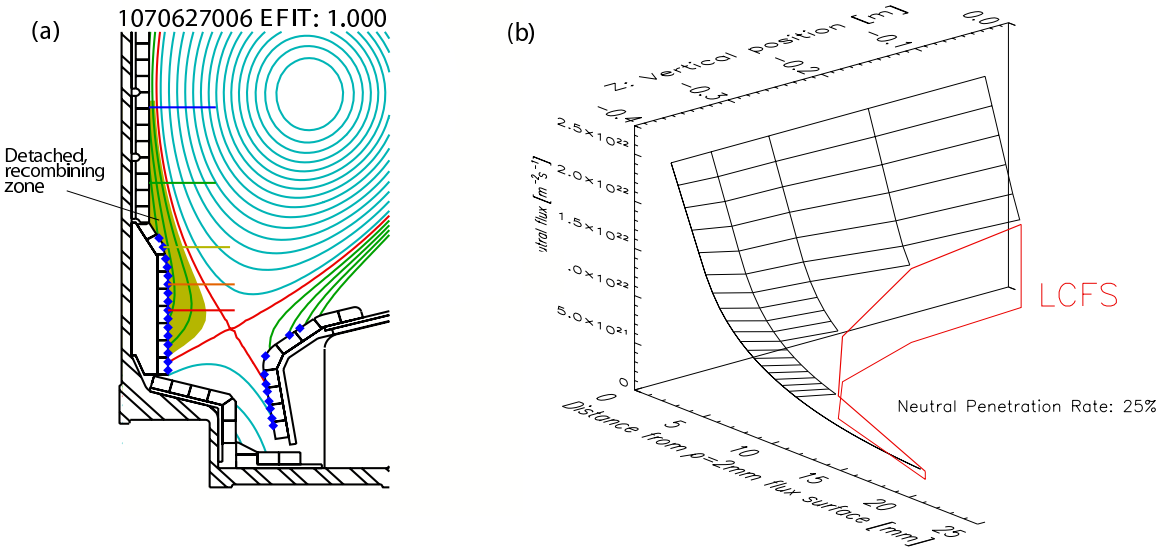

Figure 8-27: Simulation geometry and results for neutral penetration rate into the core from a region of volume recombination located outside the $\rho = 2$ mm flux surface.

the near SOL and be swept to the inner divertor, which in turn requires the inner divertor flux to be six times the WASP flux for the case of no recycling. This is not observed, so a volume recombination zone 5 mm from the LCFS cannot explain our results. In order to get sufficient neutral penetration the recombination zone needs to be closer to the core.

The KN1D simulations were re-run for the case of a volume recombination zone located at 2 mm in ρ-space. The results are shown in Fig. 8-27. In this case, the neutral penetration rate is about 25%. It is now possible to satisfy particle continuity with the inner divertor receiving a net particle flux only about three times higher than that at passing the WASP. For the neutral flux to the core to balance the observed poloidal flux passing the WASP location of 3.1×10^{21} m^{-2}s^{-1}, a neutral pressure in the volume recombination region of $\sim$6 mTorr is required. This mechanism is is a feasible alternative to those that our observations have ruled out, but the volume recombination region must be vertically extended, and very close to the confined plasma. In addition, the 75% of neutrals that are ionized in the near SOL and flow to the divertor must somehow find their way back into the recombining region. We are not aware of feasible mechanism by which this might occur. Adding the fact

that we must push the model to the limits of feasibility to get close to quantitative agreement means that neutral penetration is not likely to be the soul mechanism returning particles to the core. However, we find that it could play a significant role.

To determine more conclusively whether this type of volume recombination is important in producing the near-sonic parallel flows observed at the HFS midplane requires a 2-D edge simulation that includes this effect. Such a simulation is beyond the scope of this work, but it is recommended that volume recombination effects be included in future edge simulations. From an empirical perspective, one way to investigate this hypothesis would be to run helium discharges where the level of volume recombination would be greatly reduced. If a dramatic change in HFS conditions is observed in helium discharges, it would support the idea that volume recombination plays an important role in closing the HFS mass flow loop.

8.3 Poloidal Heat Flux

Having determined the total flow vector in the SOL, we are now in a position to evaluate the total heat flux in the poloidal direction (along and across field lines) and its dependence on discharge parameters. Section 8.3.1 discusses the methods used to extract the poloidal heat flux from the data. The relative importance of convection (parallel and perpendicular) in the HFS SOL power balance is examined in section 8.3.2. It is found that convection plays an important role in the poloidal heat flow, particularly in the far SOL where T_e is low and parallel conduction becomes less important than convection. $E_r \times B$ drifts also play an important role, carrying heat to the inner divertor in favorable topologies and away from the inner divertor in unfavorable topologies. This trend is found to offer an explanation for the formation of low-T_e conditions in the HFS SOL in normal field direction, LSN discharges at low densities.

8.3.1 Methods for Calculating Poloidal Heat Flux

In order to calculate the total poloidal heat flow, we to include parallel conduction and convection, as well as perpendicular convection. We begin with the equation for parallel heat flux, including both conductive and convective terms. We neglect classical perpendicular conduction as much smaller than parallel conduction[2]. We also make the assumptions that $T_i = T_e$ and $n_i = n_e$.

$$q_\parallel = q_{conv} + q_{cond} = 5nkT_e v_\parallel - \kappa_\parallel^e \nabla_\parallel T_e \tag{8.9}$$

$$= 5nkT_e M_\parallel c_s - 320\frac{6\pi\sqrt{2\pi}\varepsilon_0^2 (kT_e)^{5/2}}{\sqrt{m_e}\ln\Lambda e^4}\nabla_\parallel T_e \qquad [\mathrm{Wm}^{-2}] \tag{8.10}$$

$$= 5nkT_e M_\parallel \sqrt{\frac{2kT_e}{m_i}} - 1.82\times 10^5 T_e^{5/2}\nabla_\parallel T_e \qquad [\mathrm{Wm}^{-2}] \tag{8.11}$$

$$= 770 n_{20} M_\parallel T_e^{3/2} - 52\nabla_\parallel T_e^{7/2} \qquad [\mathrm{kWm}^{-2}] \tag{8.12}$$

The coefficient of 5 for the convective heat flux is characteristic of convective energy transfer by an isenthalpic steady flow, where an energy of $\frac{5}{2}kTv$ is carried by each species. It has been simplified for the case of a deuterium plasma. The conductive heat flux is the standard form for a hydrogenic plasma with the thermal conductivity $\kappa_\parallel^e$ as given in [44], but expressed in SI units. T_e here is in eV and n_{20} is density in units of 10^{20} m^{-3}. The Boltzmann constant for this temperature convention is $k = 1.602\times 10^{-19}$ J/eV. Eqn. 8.12 casts the parallel heat flux in terms of measured quantities, requiring a gradient only in $T_e^{7/2}$.

Having described the parallel heat flux in Eqn. 8.12, we next project this result into poloidal space. The field line pitch angle $\zeta = \arctan(B_\theta/B_\phi)$ is used to project the parallel heat flux into poloidal space. By analogy to the parallel convection, we can add a term describing perpendicular convection using the measured perpendicular velocity[3].

[2]The ratio of perpendicular to parallel thermal conductivity is given by: $\kappa_\perp^e/\kappa_\parallel^e \approx (\nu_{ee}/f_{ce})^2$. In the C-Mod edge, cyclotron frequency is always at least 1000 times the collision frequency, so even accounting for the field line pitch angle, $\kappa_\perp^e \ll \kappa_\parallel^e \sin\zeta$ is always well satisfied.

[3]Velocity is used in this term instead of Mach number because the immediate result of the

$$q_\theta = (770 n_{20} M_\parallel T_e^{3/2} - 52 \nabla_\parallel T_e^{7/2}) \sin\zeta + 0.08 n_{20} T_e v_\perp \cos\zeta \quad [\mathrm{kWm}^{-2}] \qquad (8.13)$$

We again use the measured $E_r \times B$ perpendicular velocity and neglect diamagnetic velocity. For case of the heat flux calculation, we do not invoke the argument that diamagnetic fluxes are not collected at the divertor, because we are also interested in the temperature of the HFS plasma. However, given similar ion and electron temperatures, the diamagnetic heat fluxes from ions and electrons are equal and opposite, and thus do not lead to heat poloidal heat flow to first order.

The challenge in evaluating Eqn. 8.13 is obtaining the parallel gradient in T_e. This requires a fit to the measured temperature data in parallel space. To determine the best method of fitting the temperature, it is instructive to consider the case where parallel conduction is the dominant heat transport mechanism. In this case, heat flux goes simply as $\nabla_\parallel T^{7/2}$. We therefore expect that if $q_\parallel$ is constant, then $T^{7/2}$ varies linearly with parallel distance. If there is a heat source at some location, due to the divergence of the perpendicular heat flux, then the curvature of $T^{7/2}$ is negative. Likewise, a heat sink appears as positive curvature. Fig. 8-28 shows the expected heat flux and temperature profiles for the case of ballooning-like transport, characterized by Gaussian distribution of radial heat flux on the LFS. Based on this exercise, it is evident that the heat flux distributions will be very sensitive to the shape of the fit chosen for T_e. To avoid biasing the result, we will use the simplest possible fitting technique; straight lines are drawn between $T_e^{7/2}$ data in parallel space. The conductive heat flux at each probe location is then taken to be proportional to the average value of $\nabla_\parallel T_e^{7/2}$ on either side of the probe.

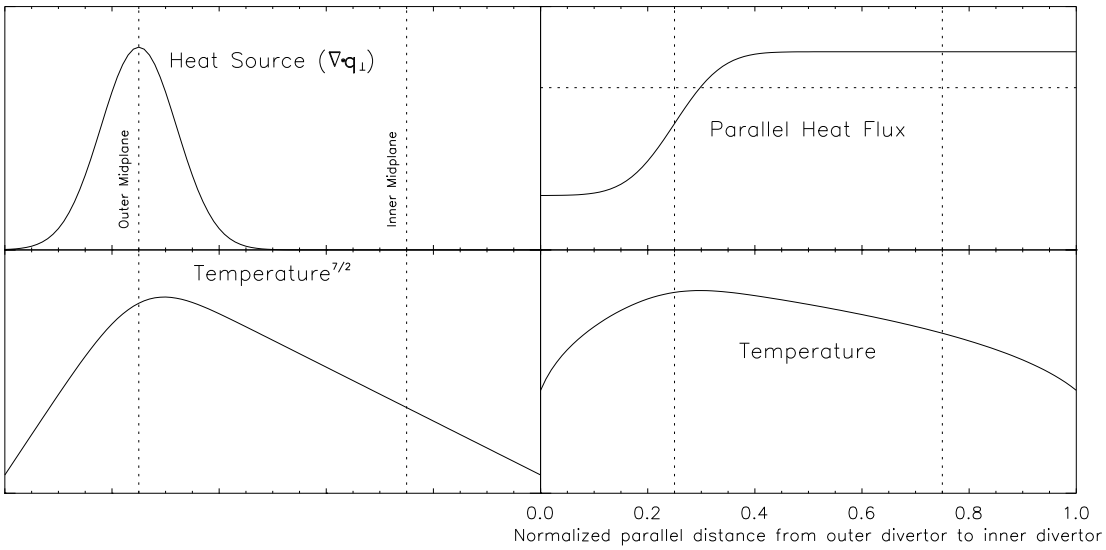

Figure 8-28: Sample parallel profiles expected from a ballooning-like poloidal transport distribution. The source results in an area of negative curvature in the resulting $T^{7/2}$ profile. Otherwise, $T^{7/2}$ is linear. To keep the results simple yet realistic, we will conduct parallel temperature fits in $T^{7/2}$ space.

8.3.2 Topology and Density Dependence of HFS Poloidal Heat Flux Components

The results of the procedure for calculating poloidal heat flux, described in section 8.3.1, are summarized in Fig. 8-29. To produce this figure, heat flux values calculated on individual flux surfaces were binned and averaged for a variety of discharges. There are four bins separated by topology (USN vs. LSN) and density. The low density bin includes discharges with NL04 $< 0.7 \times 10^{20}$ [m^{-2}], while the high density bin is for $0.7 \times 10^{20} <$ NL04 $< 1.0 \times 10^{20}$ [m^{-2}]. In each bin, the poloidal heat flux components were calculated at each mm in ρ space from $\rho = 1$ mm to $\rho = 8$ mm at the WASP location. All data are from discharges with normal field and current direction, at standard values (5.4 T, 0.8 MA).

Several observations can be made from Fig. 8-29:

1. The convective heat flux is not negligible on the HFS. In fact, the parallel

$E_r \times B$ technique for measuring perpendicular flows is a velocity. However, a Mach number could equivalently be substituted using the same coefficient is in the first term.

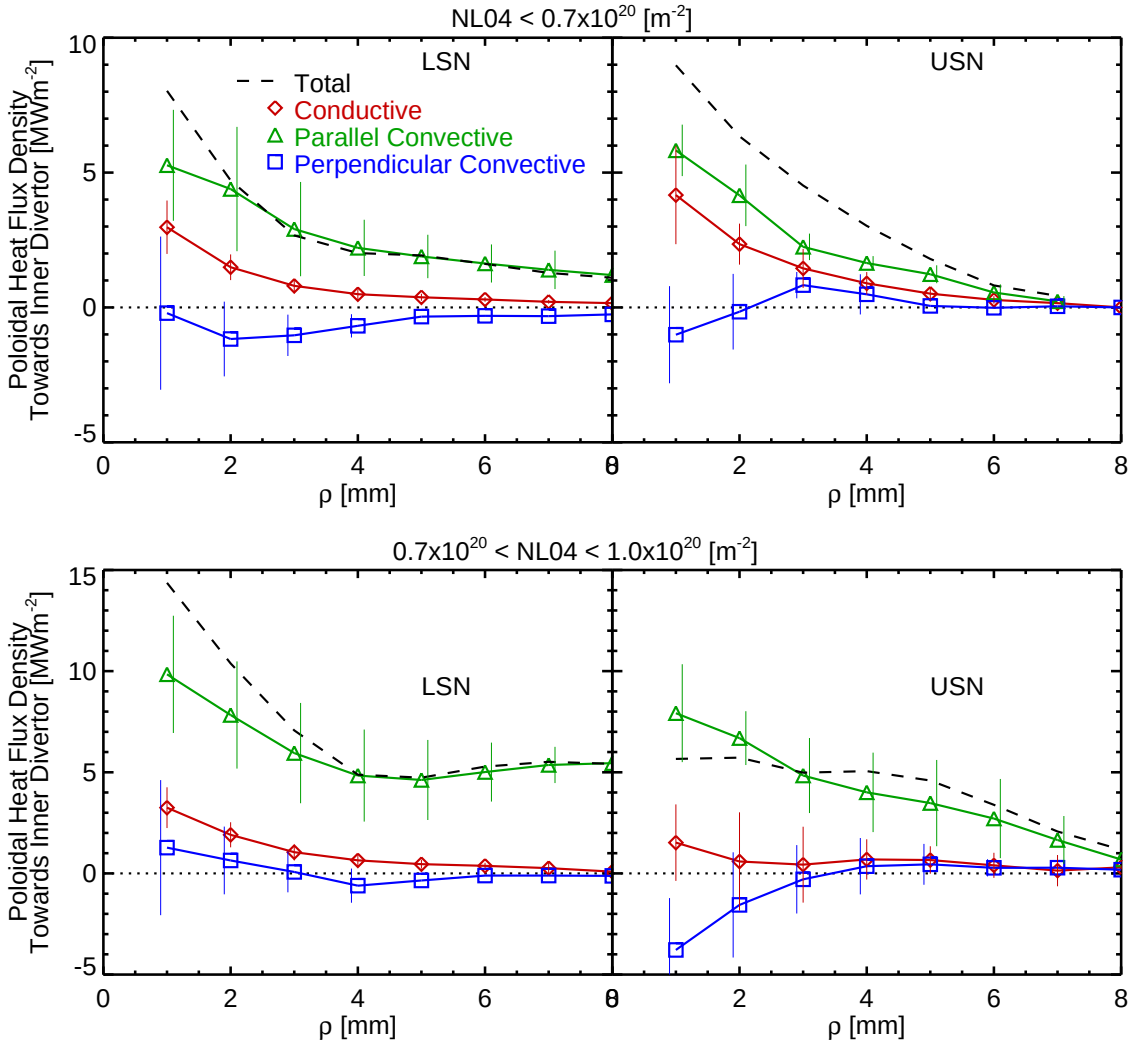

Figure 8-29: Poloidal heat flux profiles calculated from WASP probe measurements. The dashed black curve shows the net poloidal heat flux, which is the sum of the parallel and perpendicular convective components and the conductive component.

convected heat flux nearly always exceeds the conducted heat flux.

2. The parallel convective heat flux becomes the dominant poloidal heat transfer mechanism in the far SOL in all discharge conditions.

3. The perpendicular convective heat flux reverses direction from LSN to USN, as expected for a drift-driven effect. At low density, it is away from the inner divertor in LSN and towards the inner divertor in USN for 2 mm $< \rho <$ 4 mm.

4. At high density, the perpendicular convective component still shows reversal with topology, but the dominant feature is a tendency in the near SOL ($\rho <$ 2 mm) toward the inner divertor in LSN and away from the inner divertor in USN. This flow pattern is the result electric fields that point inward in minor radius, normally characteristic of closed field lines.

5. At high density, the parallel convective term is larger in the far SOL for LSN than USN discharges, and the conductive term is large in the near SOL for LSN than USN discharges. These two effects, combined with the perpendicular convective reversal lead to much higher poloidal heat flux toward the divertor in LSN than USN at high density.

Observation (3) may be an explanation for the systematically reduced HFS temperatures in LSN discharges at low density. This observation is illustrated in Fig. 8-30. The temperature at the WASP decreases and the floating potential increases in a density range of NL04 between 0.5×10^{20} and 0.7×10^{20} m^{-2}. The temperature reduction is most pronounced around $\rho = 4$ mm, the same location where the perpendicular convective heat flux is maximized. It thus seems likely that the change in direction of the $E_r \times B$ drift relative to the divertor location is causing the total heat flux from the LFS to the HFS to change enough to affect the HFS temperature.

These observations are consistent with those reported by Hutchinson *et al.* [46][4]. They observed colder inner divertors in favorable drift direction than in unfavorable

[4]In this case, field reversal was used rather than topology reversal to change the direction of $B \times \nabla B$ with respect to the x-point.

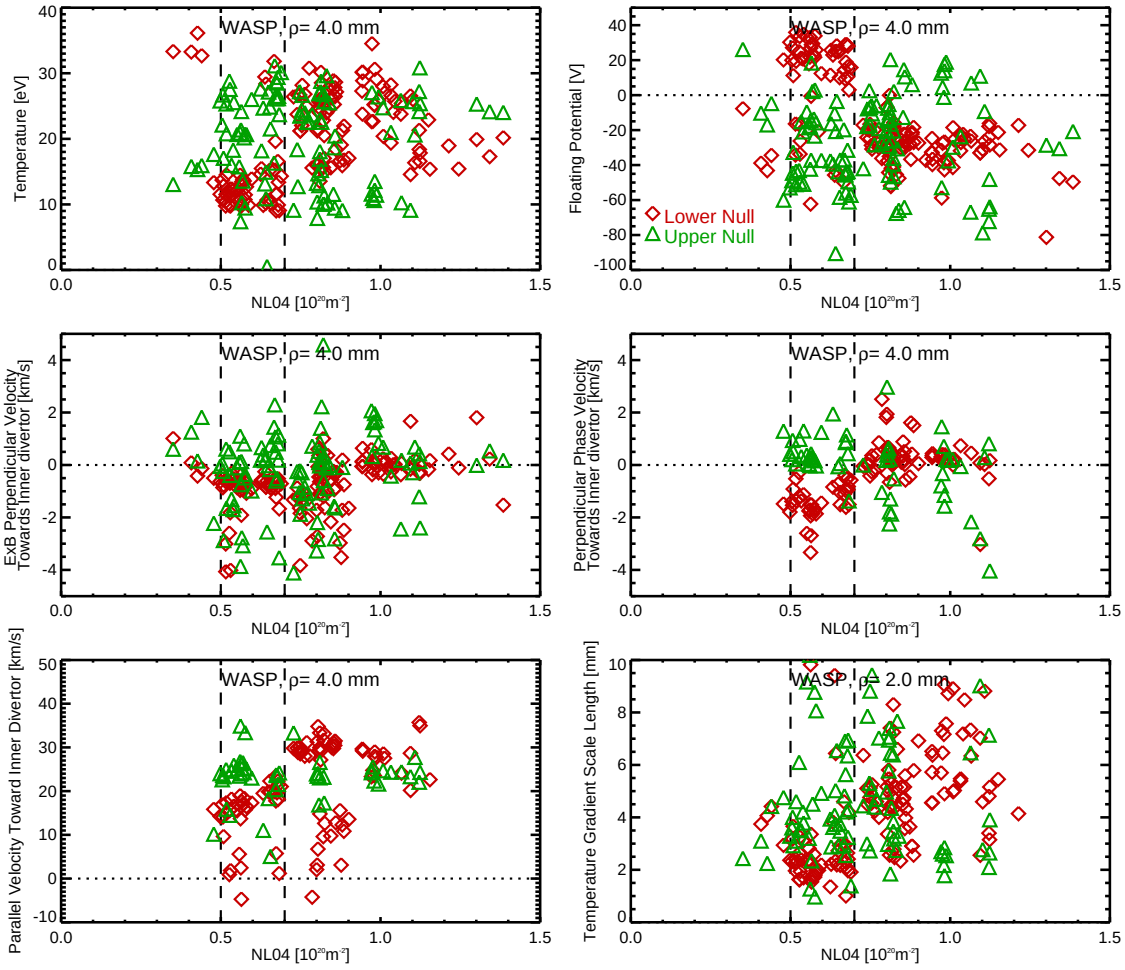

Figure 8-30: The temperature depression observed at the WASP location at low density in LSN. The dashed lines indicate the approximate density range where these conditions are observed.

drift direction. It was shown that the asymmetry was more likely the result of a heat flux asymmetry than a pressure asymmetry. $E \times B$ convection was proposed as a possible cause for the observed asymmetry, consistent with the heat flux measurements presented here.

Hutchinson *et al.* also observed that divertor heat flux asymmetries between favorable and unfavorable drift directions are greatly reduced at high density, as are radiation asymmetries from the divertor legs. This is consistent with our observations as well. At higher densities, above NL04 = 0.7×10^{20} m^{-2} (see Fig. 8-30), the the temperature asymmetry between topologies is not observed. The poloidal heat flux measurements indicate that at higher density, the $E_r \times B$ convection is a relatively small portion of the total heat flux in much of the HFS SOL ($\rho > 2$ mm). Therefore, its reversal should not have so great an effect on the HFS SOL conditions as it does at low density.

The $E_r \times B$ drift is not the only component of the heat flux that shows sensitivity to the drift direction. Observations (4) and (5) indicate that at high density, the USN discharges have reduced poloidal heat flux toward the inner divertor. This is consistent with the observation of the reduced density threshold for MARFE onset in unfavorable drift direction, which was described in section 8.2.5. If the poloidal heat flux toward the inner divertor is reduced, then the HFS SOL can more easily reach temperatures low enough for volume recombination. The dominant factor here would appear to be the parallel convective heat flux in the far SOL, which may be connected to the volume recombination physics proposed in 8.2.7, and its dependence on divertor and x-point geometry. The change in conductive heat flux should not be involved in MARFE onset, because the high inner divertor temperatures (see [70, 21] and Figs. 8-15 and 8-16) leading to reduced conduction in USN do not persist in the case of a MARFE.

Chapter 9

Concluding Remarks

In this section, the work and findings of this thesis are briefly summarized. A list of unique contributions to the field of tokamak edge physics is presented. Finally, some possible directions for future work are suggested.

9.1 Summary of Work

In order to investigate the origins of near-sonic parallel flows in the HFS SOL on Alcator C-Mod, a novel, magnetically-actuated scanning Langmuir probe was constructed and installed on the tokamak inner wall. This probe has a linear plunge action, and a four-electrode high-heat flux tip, similar to those on the LFS pneumatic scanning probes. The new HFS probe and the LFS probes were outfitted with novel high-heat flux Gundestrup electrode geometries for the 2007-2009 campaigns. This configuration is capable of measuring the parallel flow velocities, perpendicular velocities and radial fluctuation-induced velocities throughout the SOL and a few mm into the confined plasma.

Two techniques are available for measuring perpendicular plasma velocity. The standard technique uses measurements of floating potential and electron temperature to infer radial profiles of plasma potential. This is used to evaluate the radial electric field and associated perpendicular $E_r \times B$ drift velocity. The $E_r \times B$ technique suffers from several sources of uncertainty so a new method of measuring perpendicular fluid

velocity was sought. The Gundestrup technique uses an array of angled facets to infer perpendicular plasma motion from a fluid model of the plasma-probe interaction. It was thought that this technique would provide more reliable results than the $E_r \times B$ technique.

Gundestrup measurements on C-Mod made with the new probes show unexpectedly large velocities in the electron diamagnetic direction. These are present far into the SOL for a variety of plasma conditions. This flow pattern disagrees with the $E_r \times B$ pattern even in cases where $E_r \times B$ measurements are thought to be reliable. Several attempts were made to identify the cause of the observed offset between the two techniques. Validity of the fluid model, flux surface misalignment, diamagnetic corrections, non-linear effects due to drift waves and probe-induced perturbations were all considered as potential explanations for the discrepancy. Unfortunately, we were unable to identify the cause of the offset. We proceeded using the $E_r \times B$ method of measuring perpendicular flows. Though this technique suffers from some uncertainty, we believe it is more accurate than the Gundestrup technique.

A variety of experiments were conducted using the array of scanning probes. One goal was to look for direct evidence of edge-core momentum coupling. Specifically, we wanted to know whether the HFS transport-driven flows are responsible for the observed changes in core rotation from USN to LSN discharges. To accomplish this, we used a 'nose-grazing' magnetic topology to produce LSN-like HFS flows with USN-like magnetic topology. The results of this experiment were inconclusive. We did succeed in creating LSN-like flows in the near SOL on the HFS, but did not observe the co-current increment in core rotation that normally accompanies a topology reversal from USN to LSN. However, this may be due to the fact that our experiment did not produce a LSN-like flow pattern in the far SOL, which may play a critical role in core-momentum coupling through volume recombination and neutral penetration.

Another goal was to examine the flow shearing rates and their dependence on collisionality and topology. An analysis was carried out at the LFS midplane location to examine the shearing rates observed there. We find that a 'shear layer' is usually present in measurements of perpendicular velocity. It is located at or a few mm outside

the LCFS and is characterized by peak shearing rates of 1-4 MHz. The observed shearing rate depends on both discharge collisionality and magnetic topology. At low collisionality, we see the highest shearing rates, typically around 3 MHz, which have very little dependence on magnetic topology. At higher collisionality, the shearing rate is reduced to 1-2 MHz, and becomes dependent on magnetic topology. The high collisionality cases have higher shearing rates in favorable $B \times \nabla B$ drift direction than in unfavorable drift direction. The observed shearing rates are similar in magnitude to the ideal ballooning mode growth rate calculated from the measured pressure gradients (~ 2 MHz). The calculated ideal ballooning mode growth rate does not show strong dependence on collisionality, but does show a similar topology dependence at high collisionality to that observed for the flow shearing rates. These observations suggest that the LFS transport is dominated by ballooning-like instabilities that are regulated by perpendicular flow shear.

In order to make contact with the existing body of work on edge flows, we compared our results to the results of edge simulations. Two recent edge simulations directly address C-Mod. The first is a B2 Eirene SOLPS5.0 simulation conducted by Bonnin *et al.* [41, 69]. This code did not match the measured LFS parallel flows or the measured perpendicular flows. The $E_r \times B$ flow results from the code were consistent with radially inward electric fields in the SOL. This is in disagreement with the measured radial electric field, which is usually outward in the SOL. Perpendicular flows and LFS parallel flows in the simulation were generally several times larger in magnitude than those measured. The code roughly matched the HFS parallel flows observed on C-Mod, but did so without implementing any transport asymmetry, which we believe to be the primary cause of the experimentally observed parallel flows on the HFS.

The second simulation addressing the C-Mod edge was carried out by Pigarov *et al.* using the UEDGE code [14] with a focus on matching the observed HFS parallel flows. In order to reproduce the flow pattern observed on C-Mod, this simulation imposed a convective radial plasma flow of 20 m/s from the HFS divertor region into the private flux region. We are not equipped to search for radial flows into the

private flux region experimentally, but our HFS midplane WASP observations show radial velocities that are approximately zero, with an uncertainty less than 5 m/s. Clearly, a substantial amount of work remains to bring simulation and experimental observations into agreement.

Our measurements of the total flow vector allow us to assemble a picture of the net poloidal transport of heat and particles in the edge, and extract the systematic dependence of the flows on magnetic field direction and magnetic topology. Poloidal flows that are dependent on magnetic topology are called transport-driven flows, which are thought to be the result of pressure gradients resulting from poloidal asymmetries in radial transport. Poloidal flows that are dependent on magnetic field direction are called drift-driven flows. These result from particle drifts caused by the toroidal magnetic field and radial gradients of plasma parameters. These two poloidal flow components change direction relative to one another depending whether the discharge is in a favorable ($B \times \nabla B$ toward the x-point) or unfavorable ($B \times \nabla B$ away from the x-point) configuration. By comparing measurements from favorable and unfavorable cases, we can unambiguously extract these two flow components. We expect the transport-driven component to have a divergence that is reflective of the poloidal distribution of radial transport, while the drift-driven component should be divergence-free. The data agree with this model, showing values of nv_θ/B_θ that are poloidally invariant for the drift-driven component, and a transport-driven poloidal flow on the HFS that is consistent with that expected from the divergence of the measured LFS radial particle flux. These observations provide a valuable consistency check, which enhances our confidence in the measurements of the various flow components. The flow decomposition procedure also allows us to unambiguously identify the contribution of Pfirsch-Schlüter ion flows, toroidal rotation and transport-driven flows to the observed parallel flows.

The total flow data show that the HFS transport-driven parallel flows are the dominant contributor to poloidal flows at that location, and confirms that the understanding arrived at by measurement of the parallel flows alone is correct. On the LFS, the drift-driven components are the dominant contributor to the poloidal flows, with

both parallel and perpendicular flows making significant contributions. We observe that the net poloidal flow approaches zero a few mm inside the LCFS, consistent with the expectation that inward radial electric fields should balance the the pressure gradient force on closed flux surfaces.

Poloidal flow measurements were used to characterize the bulk poloidal motion of particles in the SOL. This was done by integrating poloidal guiding center motions over the available radial extent of the data at each scanning probe location. The result shows that the poloidal stagnation point varies with magnetic topology. It is found to be closer to the x-point in normal field LSN (favorable) discharges and closer to the crown in normal field USN (unfavorable) discharges. This is due to drift-driven Pfirsch-Schlüter flows that shift the stagnation point in the electron diamagnetic direction, and not due to any change in the poloidal distribution of radial transport. The poloidal flow data also show that the particle flux to the inner divertor does not greatly exceed the flux measured at the WASP even in cases where divertor measurements indicate that the near SOL is in a high-recycling state. This is in contrast to the behavior of the outer divertor in similar conditions. The particle flux to the outer divertor is greatly enhanced over that observed upstream when the divertor is in a high-recycling state. These observations suggest that another mechanism is returning particles to the core on the HFS. Candidates for this mechanism include radially inward convection and volume recombination.

Measurements of fluctuation-induced particle flux at the HFS midplane show that the fluctuation-induced radial convective velocity is zero, and that a turbulent inward particle pinch is not present at this location. We therefore look to volume recombination to explain the HFS particle flux observations. One way we can directly observe the effect of volume recombination is to look at discharges in which a MARFE is present. Data from discharges with a MARFE located poloidally between the LFS and the WASP location show that the plasma pressure measured by the WASP is greatly reduced from the MARFE-free case. The parallel velocity of the HFS plasma in the cases with a MARFE is toward the MARFE rather than toward the x-point as is normally observed. These observations show that the MARFE is capable of

absorbing all of the incident plasma flow from the LFS.

The MARFE observations provide a hint that volume recombination near the HFS divertor may also be capable of absorbing the incident poloidal particle flux. We propose that neutral penetration from a zone of volume recombination could play a significant role in returning particles to the core, even in low density discharges. This hypothesis is based on the observation that the state of the inner divertor does not change a great deal with discharge density. This is in contrast to the outer divertor, which progresses from sheath-limited to high-recycling to detached regimes as the density is raised. At the inner divertor, the near SOL is nearly always attached while the far SOL is detached. This indicates that a region of volume recombination may be present in the far SOL that absorbs the bulk of the plasma flux from the LFS and delivers a substantial neutral flux to the core through a thin, hot layer of attached plasma in the near SOL. 1-D neutral penetration simulations indicate that this mechanism is capable of delivering significant neutral flux to the core if the attached layer is very thin ($\sim$2 mm). However, this mechanism by itself cannot explain the reduced particle flux to the inner divertor.

Measurements of total poloidal flow can be combined with temperature measurements at the three poloidal scanning probe locations to calculate the total poloidal heat flux in the HFS SOL. This is composed of parallel conduction and parallel and perpendicular convection arising from the flow velocities. We find that convective heat flux is not only an important contributor to the total poloidal heat flux, but is often the dominant heat flux mechanism. Perpendicular convection plays an important role as well, reversing direction from toward the inner divertor in unfavorable drift direction to away from the inner divertor in favorable drift direction. For low density discharges, this results in relatively cold HFS SOL plasma in favorable drift direction where the perpendicular convective heat flux is away from the divertor. At high density, we observe different trends with magnetic topology that appear to be connected to the inner divertor state. In this case we observe higher heat flux toward the inner divertor in LSN, not due to perpendicular convective effects, but a combination of parallel convective and conductive effects. The conductive effect comes into

play in the near SOL, possibly due to the different divertor temperatures observed in USN vs. LSN. In normal field, USN, the inner divertor is hotter than in LSN. This may lead to reduced conductive heat flux toward the inner divertor. In the far SOL, parallel convection is observed to change with topology. Parallel flows are found to be stronger toward the inner divertor in LSN than USN. This may be connected to the volume recombination effects mentioned in section 8.2.7, which are likely sensitive to the inner divertor geometry. To summarize, the poloidal heat flux toward the inner divertor in normal field direction is slightly higher in USN than LSN at low density, and higher in LSN than USN at high density.

9.2 Unique Contributions

This thesis has made the following unique contributions to the field of edge physics:

1. Development of a compact 'pop-up' Mach probe (WASP).

2. First-of-a-kind total flow vector measurements on low and high-field side midplanes.

3. Showed that the total flow vector can be understood in a quantitatively consistent way as a superposition of drift-driven and transport-driven components.

   - Consistency of drift-driven component: measured flow is divergence-free.
   - Consistency of transport-driven component: radial fluctuation-induced fluxes quantitatively account for transport-driven poloidal flow.

4. Measured fluctuation-induced radial particle flux at the high-field midplane, showing that there is no turbulent inward pinch present at that location.

5. Found that heat convection (parallel and $E_r \times B$) is an important player on the high-field side SOL.

6. Found that $E_r \times B$ convective heat fluxes to inner divertor led to a colder (hotter) high-field SOL in favorable (unfavorable) $B \times \nabla B$ drift direction for

low density discharges, in agreement with previous divertor asymmetry studies [46].

9.3 Future Work

The advances in understanding accomplished in this thesis of course lead to new open questions that fall to future researchers to investigate. A few specific experiments are suggested in this section that would address these open questions directly.

One observation that begs for additional inquiry is the disagreement between $E_r \times B$ and Gundestrup measurements of the perpendicular velocity. Though our investigations failed to conclusively determine the cause of this disagreement, additional experiments could provide more insight into the problem. Ideally, a third measurement of the perpendicular velocity could be used as a 'tie-breaker' between the other two methods. For instance, the perpendicular flows could be measured spectroscopically perhaps using CXRS measurements of the bulk species. If CXRS and probe diagnostics could be designed so as to have an overlapping operational range, then their measurements of perpendicular flow could be compared directly.

Another method of resolving our problems with perpendicular flow measurements is to gather additional data about the validity of the techniques we are using. One possibility is the use of a scanning emissive probe to measure Φ_p directly, in order to verify the accuracy of our measurements of $E_r \times B$ flow. Turning to the Gundestrup probe, we could use retarding field analyzer (RFA) probe [73] to measure ion temperature directly. This method would allow direct evaluation of all the diamagnetic terms in Hutchinson's Gundestrup formula [11] (Eqn. 2.6b), including those that require a measurement of the ion temperature gradient. Another possible experiment would be the use of additional Langmuir electrodes on the probe shaft to investigate the possibility of $E \times B$ circulation of the probe body pre-sheath due to temperature gradients, as discussed in section 5.5.2. Electrodes placed in the probe shadow in the parallel direction could be used to investigate pre-sheath temperature drop and its influence on the Gundestrup perpendicular flow measurements.

Another open question resulting from this work is whether there exists a turbulent particle pinch in the vicinity of the x-point. Based on our investigations in section 8.2, we concluded that this was the most likely mechanism for closing the HFS mass flow loop. Additional electromagnetically actuated scanning probes, based on the WASP design, could be used to investigate radial particle fluxes in the x-point region. Because of the additional space available behind the inner divertor tiles, a probe with significantly longer stroke could be built using a similar design to the WASP. Radial particle flux measurements from such a probe could be used to quantify the magnitude of the turbulent radial particle flux that is present in the inner divertor region.

A slightly more ambitious possibility is that multiple electromagnetically actuated scanning probes could be deployed at closely space poloidal intervals. This would allow us to investigate the DC component of the poloidal electric field, and evaluate its potential role in causing particle drifts into the core plasma. To address the questions of inner divertor dynamics that have concerned us in this thesis, such an array would ideally be located between the HFS midplane and the inner divertor strike point, along the inner divertor leg.

Volume recombination was investigated in section 8.2.7. It was found that it might play a role in closing the HFS mass flow loop. One method to investigate this possibility in more detail is to use discharges with a helium majority. Because fully stripped helium ions are doubly charged, volume recombination is substantially reduced. If significant changes in the HFS parallel flows were observed in helium majority discharges as compared to deuterium discharges, it would imply that volume recombination plays a major role in closing the mass flow loop. Another possibility is to run extremely low-density discharges and attempt to obtain fully-attached inner divertor conditions. If this caused a substantial change in HFS flows, it would also be suggestive of the importance of volume recombination.

This thesis was focused exclusively on studying edge flows in L-Mode discharges, but some features of the WASP make it ideal for studying flows in H-modes as well. Its location on the HFS has been observed to substantially reduce sheath-rectification problems that are normally associated with operating the LFS scanning probes during

RF-heated discharges. It appears that there is sufficient single-pass absorption to limit these effects in the HFS SOL. Studies of HFS flows in H-mode plasmas might be useful for determining the relative magnitude of perpendicular flow shear in high and low confinement modes. The physics of L-H transition power threshold and its dependence on magnetic topology could also be investigated, with the HFS probe location ideally suited for evaluating the possible role of the near-sonic, transport-driven parallel flows in the transition.

Appendix A

Calculation of Transport Implied by HFS Poloidal Particle Flux

A.1 Coordinate System

Consider a toroidal coordinate system (r, θ, ϕ) that describes concentric circular flux surfaces. R is the major radius and θ is measured from the outer midplane. The scale factors are:

$$h_r = 1 \tag{A.1}$$

$$h_\theta = r \tag{A.2}$$

$$h_\phi = (R + r\cos\theta) \tag{A.3}$$

The divergence operator can be expressed as:

$$\begin{aligned}\nabla \cdot \vec{u} = &\frac{1}{r(R + r\cos\theta)}\frac{\partial}{\partial r} r(R + r\cos\theta)u_r \\ &+ \frac{1}{r(R + r\cos\theta)}\frac{\partial}{\partial \theta}(R + r\cos\theta)u_\theta + \frac{1}{(R + r\cos\theta)}\frac{\partial}{\partial \phi}u_\phi\end{aligned} \tag{A.4}$$

A.2 Approximations

In the case of the SOL, $r \approx a$ and h_ϕ can be expressed as $h_\phi \approx R(1 + \varepsilon \cos\theta)$ where ε is the inverse aspect ratio, $\varepsilon = a/R$. We also invoke toroidal symmetry so that $\frac{\partial}{\partial \phi} = 0$. The divergence operator then becomes:

$$\nabla \cdot \vec{u} = \frac{\partial}{\partial r} u_r + \frac{1}{a(1 + \varepsilon \cos\theta)} \frac{\partial}{\partial \theta} (1 + \varepsilon \cos\theta) u_\theta \tag{A.5}$$

Next, we note that in this simplified geometry, $B_\theta \sim 1/R$, and can be written as:

$$B_\theta = \frac{B_o(r)}{1 + \varepsilon \cos\theta} \tag{A.6}$$

This allows us to write Eqn. A.5 as:

$$\nabla \cdot \vec{u} = \frac{\partial}{\partial r} u_r + \frac{B_\theta}{a} \frac{\partial}{\partial \theta} \frac{u_\theta}{B_\theta} \tag{A.7}$$

A.3 Assumptions

We work with the continuity equation $\nabla \cdot n\vec{v} = S$. We will make the assumption that the particle source due to ionization is zero, so we have: $\nabla \cdot n\vec{v} = 0$. In the case where transport is zero and we have toroidal symmetry, the simple result is that $\partial/\partial\theta = 0$, or $nv_\theta/B_\theta = \text{const}$. We now make the assumption that the transport not generally zero, and has a divergence localized to the low-field side (LFS). This divergence is balanced by a divergence in the poloidal flow such that:

$$\frac{nv_\theta}{B_\theta} = \begin{cases} k(r) \sin\theta & (|\theta| < \frac{\pi}{2}) \\ k(r) & (|\theta| \geq \frac{\pi}{2}) \end{cases} \tag{A.8}$$

we can identify the constant as:

$$k(r) = \left. \frac{nv_\theta}{B_\theta} \right|_{HFS} \tag{A.9}$$

A.4 Derivation

Given the above assumptions, we now express the radial particle flux at the LFS in terms of the poloidal particle flux on the HFS. We have, from Eqn. A.7:

$$\frac{\partial}{\partial r} a n v_r = -B_\theta \frac{\partial}{\partial \theta} \frac{n v_\theta}{B_\theta} \tag{A.10}$$

$$\frac{\partial}{\partial r} a n v_r = -B_\theta \frac{\partial}{\partial \theta} \begin{cases} k(r) \sin\theta & (|\theta| < \frac{\pi}{2}) \\ k(r) & (|\theta| > \frac{\pi}{2}) \end{cases} \tag{A.11}$$

$$\frac{\partial}{\partial r} a n v_r = -B_\theta \begin{cases} k(r) \cos\theta & (|\theta| < \frac{\pi}{2}) \\ 0 & (|\theta| > \frac{\pi}{2}) \end{cases} \tag{A.12}$$

Evaluating this expression at the LFS ($\theta = 0$) gives:

$$\frac{\partial}{\partial r} a n v_r \bigg|_{LFS} = -B_{\theta,LFS} k(r) \tag{A.13}$$

We now integrate with respect to r, producing:

$$a n v_r|_{LFS} = \int_{wall}^{r} \mathrm{d}r B_\theta|_{LFS} k(r) + a n v_r|_{wall} \tag{A.14}$$

$$n v_r|_{LFS} = \frac{1}{a} \int_{wall}^{r} \mathrm{d}r B_\theta|_{LFS} \frac{n v_\theta}{B_\theta} \bigg|_{HFS} + n v_r|_{wall} \tag{A.15}$$

We now use the fact that the B_θ's vary little over the extent of the SOL to remove them from the integral:

$$n v_r|_{LFS} = \frac{1}{a} \frac{B_{\theta,LFS}}{B_{\theta,HFS}} \int_{wall}^{r} \mathrm{d}r \; n v_\theta|_{HFS} + n v_r|_{wall} \tag{A.16}$$

Note that $\frac{B_{\theta,LFS}}{B_{\theta,HFS}}$ can also be written as $\frac{1-\varepsilon}{1+\varepsilon}$. For Alcator C-Mod in typical operating conditions, we have $\varepsilon \approx 0.3$, $\frac{1-\varepsilon}{1+\varepsilon} \approx 0.54$ and $1/a \approx 5$ m^{-1} so the result is:

$$nv_r|_{LFS} = 2.7 \int_{wall}^{r} \mathrm{d}r \; nv_\theta|_{HFS} + nv_r|_{wall} \tag{A.17}$$

Bibliography

[1] I. H. Hutchinson, R. Boivin, F. Bombarda, P. Bonoli, S. Fairfax, C. Fiore, J. Goetz, S. Golovato, R. Granetz, M. Greenwald, S. Horne, A. Hubbard, J. Irby, B. LaBombard, B. Lipschultz, and et al. First results from Alcator-C-MOD. *Physics of Plasmas*, 1:1511–1518, May 1994.

[2] N. Asakura, ITPA SOL, and Divertor Topical Group. Understanding the SOL flow in L-mode plasma on divertor tokamaks, and its influence on the plasma transport. *Journal of Nuclear Materials*, 363:41–51, June 2007.

[3] C. F. Figarella, S. Benkadda, P. Beyer, X. Garbet, and I. Voitsekhovitch. Transport Reduction by Rotation Shear in Tokamak-Edge Turbulence. *Physical Review Letters*, 90(1):015002, January 2003.

[4] John Wesson. *Tokamaks*, section 4.4, pages 149–152. Oxford University Press, New York, NY, second edition, 1997.

[5] Ian H. Hutchinson. *Principles of Plasma Diagnostics*, chapter 3. Cambridge University Press, 40 West 20th Street New York, NY 10011-4211, USA, second edition, 2002.

[6] B. LaBombard. An interpretation of fluctuation induced transport derived from electrostatic probe measurements. *Physics of Plasmas*, 9:1300–1311, April 2002.

[7] P. C. Stangeby. Plasma sheath transmission factors for tokamak edge plasmas. *Physics of Fluids*, 27:682–690, March 1984.

[8] R. A. Langley, J. Bohdansky, W. Eckstein, P. Mioduszewski, J. Roth, E. Taglauer, E. W. Thomas, H. Verbeek, and K. L. Wilson. Data Compendium for Plasma-Surface Interactions. *Nuclear Fusion*, Special Issue, August 1984.

[9] C. S. Maclatchy, C. Boucher, D. A. Poirier, and J. Gunn. Gundestrup: A Langmuir/Mach probe array for measuring flows in the scrape-off layer of TdeV. *Review of Scientific Instruments*, 63:3923–3929, August 1992.

[10] I. H. Hutchinson. The magnetic presheath boundary condition with $E \times B$ drifts. *Physics of Plasmas*, 3:6–7, January 1996.

[11] I. H. Hutchinson. Oblique ion collection in the drift approximation: How magnetized Mach probes really work. *Physics of Plasmas*, 15(12):123503, December 2008.

[12] B. D. Scott. Drift wave versus interchange turbulence in tokamak geometry: Linear versus nonlinear mode structure. *Physics of Plasmas*, 12(6):062314, June 2005.

[13] J. R. Myra and D. A. D'Ippolito. Edge instability regimes with applications to blob transport and the quasicoherent mode. *Physics of Plasmas*, 12(9):092511, September 2005.

[14] A. Y. Pigarov, S. I. Krasheninnikov, B. LaBombard, and T. D. Rognlien. Simulation of Parallel SOL Flows with UEDGE. *Contributions to Plasma Physics*, 48:82–88, March 2008.

[15] G. S. Kirnev, G. Corrigan, D. Coster, S. K. Erents, W. Fundamenski, G. F. Matthews, and R. A. Pitts. EDGE2D code simulations of SOL flows and in out divertor asymmetries in JET. *Journal of Nuclear Materials*, 337:271–275, March 2005.

[16] J.D. Elder, A.G. McLean, P.C. Stangeby, S.L. Allen, J.A. Boedo, B.D. Bray, N.H. Brooks, M.E. Fenstermacher, M. Groth, A.W. Leonard, D.L. Rudakov, W.R. Wampler, J.G. Watkins, W.P. West, and D.G. Whyte. Indications of an inward pinch in the inner SOL of DIII-D from 13C deposition experiments. *Journal of Nuclear Materials*, 390-391:376 – 379, 2009. Proceedings of the 18th International Conference on Plasma-Surface Interactions in Controlled Fusion Device, Proceedings of the 18th International Conference on Plasma-Surface Interactions in Controlled Fusion Device.

[17] M. Groth, S. L. Allen, J. A. Boedo, N. H. Brooks, J. D. Elder, M. E. Fenstermacher, R. J. Groebner, C. J. Lasnier, A. G. McLean, A. W. Leonard, S. Lisgo, G. D. Porter, M. E. Rensink, T. D. Rognlien, D. L. Rudakov, P. C. Stangeby, W. R. Wampler, J. G. Watkins, W. P. West, and D. G. Whyte. Scrape-off layer transport and deposition studies in DIII-D. *Physics of Plasmas*, 14(5):056120, May 2007.

[18] B. LaBombard. An adaptation of perpendicular Mach probe theory to the C-Mod pyramidal Mach probe. Internal C-Mod Memo, March 2005.

[19] B. LaBombard, J.E. Rice, A.E. Hubbard, J.W. Hughes, M. Greenwald, J. Irby, Y. Lin, B. Lipschultz, E.S. Marmar, C.S. Pitcher, N. Smick, S.M. Wolfe, S.J. Wukitch, and the Alcator Group. Transport-driven scrape-off-layer flows and the boundary conditions imposed at the magnetic separatrix in a tokamak plasma. *Nuclear Fusion*, 44(10):1047–1066, 2004.

[20] B. Lipschultz, J. L. Terry, C. Boswell, A. Hubbard, B. LaBombard, and D. A. Pappas. Ultrahigh Densities and Volume Recombination inside the Separatrix

of the Alcator C-Mod Tokamak. *Physical Review Letters*, 81:1007–1010, August 1998.

[21] I. H. Hutchinson, J. A. Goetz, D. F. Jablonski, B. LaBombard, B. Lipschultz, G. M. McCracken, J. A. Snipes, and J. L. Terry. Particle drift effects on the Alcator C-Mod divertor. *Plasma Physics and Controlled Fusion*, 38:A301–A309, 1996.

[22] D. Jablonski, B. LaBombard, G. M. McCracken, S. Lisgo, B. Lipschultz, I. H. Hutchinson, J. Terry, and P. C. Stangeby. Local impurity puffing as a scrape-off layer diagnostic on the alcator c-mod tokamak. *Journal of Nuclear Materials*, 241-243:782 – 787, 1997.

[23] C. S. Pitcher, B. LaBombard, R. Danforth, W. Pina, M. Silveira, and B. Parkin. Divertor bypass in the Alcator C-Mod tokamak. *Review of Scientific Instruments*, 72:103–107, January 2001.

[24] N. Smick, B. LaBombard, and C. S. Pitcher. Plasma profiles and flows in the high-field side scrape-off layer in Alcator C-Mod. *Journal of Nuclear Materials*, 337:281–285, March 2005.

[25] N. Smick and B. Labombard. Wall scanning probe for high-field side plasma measurements on Alcator C-Mod. *Review of Scientific Instruments*, 80(2):023502–+, February 2009.

[26] Spec Finger Spring Washers: model numbers F0595-010, F0728-006.

[27] B. LaBombard and L. Lyons. Mirror Langmuir probe: A technique for real-time measurement of magnetized plasma conditions using a single Langmuir electrode. *Review of Scientific Instruments*, 78(7):073501, July 2007.

[28] Huber and Suhner SMA connecters: model numbers 11SMA-50-2-65/119NE, 21SMA-50-2-15/111NE.

[29] L. L. Lao, H. St.John, R. D. Stambaugh, A. G. Kellman, and W. Pfeiffer. Reconstruction of current profile parameters and plasma shapes in tokamaks. *Nuclear Fusion*, 25:1611–1622, 1985.

[30] I. H. Hutchinson, S. Horne, G. Tinios, Wolfe S. M., and R. S. Granetz. Plasma shape control: A general approach and its application to Alcator C-Mod. Technical report, MIT Plasma Science and Fusion Center, 2001.

[31] Brian LaBombard. T_e at the separatrix in C-Mod. Technical report, MIT Plasma Science and Fusion Center, 2000.

[32] Rachel M McDermott. *Edge Radial Electric Field Studies Via Charge Exchange Recombination Spectroscopy*. PhD dissertation, Massachusetts Institute of Technolmogy, Department of Nuclear Science and Engineering, 2009.

[33] R. M. McDermott, B. Lipschultz, J. W. Hughes, P. J. Catto, A. E. Hubbard, I. H. Hutchinson, R. S. Granetz, M. Greenwald, B. LaBombard, K. Marr, M. L. Reinke, J. E. Rice, D. Whyte, and Alcator C-Mod Team. Edge radial electric field structure and its connections to H-mode confinement in Alcator C-Mod plasmas. *Physics of Plasmas*, 16(5):056103, May 2009.

[34] The Alcator C-Mod Group, B. Lipschultz, Y. Lin, E. S. Marmar, D. G. Whyte, S. Wukitch, I. H. Hutchinson, J. Irby, B. LaBombard, M. L. Reinke, J. L. Terry, G. Wright, and The Alcator C-Mod Group. Influence of boronization on operation with high-Z plasma facing components in Alcator C-Mod. *Journal of Nuclear Materials*, 363:1110–1118, June 2007.

[35] Alexander T Graf. *Doppler Measurements in the Edge of the Alcator C-Mod Tokamak using a High-Resolution Visible Spectrometer*. PhD dissertation, University of California, Davis, Department of Physics, 2008.

[36] I. Cziegler, J. L. Terry, and B. LaBombard. Structure of the Broadband Edge Turbulence in L-mode and pre-H-mode Plasmas in Alcator C-Mod. *APS Meeting Abstracts*, page 3010, November 2007.

[37] Bálint Vető. Fast photodiode diagnostic on Alcator C-Mod tokamak to study the plasma edge/SOL structure. Masters thesis, Massachusetts Institute of Technology, Department of Nuclear Science and Engineering, sept 2005.

[38] S. J. Wukitch, Y. Lin, B. Lipschultz, A. Parisot, M. Reinke, P. T. Bonoli, M. Porkolab, I. H. Hutchinson, and E. Marmar. ICRF Performance with Metallic Plasma Facing Components in Alcator C-Mod. In P. Ryan and D. Rasmussen, editors, *Radio Frequency Power in Plasmas*, volume 933 of *American Institute of Physics Conference Series*, pages 75–82, September 2007.

[39] J. R. Myra, D. A. D'Ippolito, D. A. Russell, L. A. Berry, E. F. Jaeger, and M. D. Carter. Nonlinear ICRF-plasma interactions. *Nuclear Fusion*, 46:455, July 2006.

[40] J. A. Snipes, R. S. Granetz, M. Greenwald, I. H. Hutchinson, D. Garnier, J. A. Goetz, S. N. Golovato, A. Hubbard, J. H. Irby, B. LaBombard, T. Luke, E. S. Marmar, A. Niemczewski, P. C. Stek, Y. Takase, J. L. Terry, and S. M. Wolfe. LETTER: First ohmic H modes in ALCATOR C-MOD. *Nuclear Fusion*, 34:1039–1044, July 1994.

[41] X. Bonnin, D. Coster, R. Schneider, D. Reiter, V. Rozhansky, and S. Voskoboynikov. Modelling and consequences of drift effects in the edge plasma of alcator c-mod. *Journal of Nuclear Materials*, 337-339:301 – 304, 2005. PSI-16.

[42] C. J. Boswell, J. L. Terry, B. LaBombard, B. Lipschultz, and C. S. Pitcher. Interpretation of the D_α emission from the high field side of Alcator C-Mod. *Plasma Physics and Controlled Fusion*, 46:1247–1257, August 2004.

[43] M. Kočan and J. P. Gunn. First evidence for poloidal asymmetries of radial ion energy transport by ion temperature measurements in the scrape-off layer of Tore Supra. *Presented at EPS*, P2.203, 2009.

[44] S. I. Braginskii. Transport processes in a plasma. In M. A. Leontovich, editor, *Reviews of Plasma Physics*, volume 1, pages 205–311. Consultants Bureau Enterprises, Inc., New York, 1965.

[45] P. C. Stangeby and A. V. Chankin. Simple models for the radial and poloidal $E \times B$ drifts in the scrape-off layer of a divertor tokamak: Effects on in/out asymmetries. *Nuclear Fusion*, 36:839–852, July 1996.

[46] I. H. Hutchinson, B. LaBombard, J. A. Goetz, B. Lipschultz, G. M. McCracken, J. A. Snipes, and J. L. Terry. The effects of field reversal on the Alcator C-Mod divertor. *Plasma Physics and Controlled Fusion*, 37:1389–1406, December 1995.

[47] J. P. Gunn, C. Boucher, P. Devynck, I. Ďuran, K. Dyabilin, J. Horaček, M. Hron, J. Stöckel, G. van Oost, H. van Goubergen, and F. Žáček. Edge flow measurements with Gundestrup probes. *Physics of Plasmas*, 8:1995–2001, May 2001.

[48] G. F. Matthews, S. J. Fielding, G. M. McCracken, C. S. Pitcher, P. C. Stangeby, and M. Ulrickson. Investigation of the fluxes to a surface at grazing angles of incidence in the tokamak boundary. *Plasma Physics and Controlled Fusion*, 32:1301–1320, December 1990.

[49] J. L. Terry, S. J. Zweben, O. Grulke, M. J. Greenwald, and B. LaBombard. Velocity fields of edge/Scrape-Off-Layer turbulence in Alcator C-Mod. *Journal of Nuclear Materials*, 337:322–326, March 2005.

[50] S. Gangadhara and B. LaBombard. Impurity plume experiments in the edge plasma of the Alcator C-Mod tokamak. *Plasma Physics and Controlled Fusion*, 46:1617–1646, October 2004.

[51] Sanjay Gangadhara. *Physics and Application of Impurity Plume Dispersal as an Edge Plasma Flow Diagnostic on the Alcator C-Mod Tokamak*. PhD dissertation, Massachusetts Institute of Technology, 77 Massachusetts Avenue, Cambridge, MA, march 2003.

[52] R. W. P. McWhirter. Spectral intensities. In S.L. Leonard R. H. Huddlestone, editor, *Plasma Diagnostic Techniques*. Academic Press, New York, 1965.

[53] D. Jablonski. Local impurity puffing as a scrape-off layer diagnostic on the Alcator C-Mod tokamak. *Journal of Nuclear Materials*, 241:782–787, February 1997.

[54] J. E. Rice, E. S. Marmar, F. Bombarda, and L. Qu. X-ray observations of central toroidal rotation in ohmic Alcator C-Mod plasmas. *Nuclear Fusion*, 37:421–426, March 1997.

[55] J. E. Rice, A. C. Ince-Cushman, M. L. Reinke, Y. Podpaly, M. J. Greenwald, B. LaBombard, and E. S. Marmar. Spontaneous core toroidal rotation in Alcator C-Mod L-mode, H-mode and ITB plasmas. *Plasma Physics and Controlled Fusion*, 50(12):124042, December 2008.

[56] J. E. Rice, A. Ince-Cushman, J. S. de Grassie, L.-G. Eriksson, Y. Sakamoto, A. Scarabosio, A. Bortolon, K. H. Burrell, B. P. Duval, C. Fenzi-Bonizec, M. J. Greenwald, R. J. Groebner, G. T. Hoang, Y. Koide, E. S. Marmar, A. Pochelon, and Y. Podpaly. Inter-machine comparison of intrinsic toroidal rotation in tokamaks. *Nuclear Fusion*, 47:1618–1624, November 2007.

[57] J. E. Rice, W. D. Lee, E. S. Marmar, P. T. Bonoli, R. S. Granetz, M. J. Greenwald, A. E. Hubbard, I. H. Hutchinson, J. H. Irby, Y. Lin, D. Mossessian, J. A. Snipes, S. M. Wolfe, and S. J. Wukitch. Observations of anomalous momentum transport in Alcator C-Mod plasmas with no momentum input. *Nuclear Fusion*, 44:379–386, March 2004.

[58] J. E. Rice, W. D. Lee, E. S. Marmar, N. P. Basse, P. T. Bonoli, M. J. Greenwald, A. E. Hubbard, J. W. Hughes, I. H. Hutchinson, A. Ince-Cushman, J. H. Irby, Y. Lin, D. Mossessian, J. A. Snipes, S. M. Wolfe, S. J. Wukitch, and K. Zhurovich. Toroidal rotation and momentum transport in Alcator C-Mod plasmas with no momentum input. *Physics of Plasmas*, 11:2427–2432, May 2004.

[59] J. E. Rice, A. E. Hubbard, J. W. Hughes, M. J. Greenwald, B. LaBombard, J. H. Irby, Y. Lin, E. S. Marmar, D. Mossessian, S. M. Wolfe, and S. J. Wukitch. The dependence of core rotation on magnetic configuration and the relation to the H-mode power threshold in Alcator C-Mod plasmas with no momentum input. *Nuclear Fusion*, 45:251–257, April 2005.

[60] W. D. Lee, J. E. Rice, E. S. Marmar, M. J. Greenwald, I. H. Hutchinson, and J. A. Snipes. Observation of Anomalous Momentum Transport in Tokamak Plasmas with No Momentum Input. *Physical Review Letters*, 91(20):205003, November 2003.

[61] B. LaBombard, J. E. Rice, A. E. Hubbard, J. W. Hughes, M. Greenwald, R. S. Granetz, J. H. Irby, Y. Lin, B. Lipschultz, E. S. Marmar, K. Marr, D. Mossessian, R. Parker, W. Rowan, N. Smick, J. A. Snipes, J. L. Terry, S. M. Wolfe, and S. J. Wukitch. Transport-driven scrape-off layer flows and the x-point dependence of the L-H power threshold in Alcator C-Mod. *Physics of Plasmas*, 12(5):056111, May 2005.

[62] P. W. Terry. Suppression of turbulence and transport by sheared flow. *Reviews of Modern Physics*, 72:109–165, January 2000.

[63] B. N. Rogers, J. F. Drake, and A. Zeiler. Phase Space of Tokamak Edge Turbulence, the L-H Transition, and the Formation of the Edge Pedestal. *Physical Review Letters*, 81:4396–4399, November 1998.

[64] T. Cho, J. Kohagura, M. Hirata, T. Numakura, H. Higaki, H. Hojo, M. Ichimura, K. Ishii, K. M. Islam, A. Itakura, I. Katanuma, Y. Nakashima, T. Saito, Y. Tatematsu, M. Yoshikawa, Y. Takemura, A. Kojima, T. Kobayashi, Y. Yamaguchi, Y. Miyata, N. Yokoyama, Y. Tomii, Y. Miyake, S. Kiminami, K. Shimizu, Y. Kubota, H. Saimaru, Y. Higashizono, A. Mase, Y. Yasaka, K. Ogura, K. Sakamoto, M. Yoshida, V. P. Pastukhov, T. Imai, S. Miyoshi, and GAMMA 10 Group. Progress in potential formation and findings in the associated radially sheared electric-field effects on suppressing intermittent turbulent vortex-like fluctuations and reducing transverse losses. *Nuclear Fusion*, 45:1650–1657, December 2005.

[65] B. LaBombard, N. Smick, A. Graf, K. Marr, R. McDermott, M. Reinke, M. Greenwald, J. W. Hughes, B. Lipschultz, J. L. Terry, and D. G. Whyte. Relationship between Edge Gradients and Plasma Flows in Alcator C-Mod. *APS Meeting Abstracts*, page 3007, November 2008.

[66] M. V. Umansky, J. Boedo, B. LaBombard, R. Maqueda, J. Terry, and S. Zweben. Simulation of turbulence in tokamak edge plasmas. *APS Meeting Abstracts*, page 8080P, November 2007.

[67] B. LaBombard, J. W. Hughes, N. Smick, A. Graf, K. Marr, R. McDermott, M. Reinke, M. Greenwald, B. Lipschultz, J. L. Terry, D. G. Whyte, S. J. Zweben, and Alcator C-Mod Team. Critical gradients and plasma flows in the edge plasma of Alcator C-Mod. *Physics of Plasmas*, 15(5):056106, May 2008.

[68] P. N. Guzdar, J. F. Drake, D. McCarthy, A. B. Hassam, and C. S. Liu. Three-dimensional fluid simulations of the nonlinear drift-resistive ballooning modes in tokamak edge plasmas. *Physics of Fluids B*, 5:3712–3727, October 1993.

[69] X. Bonnin. Improved modelling of detachment and neutral-dominated regimes using the ? code. *Journal of Nuclear Materials*, 313:909–913, March 2003.

[70] B. LaBombard. Experimental investigation of transport phenomena in the scrape-off layer and divertor. *Journal of Nuclear Materials*, 241:149–166, February 1997.

[71] N. Asakura, H. Takenaga, S. Sakurai, H. Tamai, A. Sakasai, K. Shimizu, and G. D. Porter. Particle control and SOL plasma flow in the W-shaped divertor of JT-60U tokamak. *Plasma Physics and Controlled Fusion*, 44:2101–2119, October 2002.

[72] R. A. Pitts, P. Andrew, X. Bonnin, A. V. Chankin, Y. Corre, G. Corrigan, D. Coster, I. Duran, T. Eich, S. K. Erents, W. Fundamenski, A. Huber, S. Jachmich, G. Kirnev, M. Lehnen, P. J. Lomas, A. Loarte, G. F. Matthews, J. Rapp, C. Silva, M. F. Stamp, J. D. Strachan, E. Tsitrone, and Contributors To The Efda-Jet Workprogramme. Edge and divertor physics with reversed toroidal field in JET. *Journal of Nuclear Materials*, 337:146–153, March 2005.

[73] R. A. Pitts, R. Chavan, S. J. Davies, S. K. Erents, G. Kaveney, G. F. Matthews, G. Neill, J. E. Vince, and I. Duran. Retarding field energy analyzer for the JET plasma boundary. *Review of Scientific Instruments*, 74:4644–4657, November 2003.

[74] D. Pfirsch and A. Schlüter. Der einfluss der elecktrischen Leitfähigkeit auf das gleichgewichtsverhalten von plasmen neidrigen drucks in stellaratoren. Technical Report MPI/PA/8/62, Max-Planck-Institut, 1962.

[75] P. J. Catto and A. N. Simakov. Magnetic topology effects on Alcator C-Mod flows. *Physics of Plasmas*, 13(5):052507, May 2006.

[76] P. J. Catto and A. N. Simakov. Erratum: "Magnetic topology effects on Alcator C-Mod flows" [Phys. Plasmas 13, 052507 (2006)]. *Physics of Plasmas*, 14(2):029901, February 2007.

[77] R. A. Pitts, J. Horacek, W. Fundamenski, O. E. Garcia, A. H. Nielsen, M. Wischmeier, V. Naulin, and J. Juul Rasmussen. Parallel SOL flow on TCV. *Journal of Nuclear Materials*, 363:505–510, June 2007.

[78] J. P. Gunn, C. Boucher, M. Dionne, I. Ďuran, V. Fuchs, T. Loarer, I. Nanobashvili, R. Pánek, J.-Y. Pascal, F. Saint-Laurent, J. Stöckel, T. van Rompuy, R. Zagórski, J. Adámek, J. Bucalossi, R. Dejarnac, P. Devynck, P. Hertout, M. Hron, G. Lebrun, P. Moreau, F. Rimini, A. Sarkissian, and G. van Oost. Evidence for a poloidally localized enhancement of radial transport in the scrape-off layer of the Tore Supra tokamak. *Journal of Nuclear Materials*, 363:484–490, June 2007.

[79] A. V. Chankin and P. C. Stangeby. The effect of diamagnetic drift on the boundary conditions in tokamak scrape-off layers and the distribution of plasma fluxes near the target. *Plasma Physics and Controlled Fusion*, 36:1485–1499, September 1994.

[80] Brian LaBombard. KN1D: A 1-D space, 2-D velocity, kinetic transport algorithm for atomic and molecular hydrogen in an ionizing plasma. Technical report, MIT Plasma Science and Fusion Center, 2001.